Structural Features and Thermoelectric Properties

of PbTe-based Materials

DISSERTATION

zur Erlangung des akademischen Grades

Doctor rerum naturalium

(Dr. rer. nat.)

vorgelegt

dem Bereich Mathematik und Naturwissenschaften

der Technischen Universität Dresden

von

M. Eng. Xinke Wang

geboren am 28.08.1989 in Henan, China

Eingereicht am 26.02.2019

Die Dissertation wurde in der Zeit von 07 / 2015 bis 01 / 2019

am Max-Planck-Institut für Chemische Physik fester Stoffe angefertigt.

Day of defense: May 06, 2019

Referees: Prof. Juri Grin

               Prof. Dr. Michael Ruck

Abstract

Thermoelectric (TE) materials are used to directly interconvert heat and electricity. The semiconductor PbTe with narrow band gap is one of the leading thermoelectric materials in mid-temperature range due to intrinsically low lattice thermal conductivity and large Seebeck coefficient. Recently, various strategies have produced p-type and n-type PbTe-based materials with greatly enhanced TE properties. However, there are still many fascinating features which are needed to be studied. First, phase analysis and TE properties of binary polycrystalline Pb–Te samples prepared by various heat treatments have been investigated. Since europium with its $4f$ electrons was expected to have strong influence on the thermoelectric behavior of PbTe, the constitution and thermoelectric behavior of two substitution schemes with possible Eu^{2+} and Eu^{3+} in the Pb–Eu–Te ternary system have been examined. As sodium is widely used as substituting element for p-type PbTe-based TE materials, the crystal structural features and TE properties of two series of polycrystalline samples $Pb_{1-y}Na_yTe_{1-y/2}$ and $Pb_{1-x}Na_xTe$ have been studied. The local atomic arrangement of sodium by different substitution schemes has been revealed by NMR. Finally, we present the reproducibility of TE properties and microstructure evolutions of high-ZT Eu-substituted and Na-substituted PbTe during different heat treatments. From binary PbTe to ternary Pb–Eu–Te and Pb–Na–Te, and final with quaternary Pb–Eu–Na–Te, the comprehensive picture of the structure and TE properties for Pb–Eu–Na–Te system is constructed.

Contents

Contents

Contents

Index of Figures

Index of Figures

Index of Tables

1. Introduction

This chapter presents a general introduction about thermoelectrics, which includes thermoelectric (TE) effects, thermoelectric parameters, criteria for selection of the best thermoelectric materials, and methods for the improvement of the conversion efficiency. Following this, a readily comprehensive overview on current research on PbTe-based thermoelectric materials is provided. Finally, the goals of this dissertation, along with a summary of the main points, will be presented.

1.1. Thermoelectricity

In 1821, Thomas Johann Seebeck placed in direct contact a plate of bismuth with a plate of copper. He heated one of the corners and observed the needle movement in an electrically connected galvanometer (Figure 1.1). He also observed that a compass needle is deflected when placed near a closed loop formed from two different electrical conductors, if one of the junctions was heated.[1] This implied that the temperature resulted in an electric current in the wire and leaded to the generation of a magnetic field, that deflected the compass needle, known as Seebeck effect. If one side of *n*-type or *p*-type semiconductor material is heated and a lower temperature at the other side (Figure 1.2), the electron or hole charge carriers move faster (and thus have a lower density) at the hot side, resulting in diffusion of electrons/holes towards the cold side. An electric field is then created across the material due to the diffusion of charge carriers. An electrical potential difference (ΔV) forms with a temperature gradient between two sides of the material (ΔT). The Seebeck coefficient (S) is defined as:[2]

$$S = \frac{\Delta V}{\Delta T} \qquad (1.1)$$

1. Introduction
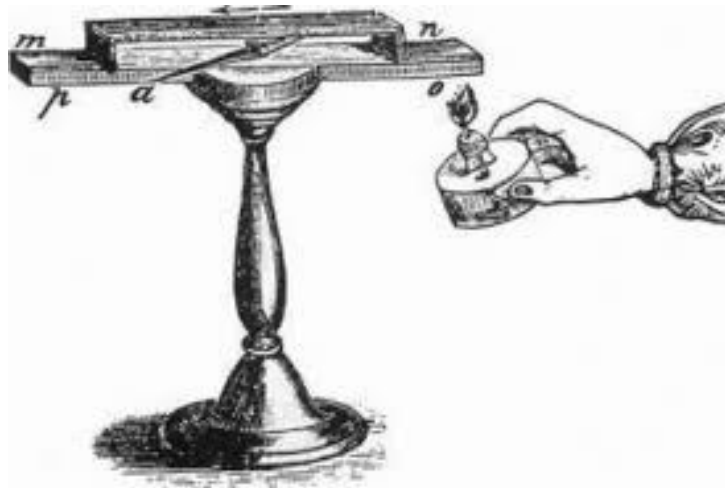
Figure 1.1. Drawing depicting Seebeck's experimental instrumentation. From Adolphe Ganot, Traité élémentaire de physique expérimentale et appliquée et de meteorologie: illustré de 568 belles gravures sure bois intercalées dans le texte !Paris: L'auteur-éditeur, 1859", p. 707.
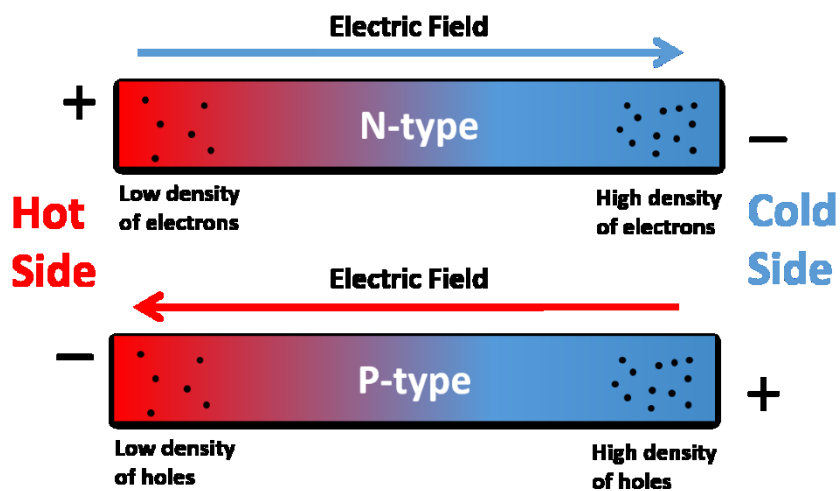
Figure 1.2. Thermal diffusion of the charge carriers in *p*- and *n*-type semiconductors (Seebeck effect).

Thermoelectric power generation is based on this effect and uses the conversion of heat directly into electricity. The inverse of the Seebeck effect was observed by Jean Charles Athanase Peltier in 1834. He found that temperature anomalies appeared near the junction between bismuth and antimony when an electric current passed through them, discovering the Peltier effect. The third thermoelectric effect called Thomson effect was observed by William Thomson: when a current passes through a material with a gradient of

temperature, the material exchanges heat with the outside medium. Conversely, a current is produced when a heat flux passes through a material with a temperature gradient.[2]

Thermoelectric energy converters have attracted considerable attention because of their advantages for solid-state operation, lack of mechanical moving parts, absence of greenhouse gases release, high reliability, good stability, and long operating life.[2-3] According to above-mentioned thermoelectric effects, the solid-state TE devices can directly convert heat from the sun, radioisotopes, industrial machines, automobiles, or even the human body to electricity. Conversely, electricity can drive a TE device to work as a solid-state heat pump for refrigeration.[4-5] They have been utilized or are currently at the trial stage in fields such as aerospace, transportation, medical services, military, electronics, temperature detecting and measuring instruments. Moreover, TE devices meet the demands for wasted energy harvesting and environmental protection.[2]

1.2. Thermoelectric figure-of-merit

TE devices appear to useful, while they are not widely used, due to low efficiency. In the early 1900s, E. Altenkirch expressed the relationship between physical properties and the efficiency of a simplified thermoelectric generator mathematically.[6] Later, Abram F. Ioffe incorporated these parameters into the thermoelectric figure-of-merit.[7] It shows that a good thermoelectric material should have high electrical conductivity to minimize Joule heating, low thermal conductivity to retain heat at the junctions and maintain a large temperature gradient, and a large Seebeck coefficient for maximum conversion of heat to electrical power or electrical power to cooling. The commonly used dimensionless figure-of-merit (ZT) of a thermoelectric material is defined as:

$$ZT = \frac{S^2 \cdot \sigma}{\kappa} T \qquad (1.2)$$

where S is the Seebeck coefficient (the S value is positive for p-type (hole) conduction and negative for n-type (electron) conduction), σ is the electrical conductivity, κ is the thermal conductivity and T is absolute temperature.[7-8] For power generation, the thermoelectric efficiency is defined by combining the Carnot efficiency ($\Delta T/T_{hot}$) and the figure-of-merit ZT, as shown in Equation 1.3:

$$\eta = \frac{\Delta T}{T_{hot}} \frac{\sqrt{1+ZT_{avg}}-1}{\sqrt{1+ZT_{avg}}+\frac{T_{cold}}{T_{hot}}} \qquad (1.3)$$

3

1. Introduction

where T_{cold} and T_{hot} are the temperature of the cold and hot ends in a thermoelectric module, $T_{avg} = (T_{cold} + T_{hot})/2$ and $\Delta T = T_{hot} - T_{cold}$. This equation indicates that increasing efficiency requires both high ZT values and a large temperature gradient across the thermoelectric materials.[9-11] Currently, the efficiency of TE devices is lower than other energy-conversion technologies because of the low ZT values (Figure 1.3). As shown in Figure 1.4, there are only a few state-of-the-art TE materials with the maximum ZT values between 1.0 and 2.5.[3] From an efficiency point, a ZT value around 4 is needed for thermoelectrics to compete with other energy-generation technologies.[3,12] However, any small improvement in thermoelectric efficiency will result in many new applications for these devices. This technology is environmentally cleaner and more reliable than traditional compressor systems. Therefore, it is worth exploring the possibility of increasing the figure-of-merit (ZT) of a thermoelectric material.
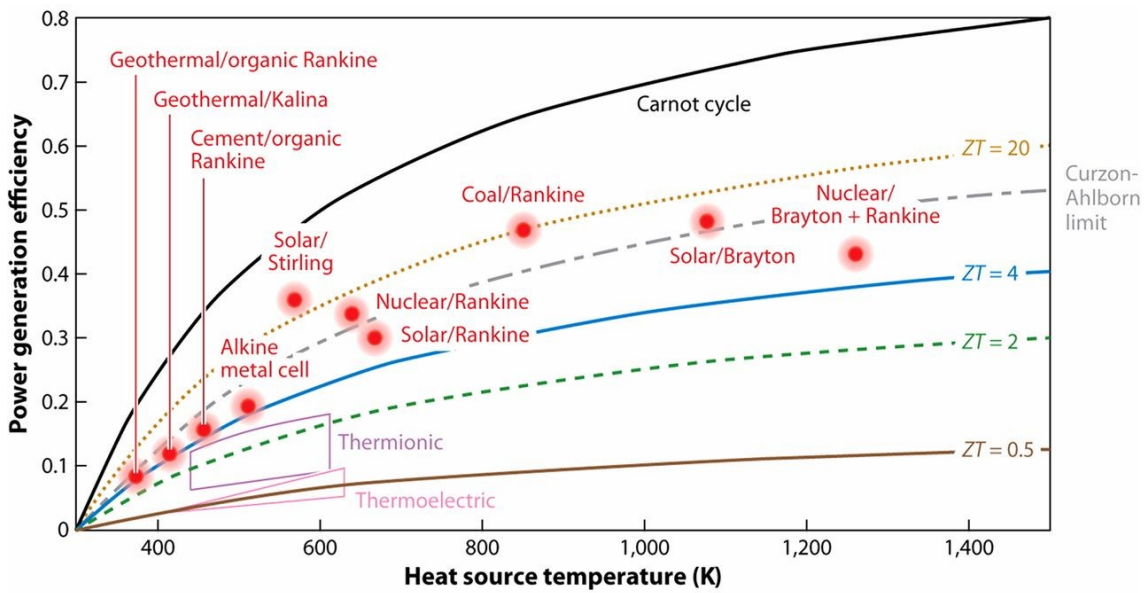
Figure 1.3. The efficiency comparison of thermoelectric with other energy-conversion technologies as a function of the heat-source temperature. The ZT values are assumed to be temperature independent, and the heat-sink temperature is set at room temperature. (He and Tritt, 2017)[3]
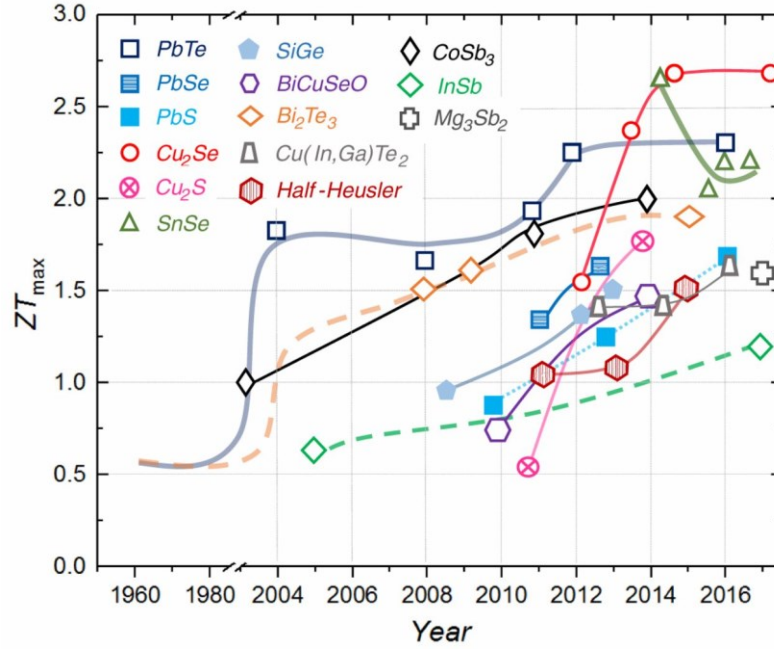
Figure 1.4. Timeline of the maximum *ZT* values for several representative families of TE materials. (He and Tritt, 2017)[3]

1.3. Optimization of thermoelectric performance

Through Eq. 1.2, the challenge to create high *ZT* thermoelectric materials lies in achieving simultaneously high electronic conductivity (σ), high Seebeck coefficient (*S*), and low thermal conductivity (*κ*) in the same material. These parameters are determined by the details of the electronic structure and scattering of charge carriers, and thus are not independently controllable.[9] Boltzmann transport theory describes both electrical and thermal transport in the vast majority of solids. This theory provides a general understanding of the Seebeck coefficient (*S*) and electrical conductivity (σ):

$$S = \frac{8\pi^2 k_B^2}{3eh^2} \; m^* T (\frac{\pi}{3n})^{2/3} \qquad (1.4)$$

$$\sigma = \frac{1}{\rho} = ne\mu \qquad (1.5)$$

where k_B is the Boltzmann constant, *e* is the carrier charge, *h* is Planck constant, m^* is the effective mass of the charge carrier, *ρ* is the electrical resistivity, *n* is the carrier concentration, and *μ* is the carrier mobility.[13-14] The quantity $S^2\sigma$ in Eq. 1.2 is called the power factor (PF) and is the key to achieving high performance. The Wiedemann−Franz law states that the total thermal conductivity is the sum of two independent components

1. Introduction

(Eq. 1.6), the lattice vibrations and charge carrier transports, called the lattice thermal conductivity (κ_L) and the electric thermal conductivity (κ_{el}):

$$\kappa = \kappa_{el} + \kappa_L \qquad (1.6)$$

$$\kappa_{el} = \sigma LT = ne\mu LT \qquad (1.7)$$

where L is the Lorentz number, typically taken as 2.45×10^{-8} W Ω K^{-2} for materials having a highly degenerate electron gas.[14-16] According to Eqs. 1.4–1.7, all thermoelectric parameters except for lattice thermal conductivity are related to charge carrier concentration. Figure 1.5 shows the fundamental challenge of designing high-ZT thermoelectric materials stems from the strong correlation of Seebeck coefficient, electrical conductivity and thermal conductivity in thermoelectric materials. It is possible to envision two approaches, aimed at increasing ZT: either the power factor ($S^2 \sigma$) is maximized or the thermal conductivity (κ) is minimized.[15,17]
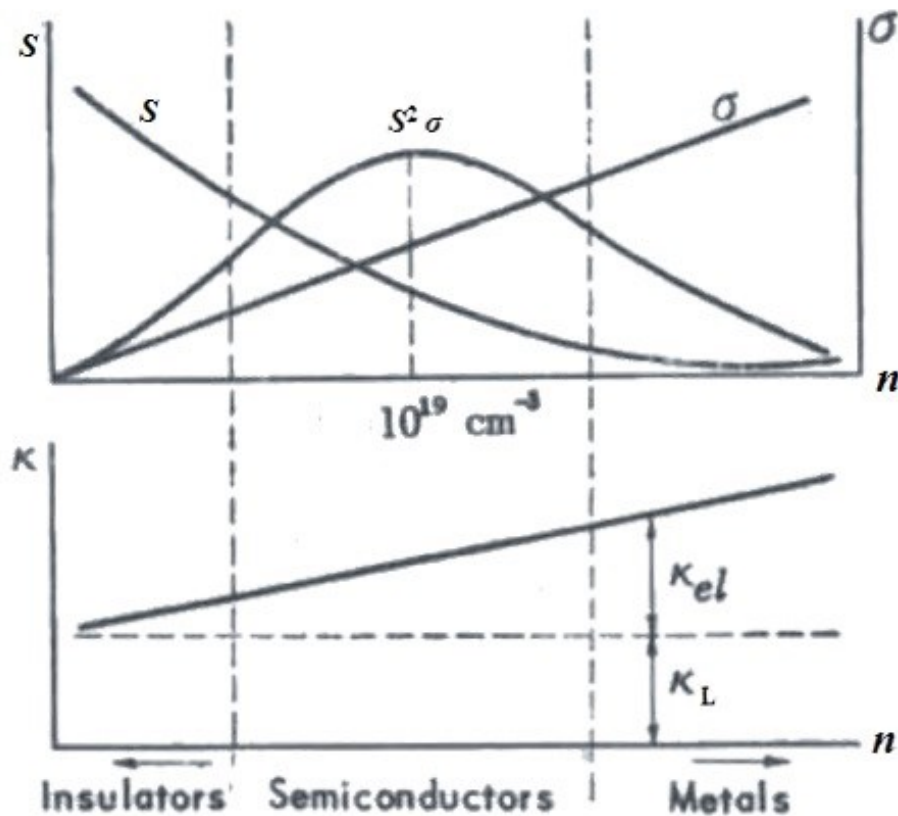
Figure 1.5. Variation of Seebeck coefficient S, electrical conductivity σ, thermal conductivity κ, and powder factor $S^2 \sigma$ as a function of charge carrier concentrations. (Ioffe, 1956)[7]

1.3.1. Increasing power factor

As discussed above, generally, the Seebeck coefficient and electrical conductivity change in opposite directions with charge carrier concentration (Figure 1.5), and thus there is an optimized set of values that should be achieved. That is why for semiconductors the basic strategy to increase power factor is optimizing carrier concentration.[9] However, to increase the power factor to much higher levels, one needs to carefully tailor the electronic structures and microstructures. Goldsmid was one of the first to utilize the thermoelectric merit factor, identifying the importance of high mobility and effective mass combination, along with low lattice thermal conductivity for good thermoelectric materials.[18] When the figure-of-merit is expressed in terms of the reduced Fermi energy for the region in which non-degenerate statistics can be employed, the dimensionless merit factor (β) of thermoelectric materials can be extracted, which was first introduced by Chasmar and Stratton:[20-21]

$$\beta = \left(\frac{k_B}{e}\right)^2 \frac{2e\mu T}{\kappa_L} \left(\frac{2\pi m^* k_B T}{h^2}\right)^{3/2} \qquad (1.8)$$

$$\beta \propto \left(\frac{\mu}{\kappa_L}\right) (m^*)^{3/2} \qquad (1.9)$$

$$m^* = (N_V)^{3/2} m_b^* \qquad (1.10)$$

where m^* is the effective mass of carriers and is related to the band effective mass m_b^* through the number of equivalent degenerated valleys of the band structure (N_V).[19-21] Thus, to increase the maximum thermoelectric properties, one needs to maximize μ, m_b^*, and N_V, and minimize κ_L (this will be discussed later) concurrently to achieve higher power factor but lower thermal conductivity.

1. Introduction
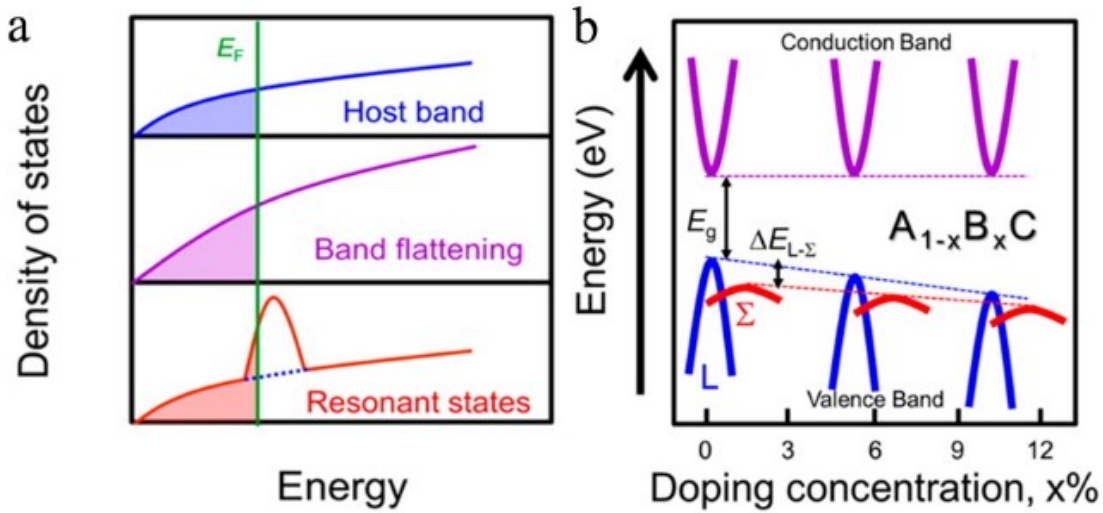
Figure 1.6. (a) Schematic representation of the density of states of a single valence band (blue line) contrasted to that of band flattening (purple line) and the introduction of resonant states (red line). (b) Band convergence effect by forming solid solution or increasing doping fraction. (Tan *et al.*, 2017)[19]

According to Eq.1.4, the common understanding of high Seebeck coefficient at a given carrier concentration is that it is due to the high effective mass m^*. The band effective mass m_b^* is related to the curvature of the bands and can be modified by distorting the band. This can increase the density of states in the vicinity of Fermi level.[19] Two commonly adopted approaches of enhancing m_b^* include band flattening[24-25] and resonant levels (Figure 1.6a).[26-27] However, the number of conducting bands and flatness of bands (high m_b^*) have different effects on the mobility and therefore the electrical conductivity. In most cases the increase of m_b^* will result in the decrease of carrier mobility and decrease the electrical conductivity. The mobility does not explicitly depend on the number of conducting bands, unless there is significant inter-valley scattering.[22] As a result, materials with large number of degenerate conducting bands are clearly beneficial to achieve high power factors. N_V is closely related to the crystal structure symmetry and can be large when the crystal structures are highly symmetric. One attractive way to increase the effective N_V is to converge different bands in the Brillouin zone within a few $k_B T$ in energy of each other (Figure 1.6b).[23,28-29] For carrier mobility improvement, three-dimensional (3D) modulation doping has been recently demonstrated to be effective in several relevant thermoelectric materials. Modulation-doped samples actually are two-phase composites made of undoped and heavily doped counterparts. The

heavily doped compound has high carrier concentrations but low carrier mobility, while the undoped pristine compound has low carrier concentration but high carrier mobility.[30-31] Other attempts to improve power factor including electron energy barrier filtering,[32-35] quantum confinement effects,[36-38] etc.

1.3.2. Reducing thermal conductivity

The minimization of thermal conductivity can come through solid-solution formation, the development of new materials with intrinsically low thermal conductivity, and structure engineering like nanostructuring. As discussed above, the lattice thermal conductivity is commonly regarded as the only independent material property of thermoelectric parameters. So usually, reduction of thermal conductivity mainly focuses on decreasing lattice thermal conductivity.[19,39]

In solid materials, the interaction between atoms produces displacements from their equilibrium lattice positions, leading to a set of vibrational waves with various wavelengths, called phonons. These phonons are heat carriers that would propagate through the lattice, which contribute to the lattice thermal conductivity κ_L.[40] Phonon waves can be scattered at crystal defects (e.g., point defects, dislocations, grain boundaries, interfaces, precipitates, etc. Figure 1.7), giving rise to additional thermal resistance and reducing κ_L.[41] According to the thermal conductivity model developed by Klemens[42] and Callaway,[43-44] mass contrast and strain field fluctuations caused by atomic point defects (formed by elemental substitution, Figure 1.7a) can significantly scatter the short-wavelength phonons, which contribute to the reduction of κ_L.
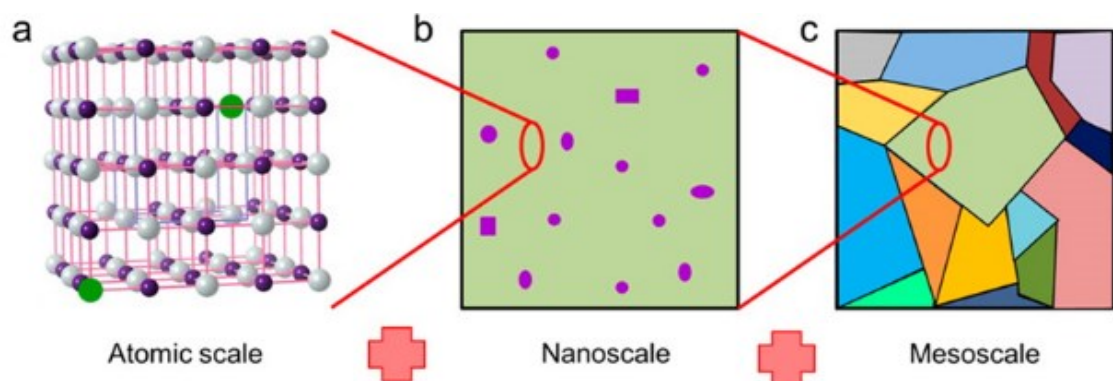
Figure 1.7. Schematic diagrams of (a) atomic-scale point defects, (b) nanoscale precipitates, and (c) mesoscale grains. (Tan *et al*., 2017)[19]

Nano-scaled defects in materials can scatter phonons with wavelengths on nanometer scale (Figure 1.7b). There are several approaches to achieving nano-scaled inhomogeneity, including ex-situ additions of guest phase by mechanical or chemical mixing[46-47] and in-situ second-phase precipitation through nucleation and growth.[48-50] For the long wavelengths, crystal defects and structure features at the length scale of micrometers or sub-micrometers are necessary (Figure 1.7c). This is so-called mesoscale, and it can be engineered into materials through careful powder processing.[19] When point defects, nanostructuring, and mesoscale structuring are all combined into a single material, we call this an all-scale hierarchical architecture.[45,51-52] In 1995, Glen Slack introduced the new concept of a "phonon glass and an electron single crystal" (PGEC), "a material that conducts heat like a glass but electricity like a crystal", which means that "a material in which the phonon mean free paths are as short as possible and in which the electron mean free paths are as long as possible".[53] Slack concluded that to be a good thermoelectric material it must be a small band-gap semiconductor formed by highly polarizable heavy elements, with electronegativity differences lower than 0.5, and with complex crystal structures containing "rattling" atoms or molecules.[15,54] Other attempts to reduce lattice thermal conductivity including lattice anharmonicity,[55-56] liquid phonons,[57-58] and bonding inhomogeneity and anisotropy,[59] etc.

1.4. PbTe-based thermoelectric materials

The development of thermoelectric materials has been greatly expanded in past half century. Inorganic materials are classic representatives used in thermoelectric research. Some examples include telluride-based materials ($PbTe$, Bi_2Te_3, etc.), Si–Ge, skutterudites, clathrates, half-Heusler (HH) alloys, chalcogenide compounds, copper ion liquid-like materials, metal oxides, BiCuSeO oxyselenides, etc.[9,15,60] New classes of materials such as carbon nanomaterials, electronically conducting polymers, and carbon nanomaterial/polymer nanocomposites have also been proposed recently.[61] The percentage contribution of these materials to thermoelectric research is presented in Figure 1.8, data was collected from Web of Science and SciFinder.[61]
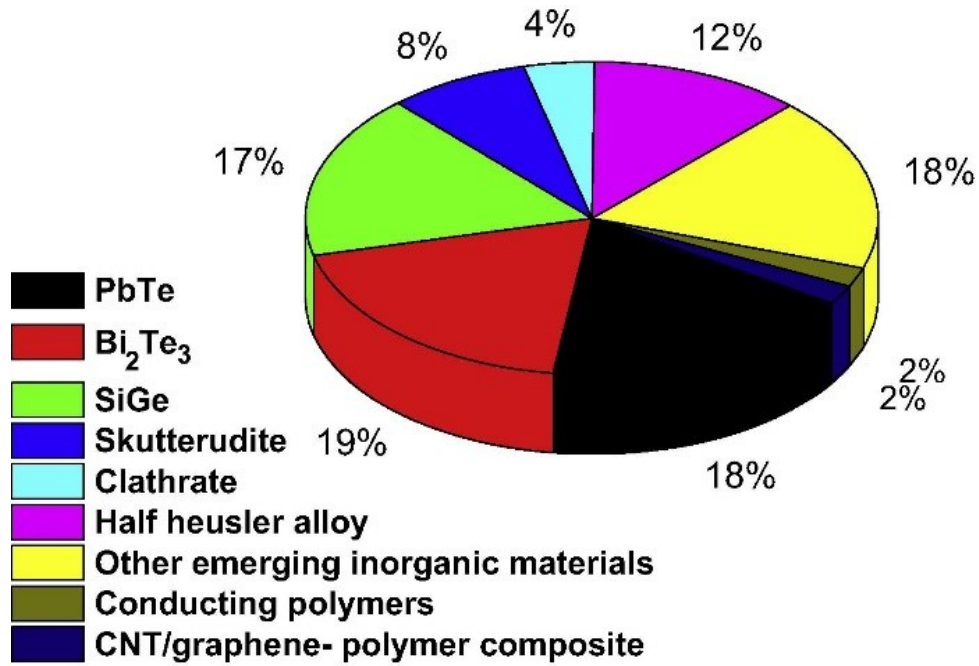
Figure 1.8. Materials used in thermoelectric research and development. (Gayner and Kar, 2016)[61]

With low thermal conductivity and suitable electronic transport properties, PbTe is one of conventional state-of-the-art thermoelectric materials that have been used for the past 50 years in the mid-temperature range.[62-63] In 1959, the first radioisotope thermoelectric generator (RTG) contained both *n*- and *p*-type PbTe materials to convert heat to electricity.[64-65] For over half a century PbTe-based thermoelectrics have successfully provided power for various NASA's missions.[2,10,66] Scientific reports on these materials started to appear in the literature in the 1950s and 1960s, and in the following period a vast amount of experimental data were gathered on PbTe-based materials for thermoelectric applications.[67-72] In this section, a brief overview will be given about phase stability, defect chemistry, local structure, and TE properties of PbTe-based thermoelectric materials.

Phase Stability

Compound semiconductor at temperature above 0 K exists as a stable phase over a range of composition near the stoichiometric proportions. This is possible through the incorporation of interstitial atoms, vacancies or anti-sites point defects.[73] Thermal analysis and microscopic studies on Pb–Te system suggested a negligible range of single phase stability (Figure 1.9).[74] However, in order to synthesize PbTe with specified

properties, more accurate data on the phase diagrams and the homogeneity regions of the compounds are required.
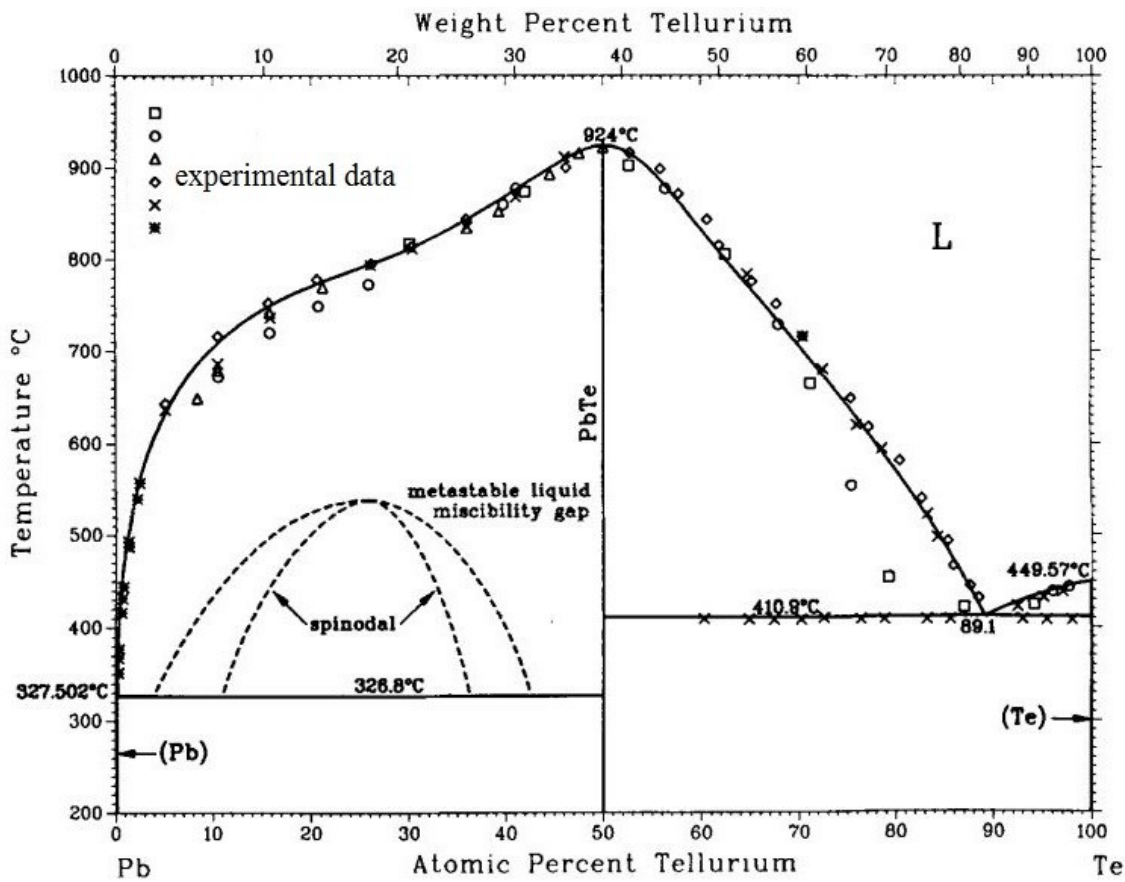
Figure 1.9. Phase diagram of PbTe. (Lin *et al.*, 1989)[75]

Since the stability range of PbTe is very narrow, typical techniques for measuring the solubility (metallography, powder X-ray diffraction) cannot be used. Instead, the measured hall carrier concentrations was used to compute the stability limits of PbTe, assuming that nonstoichiometry is caused by the presence of fully ionized vacancies on the Pb or Te sublattices.[73,76-78] Based on this method, the order of $x = 10^{-4}$ on both sides of the stoichiometric line at $x = 0.50$ was confirmed (Figure 1.10a, 1.10b).[73,75,79-83] The composition of the substance in equilibrium with the lead-rich liquid or tellurium-rich liquid, as a function of temperature, was established through a vapor diffusion process, which also revealed regions of retrograde solubility for both excess-lead and excess-tellurium specimens (Figure 1.10a).[73,84]
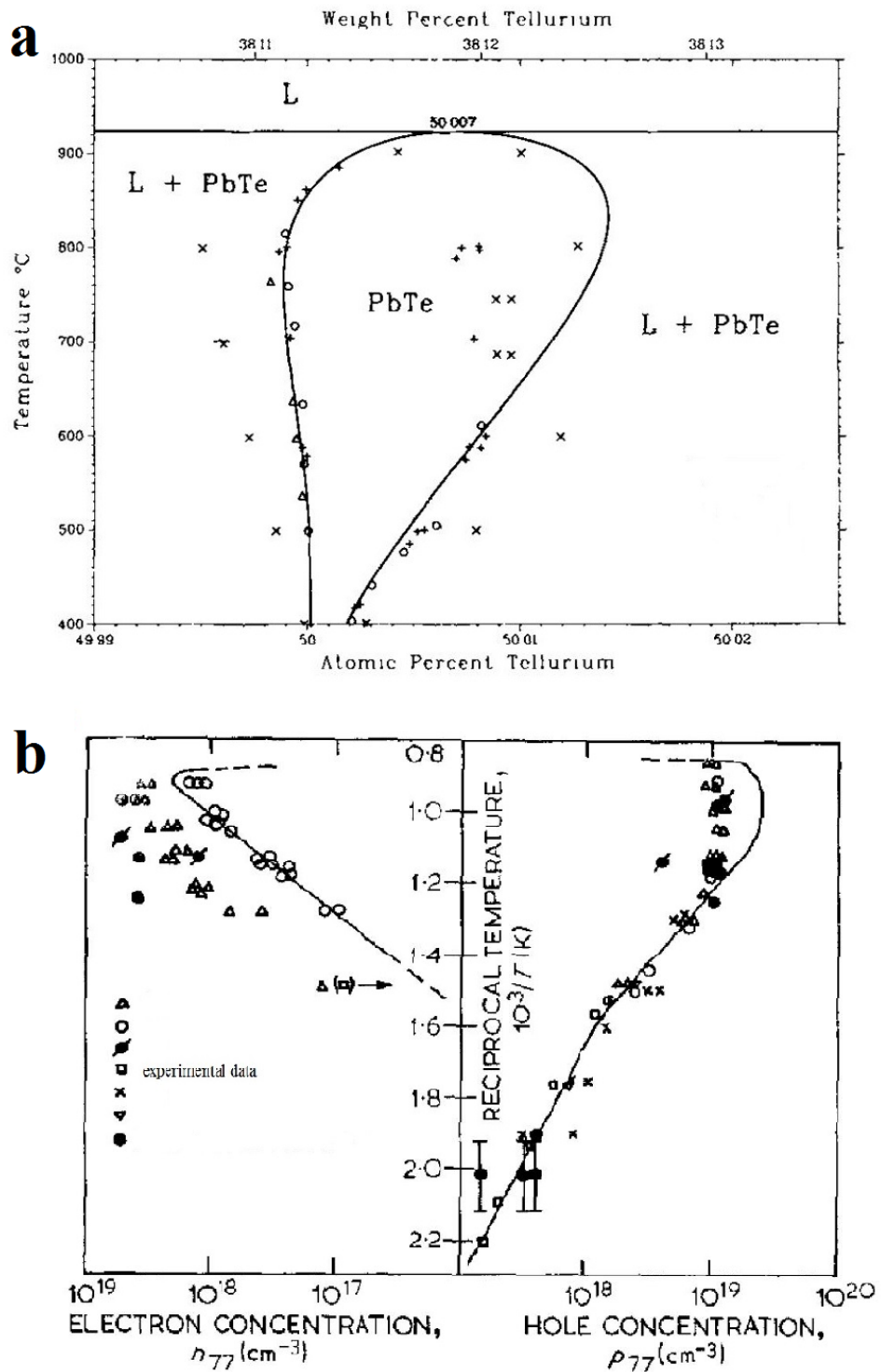
Figure 1.10. Phase stability range of PbTe: (a) dependent on composition; (Lin *et al.*, 1989)[75] (b) dependent on charge carrier concentration. (Sealy and Crocker, 1973)[79]

1. Introduction

Defect Chemistry

Point defects in semiconductors can introduce acceptor or donor levels in the electronic band structure, corresponding to *p*-type and *n*-type electrical behavior, respectively.[84-85] According to preparation and heat treatment conditions, the electronic properties of PbTe can be dramatically changed.[86] Experimental studies have found that there are metal–semiconductor transition and *p–n* transition at certain temperature range in low carrier concentration samples for both single-crystal and polycrystalline PbTe.[69,84,86-93,173] In 1955, Putley[87] claimed that perfectly reversible electrical conductivity results have be obtained up to 700 K, while appreciable irreversible changes took place for temperatures above 800 K. In 1960, Brebrick and Allgaier[73] suggested that crystals grown by Bridgman method were likely to contain an excess of lead or tellurium, precipitating on grain boundaries and dislocations. Re-solution of excess quiescent impurity atoms and vaporization of tellurium from the specimens had been considered as the reasons for the charge carrier concentration changes during the cyclic measurements.[67,94] Actually, in 1960s, it was believed that an excess of vacancies on the Pb-sublattice gives a Te-rich phase, and the *p*-type corresponds to excess Te element and *n*-type corresponds to excess Pb element.[69,73,84]

In 1961, Miller, Komarek and Cadoff[69] used a capsulating technique which would completely eliminate tellurium losses at elevated temperatures during measurements, indicated that the lattice defects, which predominantly affect the electronic properties, are Pb interstitial ions. PbTe diffusion mechanism studies showed that Pb diffused via interstitials and vacancies, which indicates that the predominant cation defect is of the Frenkel type.[95-98] The Te self-diffusion behavior suggested an interstitial mechanism, but with a much higher activation energy (1.08 eV),[98-99] which makes it difficult to predominate the transport behavior of PbTe. In 1987, Wienecke and Schen[100-101] conducted high-temperature in-situ Hall coefficient and conductivity investigations on non-stoichiometric single crystal PbTe. They showed that the formation energy of the main native defect on Te-rich side (Pb vacancy) is 0.32 eV and on Pb-rich side (Pb interstitial ions (Pb_i)) is 0.09 eV. They believed that Pb precipitation takes place by means of interstitial diffusion of Pb_i in *n*-type PbTe, and Te precipitation by Pb outdiffusion from certain areas via a Pb vacancy mechanism in *p*-type PbTe. In the same year, Te-rich precipitates have been found in stoichiometric, slightly Te-rich, and also in 0.3 at.% Pb

excess grown PbTe single crystals by TEM. For an excess of 1.0 at.% Pb, however, no Te-rich precipitates appeared.[102-103] More recently, Pb-depleted disks (Pb-vacancy aggregates) on {001} planes and pure Pb precipitates in stoichiometric PbTe were discovered by TEM.[104-105] Moreover, their measurement showed that the volume densities of Pb-depleted disks are around 9×10^{17} cm^{-3}, which are independent of the Pb/Te atomic ratios changing from 1:1.3 to 1.3:1.[105] Summarizing those investigations, it is reasonable to assume that V_{Pb}, Pb_i, Pb-rich precipitates, and Te-rich precipitates coexist in stoichiometric PbTe.

Local Structure

PbTe crystallizes in the cubic NaCl-type structure with Pb atoms at the cationic sites and Te at the anionic sites; the Pb atom is located at the origin and the Te atom is at (1/2, 1/2, 1/2).[61] Recently, synchrotron powder X-ray diffraction (SPXRD) study revealed structural disorder in PbTe and assumed Pb being located away from its high-symmetry position in [100] directions.[106-107] The lattice dynamics study, using inelastic neutron scattering, revealed a local symmetry breaking in the emergent dipole phase of PbTe.[108] While other investigations, like neutron scattering, ab initio lattice dynamics, and extended X-ray absorption fine structure experiments, concluded that lead is not off-center, but the anomalous spectral features simply arise from large-amplitude anharmonic vibrations.[56,109-111] Extremely large nearest-neighbor cubic interatomic force constant along the [100] direction was used to explain this anharmonic behavior.[112] Moreover, Iversen attributed the observed anisotropic peak broadening to anisotropic microstrain and high concentrations of lead vacancies in PbTe lattice. The anisotropic strain implies that the cubic symmetry is locally broken and the lattice spacing is modified over a finite distance.[113] The local structure in bulk PbTe crystals is the key issue for understanding the thermal conductivity, which is much lower than expected for simple rock-salt structures.

TE Properties

Excess Pb with respect to the stoichiometric ratio results in *n*-type conduction, and excess Te gives *p*-type. However, the maximum carrier numbers which can be introduced by either excess Pb or Te is 10^{19} cm^{-3}, which is one order of magnitude too low for thermoelectric applications. A dopant such as a group IV halide (e.g. PbI$_2$, PbBr$_2$,) or a

1. Introduction

group IV telluride (e.g. Ge_2Te_3,) may be used to increase the donor concentration, and Na_2Te or K_2Te would increase the acceptor concentration.[10,66] For *p*-type materials, sodium has be proved as one of the most effective dopants in controlling hole carriers in PbTe and has been extensively utilized to optimize thermoelectric properties of PbTe-based materials.[65,114-117,153] Experimental and theoretical studies indicate that Na substitution does not introduce resonant levels in the electronic band structure of PbTe but, rather, move the Fermi surface close to the heavy-hole valence band.[116,118-119] Due to large mass and atomic radii fluctuations, a reduced lattice thermal conductivity can also be achieved by Na substitution.[120-121] The Na-doped PbTe, called ''2P-PbTe'', has been used in 1959 as RTG and for several NASA missions in 1960s.[2,10] In 2011, Pei *et. al.*[65] re-evaluated the thermoelectric properties of *p*-type PbTe:Na using new reliable high-temperature thermal conductivity data. As a result, the maximum $ZT \sim 1.4$ was obtained, instead of the earlier underestimate of $ZT = 0.7$. Recently, progress has been made to obtain high ZT in Na-doped PbTe-based bulk materials using various substitutions M (Mg, Ca, Sr, Ba, Mn, Cd, Hg, Eu, Yb).[45,48,52,122-129] Alloy defects and nanostructuring are used to minimize the lattice thermal conductivity (κ_L).[45,127,130] Through reducing energy offset between the light (at the L-point of the Brillouin zone) and the heavy (along the Σ-line of the Brillouin zone) valence bands, the two sub-valence bands in PbTe, to improve the power factors.[88,131-132] Table 1 give a summary of recently reported high ZT *p*-type materials based on Na-substituted PbTe with various substituents (M) on Pb site. The authors claim that the enhancement is due to either nanostructuring or valence band convergence, or both. One exception without adding Na is Tl-substitution PbTe, which produces resonant electronic states that enhances the Seebeck coefficient and has ZT of 1.5 at 773 K.[27]

Table 1.1. High *ZT* *p*-type materials based on Na-substituted PbTe with their thermoelectric properties.

Systems	Solubility limit of substituents	Temperature range with $ZT > 1$, along with x value	ZT_{max}, temperature	σ	S	κ_L	Ref.
$Pb_{0.98}Na_{0.02}Te–xSrTe$ ($x \leq 0.12$)	$x = 0.05$	515 K – 923 K	2.5, 923 K	$\downarrow^*$	$\uparrow^*$	$\downarrow^*$	133
		$x = 0.08$					
$Pb_{0.98}Na_{0.02}Te–xMgTe$ ($x \leq 0.08$)	$x = 0.04$	540 K – 923 K	2.0, 823 K	$\downarrow$	$\uparrow$	$\downarrow$	52
		$x = 0.06$					
$Pb_{1-x}Yb_xTe:Na$ ($x \leq 0.10$)	$x > 0.10$	550 K – 850 K	1.7, 850 K	$\downarrow$	$\uparrow$	$\times$	127
		$x = 0.01$					
$Na_xPb_{0.97-x}Cd_{0.03}Te$ ($x \leq 0.02$)	no data on the Na solubility limit	550 K – 800 K	1.7, 750 K	$\downarrow$	$\times$	$\downarrow$	122
		$x = 0.012$					
$PbTe–0.01Na_2Te–xHgTe$ ($x \leq 0.03$)	$x < 0.02$	520 K – 800 K	1.6, 770 K	$\downarrow$	$\uparrow$	$\downarrow$	126
		$x = 0.02$					
$Pb_{1-x}Mn_xTe:Na$ ($x \leq 0.15$)	$x < 0.10$	500 K – 750 K	1.6, 700 K	$\downarrow$	$\uparrow$	$\downarrow$	123
		$x = 0.04$					
$PbTe–0.01Na_2Te–xCaTe$ ($x \leq 0.08$)	no data on the CaTe solubility limit	550 K – 800 K	1.5, 765 K	$\uparrow$	$\downarrow$	$\downarrow$	124
		$x = 0.06$					
$Pb_{1-x-y}Eu_xNa_yTe$ ($x \leq 0.05, y \leq 0.05$)	$x > 0.05$; no data on the Na solubility limit	500 K – 850 K	2.2, 850 K	$\downarrow$	$\uparrow$	$\downarrow$	129
		$x = 0.03; y = 0.025$					

*: ↓ decreased with respect to Na-substituted PbTe;

↑ increased with respect to Na-substituted PbTe;

× no effect or not mentioned.

Compared to *p*-type PbTe-based thermoelectric materials, high *ZT* values of *n*-type PbTe-based thermoelectric materials are less documented. The difference of thermoelectric performances between *p*- and *n*-type PbTe is mainly reflected in the power factors due to their different electronic band structures. The valance bands of PbTe near Fermi level consist of the L-Σ dual bands, which are separated by an energy gap ~0.18

eV at 0 K.[29,131] As the carrier concentration increases, the Fermi level dips into the gap and induces the electrical conduction in the heavy Σ band. In contrast, the conduction band of PbTe is much simpler, the dominant band for electrical transport is always the L band.[134] For *n*-type PbTe-based thermoelectric materials, iodine is the most used element to contribute electron carriers.[25,135] In 2011, LaLonde *et. al.* re-evaluated the thermoelectric properties of PbTe$_{1-x}$I$_x$ using new reliable high-temperature thermal conductivity, revealing a large figure of merit of 1.4 between 700–850 K.[135] Other monovalence (Ag, Cu) or trivalence (La, Y, Ce, Bi, Sb) elements have been also used for *n*-type substitution in PbTe.[25,136-141] Dual-element substitutions such as (Zn, I), (Mg, I), (Bi, I), (Sb, I), (In, I), (Ag, La), (Sn, Se), (Sb, S) and compounds alloying (NaCl), (InSb) have improved the maximum *n*-type *ZT* values to 1.0 — 1.8, and can be attributed to introduction of defect energy levels, distortion of the density of states, and formation of multiphase nanostructures, etc.[121,134,142-152]

1.5. Motivation and outline of thesis

As one of the most investigated TE materials, PbTe-based materials still have many fascinating properties which are needed to be studied. Some controversies still exist concerning the local structure and point defects in PbTe. Various strategies lead to the greatly enhanced *p*-type and *n*-type PbTe-based TE materials, however, there are quite few studies focusing on reproducibility of TE properties and microstructure evolution during different heat processes (such as compact sintering, high-temperature measurements, annealing, etc.).

In order to understand the influence of chemical substitutions and heat treatments on the stability of the PbTe-based solid solutions and their TE properties, binary PbTe, ternary Pb–Eu–Te and Pb–Na–Te, quaternary Pb–Eu–Na–Te systems were systematically investigated. The structural features and electronic properties of binary polycrystalline Pb–Te samples after various heat treatments have been investigated (chapter 3). It was expected to find the connection between structural variations and electronic properties (relating to defects chemistry) of PbTe. The constitution and thermoelectric behavior of materials with two substitution schemes in the Pb–Eu–Te ternary system are presented (chapter 4). The structural features and TE properties of two series of polycrystalline samples Pb$_{1-y}$Na$_y$Te$_{1-y/2}$ and Pb$_{1-x}$Na$_x$Te are examined (chapter 5).

The local atomic arrangement of Na by different substitution schemes is revealed by NMR. The structure and TE properties of samples $(PbTe)_{0.98-x}(EuTe)_x(NaTe)_{0.02}$ ($x = 0$ — 0.03) with three different heat treatments: after SPS, after LFA, after long-term annealing have been systemically investigated (chapter 6). The TE stability of Eu- and Na-substituted PbTe under cyclic TE measurements will be discussed. Finally, a summary on these four PbTe-based systems will be given, trying to understand the basic reasons of the thermoelectric behavior.

1. Introduction

2. Synthesis and characterization methods

Here the preparation and characterization aspects of PbTe-based thermoelectric materials are covered. A brief description of the synthesis and sintering conditions will be given, followed by specifying structural, chemical, thermal, physical and thermoelectric characterization methods.

2.1. Synthesis of PbTe-based thermoelectric materials

Bulk polycrystalline samples in the binary Pb–Te, ternary Pb–Eu–Te, Pb–Na–Te, and quaternary Pb–Eu–Na–Te systems were synthesized by melting the elements Pb (shot, 99.999 mass%), Te (chunk, 99.9999 mass%), Eu (chunk, 99.95 mass%), Na (chunk, 99.99%) in a graphite-coated and fused silica tube (Figure 2.1) at 1273 K for 6 h under a vacuum of around 10^{-4} torr. Then, the temperature was slowly lowered to 873 K and the samples were annealed for six days for homogenization (Figure 2.2). The obtained ingots were ground into powders by hand using an agate mortar in an argon atmosphere.
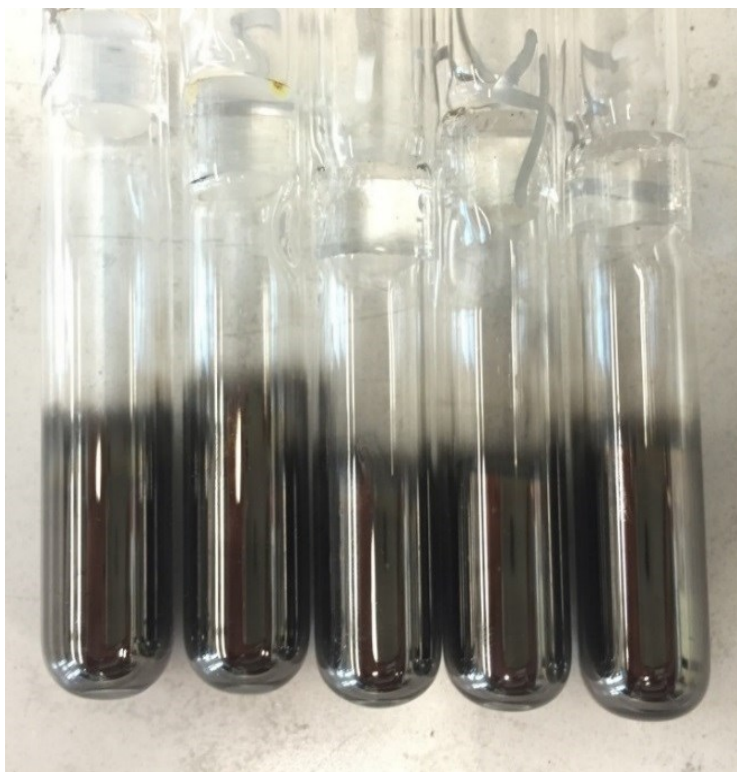
Figure 2.1. Graphite–coated silica tubes, with as-prepared materials inside.

2. Synthesis and characterization methods
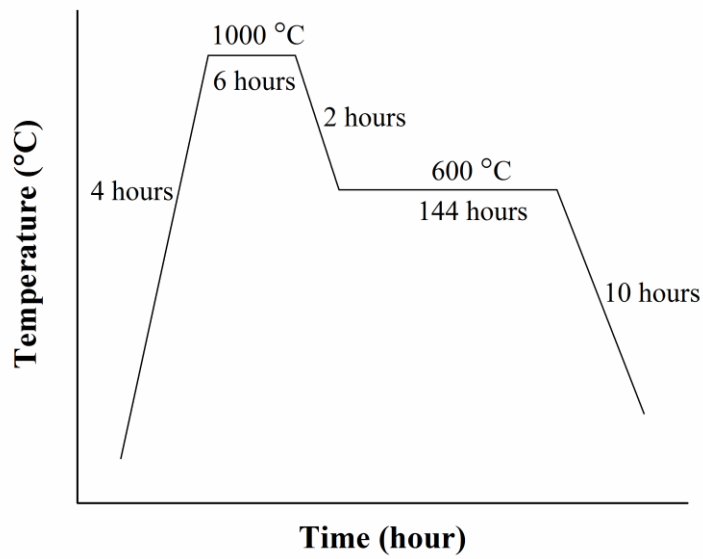
Figure 2.2. Typical temperature profile used for materials' preparation.

Figure 2.3. Sintering setup Fuji SPS-515S in glove box.

The fine powders were densified by spark-plasma sintering (SPS, Fuji SPS-515S in glove box with argon atmosphere,[154] Figure 2.3) at 673 K under a pressure of 60 MPa for 7 minutes. The polished SPS-manufactured disks (Ø = 10 mm, 2 mm thick) were first used for measurements of the thermal diffusivity. Then the disks were cut into rectangular

blocks ($2 \times 2 \times 8$ mm^3) by wire saw in order to obtain specimens for further measurements. The additional annealing was processed in Ta tubes under Ar atmosphere in fused silica tube at specific temperature, with following quenching in ice water after specific time. Na$_2$Te for the NMR investigations was synthesized according to Ref. 155, by melting Na and Te in the stoichiometric ratio in an Ar atmosphere in a sealed Ta tube at 773 K for 5 hours.

2.2. Structural characterization

2.2.1. X-ray powder diffraction

Phase identification was performed with the X-ray Guinier diffraction technique (Huber G670 camera, Cu Kα1 radiation, $\lambda = 1.54056$ Å, $\Delta 2\theta = 0.005°$, 2θ range $3.0°$ — $100°$, exposure time 6×15 min). The reflection positions, obtained by profile deconvolution, were corrected using the internal standard LaB$_6$. Lattice parameter refinements and other crystallographic calculations were performed with the program package WinCSD.[156] The samples for Huber G670 were prepared by sandwiching the powder between two sheets of Mylar films that were clamped using a metal ring.

The in-situ high-temperature powder X-ray diffraction experiments were performed at the high-resolution beamline ID22 beamline of the European Synchrotron Radiation Facility (ESRF) in Grenoble, equipped with multi-channel detector and Si (111) monochromator ($2\theta_{max} = 28.5°$, $\Delta 2\theta = 0.002°$, $\lambda = 0.354337(3)$ Å). Fine powders of sample with particle size < 20 μm were loaded into quartz capillaries with 0.3 mm diameter. The hot-air blower was used for generating of temperatures up to 500 °C.

2.2.2. Metallography investigation

The sample pieces for metallography were embedded in conductive resin, subsequently grinded and polished, finally using 0.1 μm diamond powder in a slurry. The sample homogeneity was examined by optical microscopy (Zeiss Axioplan2) in bright-field and polarized light. The element mappings were obtained by electron microprobe analysis with the energy dispersive X-ray spectroscopy (EDS, Bruker Quantax 400 system with the detector XFlash 630) on the polished bulk materials.

2.2.3. Nuclear magnetic resonance (NMR) experiments

Nuclear Magnetic Resonance (NMR) experiments were performed on a Bruker Avance 500 spectrometer with a magnetic field of $B_0 = 11.74$ T and standard Bruker MAS probes. The samples were diluted with GeO_2 and packed into 4 mm ZrO_2 rotors. The ^{23}Na signals were referenced to saturated solution of NaCl with the reference frequency of 132.29127 MHz. The spectra were obtained either from the free induction decay after a single pulse of 2 μs or from the echoes after two 90° pulses of 6 μs. The recovery time was 10 s.

2.2.4. X-ray absorption spectroscopy (XAS) experiments

X-ray absorption spectroscopy (XAS) experiments were performed at the Dragon beamline of the National Synchrotron Radiation Research Center (NSRRC) in Taiwan. The Eu $M_{4,5}$ spectra were taken at 300 K using the total electron yield (TEY) mode with a photon energy resolution of ~0.6 eV. Clean sample surfaces were obtained by cleaving the samples in situ in a vacuum of 1×10^{-9} mbar. By making weighted sums with the two reference samples of the Eu^{2+} and Eu^{3+} ion in an octahedron,[157] using the "NMimimize" function of the Mathematica software[158] to obtain the best fit to the experimental spectrum of each sample, we extracted the relative amount of Eu^{2+} and Eu^{3+} ions.

2.3. Chemical analysis

Elemental chemical analysis (for Pb, Te, Eu, O, C, Si, Al) was performed on ground powder samples (~ 100 mg) by using the inductively-coupled plasma optical-emission spectrometry (ICP-OES, Agilent 5100 SVDV setup for Pb, Te, Eu, Si, Al) and the carrier-gas hot-extraction technique (LECO C200 setup for carbon and LECO TCH600 setup for oxygen).

2.4. Thermal analysis

Thermal gravimetry (TG) and differential scanning calorimetry (DSC) were performed employing the Netzsch STA 449C and Netzsch DSC 404C devices. The measurement of TG was made with a heating rate of 5 K min^{-1} between room temperature and 773 K in an open graphite crucible. Then the sample was kept for 12 hours in argon. The DSC was made between room temperature and 1248 K with a heating/cooling rate of 5 K min^{-1}. Dilatometry measurements were conducted between 293 K and 673 K with a heating/cooling rate of 5 K min^{-1} by DIL 801 Single Sample Dilatomer.

2.5. Magnetic and physical properties measurement

The Hall effect (R_H) was measured with a standard four-point ac technique in a physical property measurement system (PPMS, Quantum Design), with magnetic fields up to 9 T. The Hall carrier concentrations were calculated by $1/(R_H \cdot e)$, R_H is Hall coefficient, e is the charge of an electron. Magnetization measurements on samples in polyethylene sample holders were performed with a magnetometer system (MPMS XL-7 Quantum Design) in the temperature range 50 – 400 K and at magnetic fields up to 7 T. The effective magnetic moment per Eu atom is calculated by Curie–Weiss fitting, basing specimens' compositions achieved from ICP results. For Hall measurements, cut rectangular bars were prepared. For magnetization measurements, irregular shape of bulk materials were used.

2.6. Thermoelectric characterization

2.6.1. Electric conductivity and Seebeck coefficient

Electrical resistivity and Seebeck coefficient were measured (specimens of rectangular blocks $2 \times 2 \times 8$ mm^3) simultaneously with the ZEM-3 setup (Ulvac–Riko) in the temperature range 300 to 760 K. The uncertainty of the Seebeck coefficient and electrical conductivity measurements is ~5%. The combined uncertainty for the experimental determination of ZT is ~20%.[159-160] As described in Figure 2.4, a prism or cylindrical sample is set in a vertical position between the upper and lower blocks in the heating furnace. This measurement setup has two heating sources: a primary furnace that covers the entire measurement assembly is used to heat the sample up to a specific temperature, and the lower block contains a secondary heater used to create a set temperature gradient across the sample under measuring. Electric resistance (R) is measured by the dc four-terminal method, in which a constant current I is applied to both ends of the sample to measure and determine voltage drop dV between the same wires of the thermocouple by subtracting the thermo-electromotive force between leads attached directly to the sample. The resistivity is given by $\rho = RA/L$, where A is the end area of the sample, L is the distance between two probe thermocouples. Seebeck coefficient is measured by measuring the upper and lower temperatures $T1$ and $T2$ with the thermocouples pressed against the side of the sample, followed by measurement of thermal electromotive force

dE between the same wires on one side of the thermocouple. The Seebeck coefficient is then calculated as: $S = \frac{\Delta E}{T1-T2} - S_{probe}$.
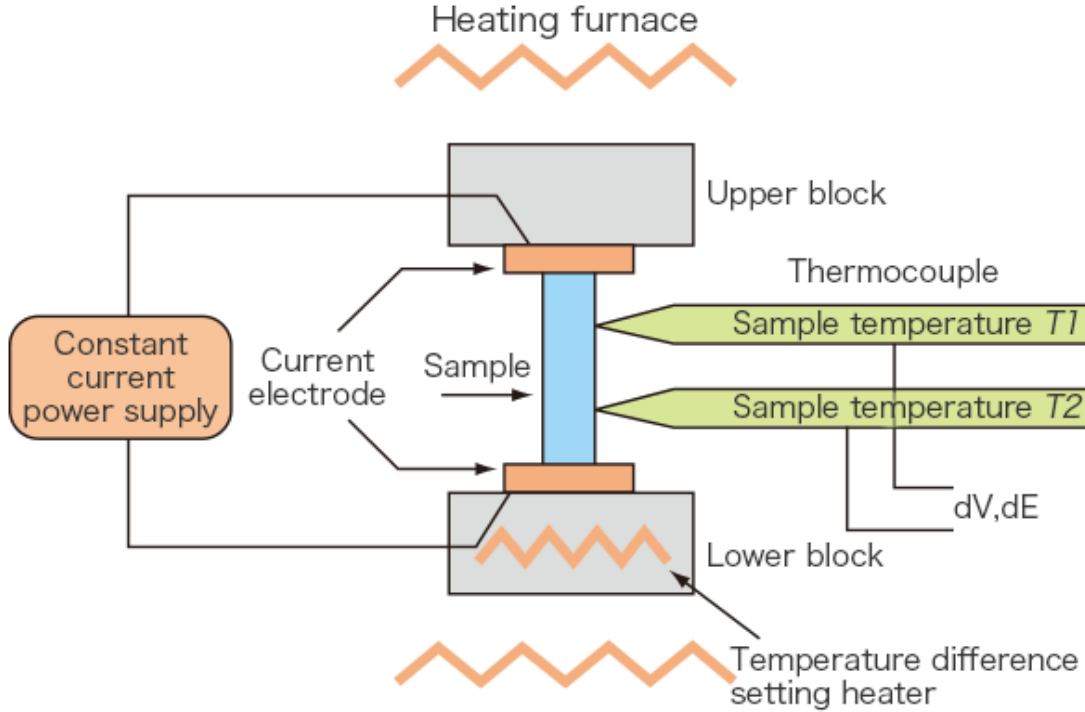
Figure 2.4. Schematic of measurement setup in ZEM-3. This picture is adopted from the instruction manual of ZEM-3 series.

2.6.2. Thermal conductivity

Thermal conductivity was calculated as $\kappa = dC_pD$, where d is the density obtained using the mass and geometric volume of the specimen disk after SPS. Thermal diffusivity (D) measurements were measured by the laser flash method using the Netzsch LFA 457 equipment (LFA). The heat capacity per atom (C_p) was estimated from the relation C_p/k_B = $3.07 + 0.00047(T - 300)$.[161] Lattice thermal conductivity (κ_L) was calculated by subtracting the electronic part $\kappa_e = L\sigma T$ from the total conductivity. For binary Pb–Te and ternary Pb–Eu–Te, the Lorenz number $L = 2.44 \times 10^{-8}$ W·Ω·K^{-2}. For other samples series, the Lorenz number is evaluated by the equation: $L = 1.5 + \exp[-\frac{|S|}{116}]$, which is accurate within 20% for PbTe.[162]

3. Structural and thermoelectric properties of binary Pb–Te system

Although as the first experimental part in this dissertation, the work of binary Pb–Te system was done during or even after the studies of other ternary and quaternary systems, in order to understand some basic behaviors occurring in polycrystalline bulk PbTe-based thermoelectric materials. In this chapter, the structure and thermoelectric properties of binary Pb–Te samples were investigated after various heat treatments using a single crystal as a reference. Powder X-ray diffraction patterns reveal the strong anisotropy reflection broadening in PbTe.[91] It was proven that the strong anisotropy in PbTe comes from the sample grinding process and could be removed by additional annealing. The chemical composition and annealing temperature will strongly influence the TE properties of the binary polycrystalline Pb–Te.

3.1. Introduction

As reported in Chapter 1, the structure and point defects of PbTe are still under discussion.[101-102,108-109,113] Metal–semiconductor and *p–n* conduction transitions have been reported in both single crystals[69,84,86-88,93] and polycrystalline PbTe.[89-92,173] In 1950s–1970s, lots of investigations based on single-crystal PbTe have been conducted. The results reveal that the metal–semiconductor transition comes from extrinsic–intrinsic conduction change[66,87] and the *p–n* conduction transition temperature increases with increasing extrinsic charge carrier concentration for *p*-type PbTe.[84] For intrinsic PbTe, the electron mobility is much higher than the hole mobility at temperatures above 300 K, and the mobility ratio increases to 2.5 above 400 K.[66-67,86] This is mainly attributed to the heavy second valence band becoming dominant for the hole transport above 400 K and causing a significant reduction of the average hole mobility.[71] In this case, the Seebeck coefficient will be negative when the conduction behavior is dominated by intrinsic carriers.[71,86,91,] According to conditions of preparation and heat treatments, the electronic properties of PbTe could be dramatically changed. Perfectly reversible electrical conductivity results have be obtained up to 700 K, while long-term annealing at 400 K in open air or increasing the measurement temperature up above 800 K will irreversibly change the electrical conduction behavior of PbTe.[86-87] The RT resistivity of Pb-excess

3. Structural and thermoelectric properties of binary Pb–Te system

PbTe shows higher value when the ingot cooling rate is reduced, indicating that the Pb solubility in PbTe decreases with decreasing temperature.[173] Since in 2011 Pei *et. al.*[65] re-evaluated the TE properties of *p*-type PbTe:Na and obtained the maximum *ZT* of 1.4, dozens of high-*ZT* PbTe-based polycrystalline bulk materials were reported.[45,48,52,121-129,134-135,142-152] However, there are few studies focusing on the phase stability and TE properties reproducibility of polycrystalline bulk PbTe-based materials. As the base material for various high-*ZT* thermoelectric material systems (Table 1.1), it is important to further investigate the structure of the binary Pb–Te system and establish the chemical composition and temperature effects on the structural and thermoelectric properties of polycrystalline PbTe.

In this work, binary polycrystalline Pb–Te samples were investigated by PXRD, SEM-EDS, and thermal analysis. Using a single crystal PbTe as a reference, the thermoelectric properties of Pb–Te samples with different chemical compositions and under different heat treatments were examined.

3.2. Experimental details

The polycrystalline samples $Pb_{0.49}Te_{0.51}$, $Pb_{0.50}Te_{0.50}$ (sample A), and $Pb_{0.51}Te_{0.49}$ (each around 3.3 g) were synthesized in the graphite-coated fused quartz tube by melting the elements at 1273 K for 6 h under a pressure of ~ 10^{-4} torr. It was then cooled down within two hours to 873 K (far above the melting points of Pb and Te) and kept at this temperature for six days for homogenization, and then, the samples were cooled down to room temperature in 10 hours. Additional $Pb_{0.50}Te_{0.50}$ (10 g) (sample B) was synthesized by the same method to clarify the reproducibility of the synthesis process, in particular with respect to their TE properties. The balance weighing error is $\pm$ 0.00050 g, for the 3.3 g $Pb_{0.50}Te_{0.50}$ samples, the Te range could be 49.984 — 50.016 at.%; for the 10 g $Pb_{0.50}Te_{0.50}$ samples, the Te range could be 49.995 — 50.005 at.%. According to Figure 1.10, the composition could be beyond the solubility range, especially at the Pb-rich side. The obtained ingots were ground into powders in an agate mortar under argon atmosphere, and then spark-plasma sintered. The sample C $Pb_{0.50}Te_{0.50}$ (10 g) was prepared by the same method, but after the six days annealing at 873 K, the material was quenched in ice water (as-cast) instead of slowly cooling, in order to examine the equilibrium state of PbTe at 873 K. The high quality single crystal sample (sample D) was grown by Prof.

Manfred Mühlberg through vertical Bridgman-Stockbarger method in 1980.[163] One Ø = 8 mm disc with (111) surface and one bar with {100} side surfaces was cut from sample D by Prof. Peter Gille. For some samples, the 673 K and 423 K (above and below the metal-semiconductor transition temperature) annealing were conducted in sealed Ta tubes in argon atmosphere. First, they were slowly heated to 673 K or 423 K and then kept there for 128 hours, and after quenched in ice water. The 773 K annealing (at this temperature PbTe starts to evaporate, see Figure 3.2d) was conducted directly in fused vacuum quartz tubes for 24 hours and then quenched in ice water. The detailed experimental strategy of this study is shown in Figure 3.1. All specimens numbers (No. *n*) correspond to the specimens number listed in Table 3.1.
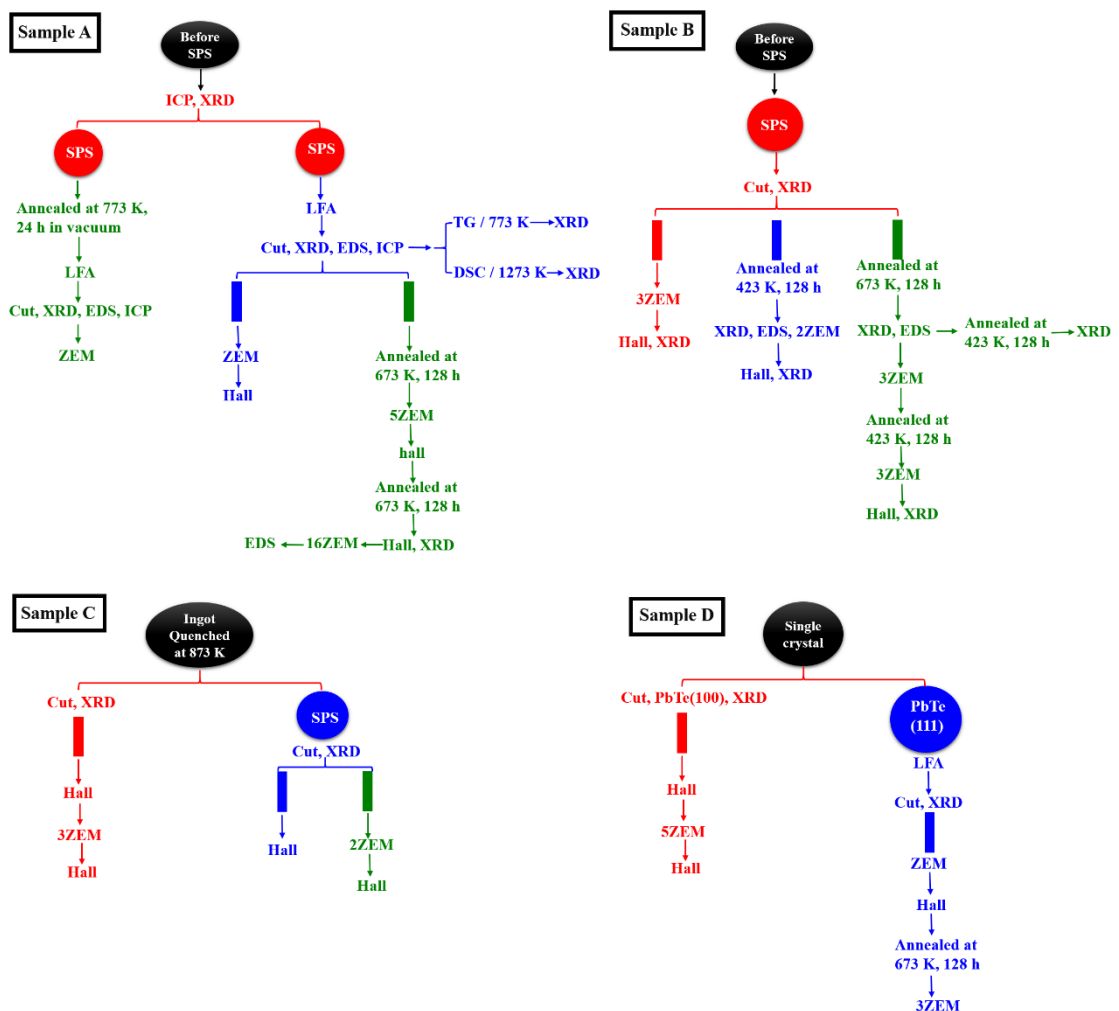
Figure 3.1. Schematic diagram of experimental processes for sample A, B, C, D.

3.3. Results and discussion

3.3.1. Phase analysis

In some previous publications, the equiatomic phase of the Pb–Te system was reported to exhibit a homogeneity range.[75,164-165] The PXRD patterns of our samples with different Pb:Te ratios around the equiatomic composition (Figure 3.2a) show that all binary samples have the same lattice parameters within the error bar. Moreover, only stoichiometric sample A $Pb_{0.50}Te_{0.50}$ is single phase, while $Pb_{0.49}Te_{0.51}$ contains elemental Te, and $Pb_{0.51}Te_{0.49}$ contains elemental Pb. The composition for sample A is 49.83 ± 0.20 at.% Pb and 50.17 ± 0.20 at.% Te according to the chemical analysis (ICP). No other elements (analyzed elements: Pb, Te, Si, O, C) were found. Compared to the reported narrow homogeneity range of Pb–Te,[73,75,166] the ICP results cannot yield the stoichiometric composition within the error bar.

The temperature dependence of the lattice parameter for sample A (No. 2) shows linear behavior which can be described by the equation $a(T) = 6.4206 + 1.4 \times 10^{-4}\,T$ (Figure 3.2b). The calculated linear thermal expansion coefficient at room temperature is 2.2×10^{-5} K^{-1}, which is in good agreement with literature values determined by capacitance $(2.04 \times 10^{-5}$ $K^{-1})$[167] and X-ray diffraction $(2.01 \times 10^{-5}$ $K^{-1})$.[107] DSC measurement on sample A (No. 2) reveal only one exothermic peak at 1180 K (Figure 3.2c), marking the melting point of PbTe, which is well in agreement with the phase diagram (1197 K).[75] According to thermogravimetric (TG) analysis, PbTe (No. 2) loses about 0.9 mass% after 12 hours at 773 K in an open graphite crucible under argon atmosphere (Figure 3.2d). Similar behavior was observed in other studies.[168-169] However, thermal analysis did not suggest a structural transformation (Figures 3.2b, 3.2c).
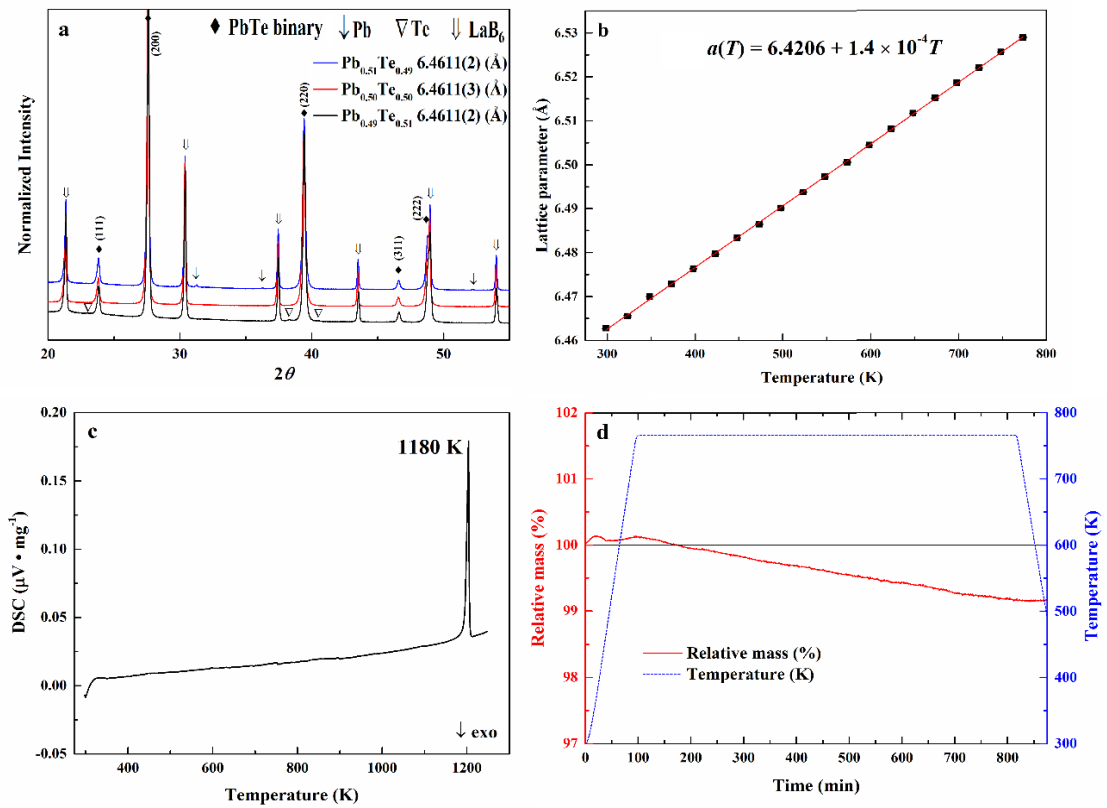
Figure 3.2. (a) X-ray powder diffraction patterns of $Pb_{0.50\pm x}Te_{0.50\pm x}$ samples. (b) Temperature-dependent lattice parameter of sample A: S + L (No. 2). (c) DSC measurement of sample A: S + L (No. 2). (d) Thermogravimetric experiment of sample A: S + L (No. 2).

To understand the reason of this mass loss, the SPS-prepared sample A (No. 4) was further annealed in vacuum at 773 K for 24 hours. Many voids appeared near the grain boundaries after annealing compared to the sample before annealing (Figures 3.3a, 3.3b). The chemical analysis shows 49.76 ± 0.10 at.% Pb, indicating that the Pb:Te ratio did not change after annealing. The lattice parameter (6.4613(2) (Å), Table 3.1) also did not change. Similar but fewer and smaller voids were also observed in the 673 K annealed sample (No. 9). According to the reported vapor pressure of Pb, Te, and PbTe at 773 K,[170-171] the easiest evaporated material is Te, then PbTe, and finally Pb. Since no structural and compositional changes were observed (Figures 3.2b, 3.2c), the lost mass could be caused by PbTe evaporation from the grain boundaries.

3. Structural and thermoelectric properties of binary Pb–Te system
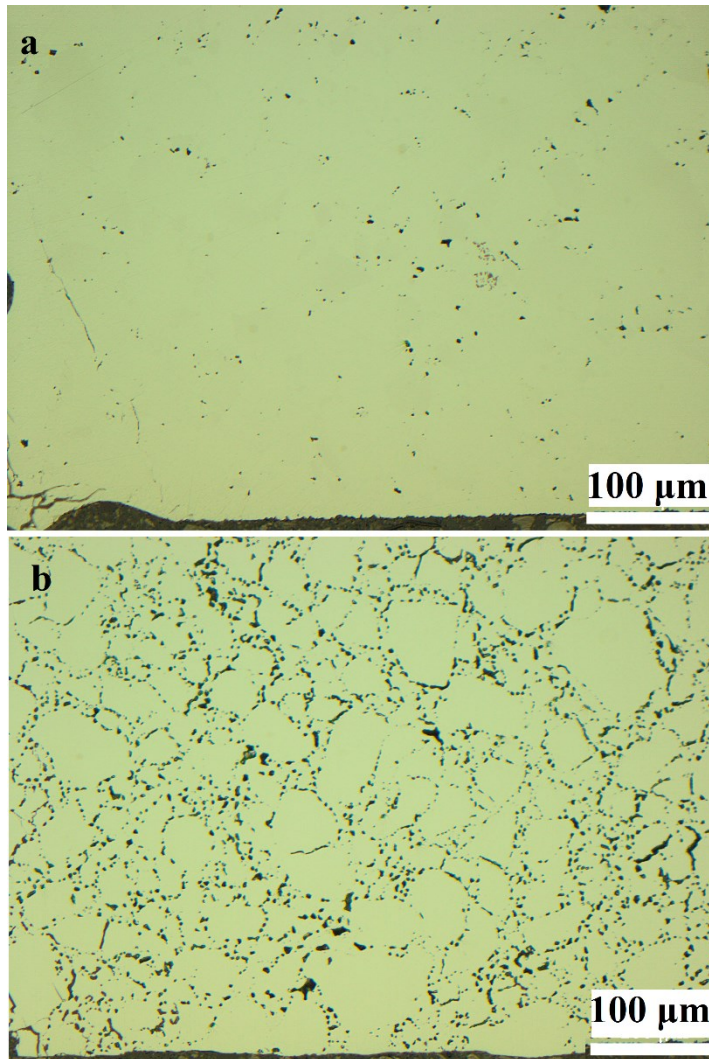
Figure 3.3. (a) Microstructure (polarized light image) of the sample A: S + L (No. 2). (b) Microstructure (polarized light images) of the sample A: S + A773K (No. 4).

Table 3.1. Lattice parameter (LP) and the corresponding resistivity and Seebeck data figures for all specimens of this chapter. Abbreviation: S-after SPS, nZ-after n cycles ZEM measurements, AxxxK-after annealing at xxx K temperature, L-after LFA measurement). No. n is used for marking each specimen appeared in the text. Samples A, B, C, D have nominal composition $Pb_{0.50}Te_{0.50}$.

No. n	Specimens	a (Å)	Resistivity	Seebeck
1	A: as-cast	6.4611(3)	—	—
2	A: S + L	6.4612(2)	Fig. 3.8a	Fig. 3.9a
3	A: S + L + Z	—	Fig. 3.8a	Fig. 3.9a
4	A: S + A773K	6.4613(2)	—	—
5	B: S	6.4616(2)	Fig. 3.8b	Fig. 3.9b
6	B: S + 2Z	6.4616(2)	Fig. 3.8b	Fig. 3.9b
7	B: S + A423K	6.4617(2)	Fig. 3.13b	Fig. 3.14b
8	B: S + A423K + 2Z	6.4613(2)	Fig. 3.13b	Fig. 3.14b
9	B: S + A673K	6.4609(2)	Fig. 3.13c	Fig. 3.14c
10	B: S + A673K + A423K	6.4617(2)	—	—
11	B: S + A673K + 3Z + A423K	—	Fig. 3.13d	Fig. 3.14d
12	B: S + A673K + 3Z + A423K + 3Z	6.4615(2)	Fig. 3.13d	Fig. 3.14d
13	C: as-cast	6.4614(2)	—	—
14	C: as-cast + 3Z	—	—	—
15	C: as-cast + S	6.4616(2)	Fig. 3.8c	Fig. 3.9c
16	C: as-cast + S + 2Z	—	Fig. 3.8c	Fig. 3.9c
17	D: SC(100)	6.4612(2)	—	—
18	D: SC(100) + 5Z	—	—	—
19	D: SC(111)	—	—	—
20	D: SC(111) + L	—	Fig. 3.8d	Fig. 3.9d
21	D: SC(111) + L + Z	6.4613(2)	Fig. 3.8d	Fig. 3.9d
22	D: SC(111) + L + Z + A673K	—	Fig. 3.16a	Fig. 3.16b
23	$Pb_{0.49}Te_{0.51}$: as-cast	6.4611(2) (with Te phase)	—	—
24	$Pb_{0.49}Te_{0.51}$: S	6.4613(2) (with Te phase)	Fig. 3.11a	Fig. 3.11b
25	$Pb_{0.49}Te_{0.51}$: S + 2Z	6.4616(2) (with Te phase)	Fig. 3.11a	Fig. 3.11b
26	$Pb_{0.51}Te_{0.49}$: as-cast	6.4611(2) (with Pb phase)	—	—
27	$Pb_{0.51}Te_{0.49}$: S	6.4614(2) (with Pb and PbO_2 phases)	Fig. 3.12a	Fig. 3.12b

3. Structural and thermoelectric properties of binary Pb–Te system
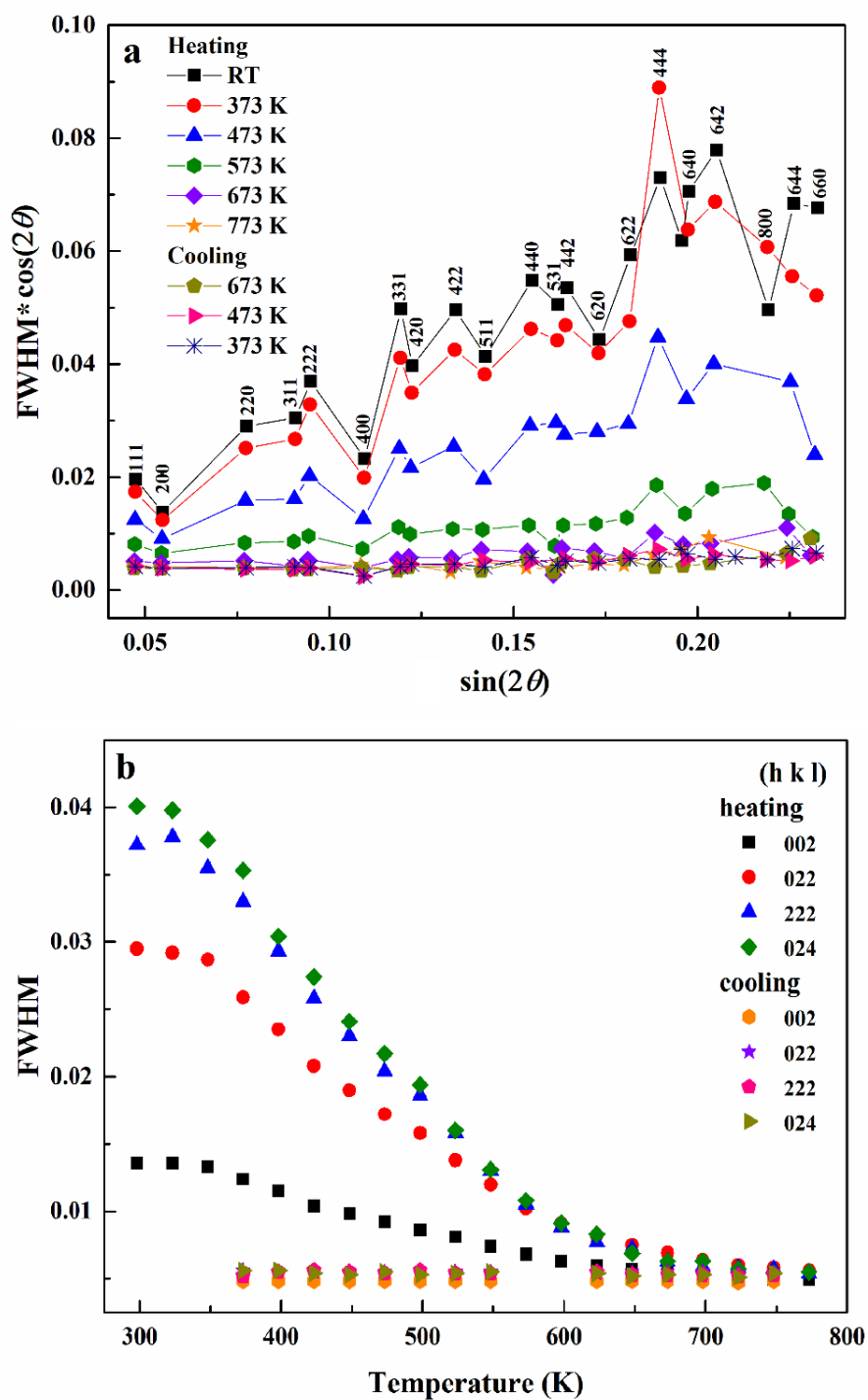
Figure 3.4. Full widths at half maximum (FWHM) of the X-ray powder diffraction reflections of sample A: S + L (No. 2) (a) as a function of the diffraction angle at selected temperatures, and (b) as a function of temperature at selected reflections.

The full widths at half maximum (FWHM) of high temperature synchrotron powder XRD pattern of sample A (No. 2) are shown in Figure 3.4. Unusual anisotropic peak broadening (Figure 3.4a) was observed below 473 K, similar to all other PbTe-based materials in our study. Looking at a few peaks with characteristic crystallographic directions, it is clear that the $\{h00\}$ peaks show much lower FWHM in comparison to the $\{hk0\}$ and $\{hhh\}$ ones for temperatures below 600 K during the heating measurements (Figure 3.4b). The anisotropy is strongly reduced in the temperature range between 473 K and 573 K and is practically non-existent above 573 K (Figure 3.4a). Moreover, the overall reflection broadening reduces with the increasing temperature. The anisotropy does not exist in the cooling data, all peaks have similar and small values of FWHM.

Two SPS-prepared specimens from sample B were annealed at 423 K (the anisotropy is still present, No. 7) and at 673 K (the anisotropy disappears, No. 9), respectively. Dilatometric measurements for both two specimens do not reveal any special effects. The thermal expansion shows liner behavior, both specimens have a linear thermal expansion coefficient of 1.3×10^{-5} K^{-1} (Figure 3.5a), which is slightly smaller compared to the value obtained from high-temperature X-ray diffraction (2.2×10^{-5} K^{-1}, cf. Figure 3.2b). The cyclic measurements of specific heat for the single-crystalline sample D (No. 20) also do not reveal any phase transitions. (Figure 3.5b).

3. Structural and thermoelectric properties of binary Pb–Te system
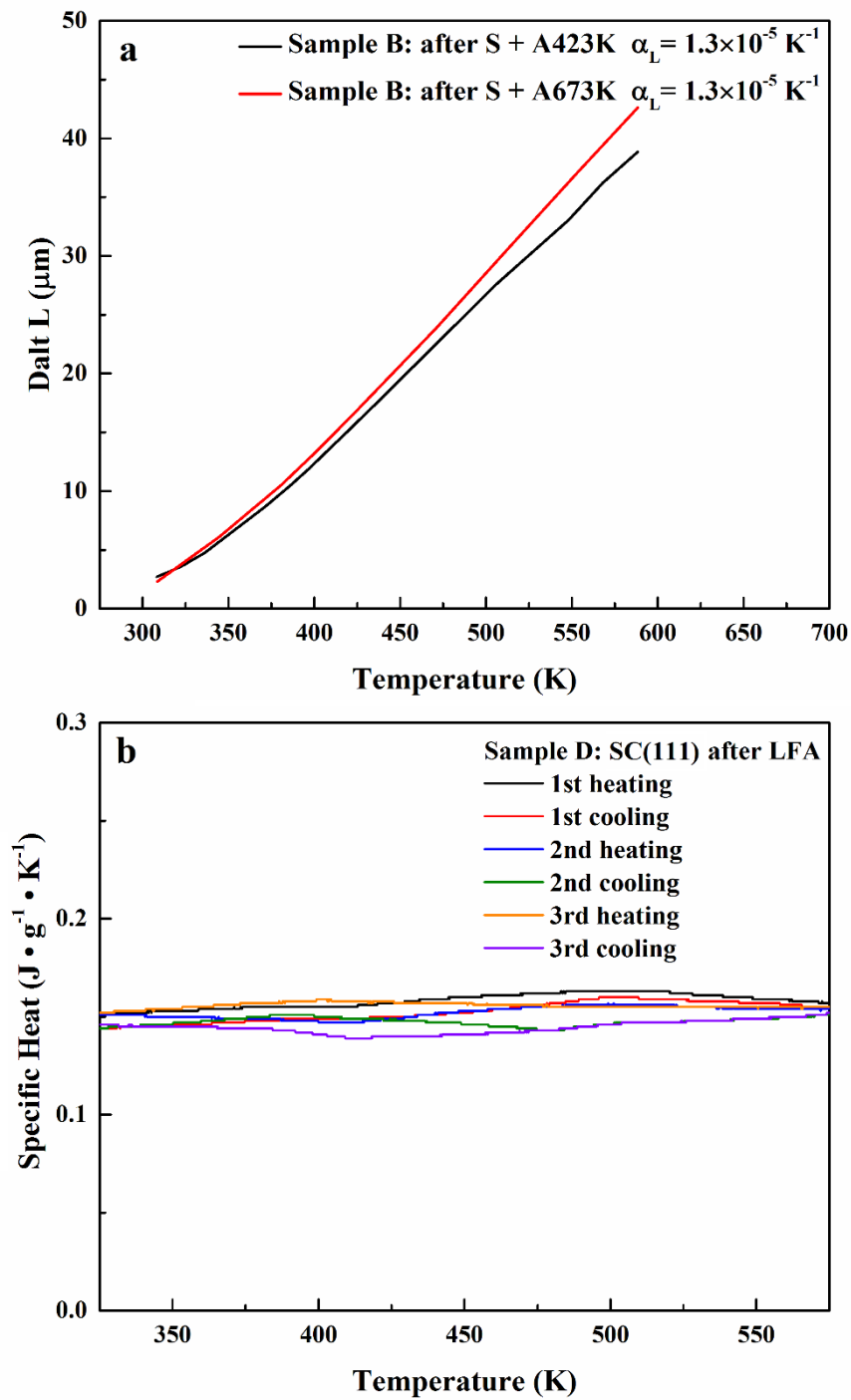
Figure 3.5. (a) Dilatometer tests for sample B: (black) S + A423K (No. 7), (red) S + A673K (No. 9). (b) Cyclic measurements of specific heat for sample D: SC(111) + L (No. 20).
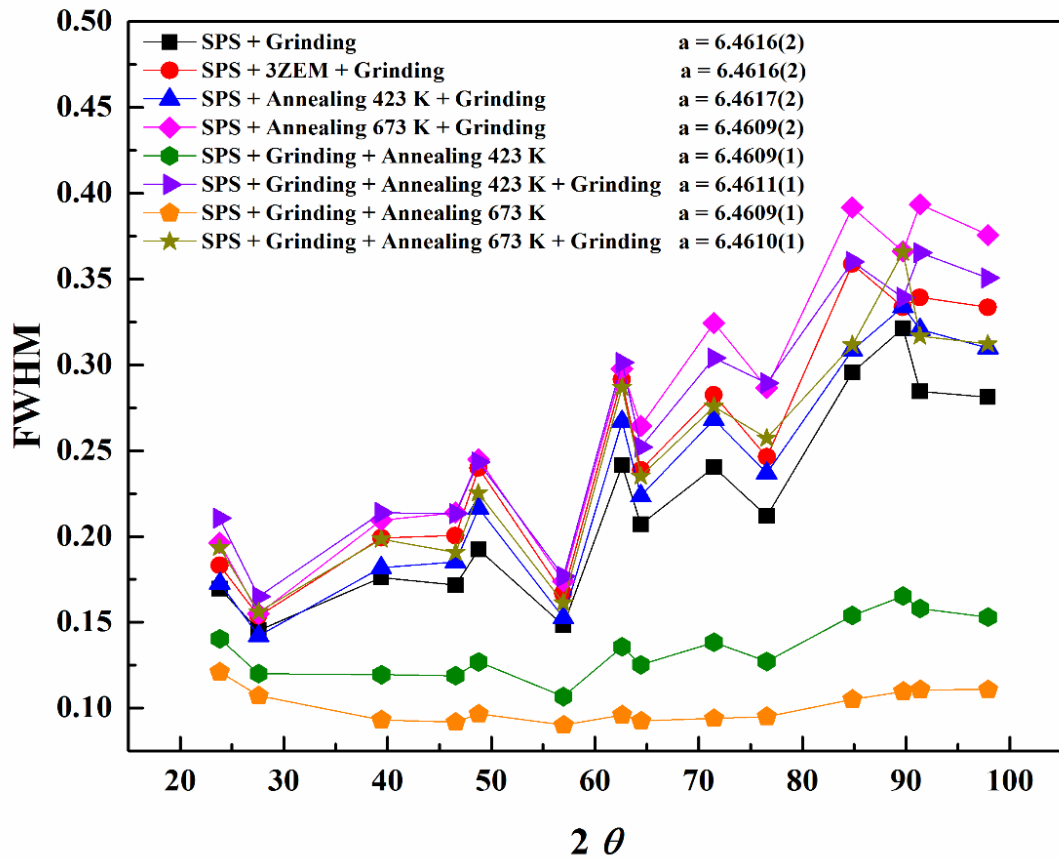
Figure 3.6. Full width at half maximum (FWHM) of powder XRD patterns from the sample B at different states.

The XRD analysis shows that all bulk specimens with or without additional annealing have the same anisotropy of the reflection broadening (Figure 3.6). However, for the annealed powder specimens (both for 423 K or 673 K annealing), the anisotropy disappears. If the annealed powders were ground and measured again, the anisotropy re-appears (Figure 3.6). Therefore, the strong anisotropy of peaks broadening comes from the mechanical stress during powder grinding and can be removed by annealing. In addition, the grinding process does not change the lattice parameter. Iversen et al.[113] explain that the observed anisotropic peak broadening is due to anisotropic microstrain and high concentrations of Pb vacancies in PbTe lattice. The annealing treatment could remove the strain and lattice defects in materials.[87] This effect has been also reflected from electronic properties (cf. discussion in chapter 3.3.3).

3.3.2. Thermoelectric properties of polycrystalline Pb–Te materials with different compositions

The electric transport properties of the sample A after SPS and LFA (No. 2), sample B after SPS (No. 5), sample C after SPS (No. 15), and sample D: SC(111) after LFA (No. 20) are presented in Figure 3.7 and Figure 3.8. All four specimens show similar metal–semiconductor and p–n transitions, which agree with published data for both single and polycrystalline materials (Figure 3.9).[69,84,86-93] The consistent electric behavior of samples A, B, and C show good reproducibility with the binary nominal stoichiometric PbTe specimens used here. The resistivity (ρ) first increases with temperature, and then starts to decrease above temperature around 500 K (Figure 3.7). Moreover, without the LFA heat treatment, the transition temperature of samples B (No. 5) and C (No. 15) decreases after the first heating and becomes stable in the further cyclic measurements (Figure 3.7b, 3.7c). The Seebeck coefficient (S) rises with increasing temperature. With further increasing temperature, S decreases rapidly through zero to negative values (Figure 3.8). The thermal conductivity of both polycrystalline (No. 2) and single crystal PbTe (No. 19) shows almost identical values. The thermal conductivity decreases from ~2.0 W m^{-1} K^{-1} at RT to ~1.4 W m^{-1} K^{-1} at 673 K of the LFA measurement temperature (Figure 3.10).
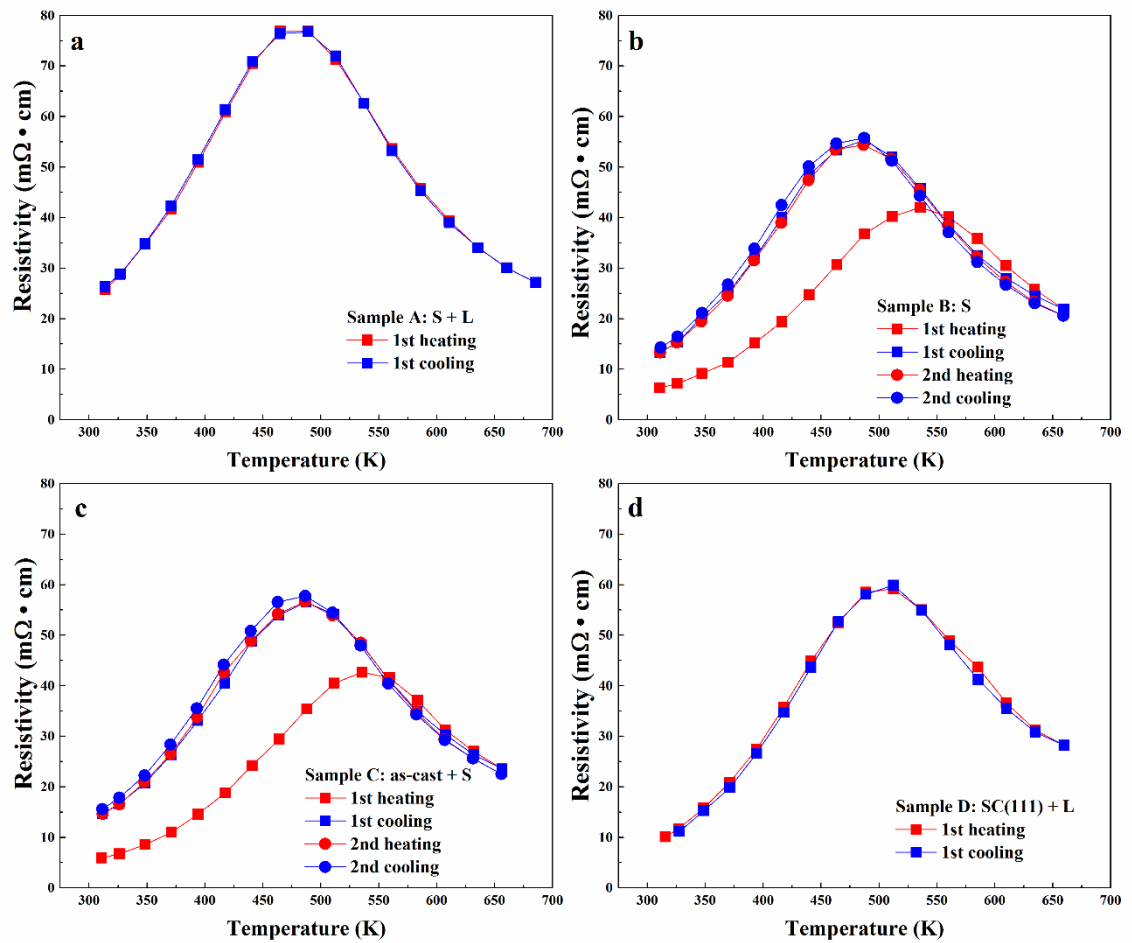
Figure 3.7. Cyclic measurements of electrical resistivity of (a) sample A: S + L (No. 2), (b) sample B: S (No. 5), (c) sample C: as-cast + S (No. 15), (d) sample D: SC(111) + L (No. 20).

3. Structural and thermoelectric properties of binary Pb–Te system
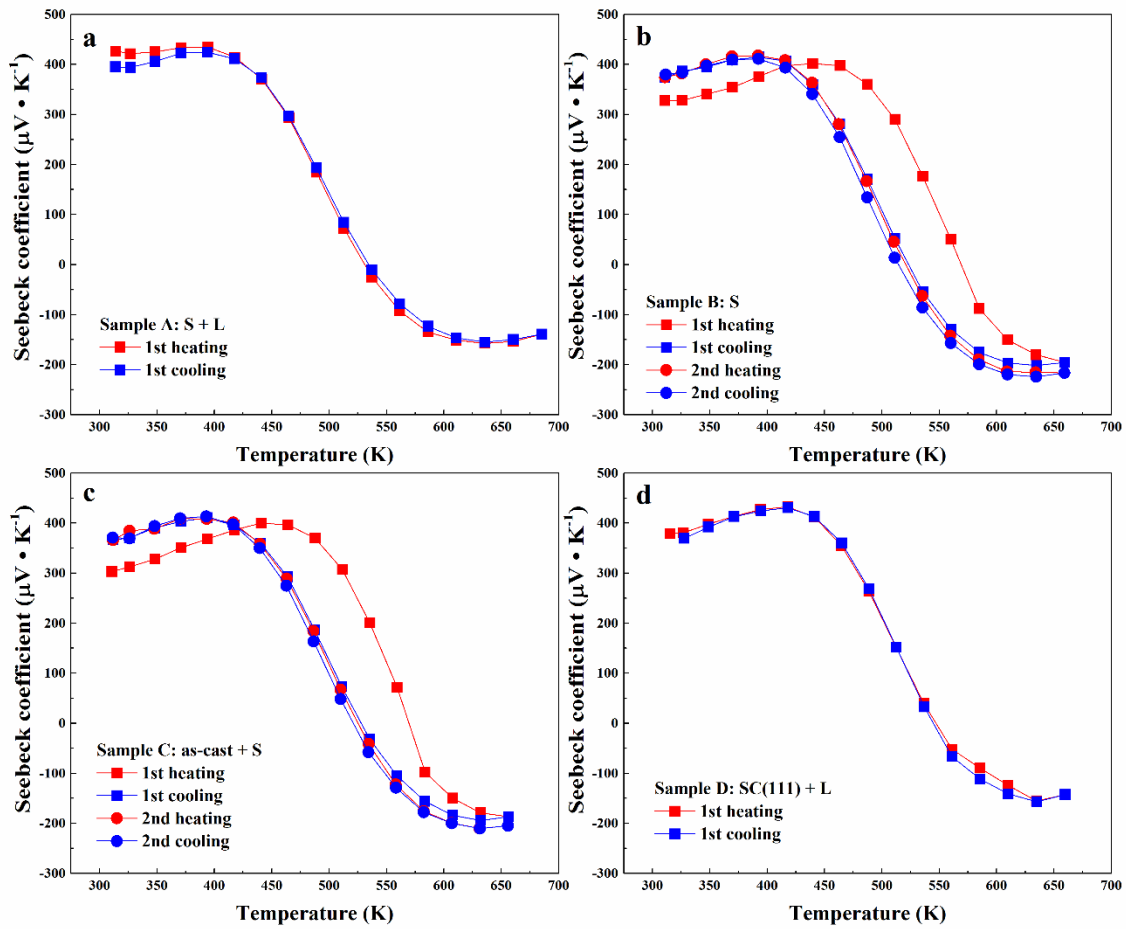
Figure 3.8. Cyclic measurements of Seebeck coefficient of (a) sample A: S + L (No. 2), (b) sample B: S (No. 5), (c) sample C: as-cast + S (No. 15), (d) sample D: SC(111) + L (No. 20).
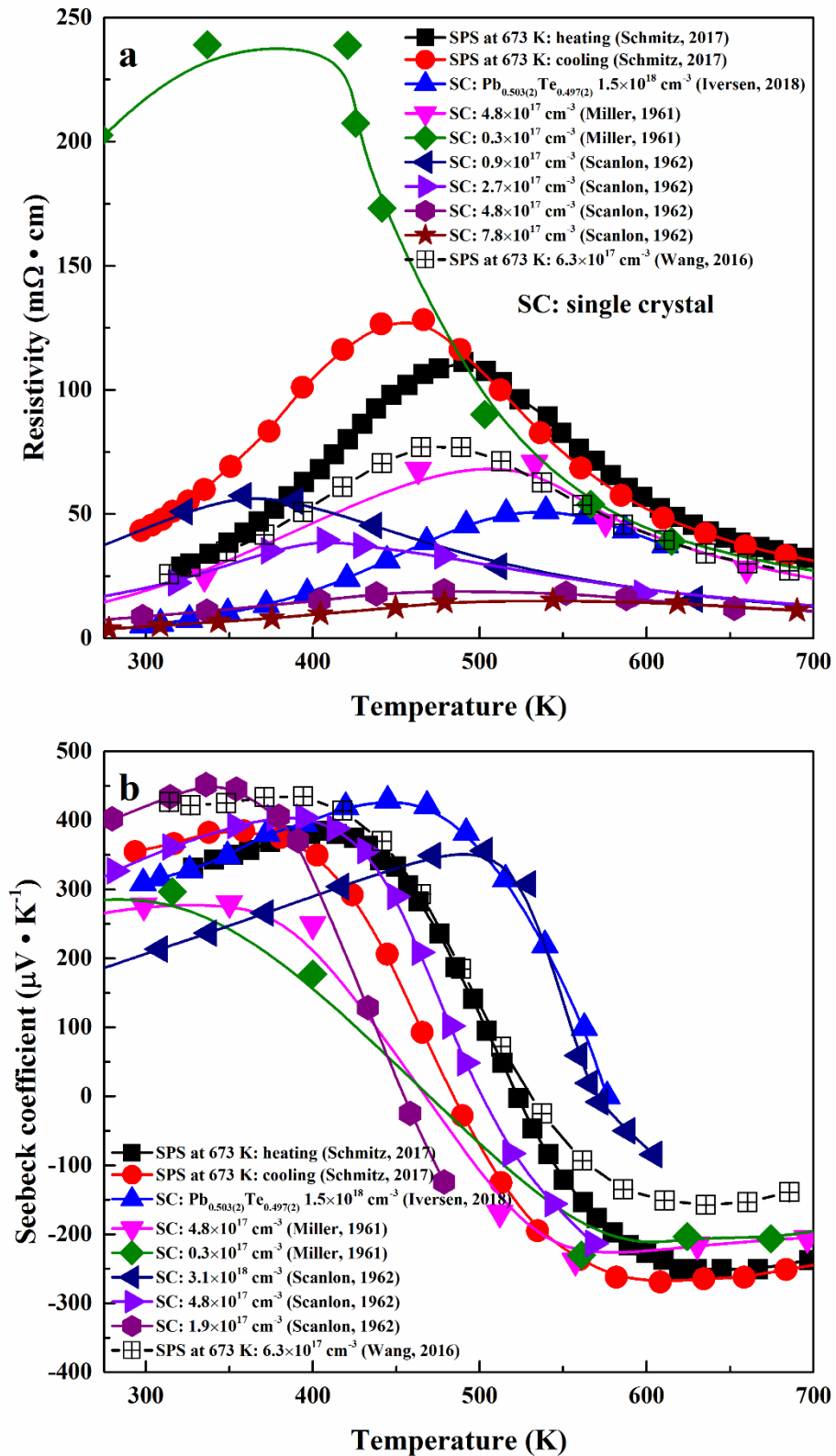
Figure 3.9. Part of literature data of PbTe for electrical resistivity (a) and Seebeck coefficient (b), which show metal–semiconductor and *p–n* transitions.

3. Structural and thermoelectric properties of binary Pb–Te system
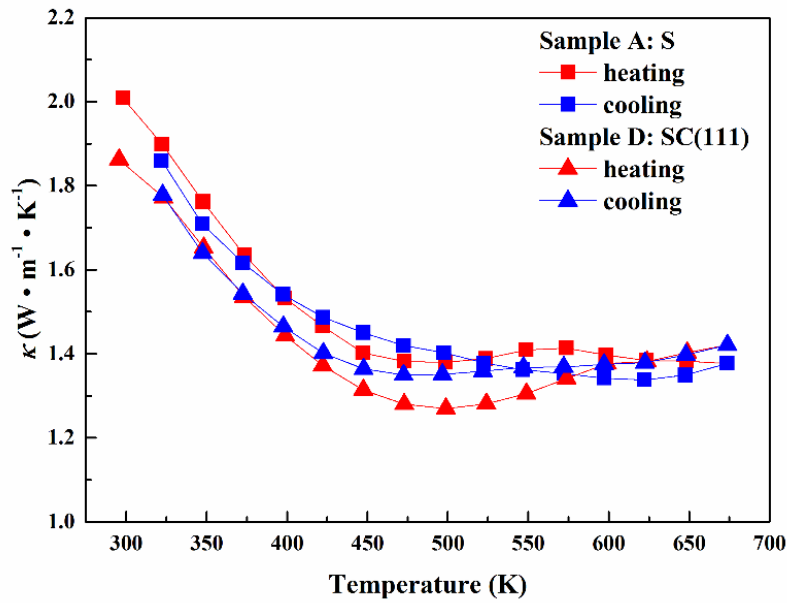
Figure 3.10. Thermal conductivity of (a) sample A: S + L (No. 2), (b) sample D: SC(111) (No. 19).

The electric properties of the two samples far out of homogeneity range Te-rich $Pb_{0.49}Te_{0.51}$ and Pb-rich $Pb_{0.51}Te_{0.49}$ were also investigated. For the $Pb_{0.49}Te_{0.51}$ (No. 24) sample, the electric properties are the same compared to $Pb_{0.50}Te_{0.50}$ (Figure 3.11). The excess Te does not ensure p-type conduction for the whole temperature range, even after long-term annealing at 673 K. This indicates that the electrical conduction behavior of binary Pb–Te will always be dominated by the intrinsic conduction (semiconductor conduction and negative Seebeck coefficient) at the high temperature range (600 K – 673 K),[87,91] which is truth according to all our investigated binary Pb–Te specimens. The $Pb_{0.51}Te_{0.49}$ (No. 27) sample, containing free Pb metal shows a higher ρ and a positive S at room temperature in the first heating cycle (Figure 3.12). With further cyclic measurements, S changes the sign at room temperature, while ρ shows a semiconductor behavior for the whole temperature range. Then decreases and shows the transition again but with a much lower transition temperature (Figure 3.12).

As discussed in chapter 1, it is well-documented that p-type carriers in binary PbTe are caused by Pb vacancies (V_{Pb}), n-type carriers are provided by either Te vacancies (V_{Te}) or Pb interstitial ions (Pb_i), or both.[69,95-98] For the $Pb_{0.51}Te_{0.49}$ (No. 27) sample, just after SPS it is p-type conductor with hole charge carriers, which corresponds to Pb vacancies.

During the cyclic ZEM measurements, the hole carriers dominate the conduction at first cycle and then turn to intrinsic behavior (2nd and 3rd cycles, Figure 3.12a), and finally becomes an electron conductor (4th cycle, n-type, Figure 3.12b). A possible explanation is that the thermal treatment during the ZEM measurement may gradually reduce the number of V_{Pb} and then increase V_{Te} or Pb_i. Moreover, the cooling data of the cyclic measurements in the $Pb_{0.51}Te_{0.49}$ always coincide with the subsequent heating data (Figure 3.12), which indicates that the changes are happening only during heating at high temperature. The highest measurement temperature is 673 K, the corresponding thermal excitation energy $k_B T$ (k_B is the Boltzmann constant) at this temperature is 0.06 eV, which is very close to the reported formation energy of Pb interstitial ions (0.09 eV).[100] Since Pb are diffused via interstitials and vacancies in PbTe,[95-98] the ZEM measurement could provide a temperature gradient and enough thermal excitation energy at 673 K during the measuring. Thus, the changing of cyclic ZEM measurements could be caused by Pb diffusion. There are two possible mechanisms that can reduce the hole carriers: Pb_i / Pb reacts with V_{Pb} ($Pb_{1-\delta}Te + \delta Pb_i$ / $\delta Pb \rightarrow PbTe$); Pb diffuses out from certain areas via a Pb vacancy mechanism to form Te precipitations, so called Pb vacancy agglomeration ($Pb_{1-\delta}Te \rightarrow (1-\delta)PbTe + \delta Te$). For the $Pb_{0.51}Te_{0.49}$ sample, the Pb source can result from the excess Pb, changing the material gradually into n-type conduction during the ZEM measurements.
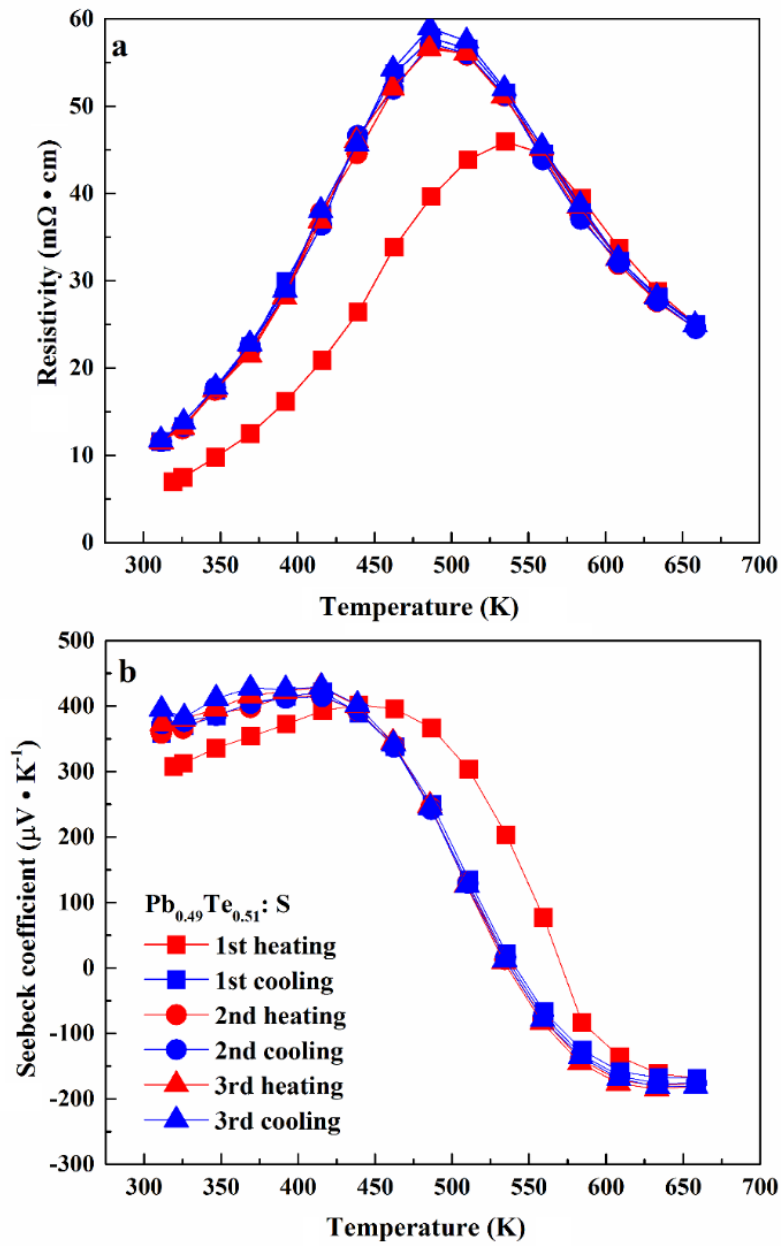
Figure 3.11. Cyclic measurements of electrical resistivity (a) and Seebeck coefficient (b) of sample $Pb_{0.49}Te_{0.51}$: S (No. 24).
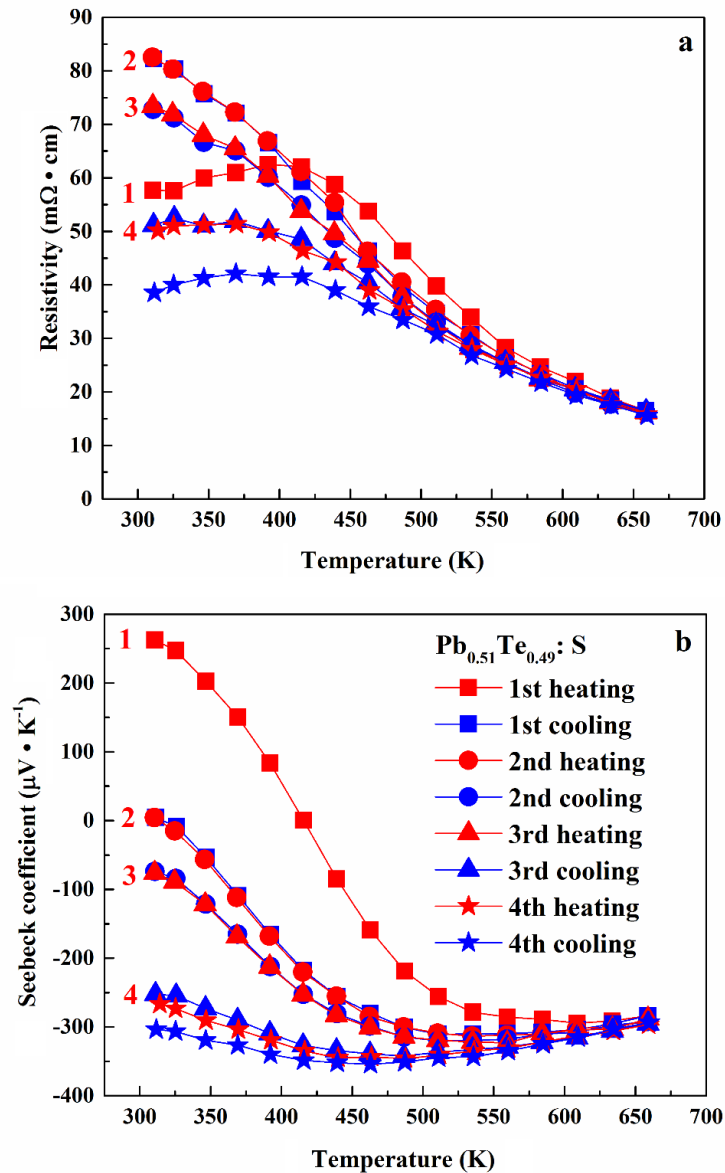
Figure 3.12. Cyclic measurements of resistivity (a) and Seebeck coefficient (b) of sample Pb$_{0.51}$Te$_{0.49}$: S (No. 27).

3.3.3. Heat treatments effect on thermoelectric properties of PbTe

As discussed above, mechanical ground powder PbTe specimens show structure changes during the heat treatment (Figure 3.4). In order to understand how heat treatments influence the TE properties of polycrystalline PbTe, three bars were cut from the after-SPS sample B: one for ZEM measurement (No. 5), one for annealing at 423 K (below the transition temperature, No. 7), and one for annealing at 673 K (above the transition

3. Structural and thermoelectric properties of binary Pb–Te system

temperature, No. 9). The bars were weighed before and after annealing, indicating that there was no mass loss. After 423 K annealing (No. 7), the cyclic measurements of ρ and S show same behavior as before annealing (Figures 3.13a, 3.13b; Figures 3.14a, 3.14b). The hole carrier concentrations after ZEM measurements are almost the same (6.6×10^{17} cm^{-3} and 7.3×10^{17} cm^{-3} respectively, see Table 3.2). After the 673 K annealing (No. 9), the electronic properties change completely. The first heating shows higher ρ with much lower transition temperature, S is still positive at RT. The further cycles change the material gradually to be n-type and towards intrinsic semiconductor conduction (Figures 3.13c, 3.14c). After three ZEM cycles, this specimen was annealed again but at 423 K (No. 11) in order to examine whether the previous state at 423 K would return. It becomes p-type with lower ρ and higher S at RT of the first heating compared to the first heating data of Figure 3.13c and Figure 3.14c. It proves that sample B changes at different temperature. Further cyclic ZEM measurements gradually make the material become n-type and intrinsic semiconductor (Figures 3.13d, 3.14d).
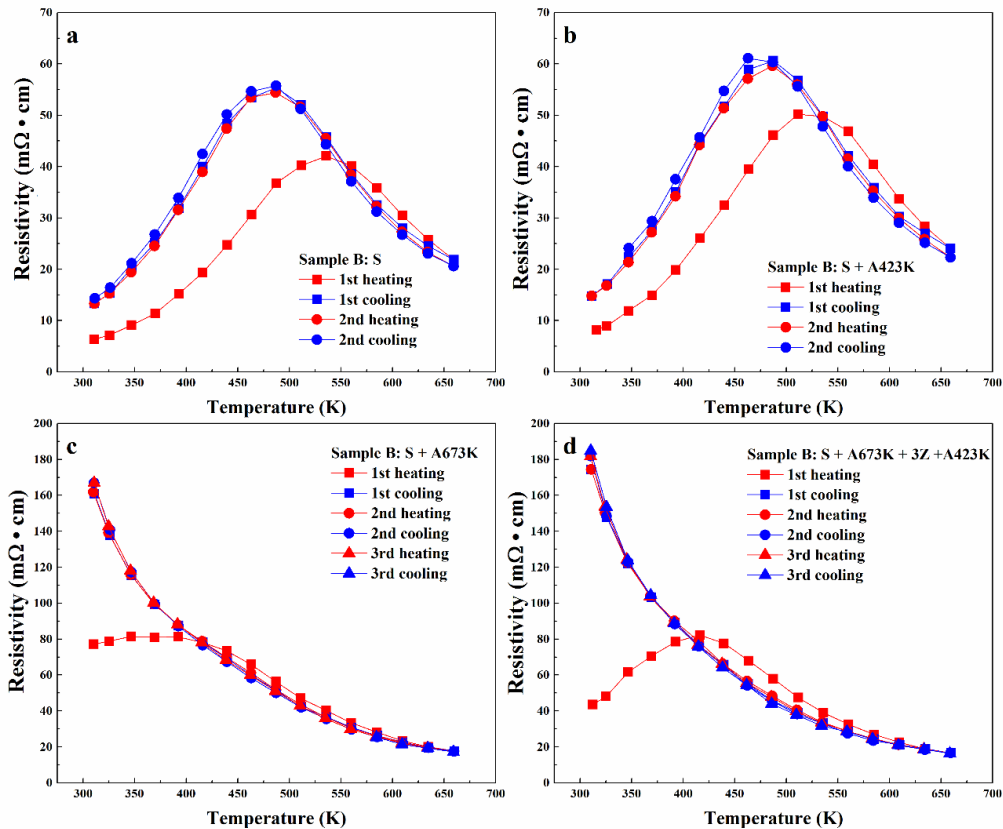
Figure 3.13. Cyclic measurements of resistivity on sample B: (a) S (No. 5), (b) S + A423K (No. 7), (c) S + A673K (No. 9), and (d) S + A673K + 3Z + A423K (No. 11).
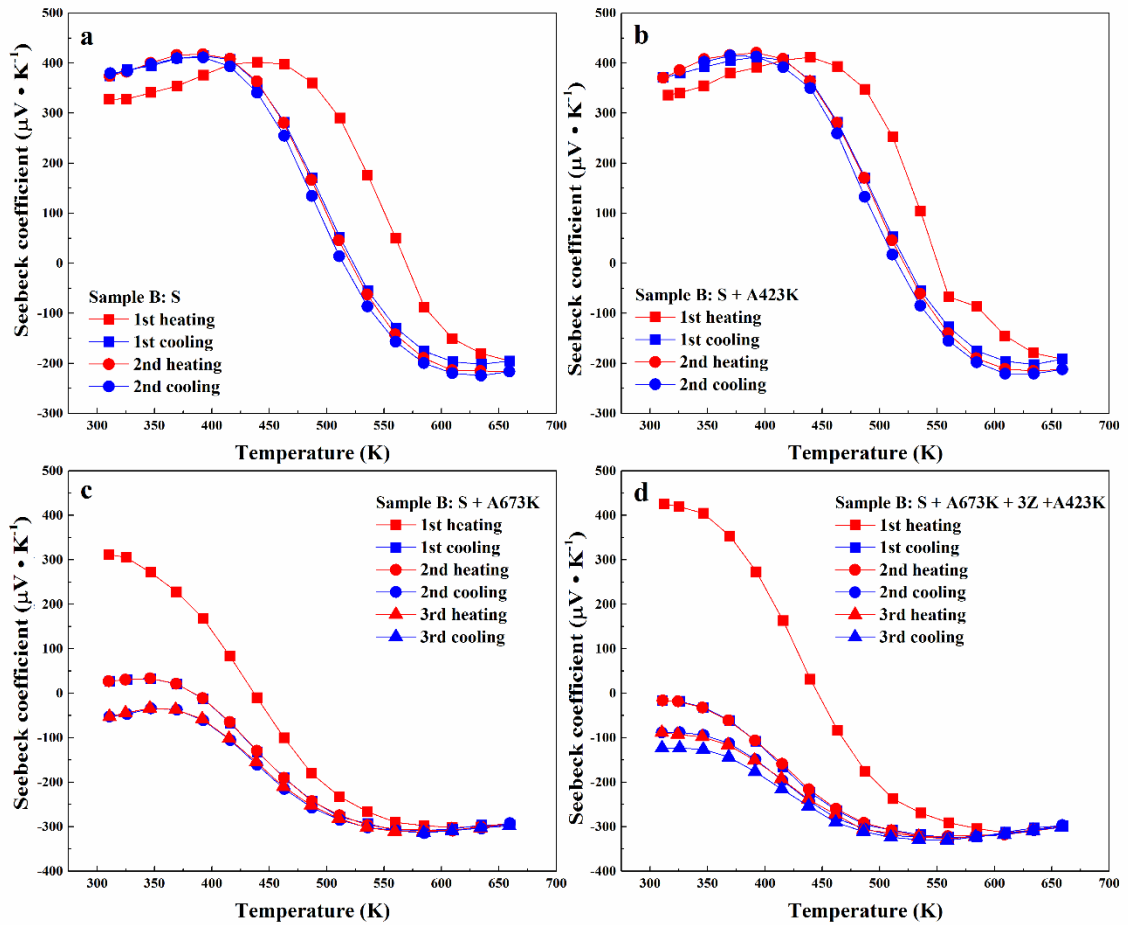
Figure 3.14. Cyclic measurements of Seebeck coefficient of sample B: (a) S (No. 5), (b) S + A423K (No. 7), (c) S + A673K (No. 9), and (d) S + A673K + 3Z + A423K (No. 11).

The high-resolution element mapping reveals that sample B after SPS (No. 5) contains some Te-rich phases of micro-scale size (Figure 3.15a). However, after annealing at 673 K (No. 9), those Te-rich phases disappear (Figure 3.15b). Dilatometer tests indicate that the annealing treatment does not change the crystal structure of PbTe (Figure 3.5a), thus the change must happen on the atomic level. According to the diffusion mechanism in PbTe, it is reasonable to assume that Pb reacts with Te to form PbTe during the 673 K annealing. The Pb source could come from Pb interstitial ions in the lattice or Pb precipitates in grain boundaries or dislocations. While for the PbTe single crystal, the same 673 K annealing (No. 22) does not change the electronic properties (Figure 3.16). Without grain boundaries, the single crystal needs much more time or higher temperature for the diffusion process to take place.[172]

3. Structural and thermoelectric properties of binary Pb–Te system
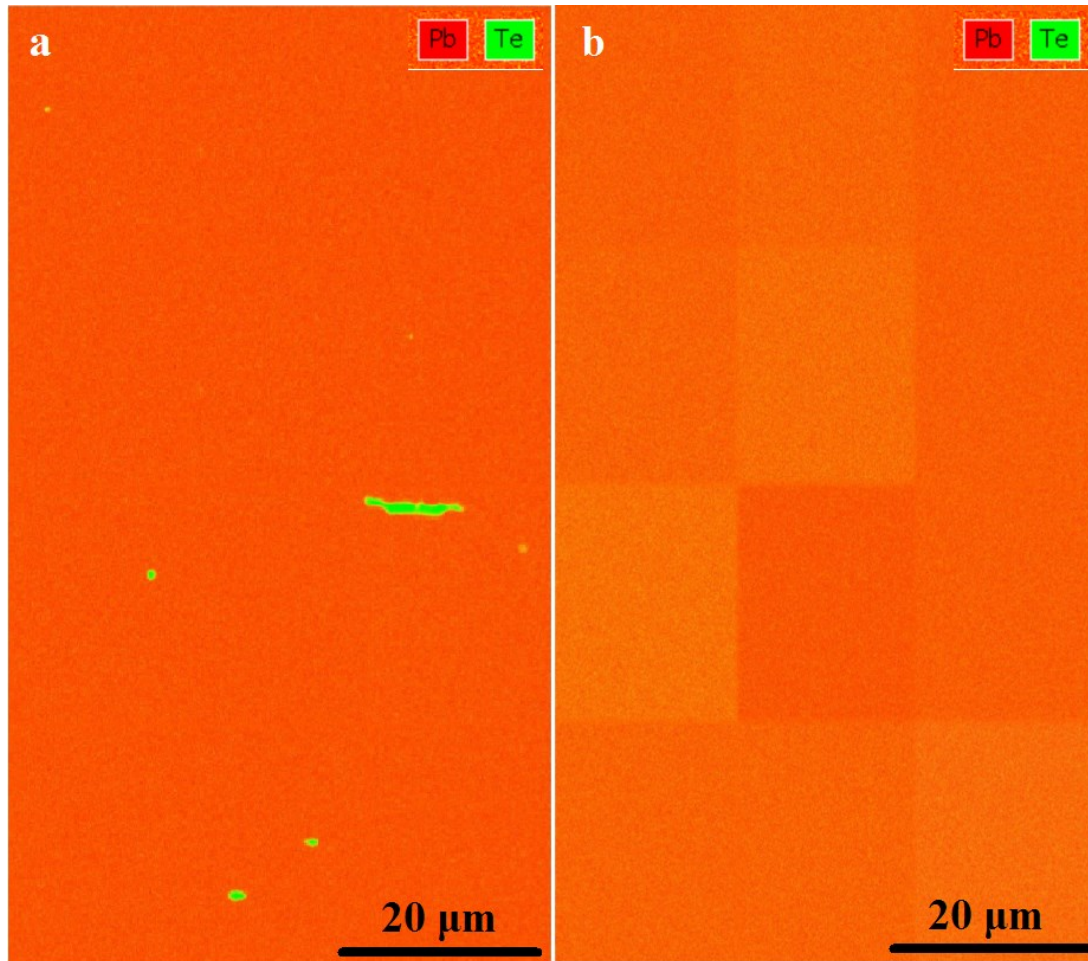
Figure 3.15. Element mapping of sample B: (a) after S (No. 5), (b) after S + A673K (No. 9).
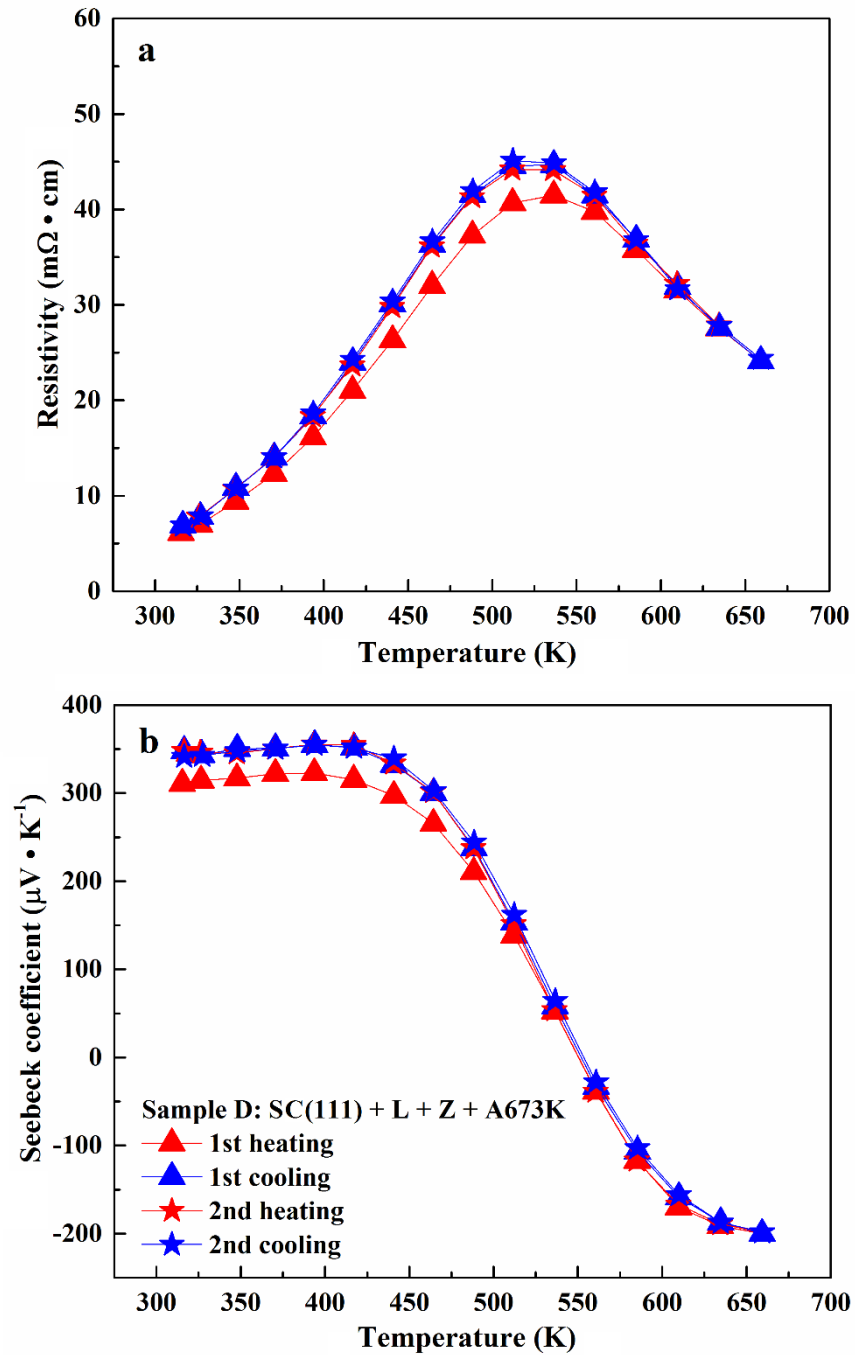
Figure 3.16. Cyclic measurements of resistivity (a) and Seebeck coefficient (b) of sample D: SC(111) + L + Z + A673K (No. 22).

The as-cast sample C (No. 13) has the highest amount of charge carriers (73.6×10^{17} cm^{-3}). This value is in good agreement with the phase diagram ($\sim 10^{19}$ cm^{-3}, Figure. 1.10b). However, the number of the charge carries is reduced by an order of magnitude after additional heat treatments (Table 3.2, samples No. 13-16). The same electric properties

3. Structural and thermoelectric properties of binary Pb–Te system

are seen for the sample C: as-cast + S + 2Z (No. 16) during the cyclic measurements. According to the phase diagram of Pb–Te, the congruent melting point does not coincide with the stoichiometric line, but differs by a Te excess of 0.016 at.%.[85,103,163] If the sample is prepared by melting, this excess Te would result in a high value of hole carrier concentration. It should be noted that lattice parameter for all specimens does not change during various treatments (Table 3.2).

Table 3.2. RT electronic properties of samples A, B, C, D, (abbreviation: S-after SPS, nZ-after n cycles ZEM measurements, AxxxK-after annealing at xxx K temperature, L-after LFA measurement).

No. n	Specimens	a (Å)	n ($\times 10^{17}$ cm^{-3})	μ (cm$^2 \cdot$ V$^{-1} \cdot$ s^{-1})	Metal–semi temperature (K)	p–n Transition temperature (K)	ρ	S
3	A: S + L + Z	—	6.3	386	480	530	Fig. 3.8a	Fig. 3.9a
6	B: S + 2Z	6.4616(2)	6.6	486	480	520	Fig. 3.8b	Fig. 3.9b
8	B: S + A423K + 2Z	6.4613(2)	7.3	471	480	520	Fig. 3.13b	Fig. 3.14b
12	B: S + A673K + 3Z + A423K + 3Z	6.4615(2)	-4.9	52	semiconductor	n-type	Fig. 3.13d	Fig. 3.14d
13	C: as-cast	6.4614(1)	73.6	112	540	565	—	—
14	C: as-cast + 3Z	—	9.5	676	500	535	—	—
15	C: as-cast + S	6.4616(2)	18.9	495	535	565	Fig. 3.8c	Fig. 3.9c
16	C: as-cast + S + 2Z	—	8.1	307	485	525	Fig. 3.8c	Fig. 3.9c
17	D: SC(100)	6.4612(2)	22.5	831	535	565	—	—
18	D: SC(100) + 5Z	—	10.4	800	500	540	—	—
21	D: SC(111) + L + Z	6.4613(2)	10.8	704	500	540	Fig. 3.8d	Fig. 3.9d

To summarize, the samples are moving towards equilibrium under the heat treatments. Polycrystalline samples after SPS and measurements (No. 3, 6, 8, 16) have similar values of the hole carrier concentration ranging from 6.3 to 8.1 × 10^{17} cm^{-3} (Table 3.2). Higher hole carrier concentrations will result in higher transition temperatures (Table 3.2). For the Hall carrier mobility, the single crystal has the highest values (No. 17, 18, 21), which indicates a good quality of crystallization. Due to a large number of grain boundaries and/or dislocations, polycrystalline samples have smaller Hall mobility values, from 307 cm$^2 \cdot$ V$^{-1} \cdot$ s^{-1} to 676 cm$^2 \cdot$ V$^{-1} \cdot$ s^{-1}. The n-type Sample B: S + A673K + 3Z + A423K + 3Z (No. 12) which shows the intrinsic semiconductor behavior (bipolar transport), the measured Hall carrier concentration and Hall carrier mobility could not reveal physically correct values.

3.4. Conclusions

Compare to the extensive investigations on single-crystal PbTe, there are less studies focusing on the binary polycrystalline PbTe. However, all recently reported high-*ZT* PbTe-based materials are polycrystalline bulk materials. With a single-crystal PbTe as a reference, the structural and thermoelectric properties of the polycrystalline bulk Pb–Te samples with different chemical compositions and heat treatments were systematically examined in this work.

It was found that the powder grinding process causes the observed anisotropic powder XRD-reflection broadening in PbTe, but without changing the lattice parameter. This mechanical effect on the lattice anisotropy could be healed by annealing. It suggests that an additional annealing treatment may be needed for the PbTe powder particles before sintering.

Compare to stoichiometric $Pb_{0.50}Te_{0.50}$, additional Te in the SPS-prepared $Pb_{0.49}Te_{0.51}$ sample has no obvious influence on the TE properties during the cyclic measurements; additional Pb in the SPS-prepared $Pb_{0.51}Te_{0.49}$ sample results in unstable electronic properties, gradually changing from *p*-type into *n*-type conduction under the cyclic measurements.

Different annealing temperatures have different influence on TE properties of the SPS-prepared stoichiometric $Pb_{0.50}Te_{0.50}$ sample. For the 423 K annealing, where the lattice anisotropy still exists, there is no obvious change of TE properties. For the 673 K annealing, where the lattice anisotropy disappears, the sample undergoes a chemical change and shows almost "intrinsic" TE properties. However, the single crystal PbTe has no obvious change during the 673 K annealing.

V_{Pb}, Pb_i, Pb precipitates, and Te precipitates may exist in SPS-prepared stoichiometric PbTe. ZEM measurement will provide a temperature gradient and enough thermal excitation energy for Pb diffusion at 673 K during the measurement (especially on grain boundaries and dislocations). The complex diffusion processes in PbTe including processes at grain boundaries and/or under contribution of dislocations provide dynamic chemical reactions during the measurements and the annealing, which should be responsible for variable electric properties in polycrystalline PbTe.

3. Structural and thermoelectric properties of binary Pb–Te system

4. Europium substitution in PbTe

Two series of polycrystalline samples $(PbTe)_{1-x}(EuTe)_x$ and $(PbTe)_{1-y}(EuTe_{1.5})_y$ were systematically investigated. The Eu solubility limit for different substitution schemes and for different annealing temperatures was established. No significant influence of Eu substitution on the thermoelectric figure-of-merit was observed in bulk stoichiometric PbTe.[91]

4.1. Introduction

All lanthanide (Y, La–Lu) monotellurides adopt the NaCl structure type.[174-175] Almost all of them are trivalent metals and are electron donors in PbTe.[25,137] However, in monotellurides, Eu, Sm, Yb and Tm are divalent and therefore, are expected to be electrically balanced in the solid solution with PbTe. However, this was proven to be the case only for Eu and Sm.[176-177] Substitution by Eu has been shown to have significant influence on the band structure of PbTe.[178-179] Largely enhanced thermoelectric figure-of-merit at room temperature (RT) have been theoretically predicted for quantum well $Pb_{1-x}Eu_xTe$ layers and confirmed experimentally for thin films.[37,180-182] Samples of the pseudo-binary system $PbTe-Eu_2Te_3$ with low concentration (less than 5.0 mol%) of Eu_2Te_3 showed (with increasing Eu content) a decrease of the thermal conductivity combined with the opposite tendency in the electrical conductivity and Seebeck coefficient (maximum Seebeck coefficient of 315 mV K^{-1} and minimum conductivity of 22.5×10^{-3} S m^{-1} at 1.0 mol% of Eu_2Te_3, with all properties were measured at RT).[184] The compounds PbTe and EuTe both crystallize in the NaCl structure type, and it is commonly assumed that $(PbTe)_{1-x}(EuTe)_x$ forms a solid solution over the entire concentration range. However, the lattice parameter increases nonlinearly and does not obey Vegard's rule.[178,184-186] According to the phase diagram of the Eu–Te system,[187] the equiatomic phase has a homogeneity range between 50 and 57 at.% of Te under 873 K and 1173 K annealing temperatures. This may indicate a presence of europium in the $4f^6$ (Eu^{3+}) state.

In order to investigate how these possibilities influence the thermoelectric properties of PbTe, we report on the constitution as well as on the thermoelectric and the carrier-transport properties of polycrystalline solid solutions $(PbTe)_{1-x}(EuTe)_x$ and $(PbTe)_{1-y}(EuTe_{1.5})_y$ in the temperature range between RT and 700 K.

4.2. Experimental details

Binary samples $Eu_{1-x}Te_x$ (x = 0.44, 0.50, 0.52, 0.55, 0.57, 0.60, 0.62, 0.64) were synthesized by melting the elements Te (chunk, 99.9999 mass%), Eu (chunk, 99.95 mass%) in a graphite-coated and fused silica tube at 1373 K for 6 h under a pressure of around 10^{-4} torr, then annealed at 1123 K for 300 hours for homogenization, and slowly cooled to RT in 12 hours. The obtained ingots were ground into powders in an agate mortar in argon atmosphere. Part of powders were sealed in Ta tube under argon atmosphere in fused silica tube for further annealing process of 360 hours at 873 K. The tubes were then quenched in ice water.

For the ternary Pb–Eu–Te system, two synthesis processes with different annealing temperatures have been realized:

Annealing at 873 K: Ternary samples $(PbTe)_{1-x}(EuTe)_x$ (x = 0.005, 0.010, 0.015, 0.02, 0.03, 0.04, 0.05, 0.07, 0.10) and $(PbTe)_{1-y}(EuTe_{1.5})_y$ (y = 0.01, 0.02, 0.03, 0.04, 0.05, 0.07, 0.10) were synthesized by melting the elements Pb (shot, 99.999 mass%), Te (chunk, 99.9999 mass%), Eu (chunk, 99.95 mass%) in a graphite-coated and fused silica tube at 1273 K for 6 h under a pressure of around 10^{-4} torr, then annealed at 873 K for 144 hours for homogenization, slowly cooled to RT in 6 hours. The obtained ingots were ground into powders in an agate mortar in argon atmosphere.

Annealing at 1123 K: Ternary samples $(PbTe)_{1-x}(EuTe)_x$ (x = 0.03, 0.04, 0.05, 0.07, 0.10, 0.15, 0.20, 0.50, 0.80) and $(PbTe)_{1-y}(EuTe_{1.5})_y$ (y = 0.02, 0.03, 0.04, 0.07, 0.08, 0.10, 0.15, 0.20, 0.50, 0.80) were synthesized by melting the elements Pb (shot, 99.999 mass%), Te (chunk, 99.9999 mass%), Eu (chunk, 99.95 mass%) in a graphite-coated and fused silica tube at 1273 K for 6 h under a pressure of around 10^{-4} torr, then annealed at 1123 K for 300 hours for homogenization, slowly cooled to RT in 12 hours. The obtained ingots were ground into powders in an agate mortar in argon atmosphere.

For thermoelectric properties measurements, the selected samples were sintered by SPS and measured with LFA and ZEM.

4.3. Results and discussion

4.3.1. Phase analysis

The shape of the solid solution of Eu in PbTe is defined by the following lines in the ternary Pb–Eu–Te phase diagram (Figure 4.1). The Eu substitution follows either the $(PbTe)_{1-x}(EuTe)_x$ scheme (blue dash line in Figure 4.1) or $(PbTe)_{1-y}(EuTe_{1.5})_y$ (green dash line in Figure 4.1). Binary Eu–Te samples ($Eu_{1-x}Te_x$) in range between 44 and 64 at.% Te (red dash line in Figure 4.1) were synthesized to verify the solid solubility range (orange solid line, cf. Ref. 187). Only $Eu_{0.56}Te_{0.44}$ shows a nearly single phase (with small amount of impurities) for the as-cast samples. After annealing for 360 hours at 873 K, the $Eu_{0.50}Te_{0.50}$ sample is single phase; other Eu–Te samples contain some additional unindexed reflections. The obtained lattice parameter value fits well in the range between 6.586 Å and 6.603 Å reported in the literature.[188] As shown in Figure 4.2, the lattice parameter of $Eu_{1-x}Te_x$ (for $x = 0.50$, 6.6010(4) Å) shows a small variation depending on the Te concentration. The lattice parameter of the as-cast specimens is slightly larger in comparison with the specimens annealed at 873 K, most probably due to the not completely equilibrium state. From the lattice parameter, the large homogeneity range of Eu–Te as reported in Ref. 187, was not confirmed at 873 K.
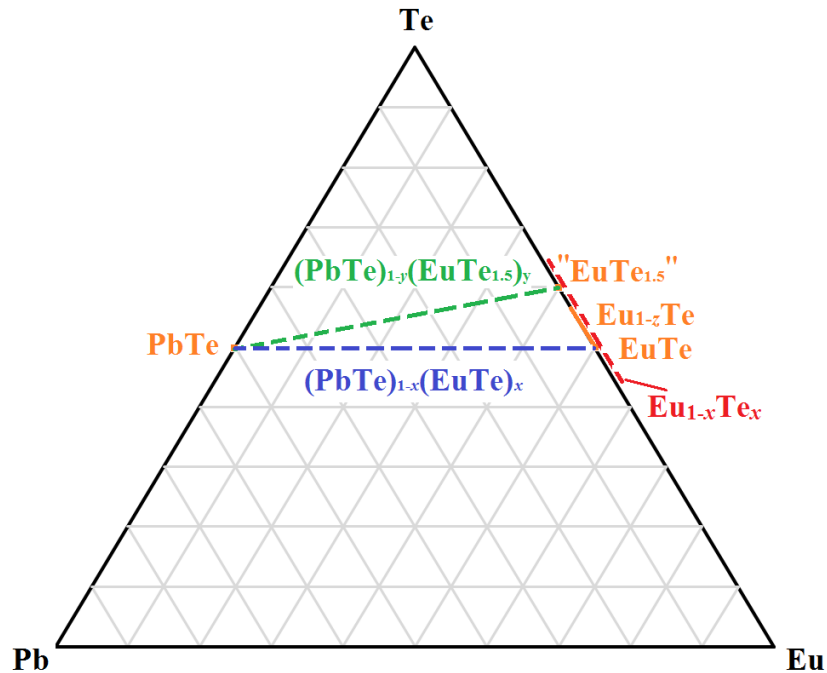
Figure 4.1. Location of the solid solution of Eu in the phase diagram Pb–Eu–Te.

4. Europium substitution in PbTe
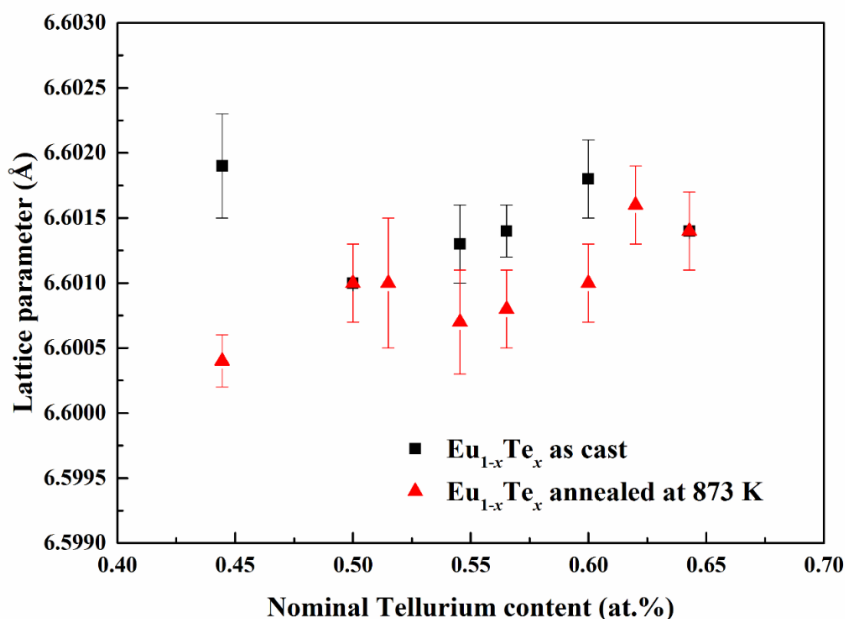
Figure 4.2. Lattice parameters of $Eu_{1-x}Te_x$ as cast (black), annealed at 873 K (red).

The samples $(PbTe)_{1-x}(EuTe)_x$ ($x = 0 — 1.0$) and $(PbTe)_{1-y}(EuTe_{1.5})_y$ ($y = 0 — 1.0$) were synthesized with additional annealing at 873 K and at 1123 K. As presented in Figure 4.3a, the lattice parameter of the $(PbTe)_{1-x}(EuTe)_x$ annealed at 873 K changes linearly with the composition for $x \le 0.02$, and then remains constant (Figure 4.3a, green squares). Therefore, the Eu solubility in $(PbTe)_{1-x}(EuTe)_x$ at 873 K is determined as $x = 0.02$. The samples with $x \ge 0.03$ contain reflections of two cubic phases (with NaCl structure): Pb-rich $(PbTe)_{1-x}(EuTe)_x$ and Eu-rich $(EuTe)_{1-z}(PbTe)_z$ (Table 4.1, for example, two cubic phases were identified in sample $x = 0.07, 0.10$, Figure 4.4). The change of the lattice parameter within the two phases range indicates that the samples are still not in equilibrium state. For samples $(PbTe)_{1-y}(EuTe_{1.5})_y$ annealed at 873 K, only sample with $y = 0.01$ is single-phase material; others contain elemental Te or tiny unknown phase or second cubic phase (Table 4.2). Thus, the Eu solubility in $(PbTe)_{1-y}(EuTe_{1.5})_y$ at 873 K is $y = 0.01$ (Figures 4.3a, 4.3c).
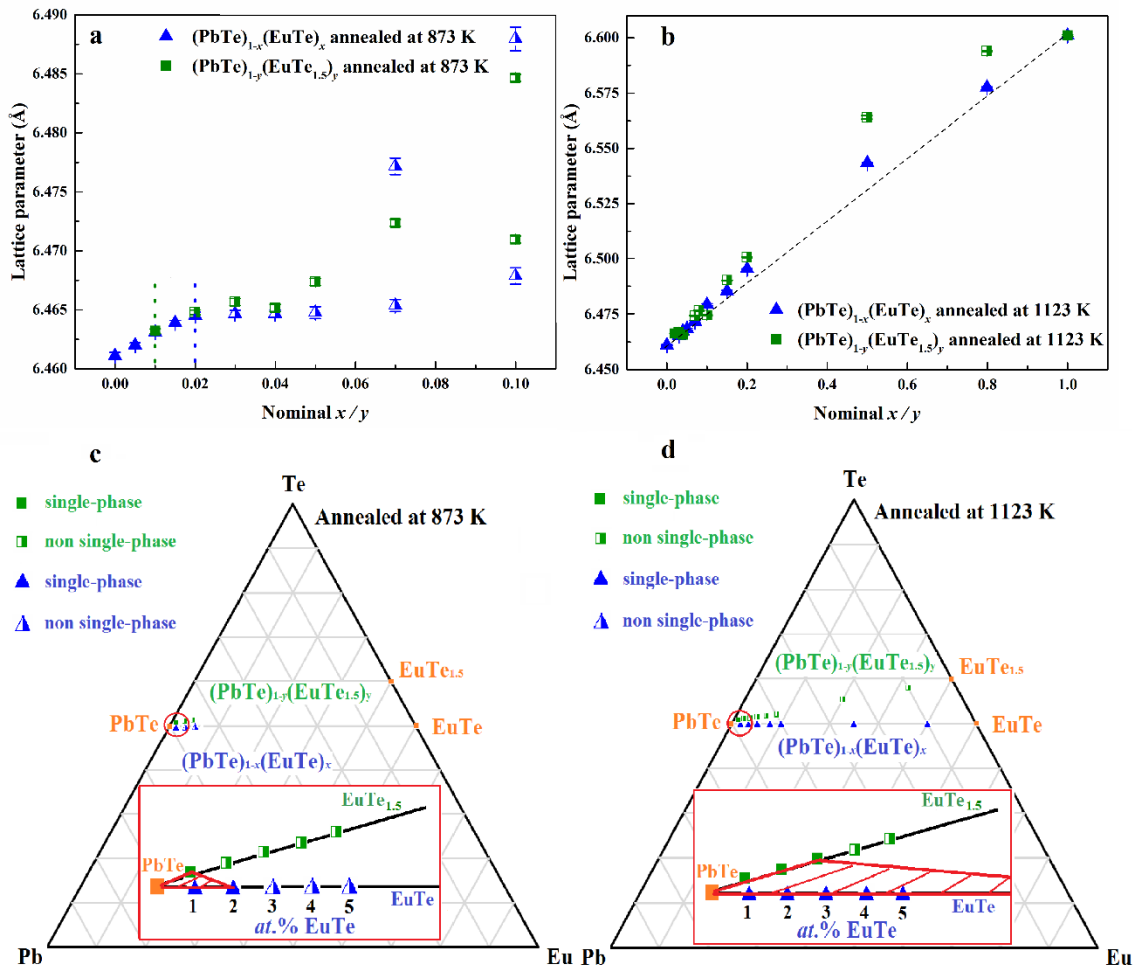
Figure 4.3. (a) Lattice parameters of $(PbTe)_{1-x}(EuTe)_x$ (green squares) and $(PbTe)_{1-y}(EuTe_{1.5})_y$ (blue triangles) annealed at 873 K. (b) Lattice parameters of $(PbTe)_{1-x}(EuTe)_x$ (green squares) and $(PbTe)_{1-y}(EuTe_{1.5})_y$ (blue triangles) annealed at 1123 K. (c) Synthesized samples and the location of the solid solution of Eu (inset, red square area) in the phase diagram Pb–Eu–Te at 873 K. (d) Synthesized samples and the location of the solid solution of Eu (inset, red square area) in the phase diagram Pb–Eu–Te at 1123 K.

When the annealing temperature is increased up to 1123 K, $(PbTe)_{1-x}(EuTe)_x$ is a solid solution over the entire concentration range (Figure 4.3b, green squares, and Table 4.2). This finding is consistent with Ref. 185. There the samples were prepared by heating components in arc-welded tantalum crucibles at 1223 K for seven days. The $(PbTe)_{1-y}(EuTe_{1.5})_y$ samples with $y \leq 0.03$ are single-phase materials (Figure 4.3d); samples with $0.04 \leq y \leq 0.20$ contain elemental Te; samples with $y = 0.50$ and 0.80 are multiphase materials (Table 4.1). However, the lattice parameter of main cubic phase increases with

4. Europium substitution in PbTe

increasing Eu. When x (or y) ≥ 0.15, the lattice parameter of $(PbTe)_{1-y}(EuTe_{1.5})_y$ is higher than the lattice parameter of $(PbTe)_{1-x}(EuTe)_x$ (Figure 4.3b, blue triangles). Therefore, the solubility and solid solution region of Eu in PbTe are larger when temperature up to 1123 K (Figure 4.3d). According to the effective magnetic moment per Eu atom calculated from magnetic susceptibility, Eu in $(PbTe)_{1-x}(EuTe)_x$ is always Eu^{2+}, while part of Eu atoms show the Eu^{3+} state in $(PbTe)_{1-y}(EuTe_{1.5})_y$. More details about Eu oxidation state in PbTe will be discussed in Chapter 6.

Table 4.1. Phase analysis of the samples $(PbTe)_{1-x}(EuTe)_x$ and $(PbTe)_{1-y}(EuTe_{1.5})_y$ annealed at 873 K and 1123 K.

Composition $(PbTe)_{1-x}(EuTe)_x$	873 K, Phase(s)	1123 K, Phase(s)	Composition $(PbTe)_{1-y}(EuTe_{1.5})_y$	873 K, Phase(s)	1123 K, Phase(s)
$x = 0.005$	single phase	—	—	—	—
$x = 0.010$	single phase	—	$y = 0.01$	single phase	—
$x = 0.015$	single phase	—	—	—	—
$x = 0.02$	single phase	—	$y = 0.02$	Te	single phase
$x = 0.03$	two cubic phases	single phase	$y = 0.03$	tiny unknown phase	single phase
$x = 0.04$	two cubic phases	single phase	$y = 0.04$	tiny unknown phase	Te
$x = 0.05$	two cubic phases	single phase	$y = 0.05$	Te	Te
$x = 0.07$	two cubic phases	single phase	$y = 0.07$	Te, two cubic phases	Te
$x = 0.10$	two cubic phases	single phase	$y = 0.10$	Te, two cubic phases	Te
$x = 0.15$	—	single phase	$y = 0.15$	—	Te
$x = 0.20$	—	single phase	$y = 0.20$	—	Te
$x = 0.50$	—	single phase	$y = 0.50$	—	multi-phases
$x = 0.80$	—	single phase	$y = 0.80$	—	multi-phases
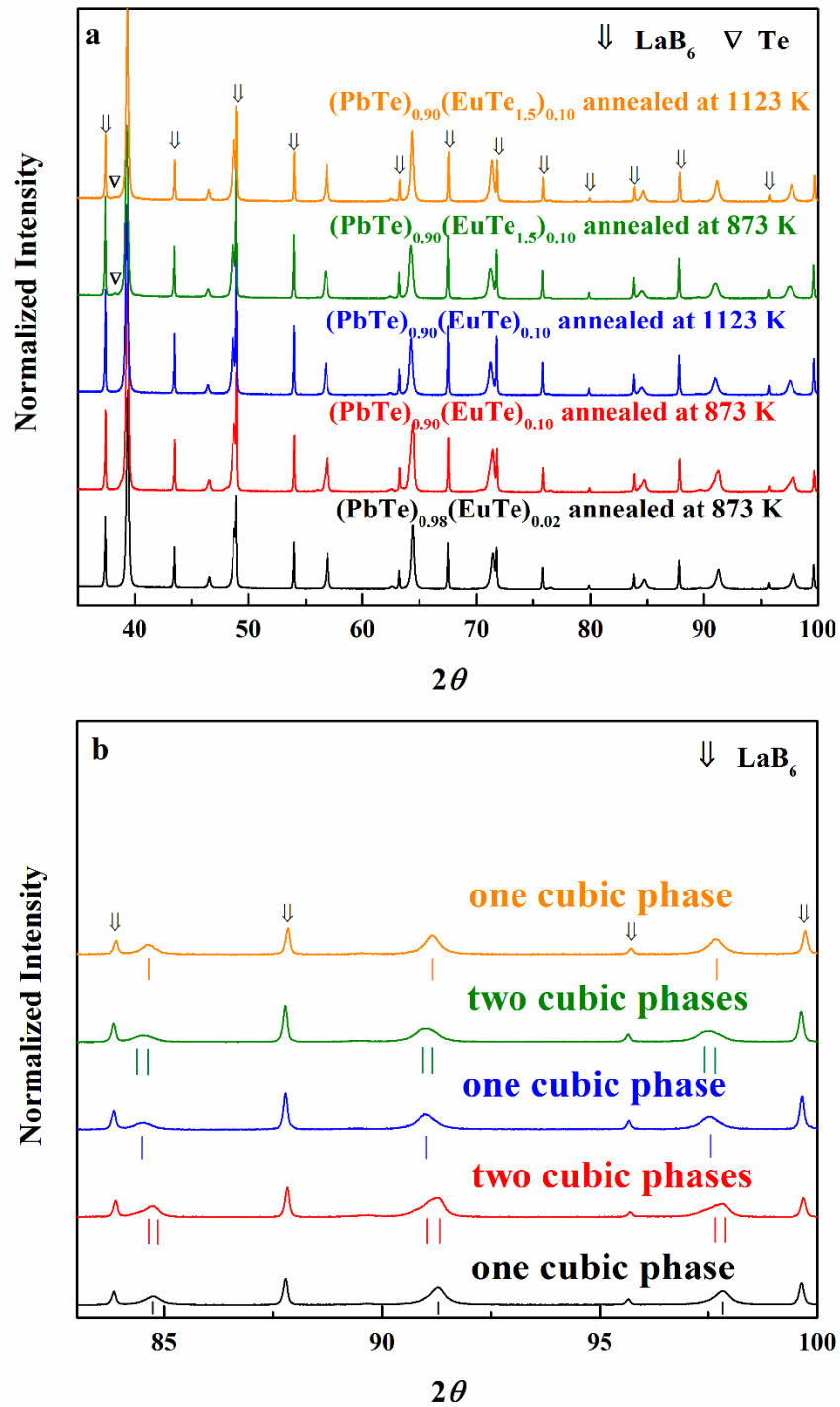
Figure 4.4. (a) X-ray powder diffraction patterns for $(PbTe)_{0.98}(EuTe)_{0.02}$ samples (black line, single phase), $(PbTe)_{0.90}(EuTe)_{0.10}$ (red line, two cubic phases) , $(PbTe)_{0.90}(EuTe_{1.5})_{0.10}$ (green line, Te phase and two cubic phases) annealed at 873 K; and samples $(PbTe)_{0.90}(EuTe)_{0.10}$ (blue line, single phase), $(PbTe)_{0.90}(EuTe_{1.5})_{0.10}$ (orange line, Te phase and one cubic phase) annealed at 1123 K. (b) The enlargement of the high-2θ range.

4. Europium substitution in PbTe

4.3.2. Thermoelectric properties

The samples annealed at 873 K have been SPS-sintered for the thermoelectric properties investigation. The electrical resistivity of samples $(PbTe)_{1-x}(EuTe)_x$ shows a bad-metal behavior in the low-temperature range below 500 K, and then changes to semiconducting one at higher temperatures (Figure 4.5a), similarly to the binary PbTe.[69,84,87-88] The Seebeck coefficient changes sign at slightly higher temperature (around 550 K) compared to binary PbTe, indicating a *p-n* transition (Figure 4.5b). The thermal conductivity decreases with temperature below the *p-n* transition and remains practically unchanged above the *p-n* transition (Figure 4.5c). With increasing europium content, the resistivity first decreases to $x = 0.01$ and then increases toward $x = 0.04$ (Figure 4.5a); the Seebeck coefficient practically does not change (Figure 4.5b); the total and lattice thermal conductivity decrease (Figures 4.5c, 4.5d). The Eu content of samples $(PbTe)_{1-x}(EuTe)_x$ ($x \leq 0.04$) does not have systematic influence on Hall carrier concentration, but the Hall carrier mobility decreases with increasing Eu content (Table 4.2).
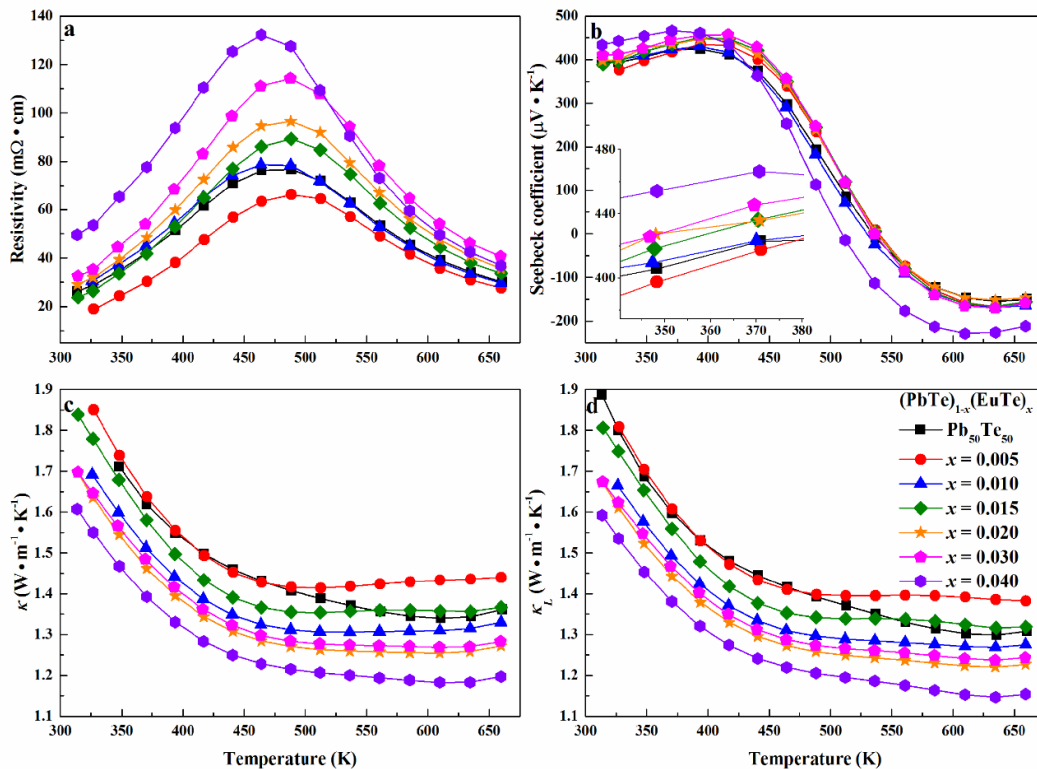
Figure 4.5. Temperature dependent thermoelectric properties of $(PbTe)_{1-x}(EuTe)_x$ annealed at 873 K: electrical resistivity (a), Seebeck coefficient (b), total thermal conductivity (c), lattice thermal conductivity (d).

Table 4.2. Room temperature Hall carrier concentration (n) and Hall carrier mobility (μ) of $(PbTe)_{1-x}(EuTe)_x$ annealed at 873 K.

$(PbTe)_{1-x}(EuTe)_x$	$x = 0$	$x = 0.005$	$x = 0.010$	$x = 0.015$	$x = 0.020$	$x = 0.030$	$x = 0.040$
n ($\times 10^{17}$ cm^{-3})	6.3	8.4	12.6	8.0	11.2	6.2	3.9
μ (cm$^2 \cdot$ V$^{-1} \cdot$ s^{-1})	386	464	378	380	282	342	279

The resistivity of $(PbTe)_{1-y}(EuTe_{1.5})_y$ samples increases with increasing Eu content until $y = 0.07$ (Figure 4.6a). The unexpected results of the $y = 0.10$ sample maybe due to the presence of two cubic phases. The Seebeck coefficient changes slightly with y at RT (Figure 4.6b, inserts). The total and lattice thermal conductivity increase with increasing Eu content (Figures 4.6c, 4.6d), which can be attributed to enhanced phonon scattering by increased point defects and impurity phase when introducing more Eu. In both series, Eu addition does increase the resistivity and decrease the thermal conductivity, but without obvious influence on Seebeck coefficient.
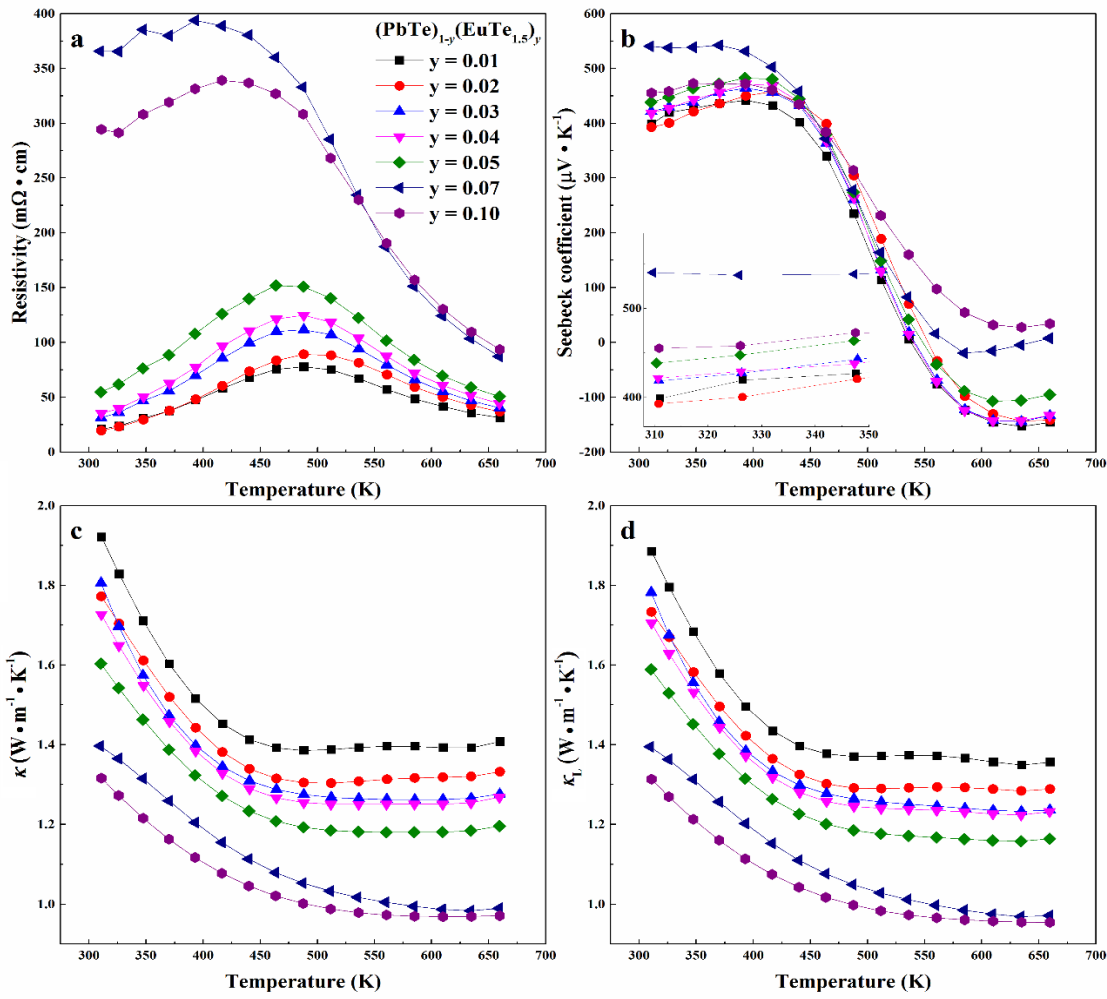
Figure 4.6. Temperature dependent thermoelectric properties of $(PbTe)_{1-y}(EuTe_{1.5})_y$ annealed at 873 K: electrical resistivity (a), Seebeck coefficient (b), total thermal conductivity (c), lattice thermal conductivity (d).

The values of the thermoelectric figure-of-merit *ZT* for both series samples are in the same range (Figure 4.7) and have maximal values at room temperature. Overall, lead-by-europium substitution does not strongly influence the thermoelectric ability of stoichiometric lead telluride. For cyclic measurements, the electrical resistivity and Seebeck coefficient are well repeatable for several cycles (Figure 4.8). This indicates that the materials annealed at 873 K are stable.
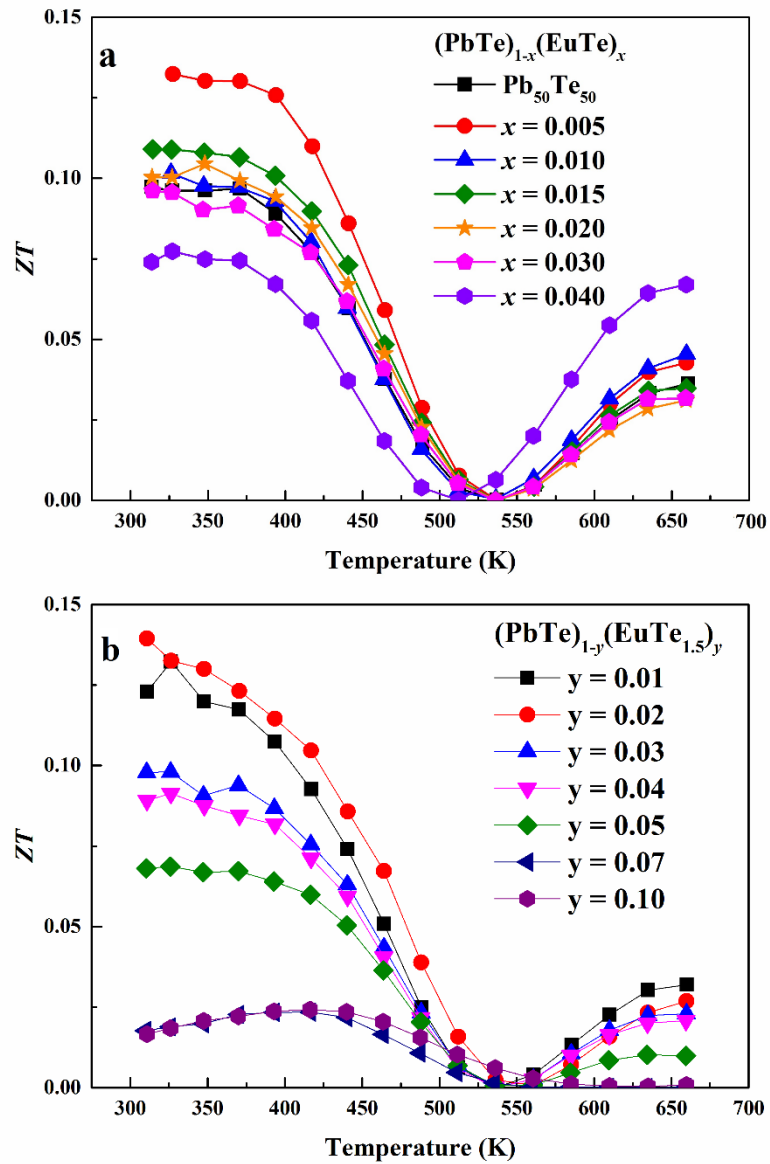
Figure 4.7. Temperature dependence of the thermoelectric figure-of-merit ZT for (a) $(PbTe)_{1-x}(EuTe)_x$ and (b) $(PbTe)_{1-y}(EuTe_{1.5})_y$ annealed at 873 K.
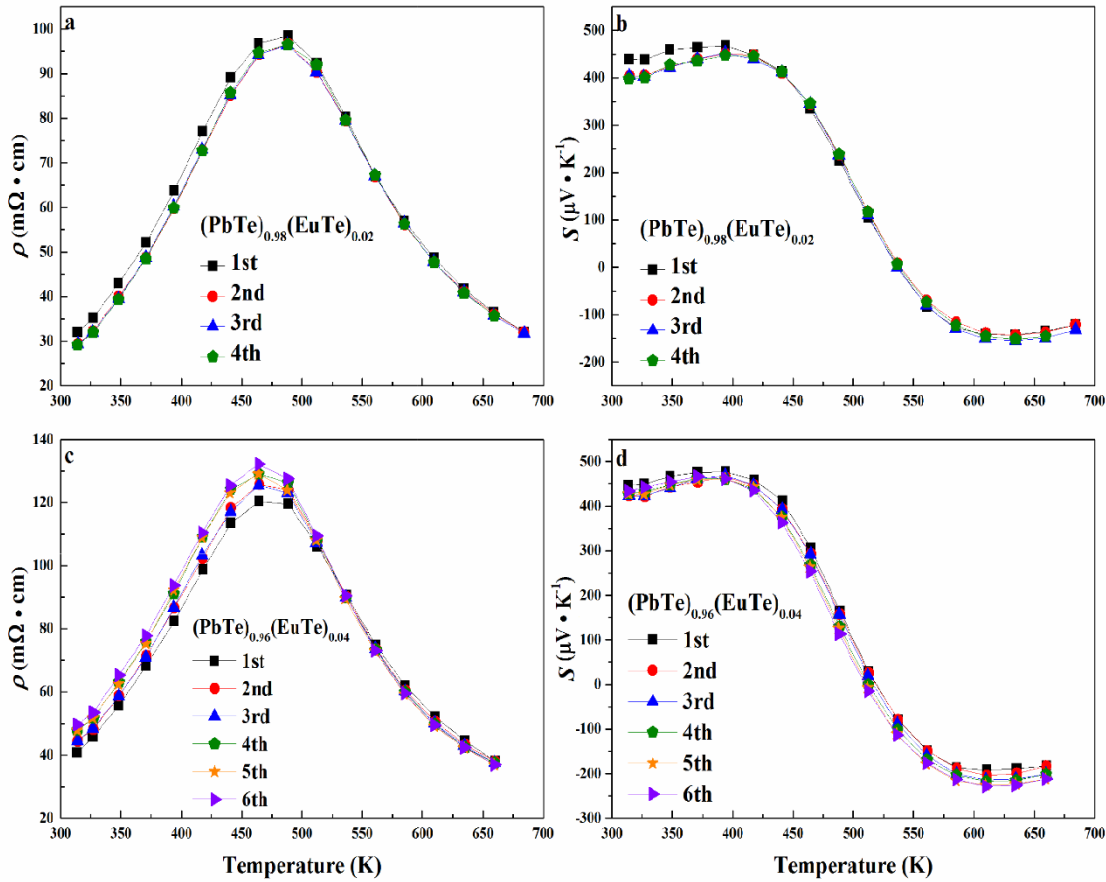
Figure 4.8. Cyclic measurements of thermoelectric properties of $(PbTe)_{1-x}(EuTe)_x$ annealed at 873 K (a, b) $x = 0.02$ and (c, d) $x = 0.04$.

It is commonly believed that Eu has strong influence on electronic band structure of PbTe, as well documented in single-crystal $Pb_{1-x}Eu_x$Te films.[178,186] Although the resistivity increases and the thermal conductivity decreases with increasing Eu content, no significant influence of these two different Eu substitution schemes on the thermoelectric figure-of-merit was observed in bulk PbTe annealed at 873 K. We examined also the single-phase samples $(PbTe)_{1-x}(EuTe)_x$ ($x = 0.03, 0.10, 0.15$) which were annealed at 1123 K. As shown in Figure 4.9, resistivity has been increased and shows a semiconductor behavior for the whole temperature range for $x = 0.10$ and 0.15. The *p-n* transition still exists but the Seebeck coefficient changes the sign twice, a *p-n-p* transition behavior is observed for $x = 0.15$ (Figure 4.9b). The total and lattice thermal conductivities decrease with increasing Eu and increasing temperature (Figures 4.9c, 4.9d). For a semiconductor, the intrinsic electric conductivity (σ) can be expressed as a

function of the activation energy (E_a) and temperature (T): $\sigma = \sigma_0 \cdot \exp(-E_a/2k_B T)$. The "thermal activation energy" of $(PbTe)_{1-x}(EuTe)_x$ (x = 0.03, 0.10, 0.15) samples is calculated from the measured resistivity. The "thermal activation energy" increases with increasing Eu content (Figure 4.10), which indicates that the Eu enlarges the band gap of PbTe, consistent with Ref. 178. However, the "thermal activation energy" of x = 0.15 sample has a sharp turn around 500 K, which may indicate that the sample has changed during the measurement. The cyclic electric measurements of single-phase samples with x = 0.03, 0.10 show stable properties. While for the sample x = 0.15, the resistivity is decreasing and the Seebeck coefficient is increasing during each cycle. After the first heating, the Seebeck coefficient becomes p-type for the whole temperature range (Figure 4.11b). The x = 0.15 sample shows broader peaks at high PXRD reflection angles after three cycles of ZEM measurements (Figure 4.12, red line). The single-phase bulk x = 0.15 sample was further annealed at 873 K for 900 hours. It decomposed into two cubic phases, the corresponding lattice parameter changed from 6.4853(3) Å into 6.4616(3) Å and 6.4895(3) Å (Figure 4.12, blue line). Similar decomposition behavior was reported in $(PbTe)_{1-x}(EuTe)_x$ thin films for x = 0.5.[189] To summarize, the high Eu content single-phase sample $(PbTe)_{0.85}(EuTe)_{0.15}$ annealed at 1123 K has larger band gap and shows completely semiconductor behavior. With additional heat treatment at lower temperature (ZEM measurements at 673 K or annealing at 873 K), the solibility of Eu in PbTe decreases, resulting in decomposed phases and changed electrical properties.

4. Europium substitution in PbTe
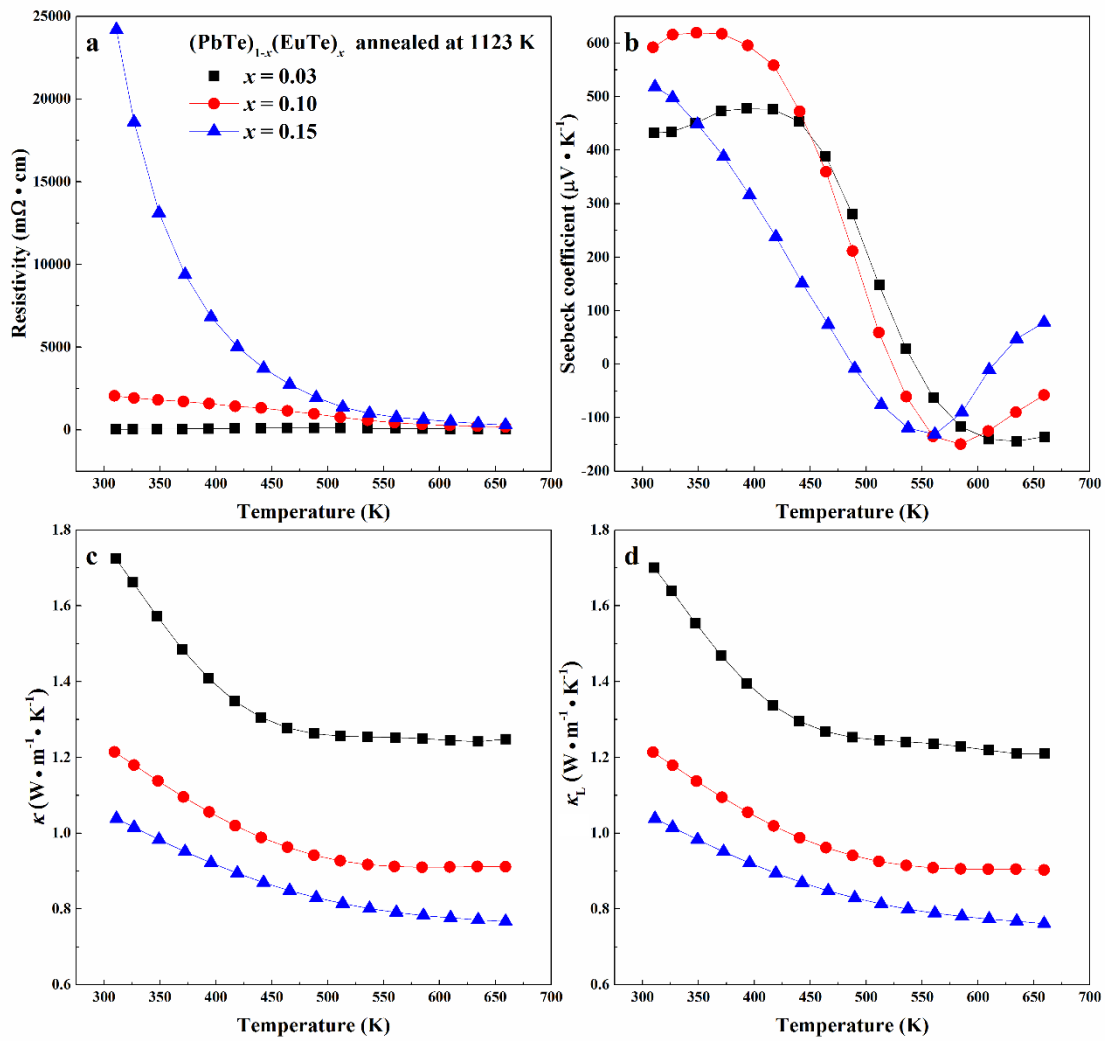
Figure 4.9. Temperature dependent thermoelectric properties of $(PbTe)_{1-x}(EuTe)_x$ annealed at 1123 K: electrical resistivity (a), Seebeck coefficient (b), total thermal conductivity (c), lattice thermal conductivity (d).
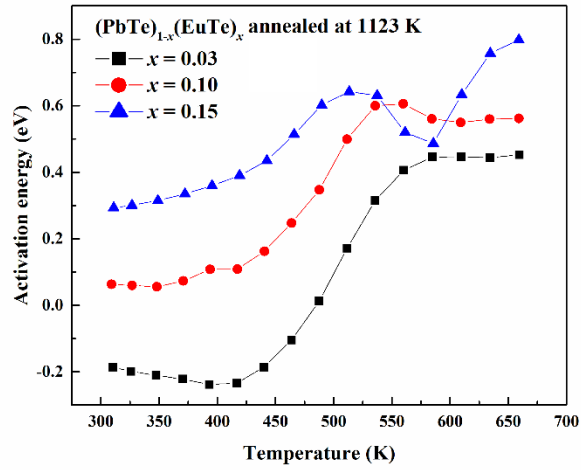
Figure 4.10. "Thermal activation energy" calculated from resistivity for (PbTe)$_{1-x}$(EuTe)$_x$ annealed at 1123 K.
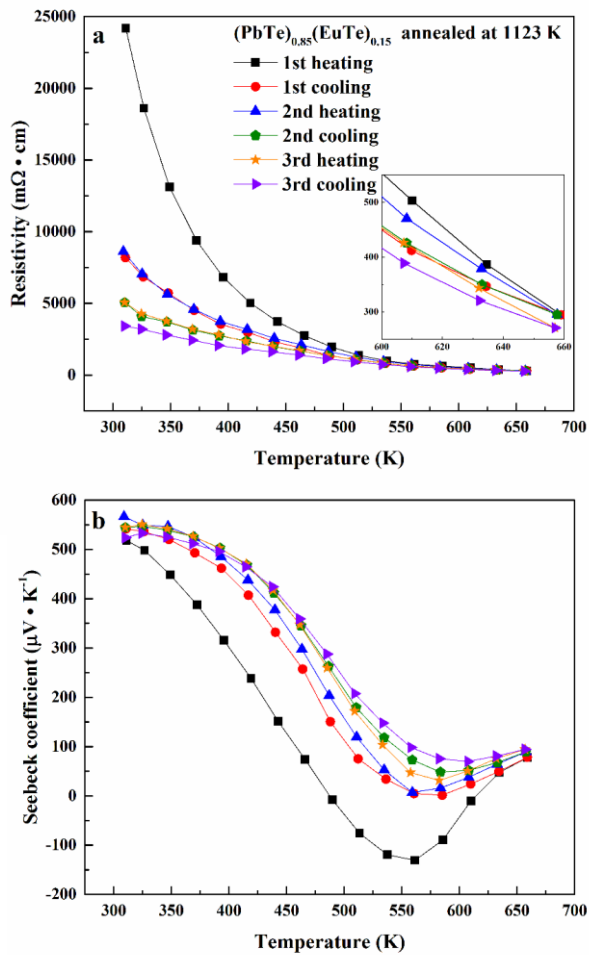
Figure 4.11. Cyclic measurements of (PbTe)$_{0.85}$(EuTe)$_{0.15}$ annealed at 1123 K (a) resistivity and (b) Seebeck coefficient.
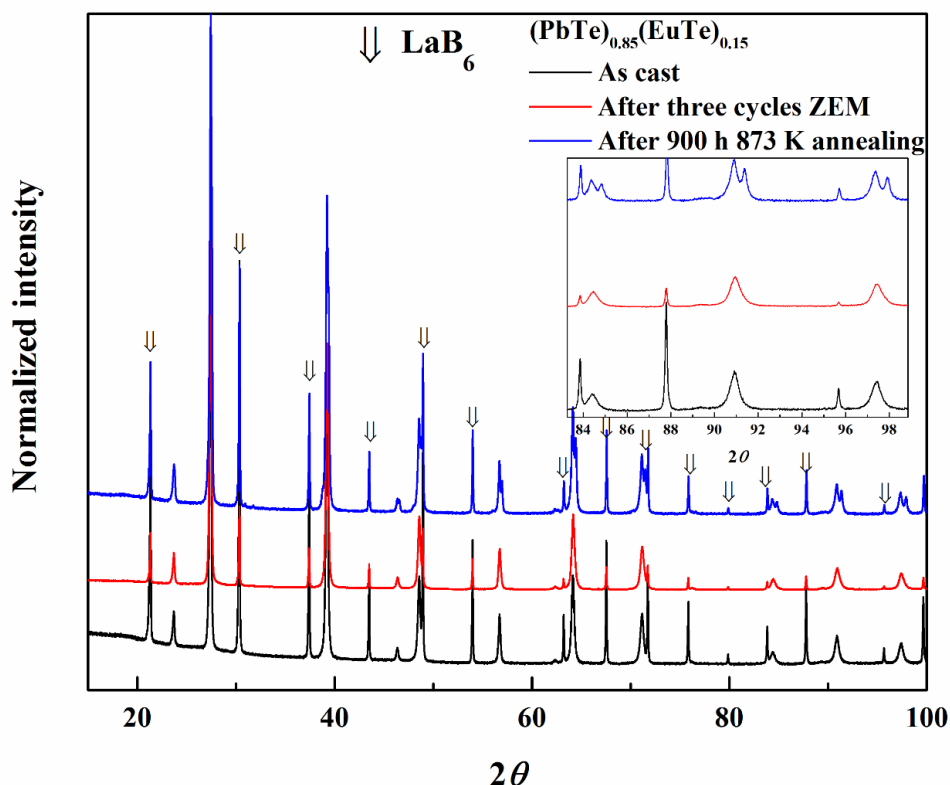
Figure 4.12. X-ray powder diffraction patterns of 1123 K annealed (PbTe)$_{0.85}$(EuTe)$_{0.15}$ sample: as-cast (black line), after three cycles ZEM (red line), after 900 hours 873 K annealing (blue line), and with LaB$_6$ as standard.

4.5. Conclusions

The pseudo-binary (PbTe)$_{1-x}$(EuTe)$_x$ and (PbTe)$_{1-y}$(EuTe$_{1.5}$)$_y$ series of samples were synthesized and annealed at temperatures 873 K and 1123 K. The shape of the solid solution of Eu in the ternary system Pb–Eu–Te under different temperature was established. Eu has small solubility range ($x = 0.02$, $y = 0.01$) in PbTe at 873 K annealing temperature. At 1123 K, (PbTe)$_{1-x}$(EuTe)$_x$ forms a solid solution over the entire concentration range. For (PbTe)$_{1-y}$(EuTe$_{1.5}$)$_y$ samples, the single-phase materials can be achieved when y ≤ 0.03.

Unlike reported (PbTe)$_{1-x}$(EuTe)$_x$ quantum well films,[37,180-182] no significant influence of these two Eu substitution schemes on the thermoelectric figure-of-merit was observed in bulk PbTe. Nevertheless, the resistivity increases and the thermal conductivity decreases with increasing Eu content.

Eu can enlarge the band gap of PbTe when it forms solid solution. However, the solid solution with high Eu content ($x \geq 0.15$) is not stable at temperatures above 673 K during the measurements or annealing. It decomposes into two cubic phases.

4. Europium substitution in PbTe

5. Sodium substitution in PbTe

Two series of polycrystalline samples $Pb_{1-y}Na_yTe_{1-y/2}$ and $Pb_{1-x}Na_xTe$ were investigated. Sodium has limited solubility in both of the series. The MAS ^{23}Na NMR analysis of $Pb_{0.98}Na_{0.02}Te$ sample after SPS reveals only one Na signal, corresponding to Na atoms coordinated by six Te atoms, indicating substitution of Pb by Na without defects in the Te sublattice. In the $Pb_{1-y}Na_yTe_{1-y/2}$ series, clustering of Na atoms with reduced coordination by Te was observed. Additional heat treatment of these samples leads to the reorganization of the Na clusters in PbTe and their equilibration with the homogenized distribution of Na in the whole volume. The maximum *ZT* values of 1.4 — 1.6 at 760 K are established for both series. Upon long-term annealing at 873 K, reorganization and redistribution of Na atoms lead to the change in carrier concentration and, consequently, the thermoelectric properties for both series.[153]

5.1. Introduction

Sodium has been proved as one of the most effective dopants in controlling hole carrier concentration in Pb*X* (*X* = Te, Se, S) and therefore has been extensively utilized in order to optimize their thermoelectric properties.[65,114-117] It is usually believed that the monovalent Na is substituting Pb. Typically Na is added to PbTe and PbTe-based materials in the form of NaTe or Na_2Te, thus giving rise to formation of acceptor centers.[65,125,155,190-193] First fundamental experiments revealed the diffusion coefficient increasing with increasing Na concentration. If Na diffuses *via* Pb vacancies, the respective diffusion coefficient would be expected to decrease. Such anomalous concentration dependence of the diffusion coefficient was explained by presence of the Te vacancies, which may indeed reduce the energy barriers for migration, temporarily making it possible for Na to reside on Te sites. In other words, the diffusion coefficient should increase with increasing Na concentration if Te vacancies take part in the diffusion mechanism.[115]

In a later study, the hole concentration was found to be considerably smaller than a value calculated from the amount of Na added to the reaction mixture, assuming one hole was produced per one Na atom. The maximum Na solubility in PbTe was experimentally determined to lie somewhere between 0.5 at.% and 1.75 at.%, although some loss of Na

5. Sodium substitution in PbTe

may occur during processing.[190-191] The maximum observed carrier concentration is 2.5×10^{20} cm^{-3}. Each Na atom donates about one hole when Na concentration is higher than $\sim 6 \times 10^{19}$ cm^{-3}, which corresponds to 0.84 at.%.[197] However, at Na concentration less than this value, one hole produced by two Na atoms was distinguished experimentally. For the nature of the acceptor centers at small Na concentrations, a proposed model implies a formation of the significant complex center (Na$_{Pb}$□$_{Te}$Na$_{Pb}$).[114]

The systematic study of PbTe–Na$_2$Te and PbTe–NaTe quasi-binary phase diagrams shows that only Na$_2$Te (anti-CaF$_2$ crystal structure[155]) and NaTe phase (own molecular-like structure[194]) are found in these systems.[195] According to the chemical analysis,[191] the maximum solubility of Na in PbTe was found to be 1.4 ± 0.3 mol% (0.7 at.% Na average values from more than 100 point analysis, by electron microprobe WDXS) at 623 K. While at 513 K, the solubility value decreases to 0.24 ± 0.14 at.%.[191] First-principles calculations of defect energy in Na-Pb-Te indicate that Na substituting Pb is the lowest-energy defect (Na$_{Pb}$$^{1-}$); here the solubility should increase with increasing temperature.[193] In recent microscopic studies on Na-doped polycrystalline PbTe samples, Na-rich nano-segregations at mesoscale imperfections, dislocations, and grain boundaries even nanoscale precipitates were formed when Na is beyond the solubility limit,[196-198] which may provide additional scattering centers and reduce the thermal conductivity[190,199] or increase the high-temperature electrical conductivity due to re-dissolution of Na at elevated temperatures.[197] However, simple 1:1 substitution Pb by Na is mostly considered in the experimental studies. The complete shape of the solid solution of Na in PbTe within the ternary system Pb–Na–Te was not established (cf. Ref. 191). As a consequence, the influence of different Pb–by–Na substitution mechanisms on the thermoelectric activity of the ternary materials remains unclear. The possibility of the two substitution schemes is indicated or assumed by different Na-additives (NaTe or Na$_2$Te) for formation of acceptor centers.

5.2. Experimental details

Bulk polycrystalline samples Pb$_{1-x}$Na$_x$Te ($0 \leq x \leq 0.04$) and Pb$_{1-y}$Na$_y$Te$_{1-y/2}$ ($0 \leq y \leq 0.10$) were synthesized by melting the elements Pb (shot, 99.999 mass%), Te (chunk, 99.9999 mass%), Na (chunk, 99.99%) in a graphite-coated and fused silica tube at 1273 K for 6 h under a vacuum of around 10^{-4} torr. Then, the temperature was slowly lowered to 873 K

and the samples were annealed for six days for homogenization. The cut sample bars (after SPS and LFA) were sealed in Ta tubes under Ar atmosphere in fused silica tube for annealing at 873 K, with following quenching in ice water after 900 hours. Na_2Te, for the NMR investigations, was synthesized by melting Na and Te in the stoichiometric ratio in an Ar atmosphere in a sealed Ta tube at 773 K for 5 hours.

Elemental chemical analysis (for Pb, Te, Na, O) was performed by ICP-OES. The ^{23}Na NMR signals of specimens from $Pb_{1-x}Na_xTe$ and $Pb_{1-y}Na_yTe_{1-y/2}$ under different heat treatments were investigated.

5.3. Results and discussion

5.3.1. Phase analysis

Two series of the samples were prepared (Figure 5.1a, top). The first series with the nominal composition $Pb_{1-x}Na_xTe$ ($x = 0.005 — 0.04$) assumes that Na atoms simply substitute Pb. All as-cast samples are single-phase materials according to the powder X-ray diffraction (PXRD). The lattice parameter decreases with the increasing Na concentration monotonically up to 1 at.% (Figure 5.1b, red squares) being consistent with the respective ionic radii of the Na^+ (0.99 Å) and Pb^{2+} (1.19 Å).[120] This signalizes the homogeneity range border in direction to the NaTe phase of about 1 at.% of Na, being well in agreement with the results obtained at 623 K.[191] Relatively small value of Na concentration can be understood given a strong difference in the crystal structure: ionic NaCl-type structure of PbTe *vs.* Te polyanions in NaTe (Figure 5.1). Above 1 at.%, the gradient of lattice parameter changes, but it is not zero as expected for the samples in the multiphase region. This observation may indicate a non-complete homogeneity of the material after the primary heat treatment. After additional SPS treatment at 673 K, the lattice parameters for samples $x > 1$ at.% remain unchanged within 2 e.s.d. (Figure 5.2a, red triangles), confirming the border of the homogeneity range.

5. Sodium substitution in PbTe
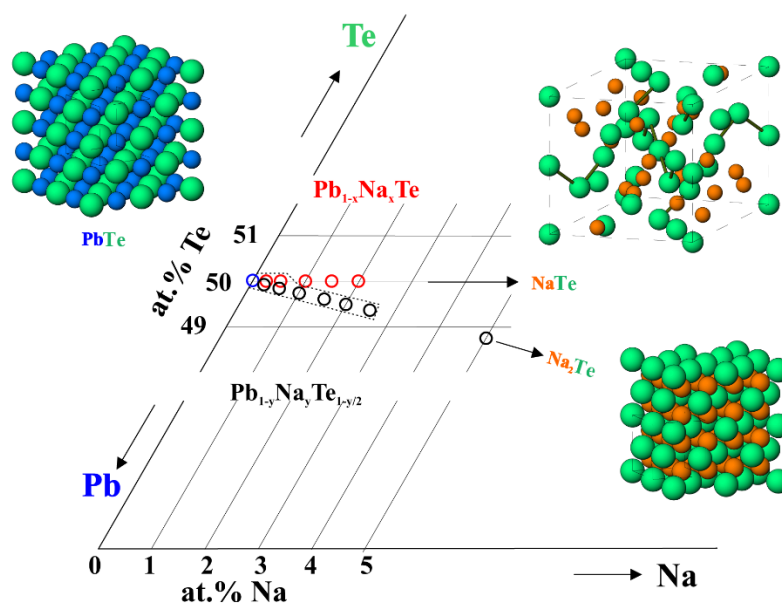
Figure 5.1. Phase diagram for Na-substituted PbTe samples.

The samples may still not be completely homogeneous, which is also revealed by the measurements of thermoelectric properties (see below). TG/DTA of sample $Pb_{0.98}Na_{0.02}Te$ (Figure 5.3a) did not reveal any mass loss and phase transformations, which indicates that the inhomogeneity of the samples can be raised on the atomic level. The only exception are small Na-rich agglomeration areas in the microstructures (Figure 5.4). The absolute values of the lattice parameters are slightly reduced after the SPS treatment, caused by further ordering in the crystal structure due to the enhanced diffusion under SPS treatment. During thermoelectric measurements, some Na was lost (Table 5.1), and the lattice parameters are becoming slightly larger for each sample (Figure 5.2a, red stars).

For the $Pb_{1-y}Na_yTe_{1-y/2}$ series ($y = 0.005 — 0.10$, Figure 5.2a, black), the change of the lattice parameters with the substitution is not as strong as in the previous case. This is understandable assuming that the reduction of the lattice parameters due to the ionic radii of Pb^{2+} and Na^{1+} is partially compensated by the repulsive interaction of the cations around the Te defect. After thermoelectric measurement, the monotonic slope of lattice parameter is observed up to 2.5 at.% of Na toward the Na_2Te phase (Figure 5.2a, black stars) which is possible to understand given the structural similarity of PbTe (NaCl type) and Na_2Te (anti-CaF$_2$ type). The relative changes of the lattice parameter with the

increasing Na content for the $Pb_{1-y}Na_yTe_{1-y/2}$ samples are similar to that of the $Pb_{1-x}Na_xTe$ series. However, depending on heat treatment, there is an opposite lattice parameter change in these two series. In the case of $Pb_{1-x}Na_xTe$, it increases after LFA measurement, as opposed to $Pb_{1-y}Na_yTe_{1-y/2}$ samples, for which the lattice parameter decreases. After annealing, the lattice parameter of both $Pb_{1-y}Na_yTe_{1-y/2}$ and $Pb_{1-x}Na_xTe$ series obeys Vegard's law and this trend is more prominent for the samples after LFA (Figures 5.2a, 5.2b). In case of $Pb_{1-y}Na_yTe_{1-y/2}$, the maximum solubility of Na is 1.5 at.%, in contrast to 2.5 at.% before annealing; and for $Pb_{1-x}Na_xTe$, 0.5 at.% as compared to 1.0 at.%.
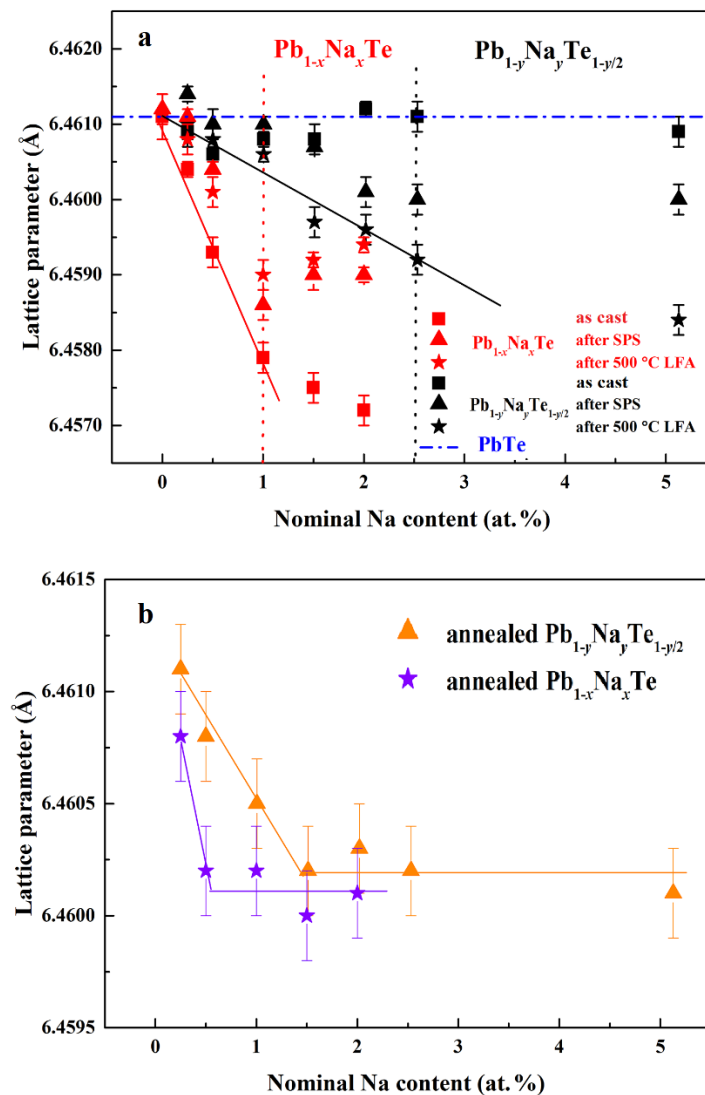
Figure 5.2. (a) Lattice parameter *vs.* nominal Na content for the $Pb_{1-x}Na_xTe$ (red) and $Pb_{1-y}Na_yTe_{1-y/2}$ (black) series. For comparison, the lattice parameter of the binary PbTe[91] is shown as a blue dash dot line. (b) Lattice parameters of annealed Na-substituted PbTe samples.

5. Sodium substitution in PbTe

Table 5.1. Chemical composition by ICP-OES and lattice parameters for the synthesized samples.

Element	Pb (at.%)	Te (at.%)	Na (at.%)	Composition	Lattice parameter (Å)
Nominal composition	49	50	1.0	$Pb_{0.98}Na_{0.02}Te$	
Composition as cast	49.15±0.21	49.82±0.56	1.03±0.01	$Pb_{0.983(4)}Na_{0.021(1)}Te_{0.996(11)}$	6.4579(2)
Composition after SPS	49.26±0.06	49.72±0.07	1.02±0.02	$Pb_{0.985(1)}Na_{0.020(1)}Te_{0.994(1)}$	6.4586(2)
Composition after SPS+LFA	49.16±0.07	49.94±0.16	0.89±0.04	$Pb_{0.983(1)}Na_{0.018(1)}Te_{0.999(3)}$	6.4590(2)
Nominal composition	48.87	49.62	1.51	$Pb_{0.97}Na_{0.03}Te_{0.985}$	
Composition as cast	49.13±0.02	49.41±0.07	1.46±0.05	$Pb_{0.975(1)}Na_{0.029(1)}Te_{0.981(1)}$	6.4608(2)
Composition after SPS	48.36±0.23	48.58±0.19	1.45±0.02	$Pb_{0.960(5)}Na_{0.029(1)}Te_{0.964(4)}$	6.4607(1)
Composition after SPS+LFA	48.49±0.32	49.51±0.37	0.97±0.10	$Pb_{0.963(6)}Na_{0.019(1)}Te_{0.983(7)}$	6.4597(2)
Nominal composition	48.10	49.37	2.53	$Pb_{0.95}Na_{0.05}Te_{0.975}$	
Composition as cast	48.23±0.13	49.24±0.27	2.53±0.05	$Pb_{0.953(3)}Na_{0.050(1)}Te_{0.972(5)}$	6.4611(2)
Composition after SPS+LFA	48.16±0.09	49.61±0.46	0.80±0.01	$Pb_{0.951(2)}Na_{0.016(1)}Te_{0.980(9)}$	6.4592(2)
Nominal composition	46.15	48.72	5.13	$Pb_{0.90}Na_{0.10}Te_{0.95}$	
Composition as cast	46.33±0.09	48.58±0.13	5.09±0.04	$Pb_{0.903(2)}Na_{0.099(1)}Te_{0.947(3)}$	6.4609(2)
Composition after SPS+LFA	47.05±0.11	49.58±0.57	1.91±0.08	$Pb_{0.917(2)}Na_{0.037(2)}Te_{0.967(11)}$	6.4584(2)
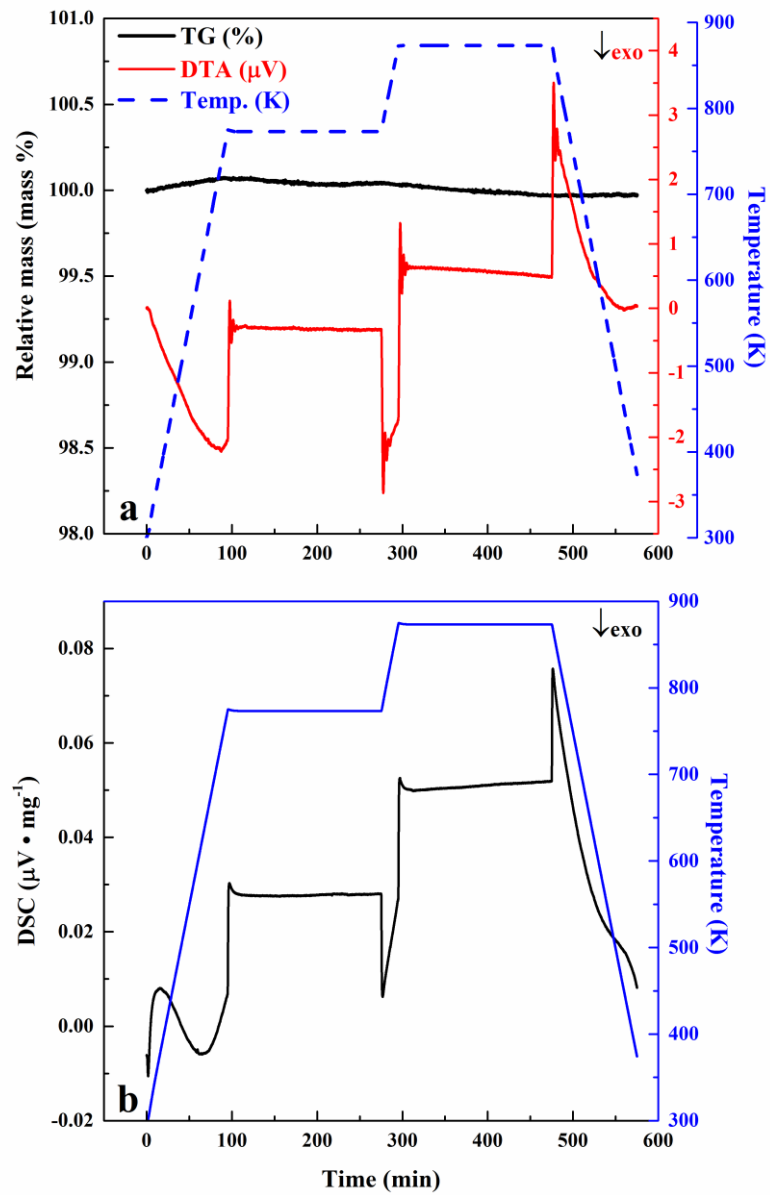
Figure 5.3. Thermal behavior of $Pb_{0.98}Na_{0.02}Te_{0.99}$ after SPS (a) TG / DTA measurement; (b) DSC measurement.
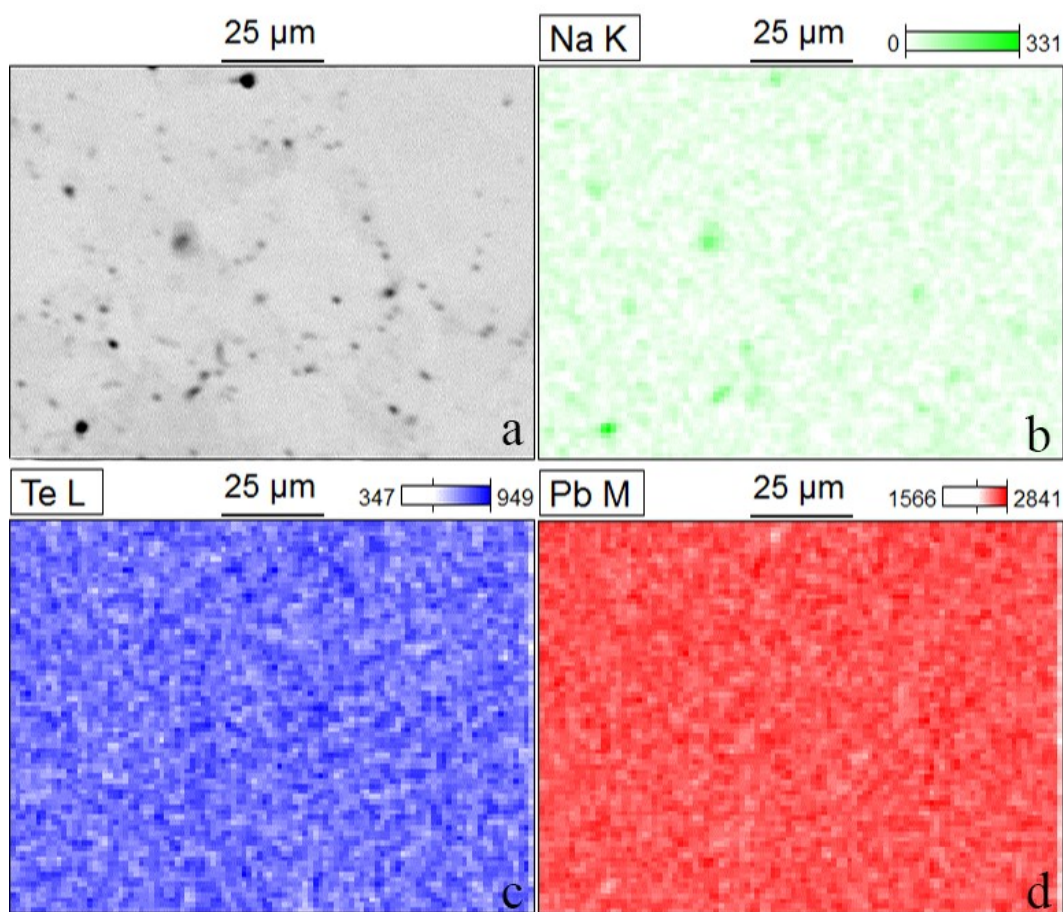
Figure 5.4. Back-scattered electrons (BSE) image (a) and element mapping of $Pb_{0.98}Na_{0.02}Te$ sample after SPS: Na K_α line (b), Te L_α lines) (c), Pb M_α line (d).

5.3.2. Local atomic arrangements of sodium atoms

This complex behavior of Na substitution raises the question of where in the crystal lattice structure Na is located. Because the XRD studies cannot yield this information, the NMR spectroscopy experiment was performed. Figure 5.5 shows the magic-angle spinning (MAS) ^{23}Na NMR spectra of the selected samples from the $Pb_{1-y}Na_yTe_{1-y/2}$ and the $Pb_{1-x}Na_xTe$ series. The MAS ^{23}Na NMR spectrum of $Pb_{0.98}Na_{0.02}Te$ after SPS (shown in black line in Figure 5.5) shows one strong peak at about -14 ppm. Because there is no evidence for another phase in this sample, and the Pb-by-Na substitution is the most probable case, the peak at -14 ppm should come from Na replacing Pb in the PbTe. The Na atom is coordinated by six Te atoms (Figure 5.5, top right). According to Ref. 200, the higher coordination of Na atoms by negatively charged atoms results in more negative chemical shifts. The MAS ^{23}Na NMR spectrum of the as cast sample $Pb_{0.95}Na_{0.05}Te_{0.975}$ is more

complex (orange line, Figure 5.5). The weak peak at −13 ppm corresponds to the main peak of the $Pb_{0.98}Na_{0.02}Te$ samples, thus it is assigned to Na replacing Pb in the PbTe structure. The main peak at +40.6 ppm corresponds to more complex arrangement of the Na atoms in the structure, the same signal is also observed in as-cast $Pb_{0.98}Na_{0.02}Te$ (Figure 5.5, blue spectra), which disappeared after additional heat treatment (Figure 5.5, black spectra).The ratio of its intensity (as cast sample $Pb_{0.95}Na_{0.05}Te_{0.975}$, including all its sidebands) to the negatively shifted peak is approximately 6:1.

The position and assignment of this effect is evaluated by comparison to the spectrum of the binary compound Na_2Te. We synthesized Na_2Te and performed the NMR experiment. The ^{23}Na NMR signal has practically the same position at +40.7 ppm (Figure 5.6). However, the MAS line of Na_2Te is significantly narrower (FWHM of 0.5 ppm compared to FWHM of 2.8 ppm for $Pb_{0.95}Na_{0.05}Te_{0.975}$). The broader line for the $Pb_{0.95}Na_{0.05}Te_{0.975}$ sample points toward the disorder in the crystal structure being in agreement with the behaviour of the lattice parameters (Figure 5.1). The relatively large positive value of chemical shift is in accordance with Na being four-coordinated by Te in Na_2Te.[200] Thus the signal at +40.6 ppm in the spectrum of $Pb_{0.95}Na_{0.05}Te_{0.975}$ is assigned to Na atoms replacing Pb in vicinity of the Te vacancy. The larger shift and the large relative intensity of the main signal can be understood assuming the clustering of the Na atoms around the Te defect in order to reduce the local excess charge appearing by the vacancy formation (Figure 5.5, top left). All these observations echo with the Crocker's idea about formation of the significant complex center ($Na_{Pb}\square_{Te}Na_{Pb}$).[114]

5. Sodium substitution in PbTe
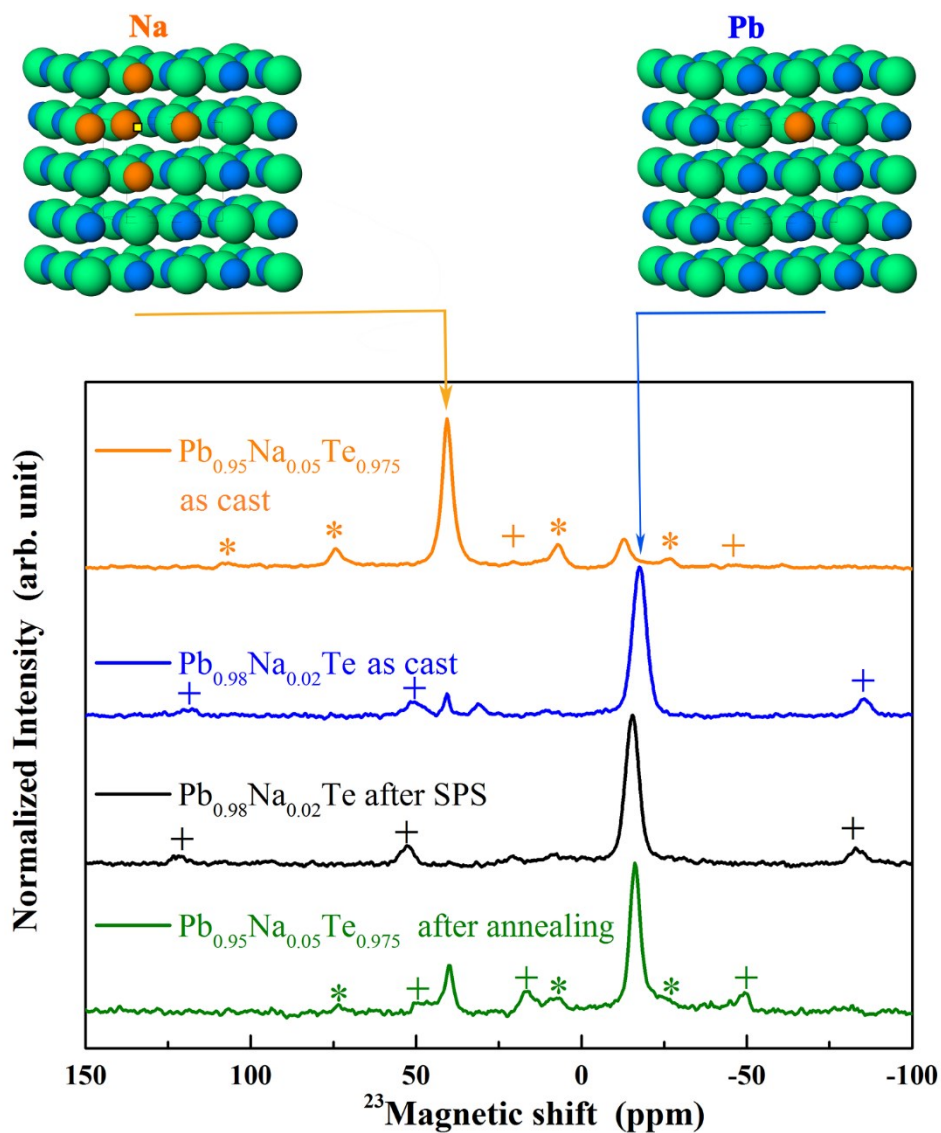
Figure 5.5. MAS ^{23}Na NMR spectra of PbTe substituted with Na: $Pb_{0.95}Na_{0.05}Te_{0.975}$ as cast (orange); $Pb_{0.98}Na_{0.02}Te$ as cast (blue); $Pb_{0.98}Na_{0.02}Te$ after SPS (black); $Pb_{0.95}Na_{0.05}Te_{0.975}$ after 900 hours annealing (green). The spinning rate was 4.5 kHz. Spinning sidebands from the left and right signals are marked by asterisks and crosses, respectively.
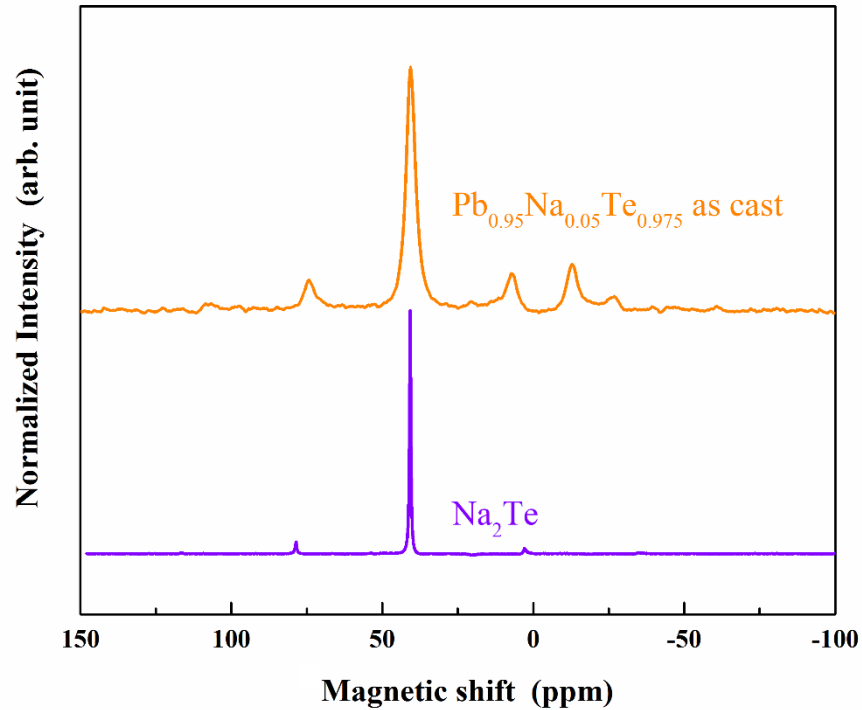
Figure 5.6. MAS ^{23}Na NMR spectra of as-cast $Pb_{0.95}Na_{0.05}Te_{0.975}$ (orange) and as-cast Na_2Te (violet).

Even small concentration of the Na improves the metallic behavior for all samples and suppresses the metal–semiconductor transition in binary PbTe.[91] All Hall measurements were conducted after SPS treatment and thermal diffusivity measurements (LFA) (Figure 5.7). The Hall carrier concentration of $Pb_{1-x}Na_xTe$ and $Pb_{1-y}Na_yTe_{1-y/2}$ decreases with increasing temperature, the values obtained at 300 K are roughly two times smaller than those at 50 K for all samples (Figure 5.7a). Similar behavior is observed for hole mobility values (Figure 5.7b). For both substitution series, the carrier concentration is smoothly increasing with the Na content within the homogeneity range of the solid solution. According to the assumption, that one Na^+ donates one hole, we calculate the theoretical carrier concentrations for the $Pb_{1-x}Na_xTe$ series (Figure 5.7a). The measured values of Hall charge carrier concentration correspond to 60 ~ 70% or less of the calculated one (Figure 5.7a), which suggests that a simple chemical one-charge model is not in complete agreement with the band structure of these materials. This conclusion is further supported by the behavior of the $Pb_{1-y}Na_yTe_{1-y/2}$ series. For the charge balance

situation, the mutual compensation between Na holes and Te defects can be assumed, so the number of charge carriers should not be directly dependent on y. The presence of such dependence in Figure 5.7a can be explained by the fact that a part of substituting Na atoms follows the behavior in the $Pb_{1-x}Na_xTe$ (cf. NMR results in Figure 5.5). Additional explanation is the appearance of new states in the band structure, caused by the environment of the Te vacancies.

5.3.3. Thermoelectric properties

As expected, all samples of both series are p-type conductors (Figures 5.8b, 5.9b). Consistent with the phase homogeneity range (Figure 5.2a), the resistivity and the Seebeck coefficient of $Pb_{1-x}Na_xTe$ samples do not have obvious change when $x \geq 0.02$ (Figure 5.8). Upon increasing of Na content, the resistivity and the Seebeck coefficient of the $Pb_{1-y}Na_yTe_{1-y/2}$ series decreases up until $y = 0.03$. Then the electronic transport properties do not change significantly (Figure 5.9). An exception is the $y = 0.10$ sample, for which a formation of Te secondary phase is observed, although it becomes single-phase material after SPS (based on XRD results). Both series show similar conductive behavior for the whole temperature range (Figures 5.8, 5.9). The Seebeck coefficient values at 300 K are comparable to the $Pb_{1-x}Na_xTe$ series, which is consistent with experimental charge carrier concentrations (Figure 5.10a). Room temperature values of Seebeck coefficient S as a function of the Hall carrier concentration for all studied samples are consistent with the published data for PbTe:Na[65,125,127] (Figure 5.10a). However, the carrier mobility values for all studied samples are much lower compared to the published PbTe:Na data[65,125,127], but higher than that for PbTe:Tl[27,123,201] (Figure 5.10b).
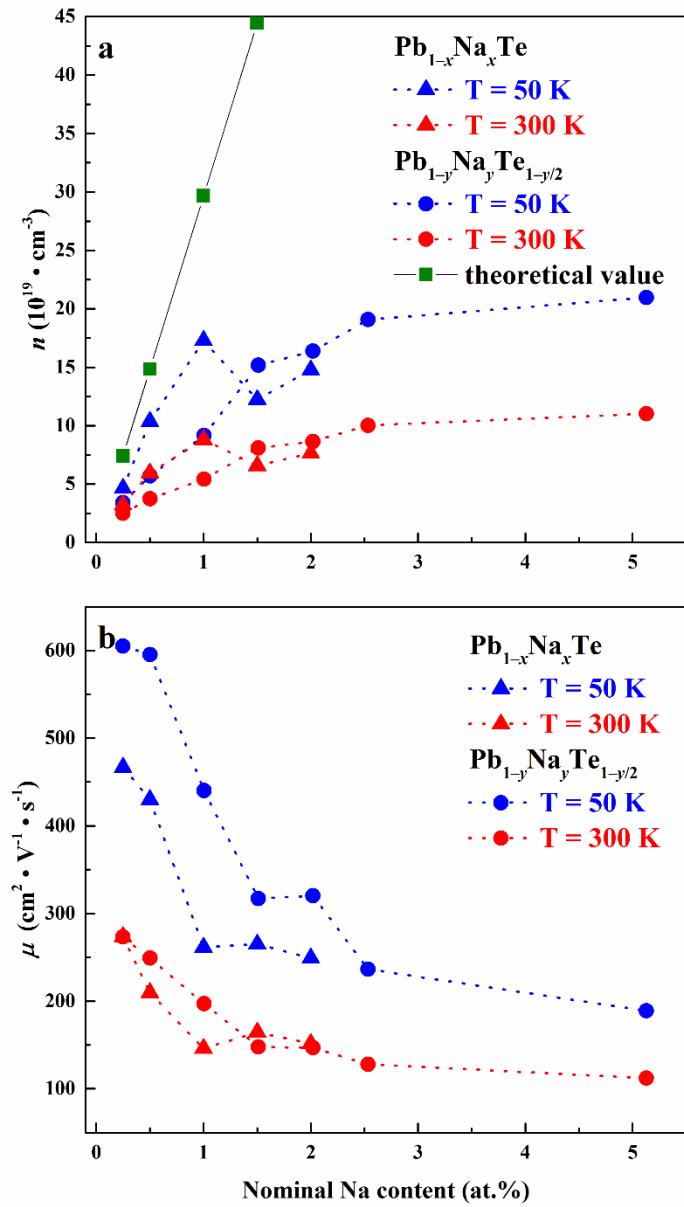
Figure 5.7. (a) Hall carrier concentrations and (b) carrier mobility of $Pb_{1-x}Na_xTe$ (triangles) and $Pb_{1-y}Na_yTe_{1-y/2}$ (circles) at 50 K (blue) and at 300 K (red). The calculated values (green squares) assuming one Na^+ donates one hole.

5. Sodium substitution in PbTe
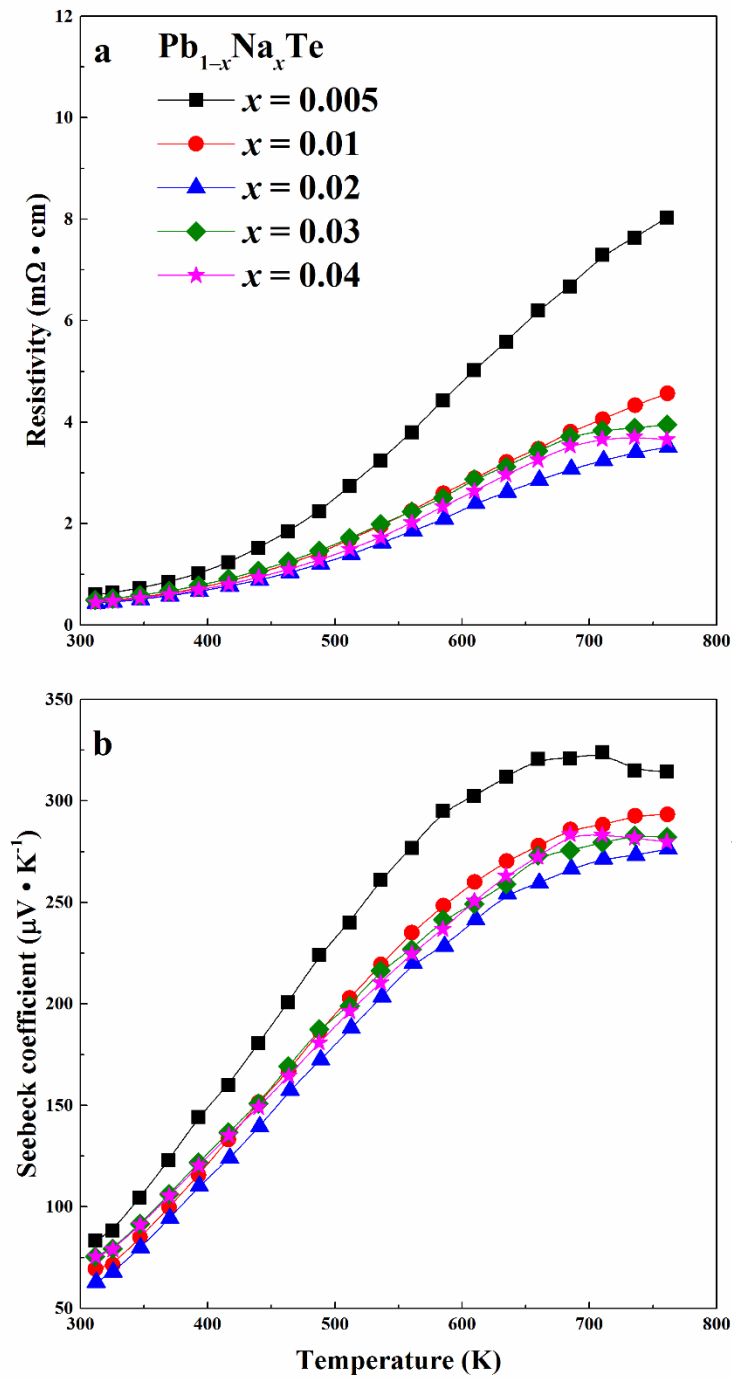
Figure 5.8. Temperature dependences of (a) electrical resistivity, (b) Seebeck coefficient for $Pb_{1-x}Na_xTe$.
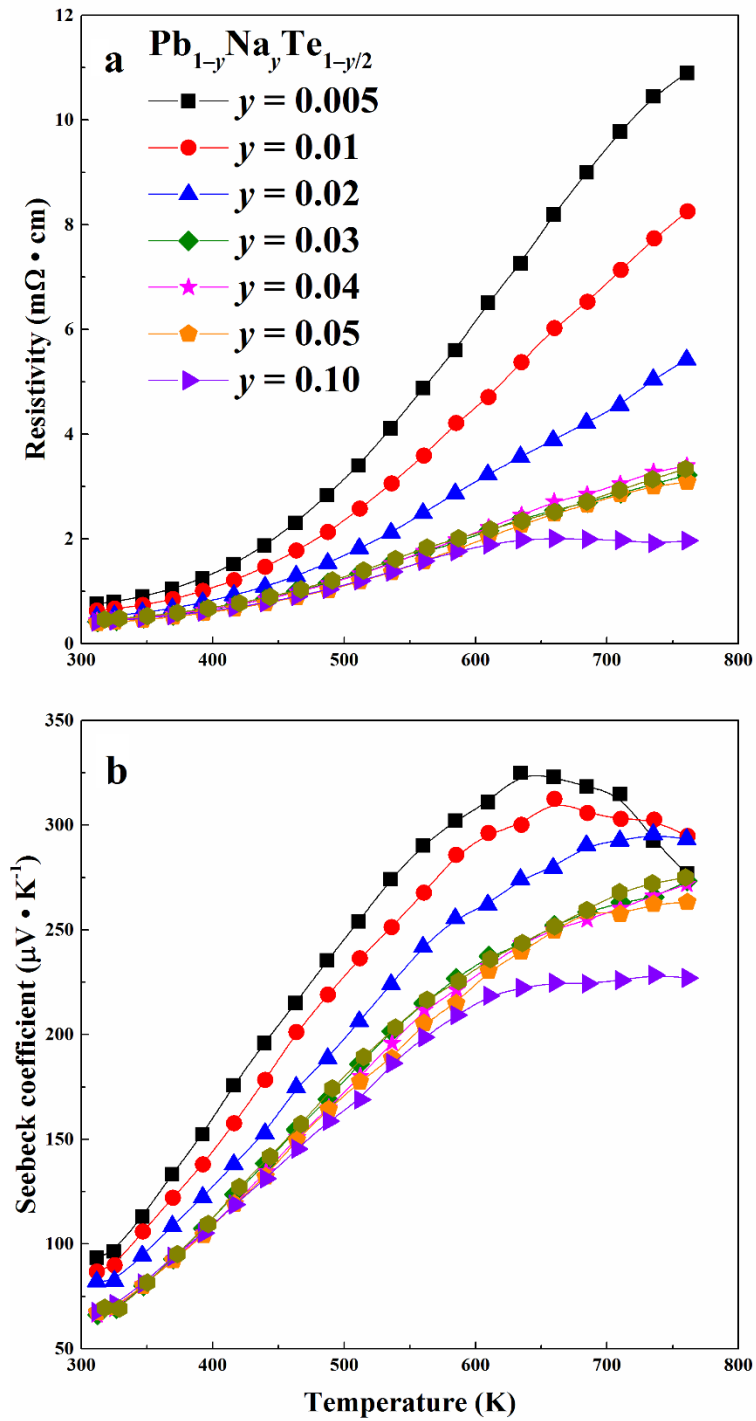
Figure 5.9. Temperature dependences of (a) electrical resistivity, (b) Seebeck coefficient for $Pb_{1-y}Na_yTe_{1-y/2}$.

5. Sodium substitution in PbTe
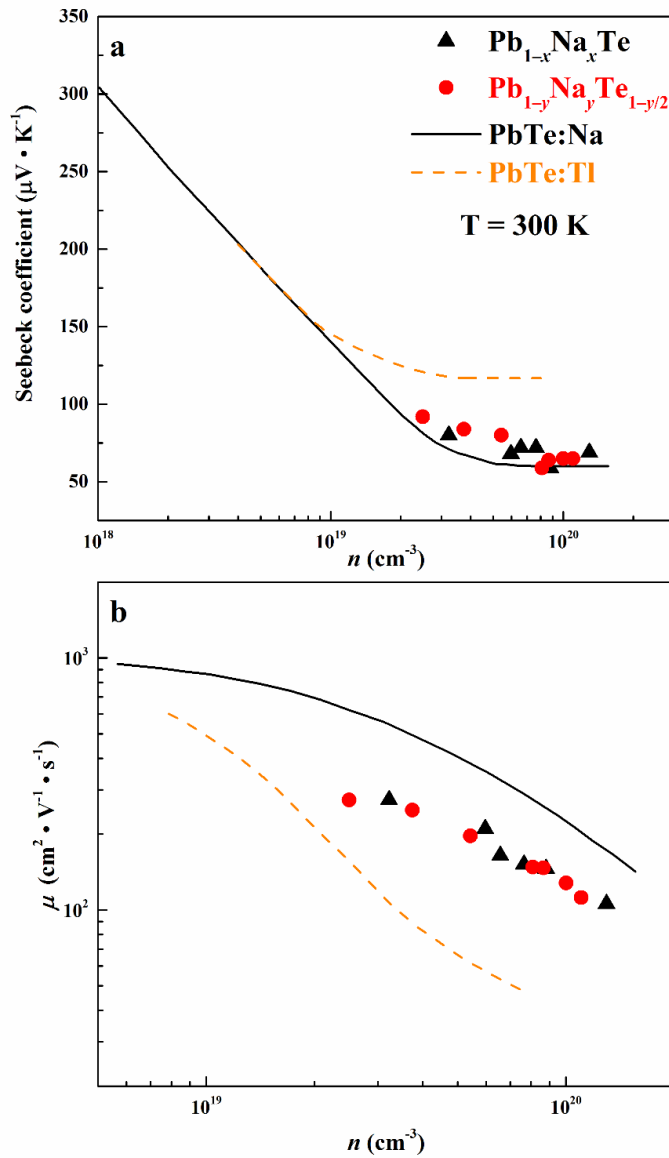
Figure 5.10. (a) Room-temperature Seebeck coefficient as a function of Hall carrier concentration n and (b) room-temperature Hall mobility μ as a function of Hall carrier concentration n for $Pb_{1-x}Na_xTe$ (triangles), $Pb_{1-y}Na_yTe_{1-y/2}$ (circles). The black and the orange lines are literature data for PbTe: Na[65,125,127] and PbTe: Tl[27,123,201], respectively.

The total and lattice thermal conductivities of the $Pb_{1-x}Na_xTe$ samples (Figure 5.11) show smaller values compared to that of $Pb_{1-y}Na_yTe_{1-y/2}$ (Figure 5.12). Generally, lattice thermal conductivity decreases with Na concentration for all samples, especially for the high temperature range (Figures 5.11b, 5.12b). Within the homogeneity range of the solid solution, the decrease of the lattice and total thermal conductivity goes along with the increasing local structural disorder according to the substitution schemes above. In the

multi-phase samples, the additional phonon scattering on the phase boundaries reduces further the total thermal conductivity. Therefore, the maximum ZT values are around 1.4 — 1.6 at 760 K for $Pb_{1-x}Na_xTe$ ($x \geq 0.02$, Figure 5.13a) and $Pb_{1-y}Na_yTe_{1-y/2}$ ($0.1 \geq y \geq 0.03$, Figure 5.14a), comparable with previous results.[65]
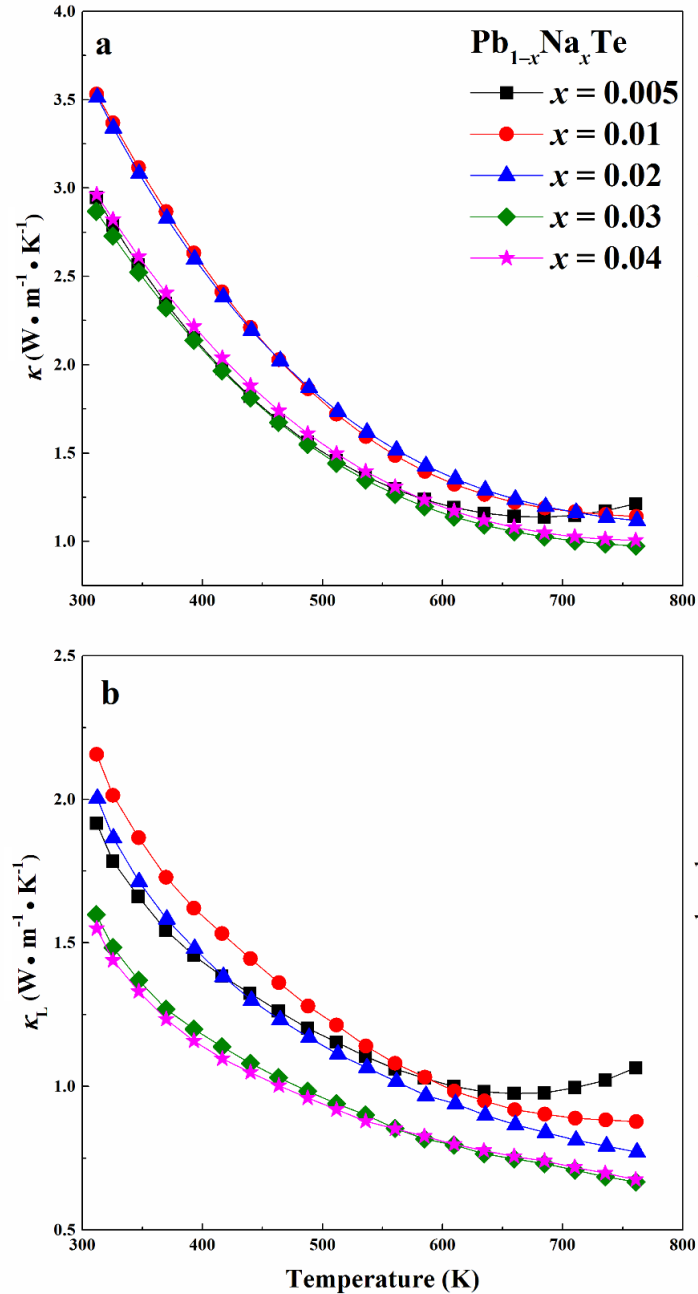
Figure 5.11. Temperature dependence of (a) total (κ) and (b) lattice thermal conductivity (κ_L) for $Pb_{1-x}Na_xTe$.

5. Sodium substitution in PbTe
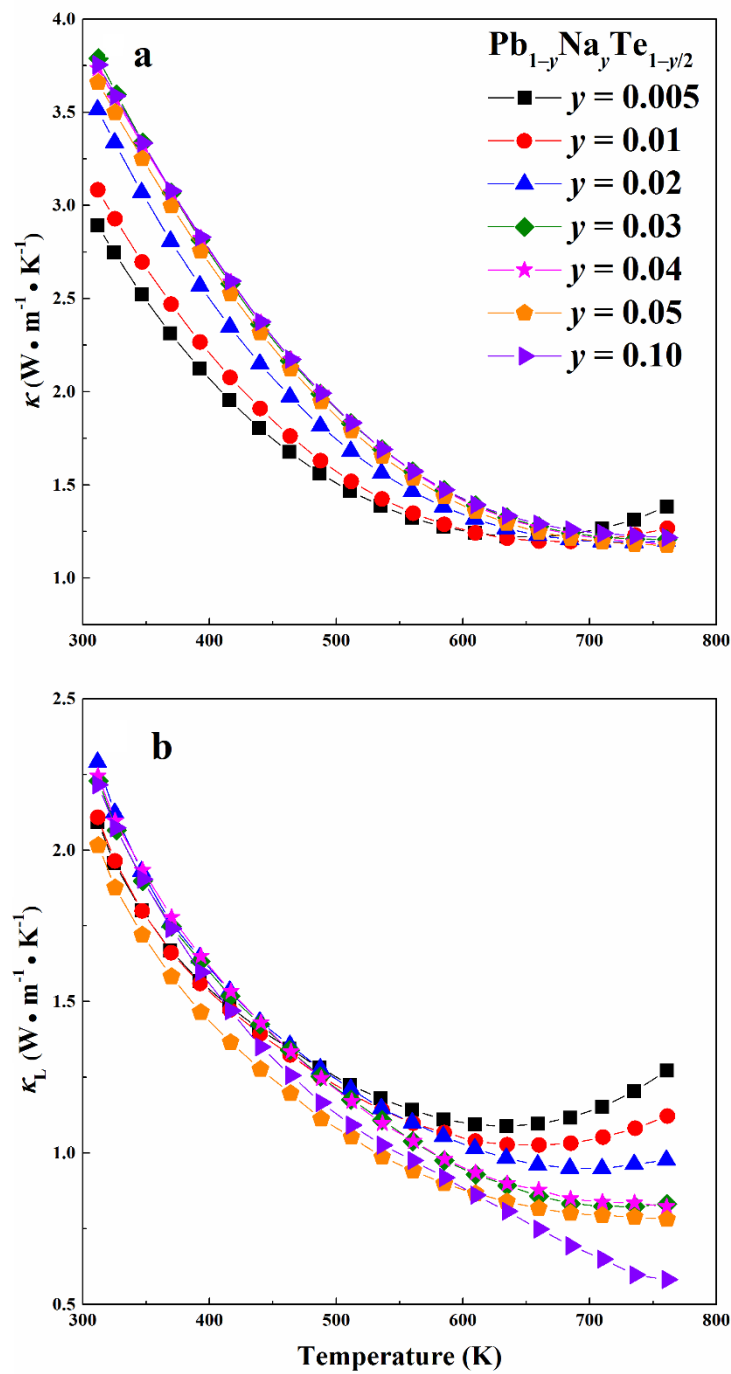
Figure 5.12. Temperature dependence of (a) total (κ) and (b) lattice thermal conductivity (κ_L) for $Pb_{1-y}Na_yTe_{1-y/2}$.
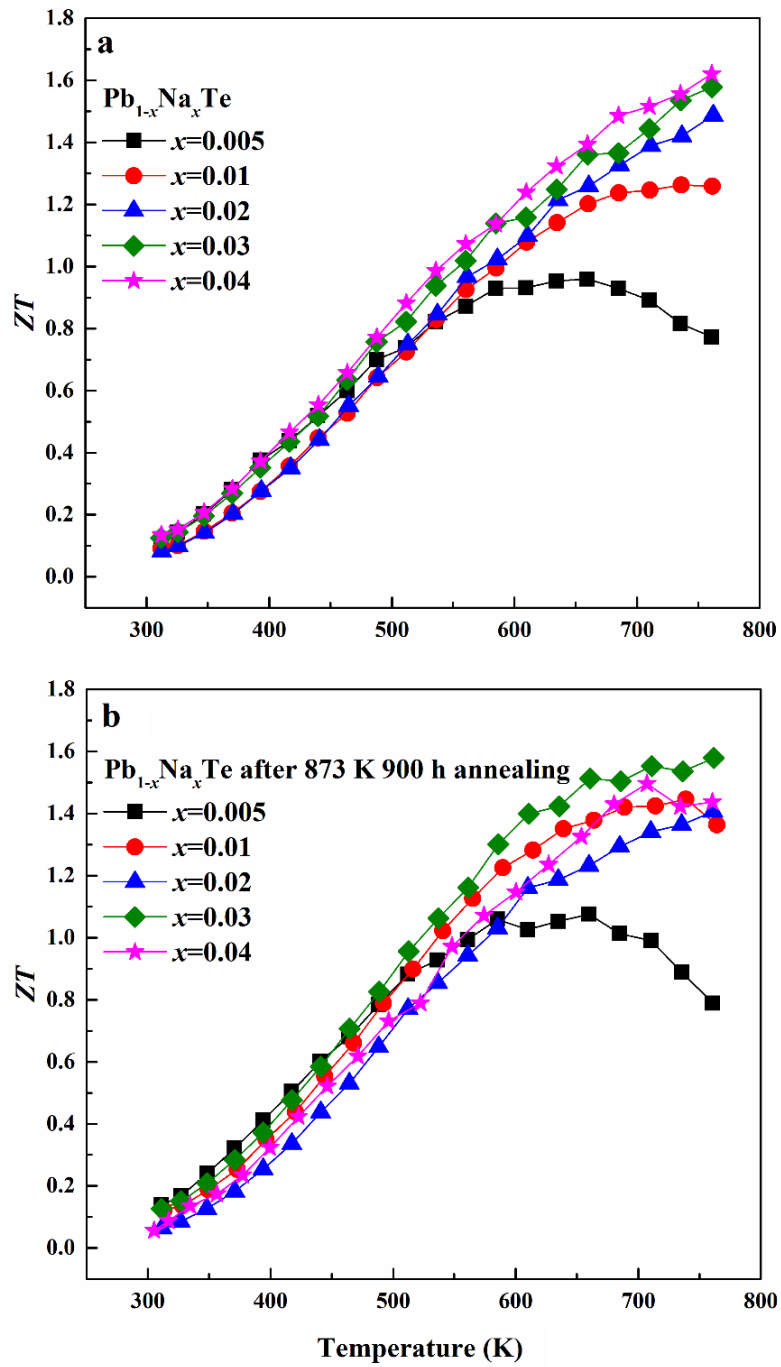
Figure 5.13. Temperature dependence of the thermoelectric figure-of-merit *ZT* for (a) Pb$_{1-x}$Na$_x$Te and (b) Pb$_{1-y}$Na$_y$Te$_{1-y/2}$;

5. Sodium substitution in PbTe
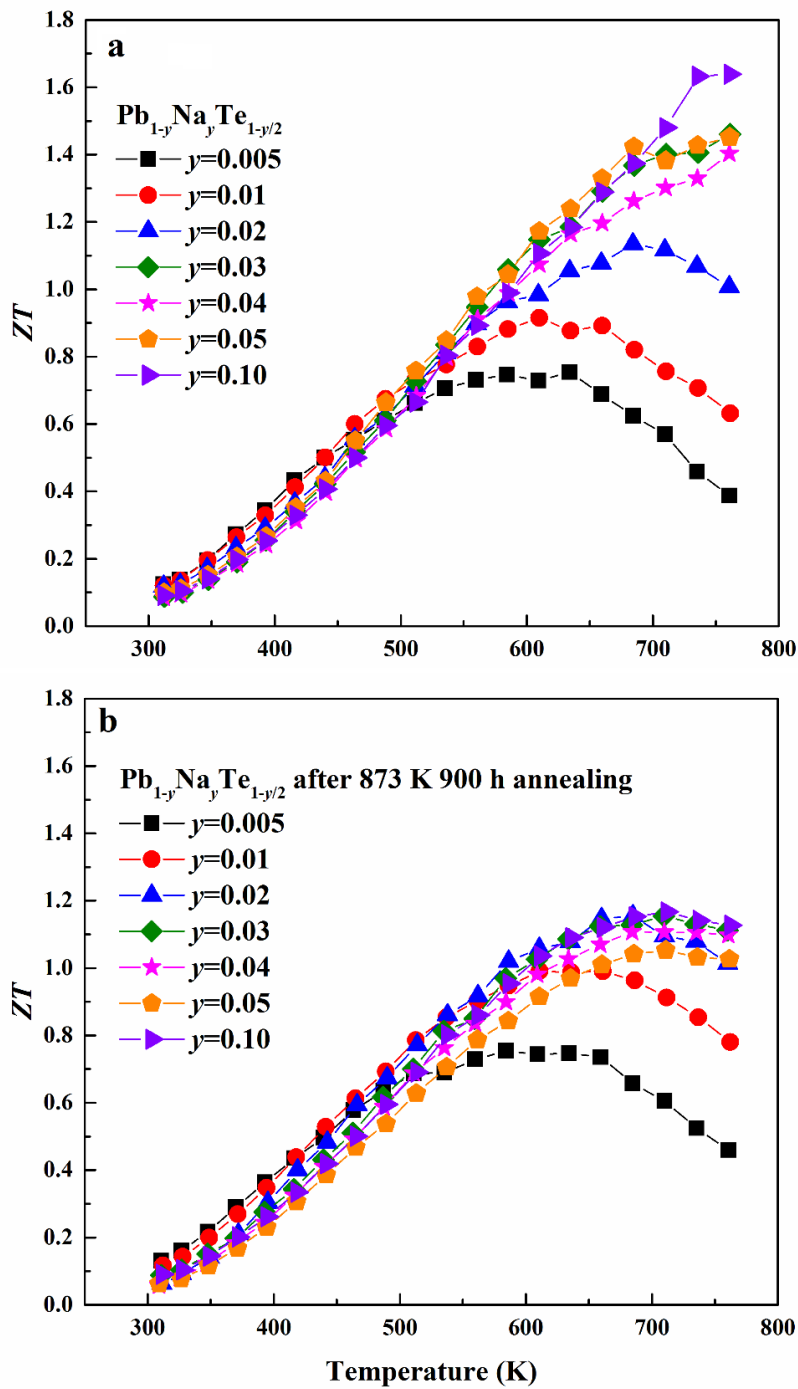
Figure 5.14. (c) Pb$_{1-x}$Na$_x$Te and for (d) Pb$_{1-y}$Na$_y$Te$_{1-y/2}$ after 900 hours annealing at 873 K.

Although both series of materials show high values of *ZT*, they degrade during the measurement. The samples of Pb$_{1-y}$Na$_y$Te$_{1-y/2}$ oxidized slightly (the surface color changed), especially those with high Na concentration ($y \geq 0.03$). During the cyclic thermal conductivity measurements, the samples of Pb$_{1-x}$Na$_x$Te ($x \geq 0.02$) show obvious

change between the first heating cycle and the following ones, whereas no such effect was found in $Pb_{1-y}Na_yTe_{1-y/2}$, even for the highest Na concentration outside the homogeneity range ($Pb_{0.90}Na_{0.10}Te_{0.95}$). For example, the thermal conductivity of samples with x and y of 0.04 (Figure 5.15) during the first heating cycle for both samples are almost the same until 650 K, while at higher temperature, the thermal conductivity of $Pb_{0.96}Na_{0.04}Te$ shows jump-like decrease, in contrast to the $Pb_{0.96}Na_{0.04}Te_{0.98}$. The cooling and all following measurements yield stable, but lower values, as compared to the initial heating curve (Figure 5.15). After full cycle measurements, including electrical and Seebeck coefficient, the $Pb_{0.96}Na_{0.04}Te$ material shows visible microscopic cracks or voids and is partially deformed (cf. inset of Figure 5.15). Contrary to this, sample of $Pb_{0.96}Na_{0.04}Te_{0.98}$ did not show any obvious microscopic changes.
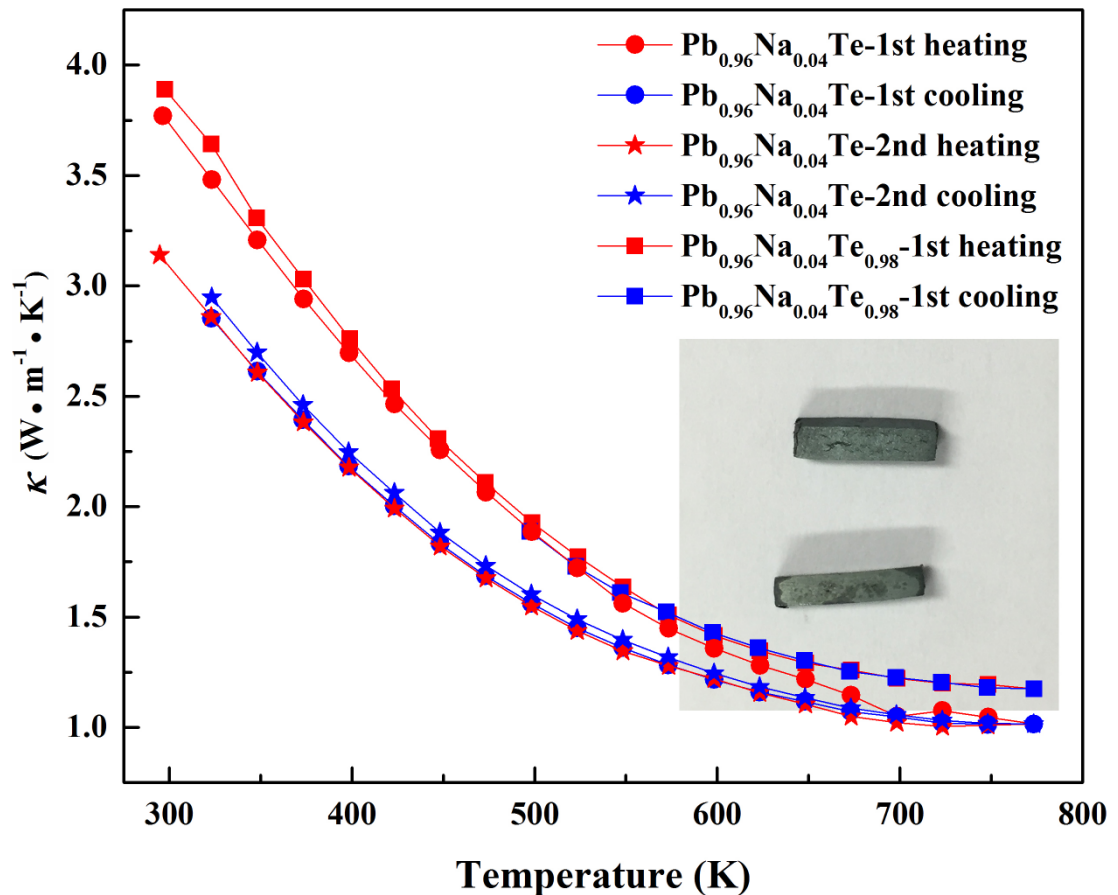
Figure 5.15. Cyclic measurements of thermal conductivity for $Pb_{0.96}Na_{0.04}Te$ and $Pb_{0.96}Na_{0.04}Te_{0.98}$. Inset: image of $Pb_{0.96}Na_{0.04}Te$ (top) and $Pb_{0.96}Na_{0.04}Te_{0.98}$ (bottom) specimens after measurement.
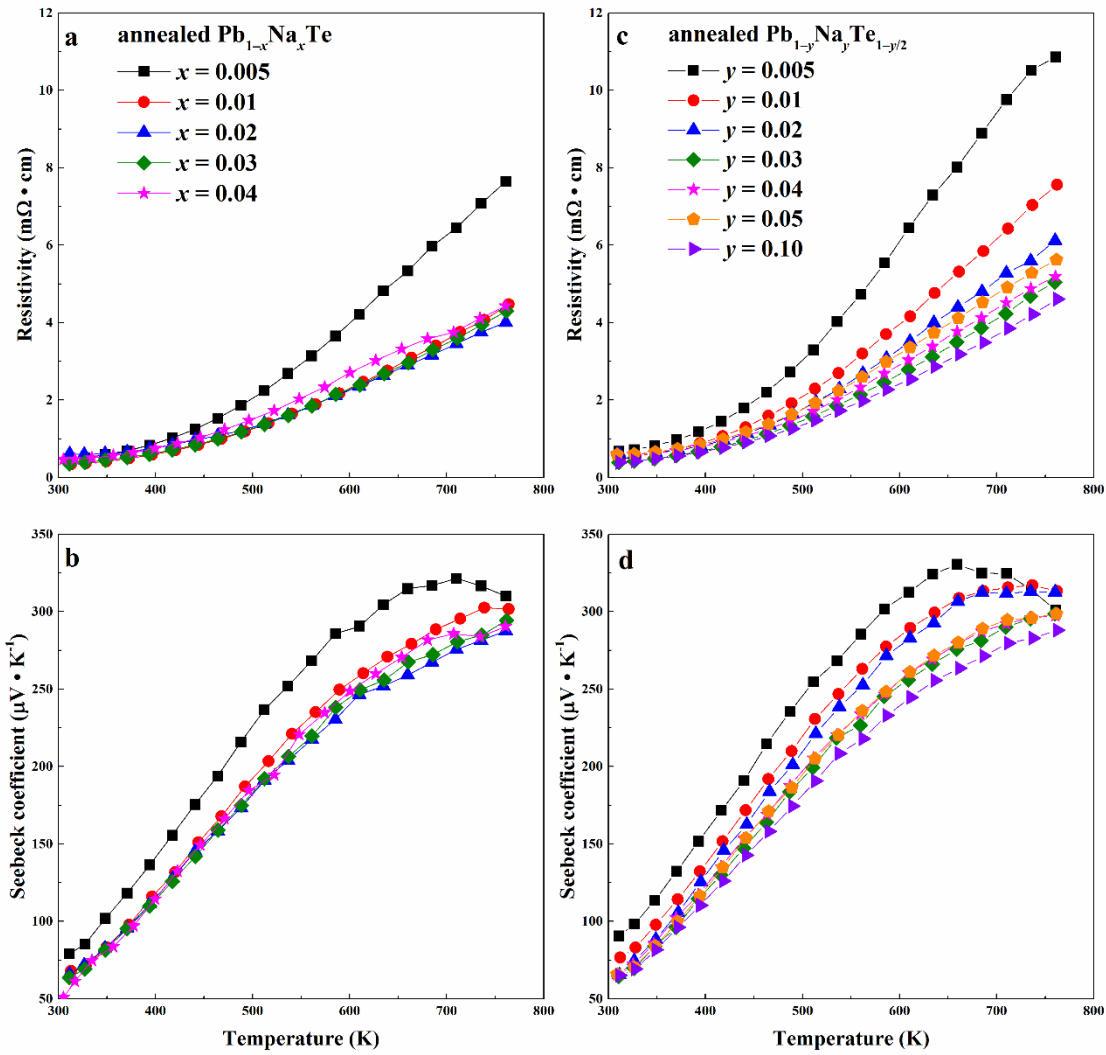
Figure 5.16. Temperature dependences of electrical resistivity and Seebeck coefficient for $Pb_{1-x}Na_xTe$ after 900 hours annealing at 873 K (a, b) and $Pb_{1-y}Na_yTe_{1-y/2}$ after 900 hours annealing at 873 K (c, d).

5.3.4. Annealing effect on thermoelectric properties

In order to evaluate the possibility of the Na-substituted PbTe in potential application in thermoelectric modules, further characterization of the thermal stability for samples annealed at 873 K for 900 hours were carried out. The chemical composition, lattice parameters, and carrier concentrations of the selected samples are presented in Table 5.2. As mentioned above, the solubility of Na is decreased according to the evolution of the lattice parameters, which is likely due to reorganization of Na clusters since no Na loss after annealing was observed in the chemical analysis (Table 5.2). The MAS ^{23}Na NMR

investigations of the annealed $Pb_{0.95}Na_{0.05}Te_{0.975}$ sample (green spectra in Figure 5.5) reveal that the ratio between the two main peaks has changed. The intensity of the peak, which is assigned to Na replacing Pb in the PbTe, is much higher as compared to the peak corresponding to a clustering of the Na atoms around the Te defect. A heat treatment leads to an equilibration and homogenisation of the samples by reorganization and distribution of the Na clusters and Te vacancies. From the powder XRD and chemical analyses, the maximum solubility of Na after long-term annealing is: ~1.0 at.% (corresponding to 1.5 at.% nominal Na content. Na loss took place during the measurements) for $Pb_{1-y}Na_yTe_{1-y/2}$ sample series and 0.5 at.% for $Pb_{1-x}Na_xTe$ (Figure 5.2b). After annealing, the resistivity values are increased for all samples, especially at the high temperature range (Figure 5.16), which can be due to reduced carrier concentration. When beyond Na solubility, the resistivity and the Seebeck coefficient values do not change significantly for $Pb_{1-x}Na_xTe$ ($x \geq 0.01$) and for $Pb_{1-y}Na_yTe_{1-y/2}$ ($y \geq 0.03$), as evident from Figure 5.16. This is consistent with the change of the lattice parameters. The power factors of $Pb_{1-x}Na_xTe$ samples are very similar with before annealing, especially at high temperature range (Figures 5.17a, 5.17b). However, all $Pb_{1-y}Na_yTe_{1-y/2}$ samples show a significant reduction of the power factors at the high temperature range after annealing (Figures 5.17c, 5.17d). As a result, the calculated *ZT* values (using same thermal conductivity values as those measured before annealing) of the annealed $Pb_{1-x}Na_xTe$ samples are still very high (Figure 5.13b), but somewhat reduced for the annealed $Pb_{1-y}Na_yTe_{1-y/2}$ samples (Figure 5.14b).

5. Sodium substitution in PbTe

Table 5.2. Comparison of composition, lattice parameter, and carrier concentration before and after annealing.

Element	Pb (at.%)	Te (at.%)	Na (at.%)	Composition	Lattice parameter (Å)	Charge carrier concentration at 300 K (10^{19} /cm^3)
Nominal composition	49.62	49.87	0.50	$Pb_{0.99}Na_{0.01}Te_{0.995}$		
After annealing	50.19±0.13	49.23±0.27	0.58±0.05	$Pb_{1.004(2)}Na_{0.012(1)}Te_{0.985(5)}$	6.4608(2)	3.7
Nominal composition	49.25	49.75	1.01	$Pb_{0.98}Na_{0.02}Te_{0.99}$		
After SPS and LFA	50.25±0.49	48.84±0.34	0.91±0.04	$Pb_{1.005(10)}Na_{0.018(1)}Te_{0.977(6)}$	6.4606(1)	5.4
After annealing	49.85±0.17	49.32±0.21	0.83±0.01	$Pb_{0.997(3)}Na_{0.017(1)}Te_{0.986(4)}$	6.4605(2)	4.6
Nominal composition	48.87	49.62	1.51	$Pb_{0.97}Na_{0.03}Te_{0.985}$		
Before annealing	48.49±0.32	49.51±0.37	0.97±0.10	$Pb_{0.963(6)}Na_{0.019(1)}Te_{0.983(7)}$	6.4597(2)	8.1
After annealing	49.65±0.06	49.41±0.16	0.94±0.06	$Pb_{0.993(1)}Na_{0.019(1)}Te_{0.988(3)}$	6.4602(2)	6.1
Nominal composition	48.10	49.37	2.53	$Pb_{0.95}Na_{0.05}Te_{0.975}$		
After SPS and LFA	48.16±0.09	49.61±0.46	0.80±0.01	$Pb_{0.951(2)}Na_{0.016(1)}Te_{0.980(9)}$	6.4592(2)	10.0
After annealing	49.71±0.33	49.38±0.32	0.92±0.04	$Pb_{0.994(7)}Na_{0.018(1)}Te_{0.986(6)}$	6.4602(2)	5.8
Nominal composition	49.5	50	0.5	$Pb_{0.99}Na_{0.01}Te$		
After annealing	49.90±0.11	49.43±0.16	0.66±0.06	$Pb_{0.998(2)}Na_{0.013(1)}Te_{0.988(3)}$	6.4602(2)	6.0
Nominal composition	49	50	1.0	$Pb_{0.98}Na_{0.02}Te$		
After SPS and LFA	49.16±0.07	49.94±0.16	0.89±0.04	$Pb_{0.983(1)}Na_{0.018(1)}Te_{0.999(3)}$	6.4590(2)	8.8
After annealing	50.16±0.09	48.96±0.45	0.88±0.01	$Pb_{1.003(2)}Na_{0.018(1)}Te_{0.979(9)}$	6.4602(2)	8.2
Nominal composition	48	50	2.0	$Pb_{0.96}Na_{0.04}Te$		
After SPS and LFA	49.43±0.23	49.66±0.20	0.91±0.05	$Pb_{0.989(5)}Na_{0.018(1)}Te_{0.993(4)}$	6.4594(1)	7.6
After annealing	49.32±0.19	49.80±0.37	0.87±0.03	$Pb_{0.986(3)}Na_{0.017(1)}Te_{0.996(7)}$	6.4601(2)	6.8
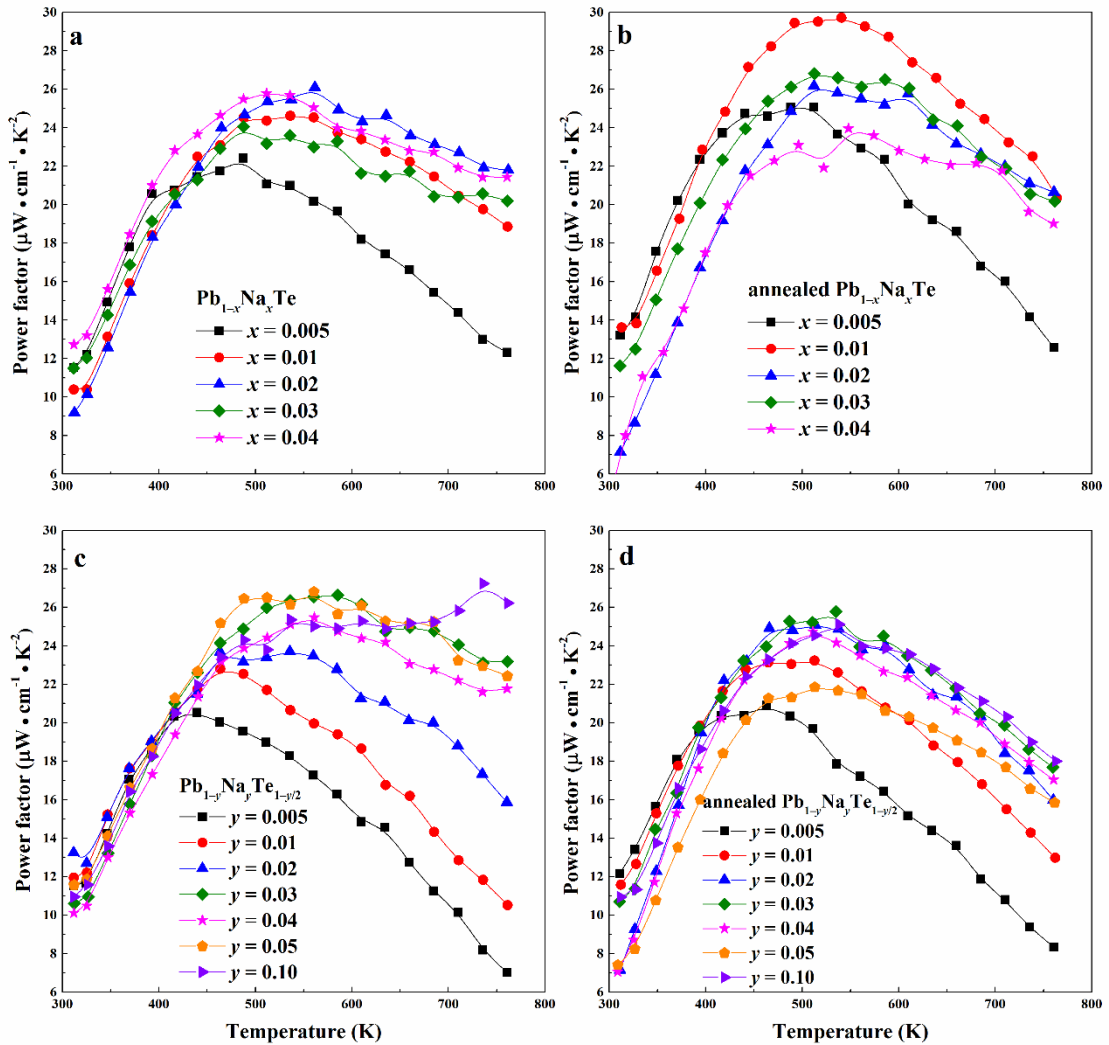
Figure 5.17. Temperature dependences of power factor for $Pb_{1-x}Na_xTe$ before (a) and after (b) 900 hours annealing at 873 K and for $Pb_{1-y}Na_yTe_{1-y/2}$ before (c) and after (d) 900 hours annealing at 873 K.

5.4. Conclusions

Two substitution series $Pb_{1-x}Na_xTe$ and $Pb_{1-y}Na_yTe_{1-y/2}$ were systemically investigated, and the shape of the solid solution of Na in PbTe in the ternary system Pb–Na–Te was established. Na has limited while different solubility range for each series: 1.0 at.% for $Pb_{1-x}Na_xTe$, and 2.5 at.% for $Pb_{1-y}Na_yTe_{1-y/2}$. The samples with high concentration of Na ($x \geq 0.02$ in $Pb_{1-x}Na_xTe$) showed a jump-like behavior above 650 K during the first heating cycle, which becomes stable and achieves lower values in further cyclic measurements.

5. Sodium substitution in PbTe

However, thermal conductivity of $Pb_{1-y}Na_yTe_{1-y/2}$ samples is stable during the measurements.

The local atomic arrangement of Na by different substitution schemes was discovered by NMR. The MAS ^{23}Na NMR of the $Pb_{0.98}Na_{0.02}Te$ after SPS revealed only one Na signal, which is assigned to Na replacing Pb in the PbTe. In sample $Pb_{0.95}Na_{0.05}Te_{0.975}$, an additional strong peak was observed, which was assigned to Na atoms replacing Pb in vicinity of the Te vacancy. The larger shift and the large relative intensity of the main signal can be understood assuming the clustering of the Na atoms around the Te defect. Moreover, those Na-aggregation structures may also be responsible for the less than 100% doping efficiency from Pb–by–Na substitution. The long-term heat treatment (900 hours) leads to an equilibration and homogenisation of the samples by reorganization and distribution of the Na clusters and Te vacancies. Concerning powder XRD analysis, the maximum solubility of Na is reduced upon long-term annealing for both sample series: ~1.0 at.% for $Pb_{1-y}Na_yTe_{1-y/2}$ and 0.5 at.% for $Pb_{1-x}Na_xTe$.

Pb–by–Na substitution has suppressed the metal-semiconductor transition in PbTe. The thermoelectric properties of Pb–Na–Te materials were proved to vary for different substitution schemes. The maximum *ZT* values of 1.4 — 1.6 at 760 K are established for both $Pb_{1-x}Na_xTe$ ($x \geq 0.02$) and $Pb_{1-y}Na_yTe_{1-y/2}$ ($0.1 \geq y \geq 0.03$) series in the multi-phase samples due to the additional reduction of the thermal conductivity on the phase boundaries. The $Pb_{1-x}Na_xTe$ substitution series exhibits better thermoelectric properties after long-term annealing. The degradation of thermoelectric properties by thermal annealing is proven.

6. Eu- and Na-substituted PbTe

The samples $(PbTe)_{0.98-x}(EuTe)_x(NaTe)_{0.02}$ ($x = 0 — 0.030$) were systemically investigated after three different kinds of heat treatments: spark plasma sintering (SPS), laser flash measurement (LFA), and long-term annealing. The solubility of Eu (*ca*.1.0 at.%) in $(PbTe)_{0.98-x}(EuTe)_x(NaTe)_{0.02}$ was established at 873 K. The most inhomogeneous samples (samples after SPS) were characterized with highest values of figure-of-merit, ZT_{max} of 2.1 at 760 K. Metallographic studies show that there are large number of micrometer-scale sodium- and europium-rich aggregations in SPS samples. After additional heat treatment (LFA measurement or long-term annealing), the ZT_{max} are reduced to 1.6. The distribution of Eu and Na of the samples becomes much more homogeneous, accompanied by increased lattice parameters and decreased carrier concentrations. The cyclic TE properties measurements show that the long-term annealed samples have the best reproducible TE properties and enhanced mechanical stability.[202] For comparison, $(PbTe)_{0.98-y}(EuTe_{1.5})_y(NaTe)_{0.02}$ samples were synthesized and investigated.

6.1. Introduction

As discussed in chapter 4, no significant influence of the europium substitution on the thermoelectric figure-of-merit was observed in stoichiometric bulk materials,[91] which is in contrast to the behavior of thin films reported in the literature.[37,180-182] Eu has been proven to be electrically neutral in PbTe, consistent with previous reports.[176-177] However, adding to the system of a monovalent element, for example Na, may change the electronic configuration of potentially mixed-valence *f*-metal. For system $Pb_{1-x}Eu_xSe$, Eu was found to be in the $4f^7$ state.[203] A part of Eu atoms changed the electron configuration to $4f^6$ when introducing Na.[204] Moreover, the study of $Pb_{1-x-y}Eu_xNa_yTe$ claims that the solubility of Na in PbTe increases with increasing EuTe content. With nanometer-scale precipitates and high density of dislocations, maximum ZT of 2.2 at 850 K was reported.[129]

Nevertheless, the additive role of the Eu- and Na- substitution for ZT enhancement of the PbTe is still under discussion, especially from chemical point of view. As shown in chapter 5, the solubility of Na in PbTe is more complex as was expected. Although there are many previous *p*-type PbTe with high values of ZT (Table 1.1), similar Pb_{1-x-}

$_y$Eu$_x$Na$_y$Te system has also been reported,[129] there are only few investigations about the stability (chemical and physical properties) of the studied materials.[52,205-207] Moreover, different compositions reported in different publications reveal problems in the reproducibility of the results. It prompts us to carefully consider all possible chemical issues for manufacturing quaternary TE materials based on PbTe.[153]

Here we present systematic investigations of structural and chemical features, carrier transports, and thermoelectric properties of the Pb–Eu–Na–Te quaternary system. We discussed the possibility to use these materials for the thermoelectric applications, based on thermal stability studies of differently heat-treated samples.

6.2. Experimental details

Bulk polycrystalline samples $(PbTe)_{0.98-x}(EuTe)_x(NaTe)_{0.02}$ (x = 0, 0.005, 0.010, 0.015, 0.020, 0.025, 0.030, 0.035) and $(PbTe)_{0.98-y}(EuTe_{1.5})_y(NaTe)_{0.02}$ (y = 0.005, 0.01, 0.02, 0.03, 0.04, 0.05, 0.07, 0.10) were synthesized by melting the elements Pb (shot, 99.999 mass%), Te (chunk, 99.9999 mass%), Eu (chunk, 99.95 mass%), Na (chunk, 99.99 mass%) in a graphite-coated and fused silica tube at 1273 K for 6 h under a pressure of around 10^{-4} torr, annealing at 873 K for six days for homogenization (the samples are marked by black in all figures). The obtained ingots were ground into powders by hand using an agate mortar in argon atmosphere before spark-plasma sintering (Fuji SPS-515S) at 673 K under a pressure of 60 MPa for 7 minutes. Two SPS-sintered disks (Ø = 10 mm, 2 mm thick) for each sample were prepared and polished (the samples are marked by red in all figures). One for thermal diffusivity (Netzsch LFA 457) measurement, and then was cut for further electric properties measurements (samples are marked by blue in all figures). Another one was directly cut for electric properties measurements and long-term annealing study. The cut sample bars were sealed in tantalum tubes under Argon atmosphere in fused silica tube for an annealing process of 900 hours at 873 K (samples are marked by green in all figures). The tubes were quenched in ice water. The scheme of the experimental study is shown in Figure 6.1.
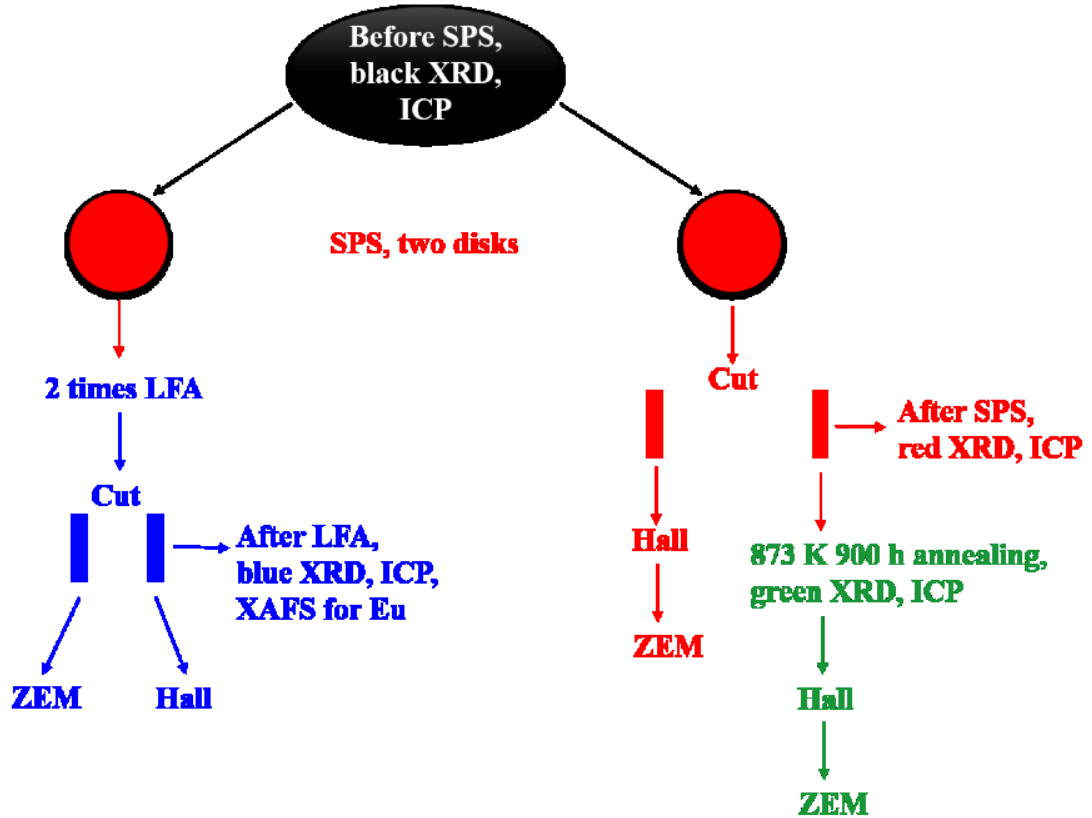
Figure 6.1. Flow diagram for experimental processes for the samples $(PbTe)_{0.98-x}(EuTe)_x(NaTe)_{0.02}$.

The samples of $(PbTe)_{0.98-x}(EuTe)_x(NaTe)_{0.02}$ after LFA were used for X-ray absorption spectroscopy (XAS) experiments. Areas of 500×500 μm² were analyzed by combining 3×4 images for element mappings. A magnification of 200× was chosen to analyze the element distributions on a larger scale. All mappings have been performed at an acceleration voltage of 10 kV and exposure time of 60 min per image. Background subtracted intensities of the M_α, Te L_α, Eu L_α, and Na K_α lines are used to visualize the variation of elements. Elemental chemical analysis (for Pb, Te, Na, Eu) was performed by ICP-OES.

6.3. Results and discussion

6.3.1. Phase analysis

The shape of the solid solution of Na and Eu in PbTe is defined by the following lines within the quaternary phase diagram Pb–Eu–Na–Te (Figure 6.2). As discussed in chapter 4 and 5, in the ternary system Pb–Eu–Te the substitution way follows either the scheme $(PbTe)_{1-x}(EuTe)_x$ or that of $(PbTe)_{1-y}(EuTe_{1.5})_y$; in the ternary system Pb–Na–Te the

substitution method is either according to the scenario $Pb_{1-x}Na_xTe$ or the $Pb_{1-y}Na_yTe_{1-0.5y}$ ones. The homogeneity range of the solid solution of Na and Eu in PbTe is located in the PbTe corner of the orange region in Figure 6.2. The high ZT values of the $Pb_{0.98-x}Na_{0.02}Eu_xTe$ system were presented in Ref. 208 ($ZT_{max} = 1.8$) and Ref. 129 ($ZT_{max} = 2.2$). In order to increase the understanding of those materials, we performed further chemical and physical characterization of the samples on the blue line $(PbTe)_{0.98-x}(EuTe)_x(NaTe)_{0.02}$ ($x = 0.005$ to 0.030, close to the PbTe corner) and the samples on the green line $(PbTe)_{0.98-y}(EuTe_{1.5})_y(NaTe)_{0.02}$ ($y = 0.005, 0.01, 0.02, 0.03$, close to the PbTe corner) located by orange dash lines (Figure 6.2, bottom). The concentration of 1 at.% of Na was chosen, because of the respective ternary sample is revealed the highest charge carrier concentration among other ternary samples.[153] With increasing Eu content, the lattice parameter increase until 1 at.% for all studied series of $(PbTe)_{0.98-x}(EuTe)_x(NaTe)_{0.02}$ (Figure 6.3). At the same time, additional heat-treatment (SPS, measurements, long-term annealing) increased the lattice parameters for all them regardless of the series of samples. The lattice parameters of the samples after SPS and LFA increase linearly, for other two series, this trend is not so obvious. The similar lattice change behavior was observed in the $Pb_{1-x}Na_xTe$ series, and it was explained by the redistribution of the some part of sodium during the heat-treatment.[153] Introducing sodium into PbTe leads to either non-balanced Pb-by-Na substitution ($r_{Na} < r_{Pb}$) or aggregation formation of defects in the Te sublattice. In both scenarios, this leads to the reduction of the lattice parameter of the majority phase. The thermal treatment leads to a partial remove of sodium from the matrix (Table 6.1) and equilibrium of the structure, which in turn increases the lattice parameter. Introducing europium as substituent of Pb increases the lattice parameter due to the size difference ($r_{Eu} > r_{Pb}$). Lattice parameters of $(PbTe)_{0.98-y}(EuTe_{1.5})_y(NaTe)_{0.02}$ ($y = 0.005$ — 0.10) samples show same behavior (Figure 6.4 inset), but with higher Eu solubility (Figure 6.4). The single phase materials are only found when $y \leq 0.01$. For samples $y \geq 0.02$, there is one unknown second phase like in ternary $(PbTe)_{1-y}(EuTe_{1.5})_y$. For samples $y \geq 0.05$, excess Te phase appears. Based on these and early published experiment data,[153] it can be deduced that with additional heat treatments, the samples become more and more homogeneously. The analysis of the full width at half maximum (FWHM) of the reflections can indirectly confirmed this suggestion (Figure 6.5). Only for the samples after long-term annealing, the FWHM values of the respective reflections for all

specimens are almost identical. With increasing Eu content, the samples become more inhomogeneous with more Eu-rich aggregations (Figure 6.6).
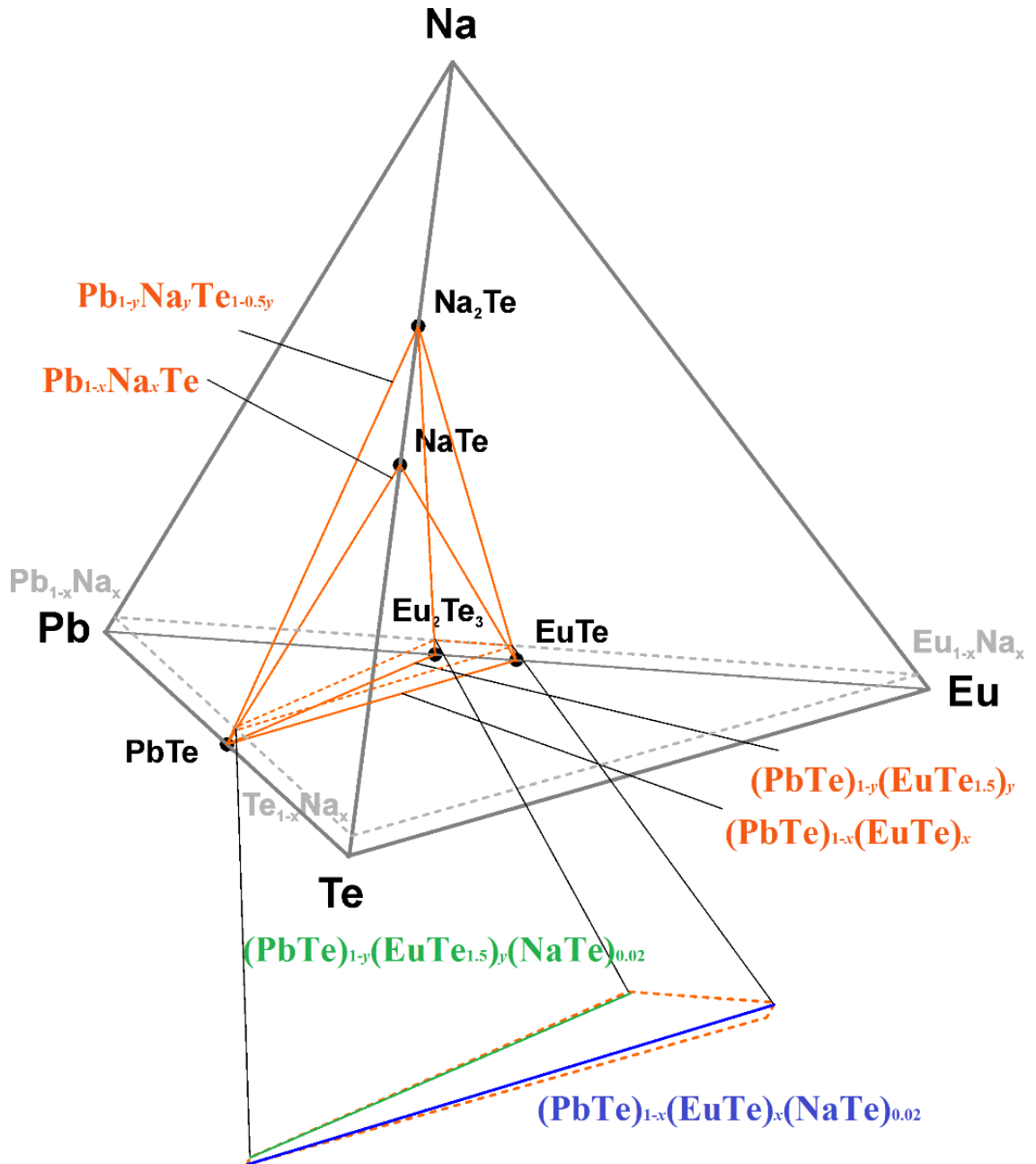
Figure 6.2. Location of the solid solution of Na and Eu in the phase diagram of Pb–Eu–Na–Te system.
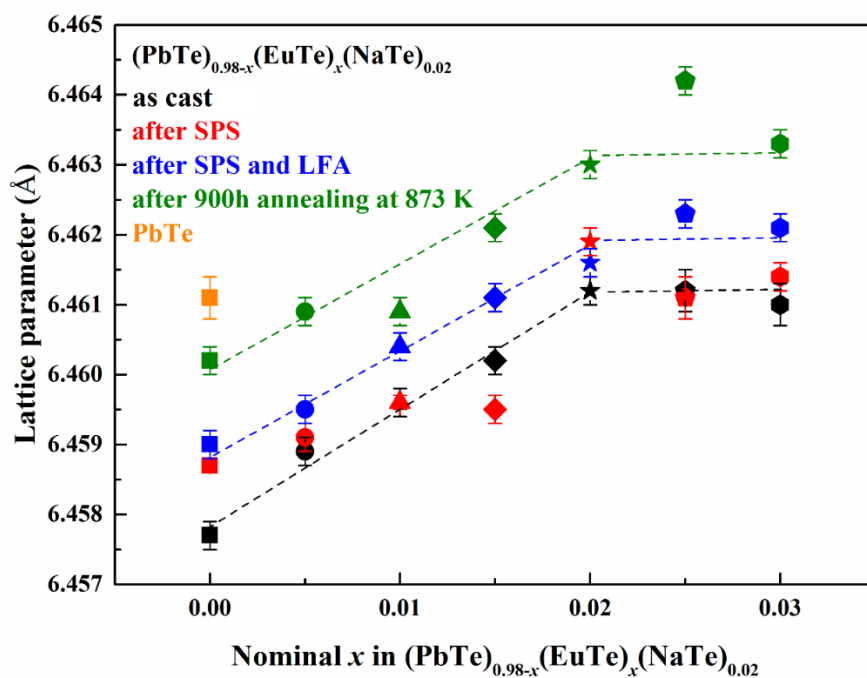
Figure 6.3. Lattice parameters of $(PbTe)_{0.98-x}(EuTe)_x(NaTe)_{0.02}$ as cast (black), after SPS (red) and LFA (blue), after 900 hours annealing at 873 K (green) and binary PbTe (orange square) as reference data.[91]
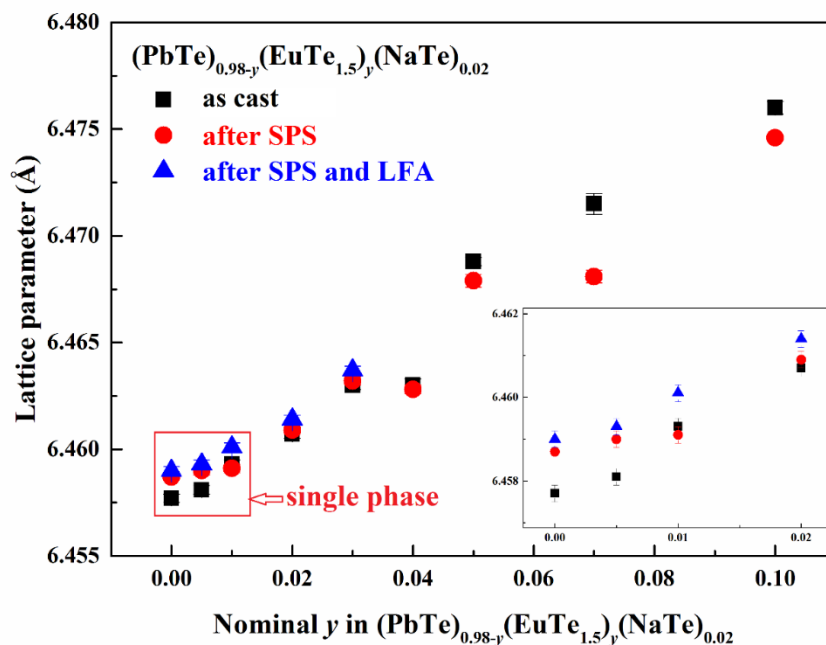
Figure 6.4. Lattice parameters of $(PbTe)_{0.98-y}(EuTe_{1.5})_y(NaTe)_{0.02}$ as cast (black), after SPS (red) and LFA (blue).
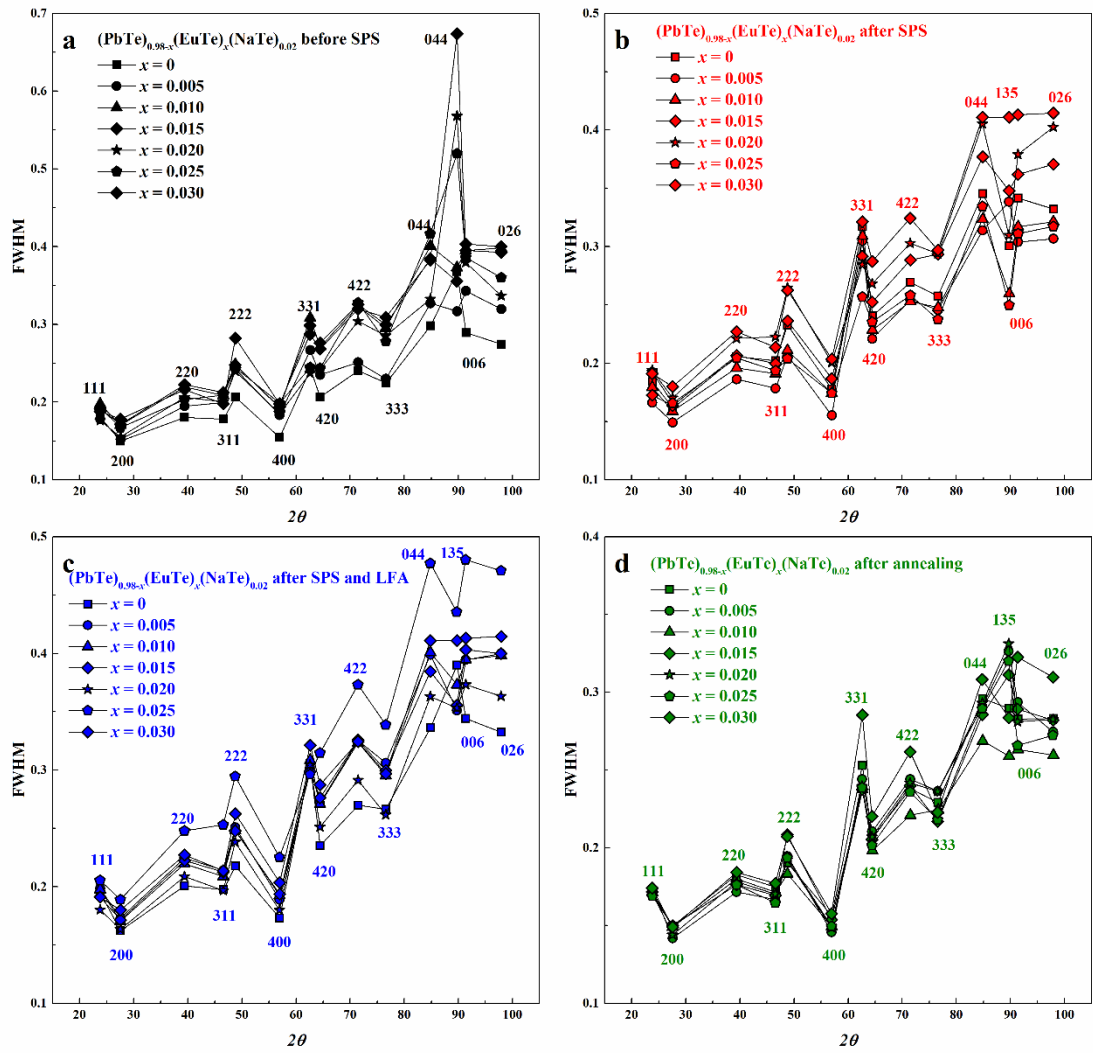
Figure 6.5. Full width at half maximum (FWHM) of powder XRD from (PbTe)$_{0.98-x}$(EuTe)$_x$(NaTe)$_{0.02}$ (a) as cast, (b) after SPS, (c) after SPS and LFA, (d) after annealing.
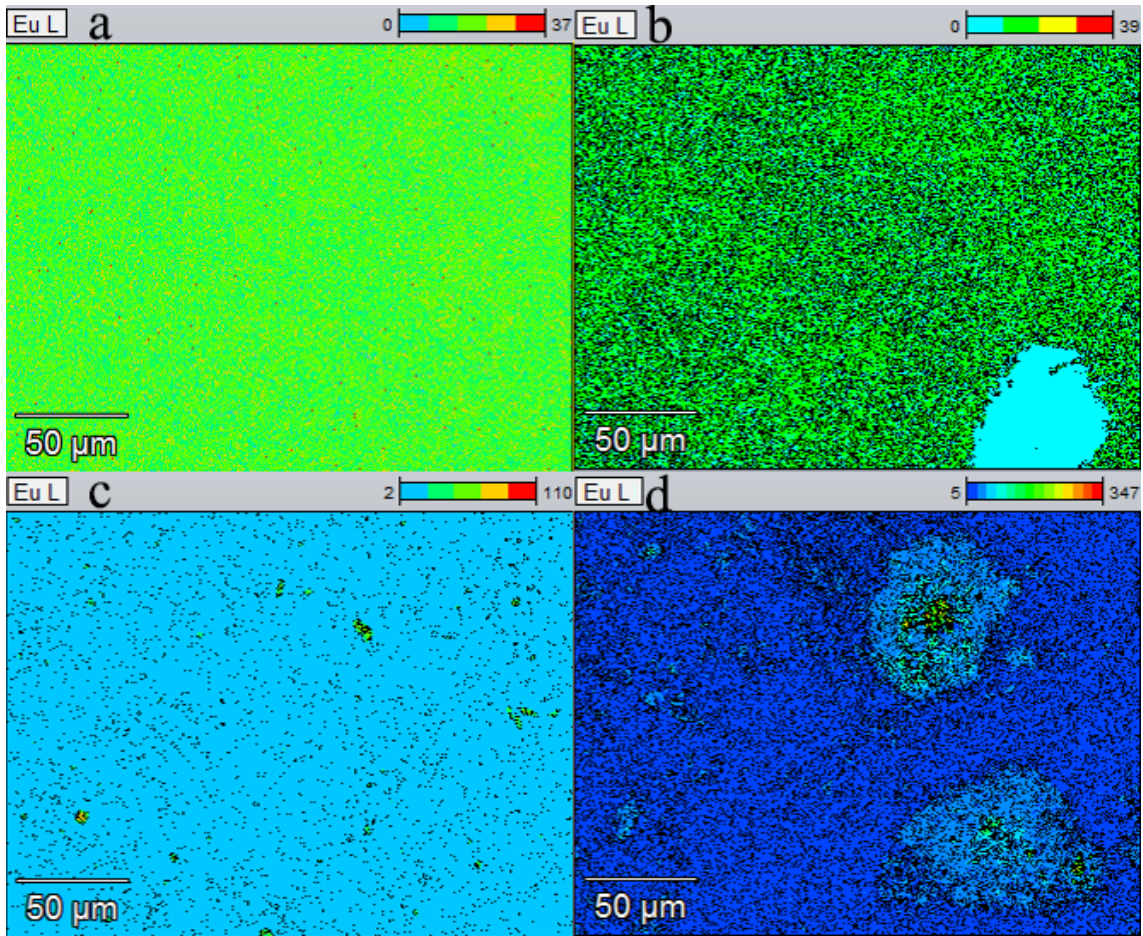
Figure 6.6. Eu element mapping of $(PbTe)_{0.98-x}(EuTe)_x(NaTe)_{0.02}$ after SPS: (a) $x = 0.010$, (b) $x = 0.015$, (c) $x = 0.020$, (d) $x = 0.025$.

Table 6.1. Chemical compositions and lattice parameters of the samples $(PbTe)_{0.98-x}(EuTe)_x(NaTe)_{0.02}$. (Considering the real errors of ICP usually are ten times of the measured errors).

Element	Pb (at.%)	Te (at.%)	Na (at.%)	Eu (at.%)	Composition	Lattice parameter (Å)
nominal content	49	50	1		$Pb_{0.98}Na_{0.02}Te$	
as cast	49.15±0.21	49.82±0.56	1.03±0.01		$Pb_{0.983(4)}Na_{0.021(1)}Te_{0.996(11)}$	6.4577(2)
after SPS	49.26±0.06	49.72±0.07	1.02±0.02		$Pb_{0.985(1)}Na_{0.020(1)}Te_{0.994(1)}$	6.4587(1)
after SPS+LFA	49.16±0.07	49.94±0.16	0.89±0.04		$Pb_{0.983(1)}Na_{0.018(1)}Te_{0.999(3)}$	6.4590(2)
after annealing	50.16±0.09	48.96±0.45	0.88±0.01		$Pb_{1.003(2)}Na_{0.018(1)}Te_{0.979(9)}$	6.4602(2)
nominal content	48.75	50	1	0.25	$Pb_{0.975}Eu_{0.005}Na_{0.02}Te$	
as cast	48.62±0.15	49.96±0.16	1.15±0.02	0.27±0.002	$Pb_{0.972(3)}Eu_{0.005}Na_{0.023(1)}Te_{0.999(3)}$	6.4589(2)
after SPS	48.55±0.06	50.05±0.16	1.14±0.05	0.27±0.001	$Pb_{0.971(1)}Eu_{0.005}Na_{0.023(1)}Te_{1.001(3)}$	6.4591(2)
after SPS+LFA	48.39±0.16	50.40±0.21	0.94±0.02	0.26±0.002	$Pb_{0.968(3)}Eu_{0.005}Na_{0.019(1)}Te_{1.008(4)}$	6.4595(2)
after annealing	49.66±0.36	49.32±0.42	0.75±0.01	0.28±0.002	$Pb_{0.993(7)}Eu_{0.006}Na_{0.015(1)}Te_{0.986(8)}$	6.4609(2)
nominal content	48.5	50	1	0.5	$Pb_{0.97}Eu_{0.01}Na_{0.02}Te$	
as cast	48.47±0.18	50.01±0.10	1.07±0.01	0.46±0.005	$Pb_{0.969(4)}Eu_{0.009}Na_{0.021(1)}Te_{1.000(2)}$	6.4596(2)
after SPS	48.43±0.04	50.05±0.39	1.05±0.02	0.47±0.001	$Pb_{0.969(1)}Eu_{0.009}Na_{0.021(1)}Te_{1.001(8)}$	6.4596(1)
after SPS+LFA	48.23±0.01	50.35±0.29	0.95±0.06	0.47±0.001	$Pb_{0.965(1)}Eu_{0.009}Na_{0.019(1)}Te_{1.007(6)}$	6.4604(2)
after annealing	49.30±0.19	49.07±0.20	1.14±0.01	0.50±0.003	$Pb_{0.986(4)}Eu_{0.010(1)}Na_{0.023(1)}Te_{0.981(4)}$	6.4609(2)
nominal content	48.25	50	1	0.75	$Pb_{0.965}Eu_{0.015}Na_{0.02}Te$	
as cast	48.21±0.12	49.94±0.41	1.10±0.07	0.75±0.02	$Pb_{0.964(2)}Eu_{0.015(1)}Na_{0.022(1)}Te_{0.999(8)}$	6.4602(3)
after SPS	48.10±0.26	50.09±0.73	1.08±0.02	0.73±0.002	$Pb_{0.962(5)}Eu_{0.015}Na_{0.022(1)}Te_{1.002(15)}$	6.4595(2)
after SPS+LFA	47.91±0.31	50.60±0.54	0.76±0.01	0.73±0.006	$Pb_{0.958(6)}Eu_{0.015(1)}Na_{0.015(1)}Te_{1.012(11)}$	6.4611(2)
after annealing	48.94±0.14	49.24±0.26	1.06±0.02	0.76±0.001	$Pb_{0.979(3)}Eu_{0.015}Na_{0.021(1)}Te_{0.985(5)}$	6.4618(2)
nominal content	48	50	1	1	$Pb_{0.96}Eu_{0.02}Na_{0.02}Te$	
as cast	48.01±0.08	49.88±0.32	1.12±0.02	1.00±0.003	$Pb_{0.960(2)}Eu_{0.020}Na_{0.022(1)}Te_{0.998(6)}$	6.4612(2)
after SPS	47.97±0.10	49.94±0.28	1.11±0.11	0.97±0.001	$Pb_{0.959(2)}Eu_{0.019}Na_{0.022(2)}Te_{0.999(5)}$	6.4619(2)
after SPS+LFA	48.01±0.42	50.12±0.42	0.88±0.01	0.99±0.002	$Pb_{0.960(8)}Eu_{0.020}Na_{0.018(1)}Te_{1.002(8)}$	6.4616(2)
after annealing	49.02±0.07	49.20±0.11	0.77±0.04	1.01±0.02	$Pb_{0.980(1)}Eu_{0.020(1)}Na_{0.015(1)}Te_{0.984(2)}$	6.4630(2)
nominal content	47.75	50	1	1.25	$Pb_{0.955}Eu_{0.025}Na_{0.02}Te$	
as cast	47.52±0.10	49.96±0.16	0.98±0.06	1.34±0.14	$Pb_{0.950(2)}Eu_{0.027(3)}Na_{0.020(1)}Te_{0.999(3)}$	6.4612(3)
after SPS	47.67±0.11	50.05±0.16	1.04±0.02	1.32±0.16	$Pb_{0.953(2)}Eu_{0.026(3)}Na_{0.021(1)}Te_{1.001(3)}$	6.4611(3)
after SPS+LFA	47.67±0.11	50.20±0.24	0.76±0.02	1.37±0.03	$Pb_{0.953(2)}Eu_{0.027(1)}Na_{0.015(1)}Te_{1.004(5)}$	6.4623(2)
after annealing	48.51±0.23	49.24±0.25	0.83±0.04	1.42±0.005	$Pb_{0.970(5)}Eu_{0.028(1)}Na_{0.017(1)}Te_{0.985(5)}$	6.4642(2)
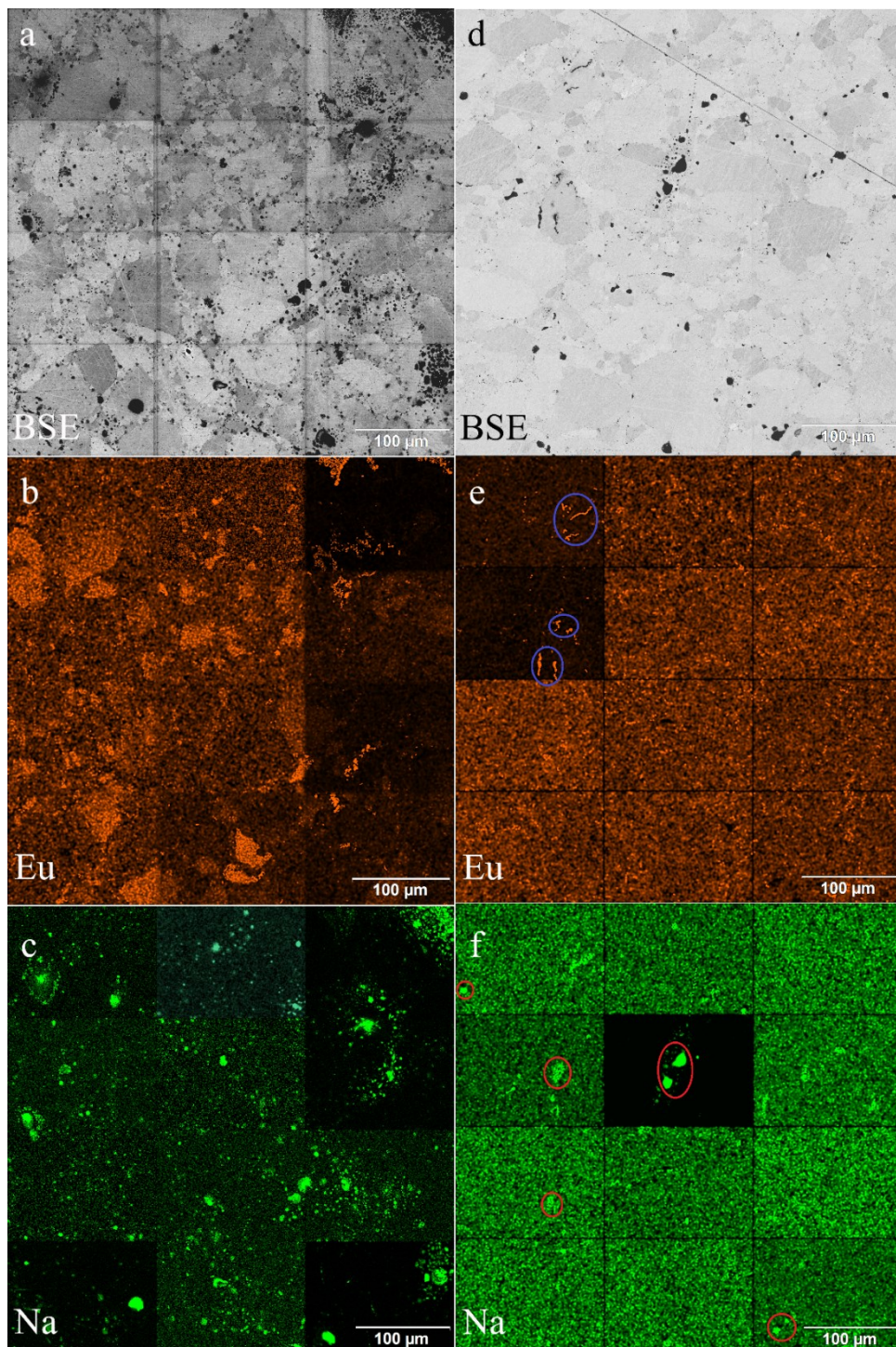
Figure 6.7. Microstructure of $(PbTe)_{0.965}(EuTe)_{0.015}(NaTe)_{0.02}$ after SPS: (a) BSE image, (b) Eu element mapping (blue circles: Eu aggregations), (c) Na element mapping; after annealing: (e) BSE image, (f) Eu element mapping (blue circles: Eu aggregations), (g) Na element mapping (red circles: Na aggregations) (800× magnification at 10 kV beam voltage, combination of 12 fragments, each fragment in b and c has individually adjusted contrast to better reveal the homogeneity).

The inhomogeneity of the samples, as can be assumed, is due to the heterogeneous distribution of the sodium and europium. The metallographic studies were provided on the big areas (500 × 500 μm^2) for the samples after SPS (believed to be most inhomogeneous) and after long-term annealing (believed to be most homogeneous), as a combination of the 12 (3 × 4) smaller areas. As expected, the $(PbTe)_{0.965}(EuTe)_{0.015}(NaTe)_{0.02}$ sample after SPS are strong inhomogeneous (Figure 6.7a). There are a large number of micrometer-scale sodium- and europium-rich aggregations (Figures 6.7b, 6.7c). The most homogeneous sample (after annealing) looks differently (Figure 6.7d), with reduced number of the black spots. The convex areas are sodium reach zones (Figure 6.7e, red circles), the elongated areas are europium rich (Figure 6.7f, blue circles). Different distribution of europium and sodium, even after long-term annealing, may corresponds to immiscibility of the elements in liquid state, which is can be deduced from the results obtained from the investigation of other rare-earth metals–lithium–gallium system.[209]
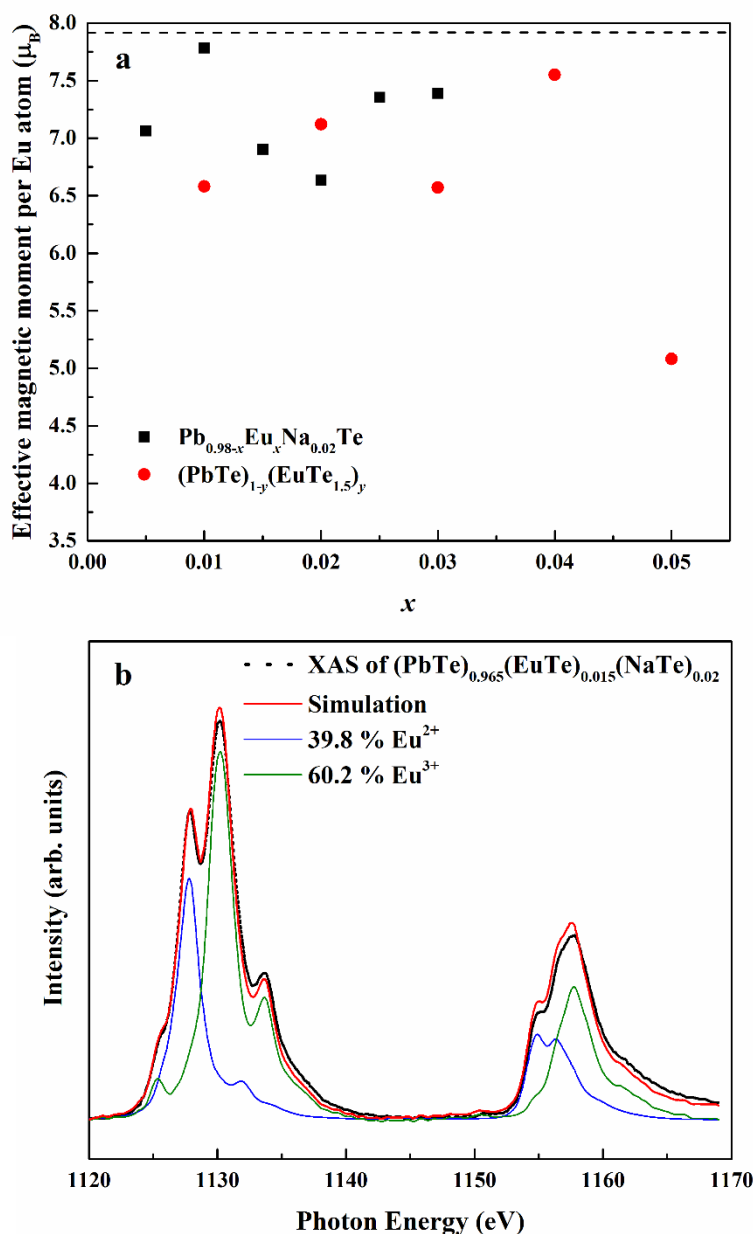
Figure 6.8. (a) Effective magnetic moment per Eu atom of $(PbTe)_{0.98-x}(EuTe)_x(NaTe)_{0.02}$ and $(PbTe)_{1-y}(EuTe_{1.5})_y$ before SPS (the dash line refers to Eu^{2+} value 7.9); (b) Eu M-edge X-ray absorption spectrum of $(PbTe)_{0.965}(EuTe)_{0.015}(NaTe)_{0.02}$ after SPS and LFA.

Aforementioned, europium remains in the $4f^7$ (Eu^{2+}) state in ternary $(PbTe)_{1-x}(EuTe)_x$ samples.[176,210] The effective magnetic moment of Eu in the $(PbTe)_{1-x}(EuTe)_x$ ($x = 0.01$; 0.02) is in good agreement with the theoretical value of the $S = 7/2$ Eu state (7.56 μ_B and 7.79 μ_B, respectively). In contrast, the magnetic moment of the Eu in the quaternary samples has the smaller values (Figure 6.8a, black square). This indicates on the partially

oxidizing of the Eu^{2+} to Eu^{3+} ($4f^{6}$). Similar reduced values of Eu effective magnetic moment are found in ternary $(PbTe)_{1-y}(EuTe_{1.5})_{y}$ system (Figure 6.8a, red circle). The addition of sodium depending on substitution scenario may force oxidation of europium towards Eu^{3+} in order to compensate the charge disbalance in the system. Since the magnetic susceptibility measurements cannot provided a precise evaluation of the ratio between $4f^{7}$/ $4f^{6}$ electronic states, we managed the XAS measurements on the series samples after SPS and LFA, which lattice parameters are obeyed to Vegard's law. XAS measurements confirmed the magnetic measurements. Eu atoms were found to be a mixed-valence state (Figure 6.8b). The amount of Eu with $4f^{6}$ state is increasing with the europium concentration in the samples (Table 6.2) until 1 at.% of Eu (limit of the solubility). The non-monotonic of Eu^{3+} ratio could originate from different deviations of the sample composition from the blue line in Figure 6.2 towards Te-rich region. In Table 6.2, one may expect that if all Na would be active, the values of row 3 and 4 would be same. However, this is obviously not the case. Some suggestions for the understanding of this effect were proposed for the Pb–Eu–Na–Se system. Adding Na prompts the Femi level moving to the Eu $4f$ level, which leads to an instability of the $4f^{7}$ configuration and drives the $4f^{7}$ — $4f^{6}$ transition.[204]

Table 6.2. Experimental Eu^{3+} and active Na^{+} contents from XAS in units of x, as well as experimental active Na^{+} content from Hall measurement in units of x. (All data are taken at RT. The error bars of Eu^{3+} (%) reflect the deviations of the fits to the experimental data.)

Nominal x	0	0.005	0.01	0.015	0.02	0.025
Experimental Eu^{3+} content from XAS (%)	0	43.2 ± 2.2	31.4 ± 1.6	60.2 ± 3.6	65.1 ± 4.1	39.9 ± 2.2
Experimental Eu^{3+} content from XAS (in units of x)	0	0.0022(1)	0.0031(1)	0.0090(1)	0.0130(1)	0.0100(1)
Experimental active Na^{+} content from XAS (in units of x)	0.02	0.0178(1)	0.0169(1)	0.0110(1)	0.0070(1)	0.0100(1)
Experimental active Na^{+} content from Hall measurement (in units of x)	0.0059(2)	0.0075(3)	0.0070(3)	0.0055(2)	0.0061(2)	0.0055(2)

6.3.2. Thermoelectric properties

In all series of samples, a complex distribution of the sodium and europium in the PbTe matrix was found. Thus, measured thermoelectric properties reflect not only the intrinsic behavior of the main phase, but also all other constituents of the microstructure (Figure 6.7). That is why it is difficult to discuss the dependence of TE properties on lattice parameter or nominal chemical composition of the main phase. In order to understand the role of material homogeneity, the thermoelectric behavior is presented here as a function of the sample history. Similar to Na-substituted materials (Chapter 5), for all investigated series p-type metal-like behavior (Figures 6.9, 6.10, 6.11) was observed due to a substitution of Pb by Na. However, the presence of europium impacts the electrical and transport properties. With increasing Eu concentration, the electrical resistivity is increased for all series of the samples. The presence of Eu also increase the Seebeck coefficients (Figure 6.12c). ZT values above two were calculated for the most inhomogeneous series (after SPS, marked by red) of $(PbTe)_{0.98-x}(EuTe)_x(NaTe)_{0.02}$ ($x =$ 0.015, 0.02) samples (Figure 6.9d). For the ZT calculations, the first heating cycle of thermal conductivity measurement was used (see below in the text). After additional heat-treatments (LFA measurements or long-term annealing), the maximum ZT values reduced to 1.6 (the second cooling cycle of thermal conductivity data was used for the ZT calculation). This is attributed to rising electrical resistivity. Since the Hall mobility shows higher values after LFA and after annealing compared to the after SPS samples (Figure 6.12b), the increased resistivity of samples after additional heat treatments should associate with a decrease in charge carrier concentration (Figure 6.12a).

Highest values of the charge carriers, which are commensurate with value of the best Na-ternary sample, were observed for the series of samples after SPS. The carrier concentrations practically did not change within the Eu solubility range (Figure 6.12a, red symbols). Additional heat treatment drastically reduced the carrier concentrations, which is due to redistribution of some sodium during the heat treatment, consistent with the lattice parameter changes. The carrier concentrations after long annealing (Figure 6.12a, green symbols) are reduced by 40 — 50% compare to the samples just only after SPS (Figure 6.12a, red symbols). For samples after LFA and samples after annealing, these carrier concentrations slightly decrease with increasing Eu contents. At the same time, samples after SPS, characterized as the most inhomogeneous, show the lowest

values of the carrier mobility (Figure 6.12b). Due to homogenization by heat treatment, the mobility increase for other series of the samples (Figures 6.12b, 6.12d). Comparing these values with PbTe: Na[65,125,127], Eu-substituted samples reveal higher Seebeck coefficient (Figure 6.12c) and lower carrier mobility (Figure 6.12d). For the case of PbTe: Tl[27,123,201], the Seebeck coefficient is lower and the mobility is significantly higher (Figures 6.12c, 6.12d). This indicates the effect of the Eu substitution on the band structure of pristine PbTe. Consistent with the microstructure evolution, only the electrical properties of annealed samples show well systematic change along with increasing Eu contents (Figures 6.11a, 6.11b). For $(PbTe)_{0.98-y}(EuTe_{1.5})_y(NaTe)_{0.02}$ ($y = 0.005 — 0.04$) samples after SPS, the values of ZT_{max} at 760 K are also around 2.0. After LFA measurements, the values of ZT_{max} at 760 K are reduced to around 1.5 (Figure 6.14f). Compare to samples $(PbTe)_{0.98-x}(EuTe)_x(NaTe)_{0.02}$, the electrical properties of $(PbTe)_{0.98-y}(EuTe_{1.5})_y(NaTe)_{0.02}$ samples show much better systematic change along with increasing Eu contents (Figure 6.14).

Thermal conductivities for all series decrease with increasing Eu concentration (Figures 6.13a, 6.13b). The structural disorder, introduced by Eu substitution, as well as additional inhomogeneity (Figure 6.6) enhance the phonon scattering, which directly affects the lattice thermal conductivity (Figures 6.13c, 6.13d). Interestingly, the samples directly after SPS show the higher values of the thermal conductivity (with respected to the consecutive heat treatments), which is mainly due to higher contribution from the electric thermal conductivity, since the samples after SPS have the highest carrier concentrations. The high lattice thermal conductivity of the samples after SPS is most probably caused by metal-rich aggregations remaining in the microstructure (Figure 6.7a). They are strongly reduced after enhanced thermal treatment (Figure 6.7b), and the thermal conductivity of the material has more intrinsic character, i.e. shows lower values. Similar to the $Pb_{1-x}Na_xTe$ series,[153] after first heating cycle in vicinity of the 650 K show jump-like decrease (Figure 6.15).
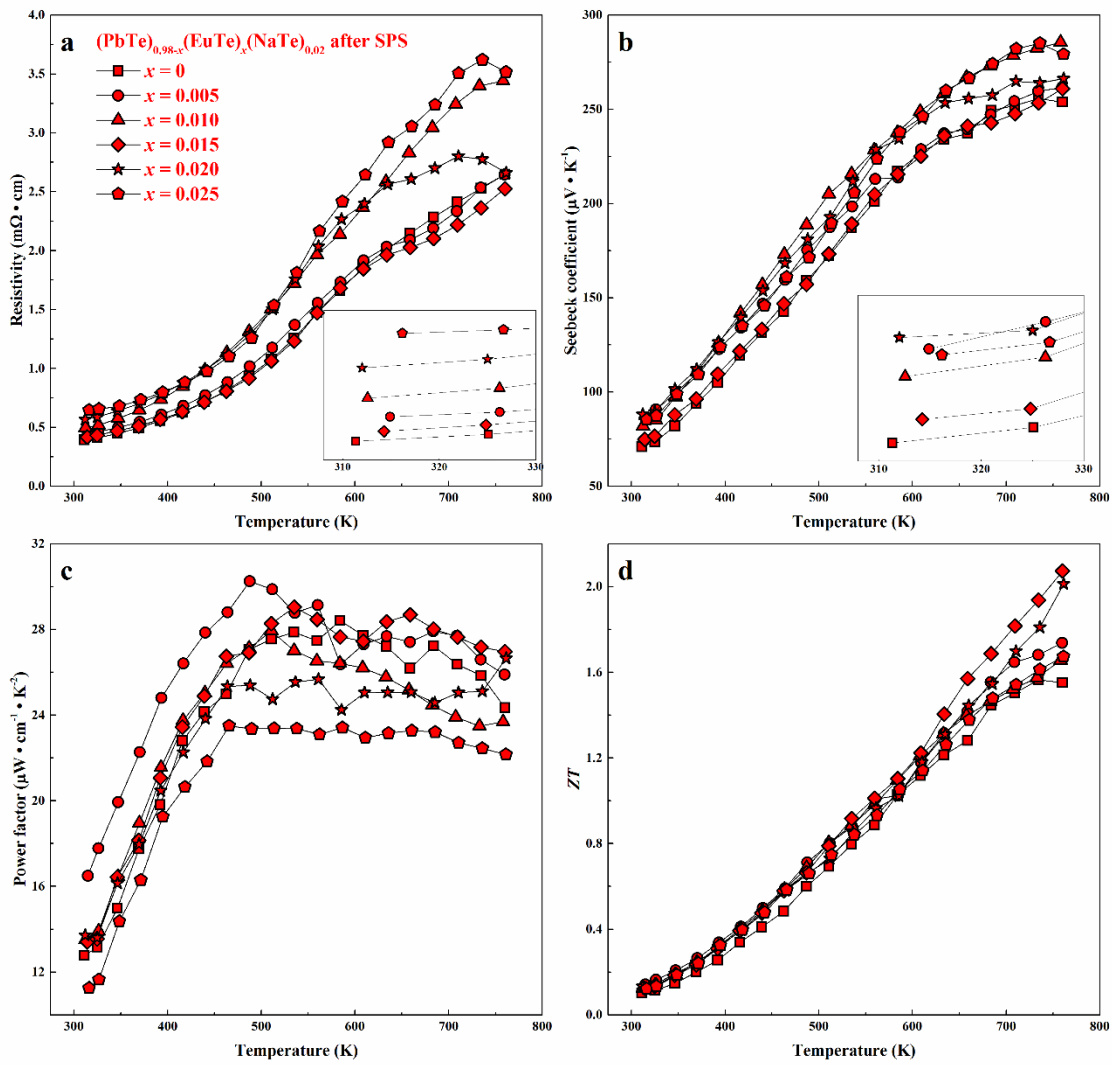
Figure 6.9. Thermoelectric properties of (PbTe)$_{0.98-x}$(EuTe)$_x$(NaTe)$_{0.02}$ after SPS (a) resistivity, (b) Seebeck coefficient, (c) power factor and (d) *ZT*.
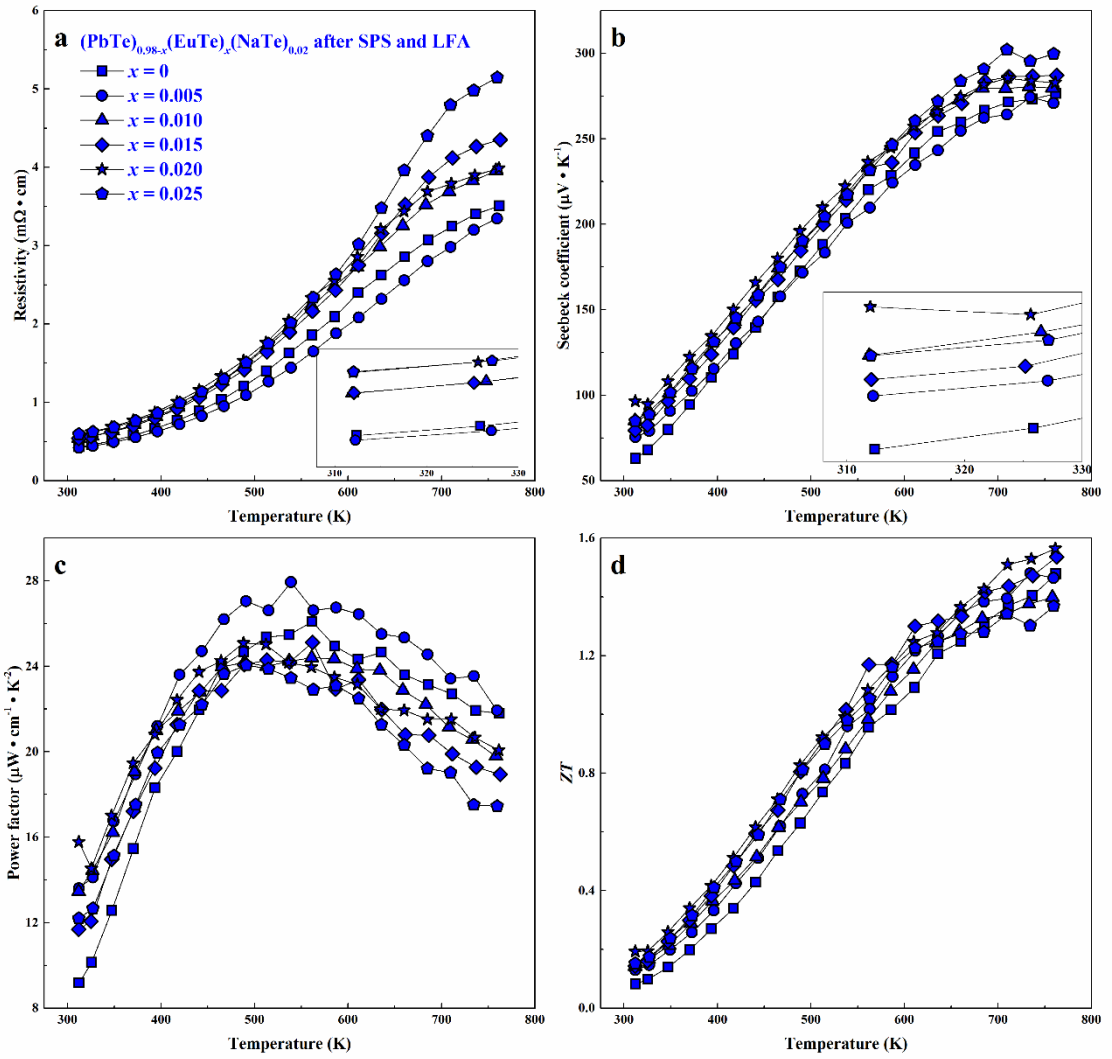
Figure 6.10. Thermoelectric properties of (PbTe)$_{0.98-x}$(EuTe)$_x$(NaTe)$_{0.02}$ after SPS and LFA (a) resistivity, (b) Seebeck coefficient, (c) power factor and (d) *ZT*.
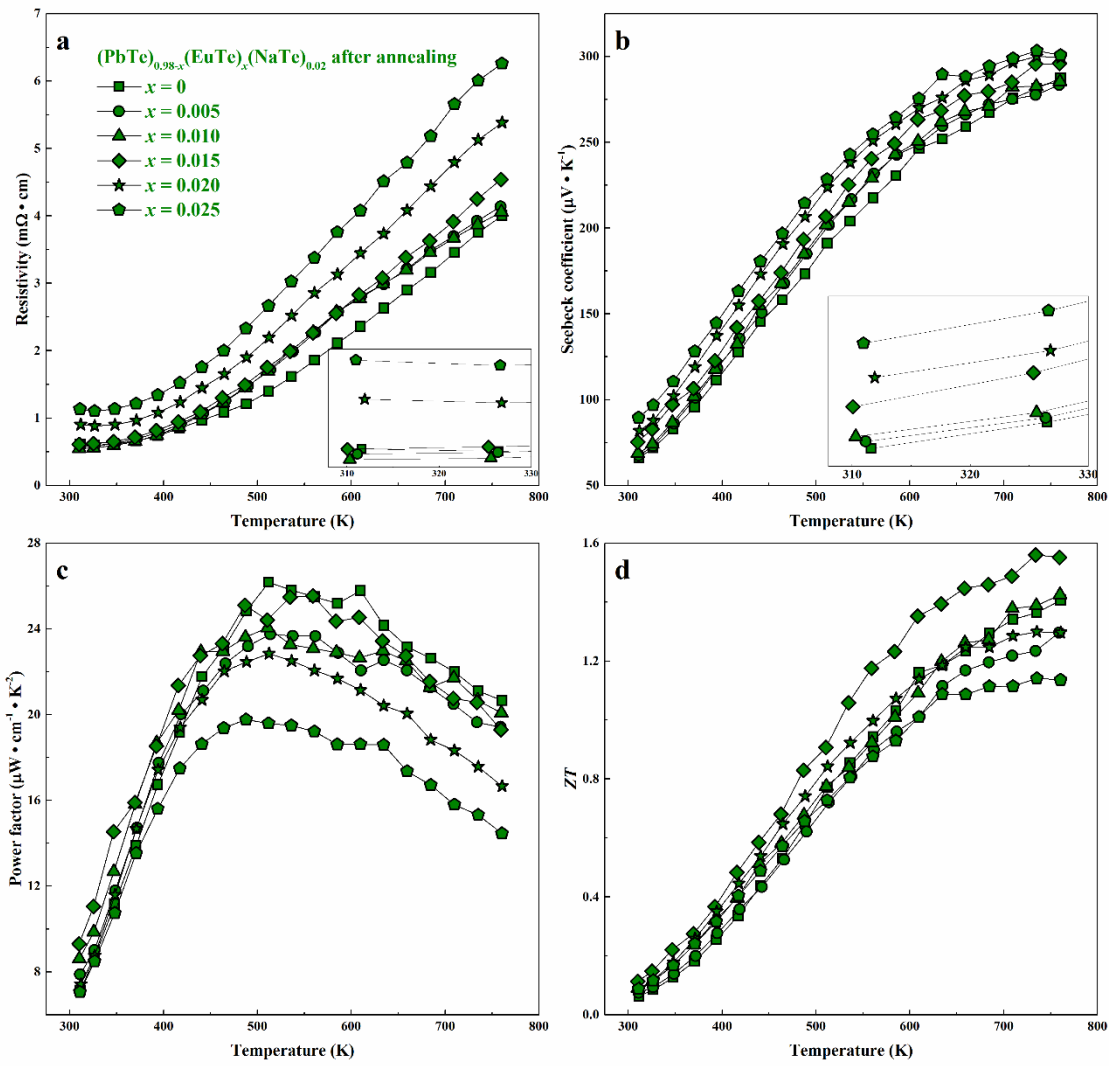
Figure 6.11. Thermoelectric properties of $(PbTe)_{0.98-x}(EuTe)_x(NaTe)_{0.02}$ after annealing (a) resistivity, (b) Seebeck coefficient, (c) power factor and (d) ZT.
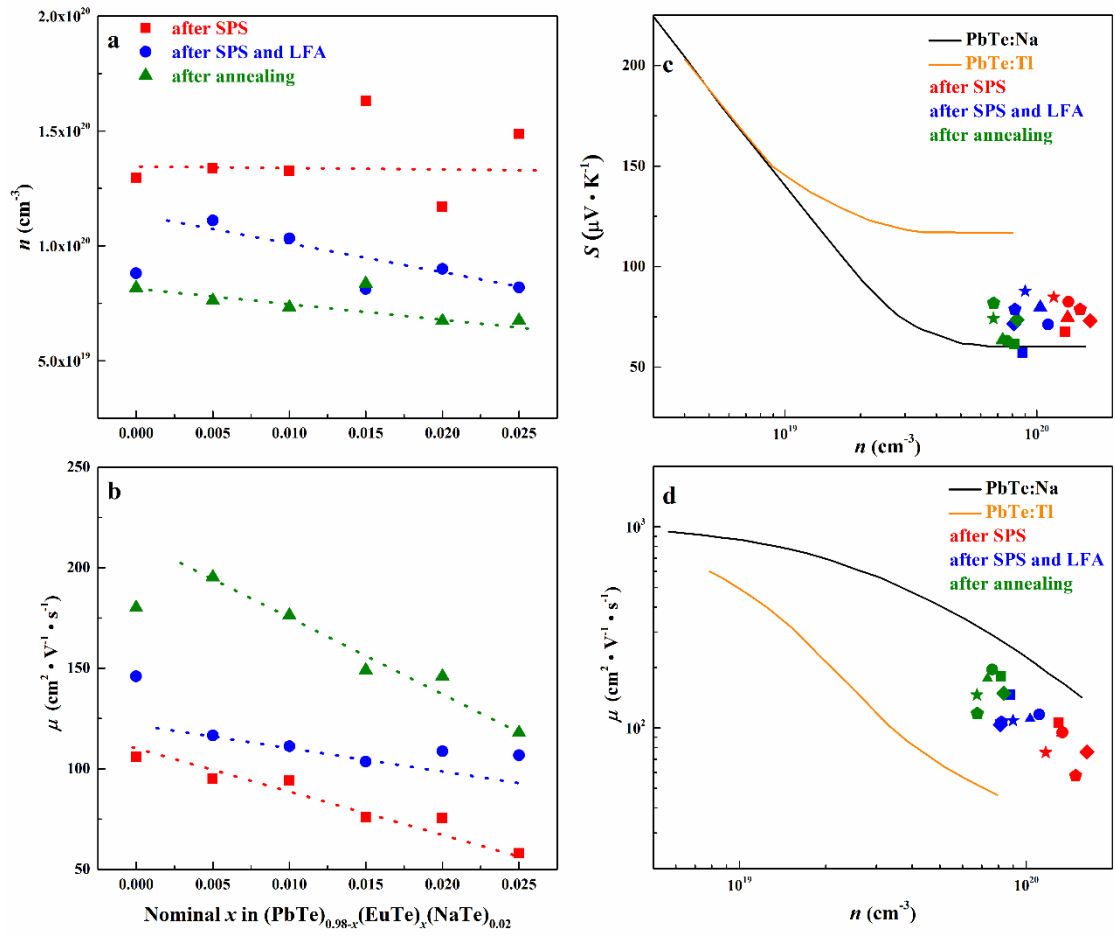
Figure 6.12. (a) Hall carrier concentrations (p) and (b) carrier mobility (μ) in $(PbTe)_{0.98-x}(EuTe)_x(NaTe)_{0.02}$ after SPS (red), after SPS and LFA (blue), after annealing (green). (c) Seebeck coefficient (S) and (d) Hall mobility (μ) versus Hall carrier concentration (p) for $(PbTe)_{0.98-x}(EuTe)_x(NaTe)_{0.02}$, PbTe: Na[65,125,127] and PbTe: Tl[27,123,201].
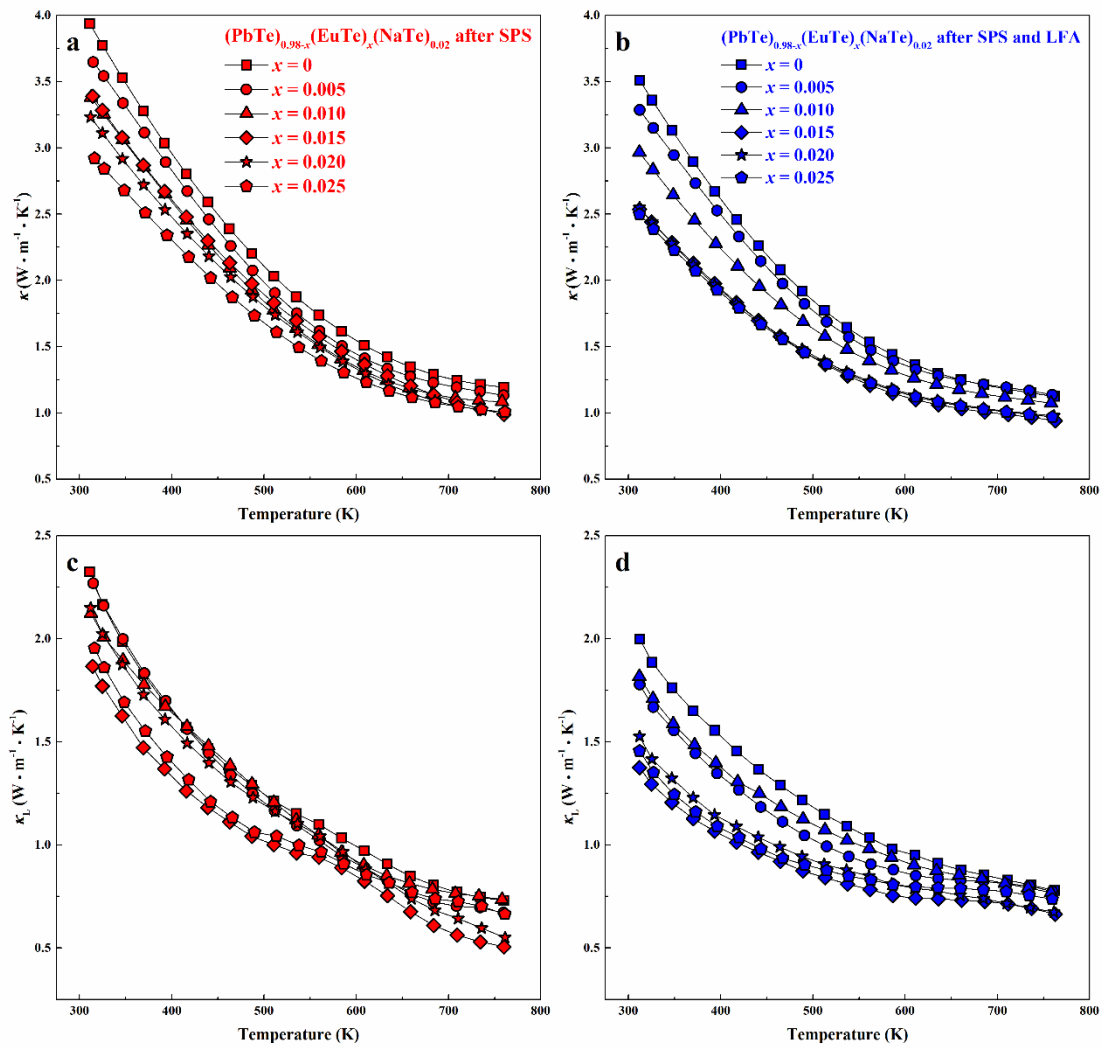
Figure 6.13. (a) Total thermal conductivity κ and (c) lattice thermal conductivity κ_L of $(PbTe)_{0.98-x}(EuTe)_x(NaTe)_{0.02}$ after SPS; (b) Total thermal conductivity κ and (d) lattice thermal conductivity κ_L of $(PbTe)_{0.98-x}(EuTe)_x(NaTe)_{0.02}$ after SPS and LFA.
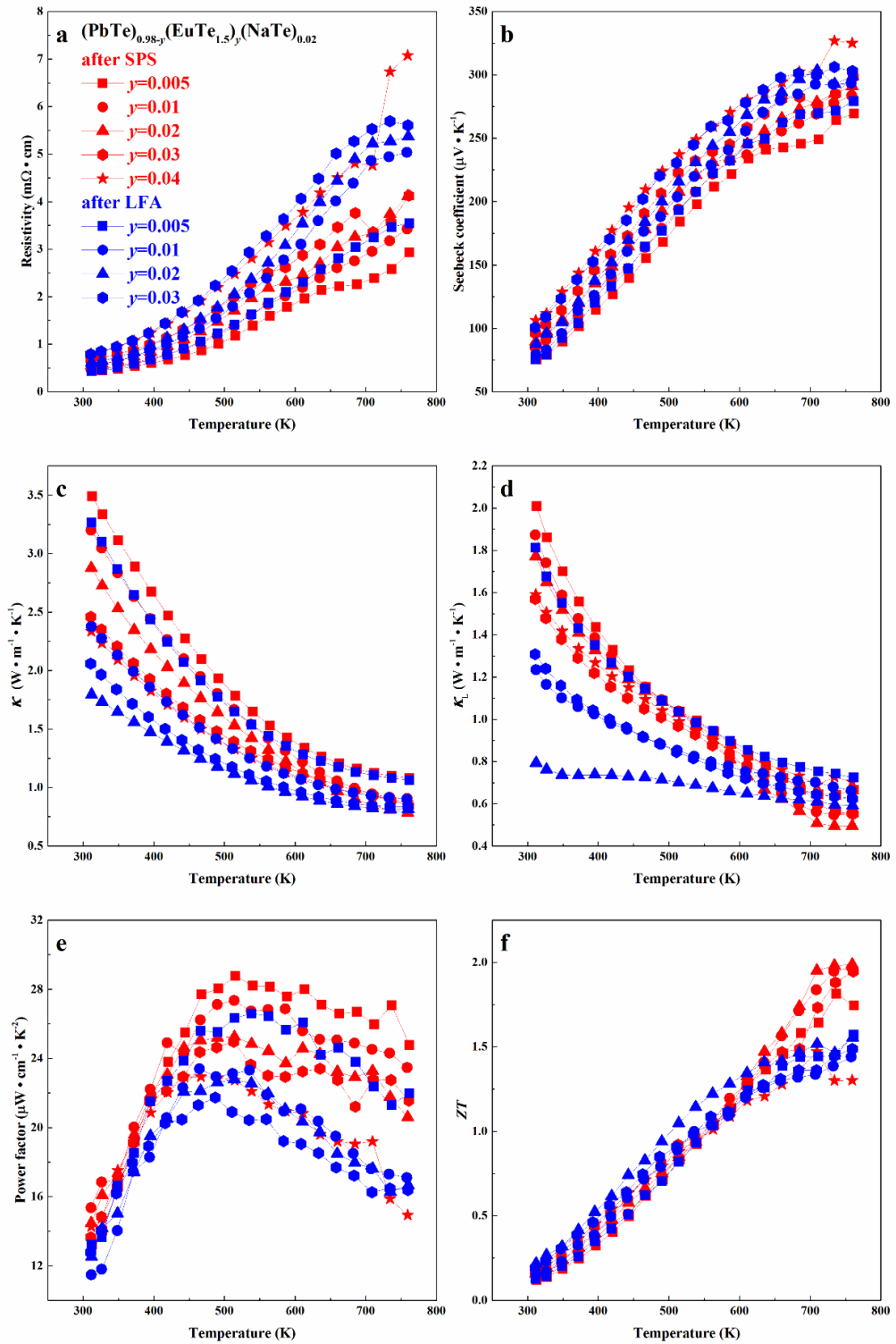
Figure 6.14. Thermoelectric properties of $(PbTe)_{0.98-y}(EuTe_{1.5})_y(NaTe)_{0.02}$ after SPS (red) and after LFA (blue) (a) resistivity, (b) Seebeck coefficient, (c) total thermal conductivity, (d) lattice thermal conductivity, (e) power factor and (f) ZT.

6.3.3. Thermal cyclic experiments

Material stability with respect to the operating temperature range is crucial for device engineering. The LFA cyclic measurements (Figure 6.15) indicate that the samples are not stable directly after SPS. The first heating cycle of the thermal conductivity measurements for all samples show higher values, compared to following cycles. There is one obvious drop for each sample at the temperature above 600 K, see e.g. arrow on the Figure 6.15c, and then thermal conductivities show quite stable values. This may indicate that the materials are structurally or chemically changed during the heat treatment.
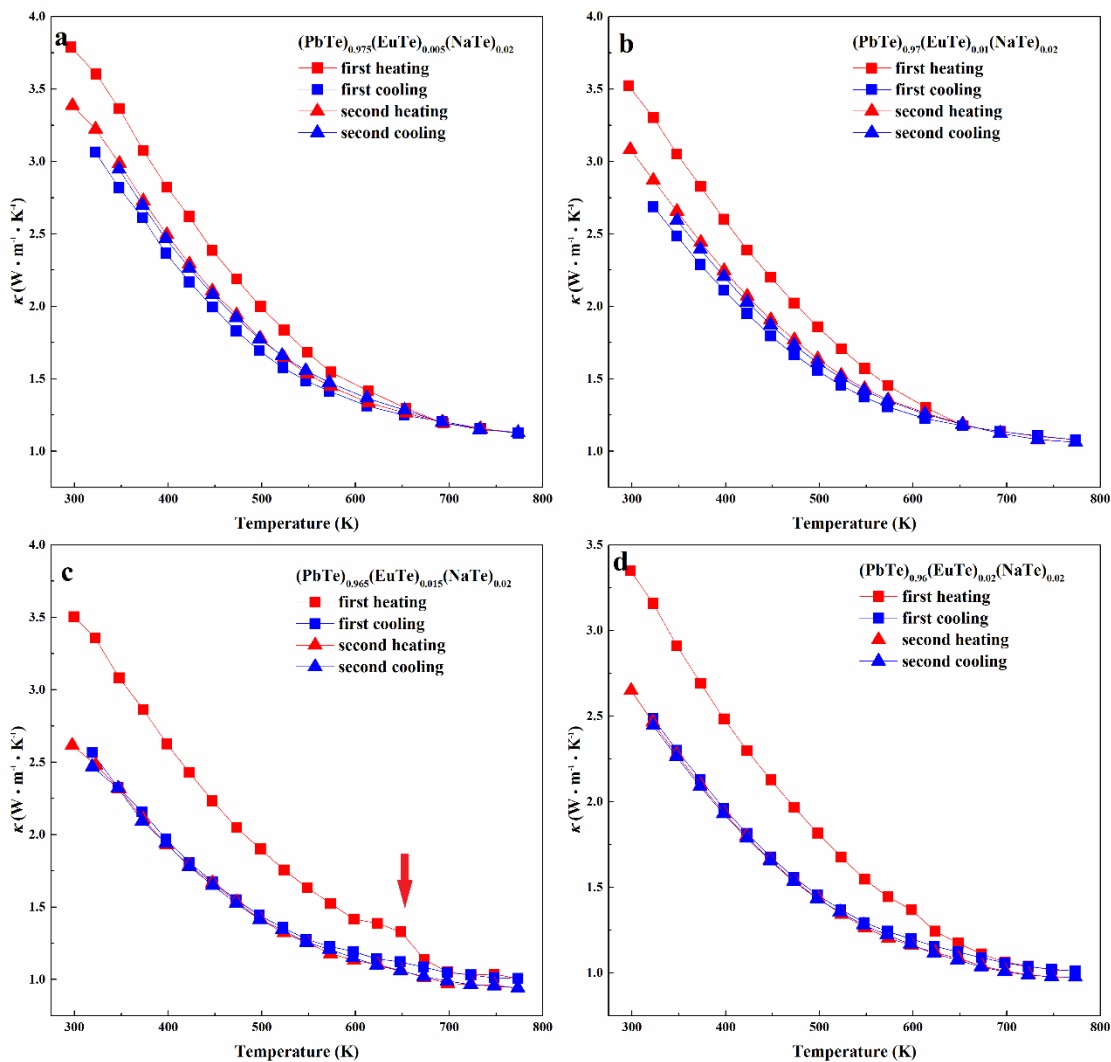
Figure 6.15. Cyclic measurement of total thermal conductivity (κ) of $(PbTe)_{0.98-x}(EuTe)_x(NaTe)_{0.02}$ (a) $x = 0.005$, (b) $x = 0.010$, (c) $x = 0.015$, (d) $x = 0.020$.

The sample $(PbTe)_{0.96}(EuTe)_{0.02}(NaTe)_{0.02}$, which was characterized with the highest *ZT,* was used for cyclic measurements (Figures 6.16, 6.17). After SPS (most inhomogeneous state), the sample maintains high *ZT* values within cycling measurements, but the resistivity and the Seebeck coefficient (Figures 6.16a, 6.16b) change, especially at the high temperature range (500 — 760 K). After cycling, the specimen bar, which was a perfect shiny-gray parallelepiped (inset Figure 6.16d, top), is bent and the surface become black and coarse (inset Figure 6.16d, down). In contrast to the after-SPS sample, all properties for the long-term annealed sample are quite repeatable and the specimen bar did not show obvious change after measurements (Figure 6.17, inset). The slight evolution of the electrical resistivity and Seebeck coefficient during first heating-cooling cycle (Figures 6.17a, 6.17b) can be attributed to the elimination of quenching effect, i.e. stress in the microstructure. For the evaluation of these materials in potential high-temperature application, further characterization of the thermal stability at 873 K were carried out. The properties are consistent with our previous measurements (Figure 6.18), the *ZT* values are also reduced for the samples after additional heat-treatment. The after-SPS specimen becomes bent (Figure 6.19, right), while the shape does not change for after annealing one (Figure 6.19, left). However, the surface of all specimens after 873 K ZEM measurements becomes white and removable (Figure 6.19). It is clear that at high temperature (873 K) and lower pressure (0.1 bar) of Helium atmosphere, the surface of the samples changed. This may be due to evaporation of Te from PbTe for temperatures above 773 K, which is especially likely to occur in vacuum condition.[10]
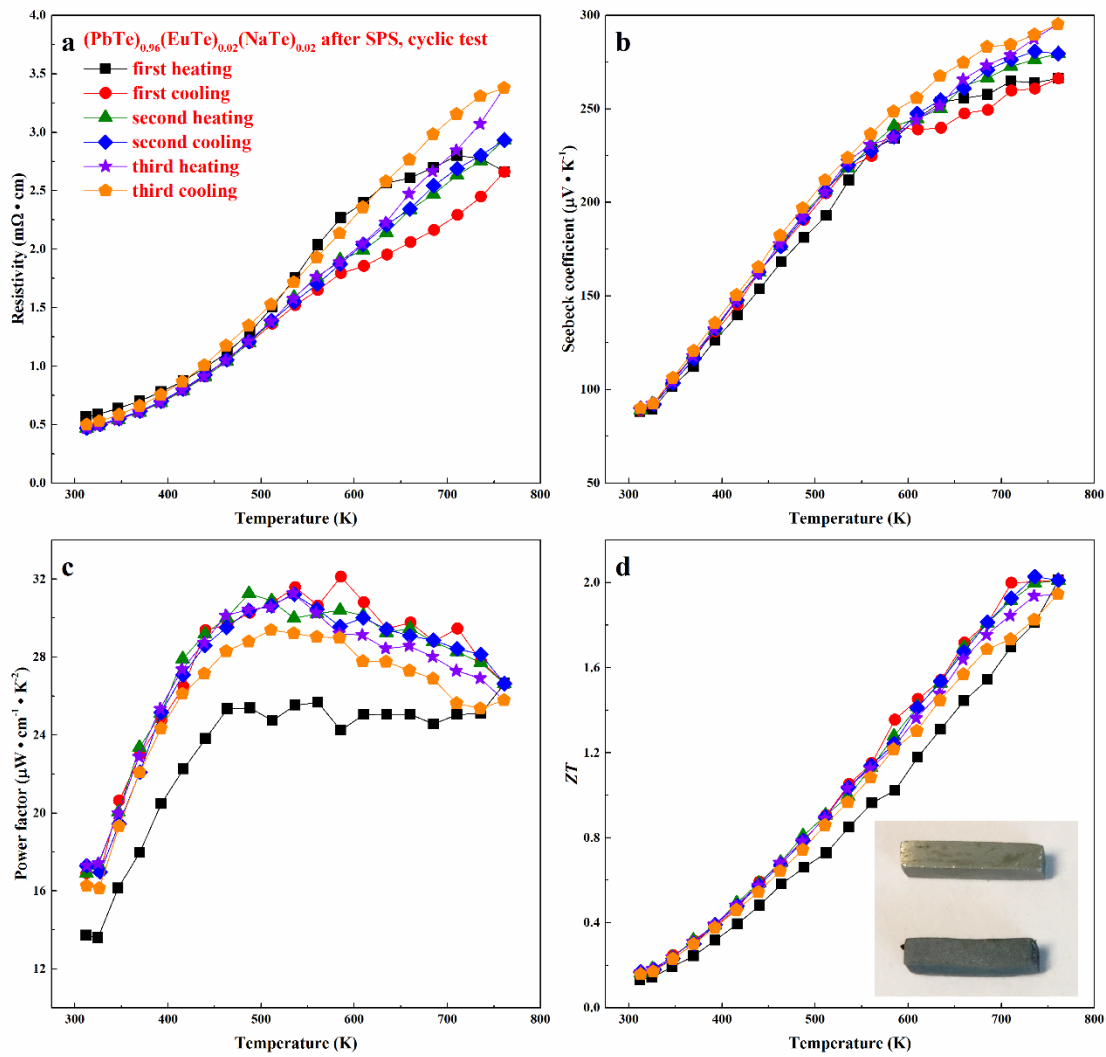
Figure 6.16. Cyclic measurement of $(PbTe)_{0.96}(EuTe)_{0.02}(NaTe)_{0.02}$ after SPS for (a) resistivity, (b) Seebeck coefficient, (c) power factor and (d) *ZT* (inset is the photo of sample bars before measurement (up) and after measurement (down)).
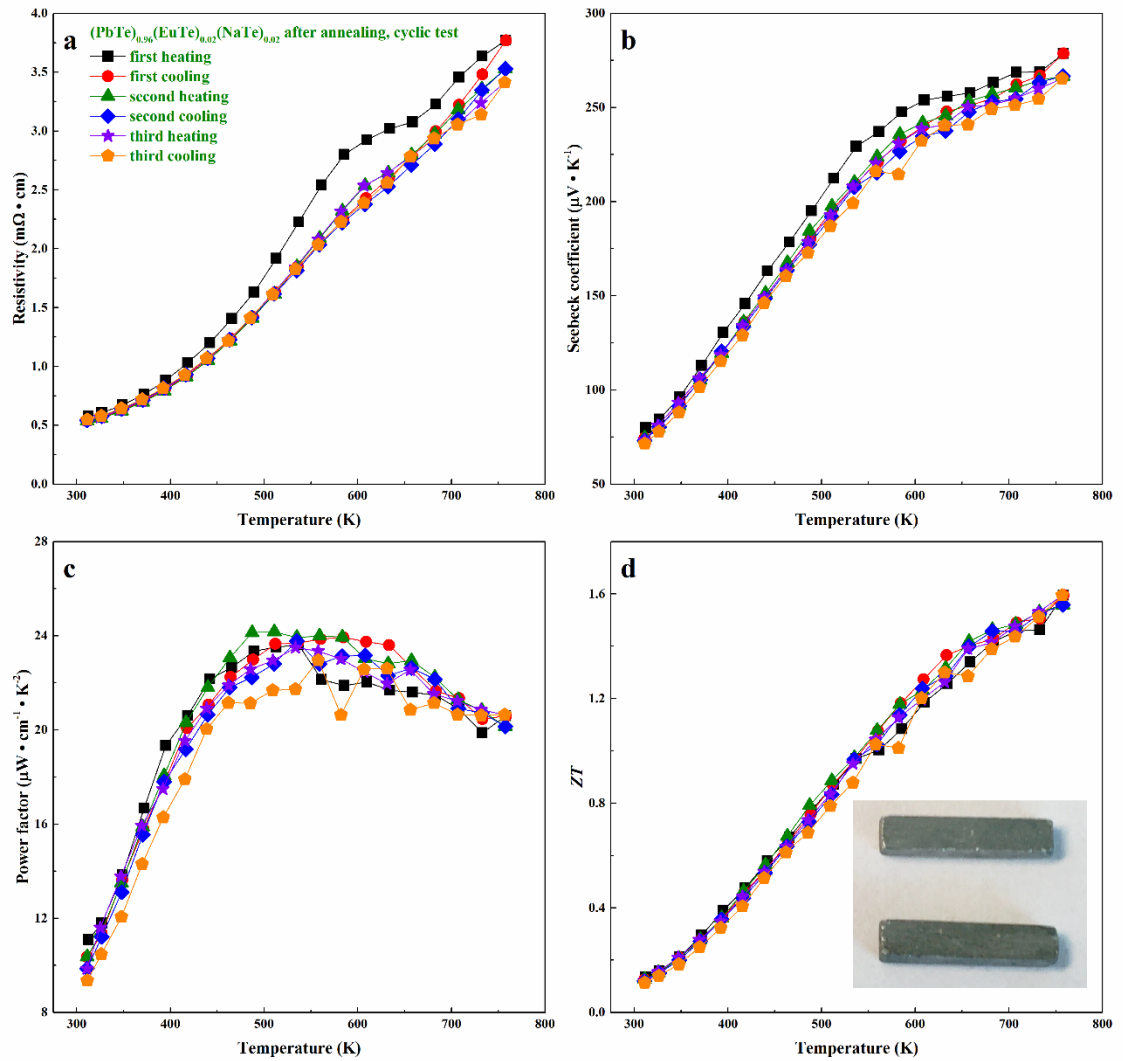
Figure 6.17. Cyclic measurement of $(PbTe)_{0.96}(EuTe)_{0.02}(NaTe)_{0.02}$ after annealing for (a) resistivity, (b) Seebeck coefficient, (c) power factor and (d) *ZT* (inset is the photo of sample bars before measurement (up) and after measurement (down)).
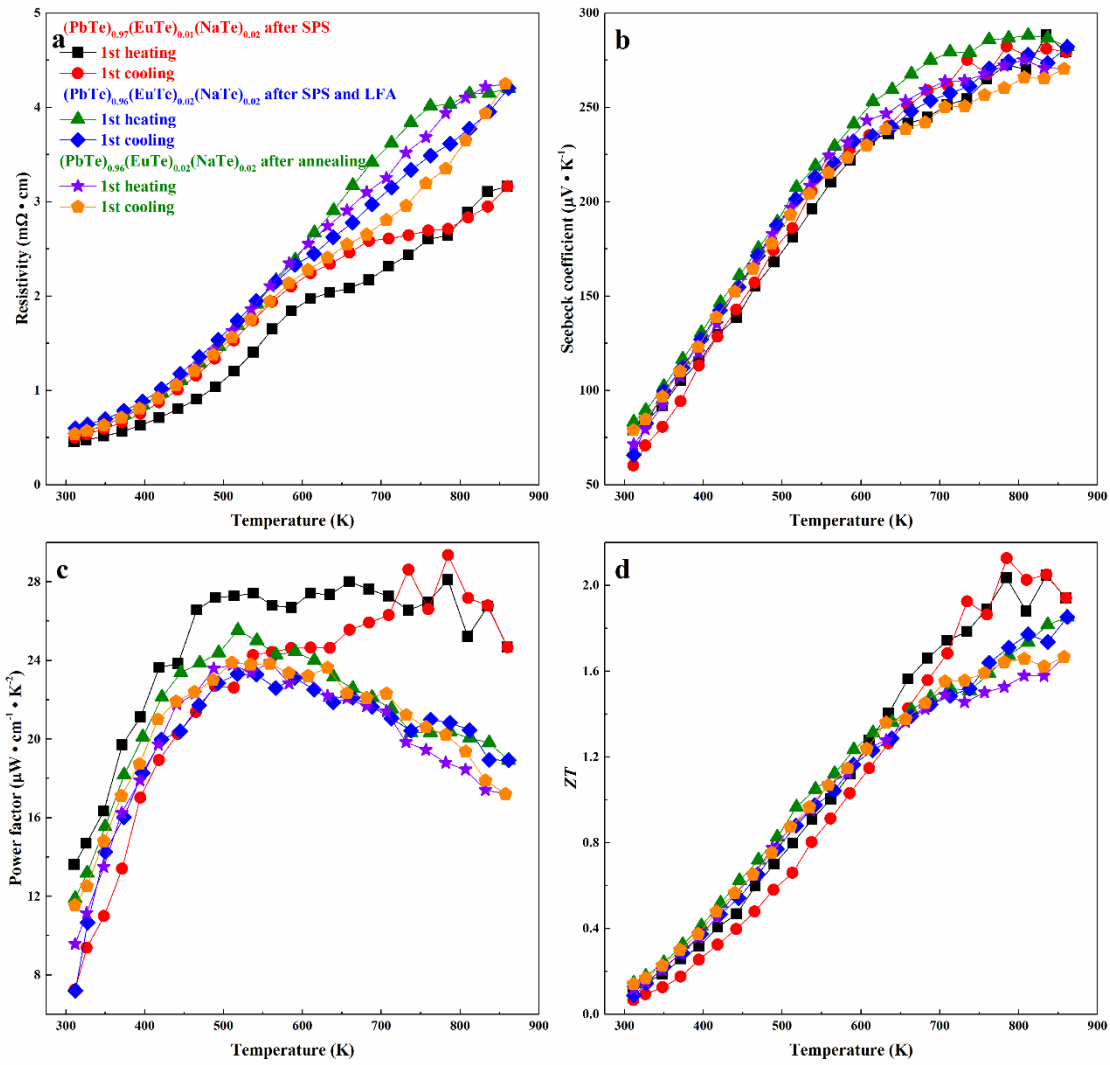
Figure 6.18. Temperature-dependent (up to 873 K) (a) resistivity, (b) Seebeck coefficient, (c) power factor and (d) ZT for samples: $(PbTe)_{0.97}(EuTe)_{0.01}(NaTe)_{0.02}$ after SPS, $(PbTe)_{0.96}(EuTe)_{0.02}(NaTe)_{0.02}$ after LFA, and after annealing.
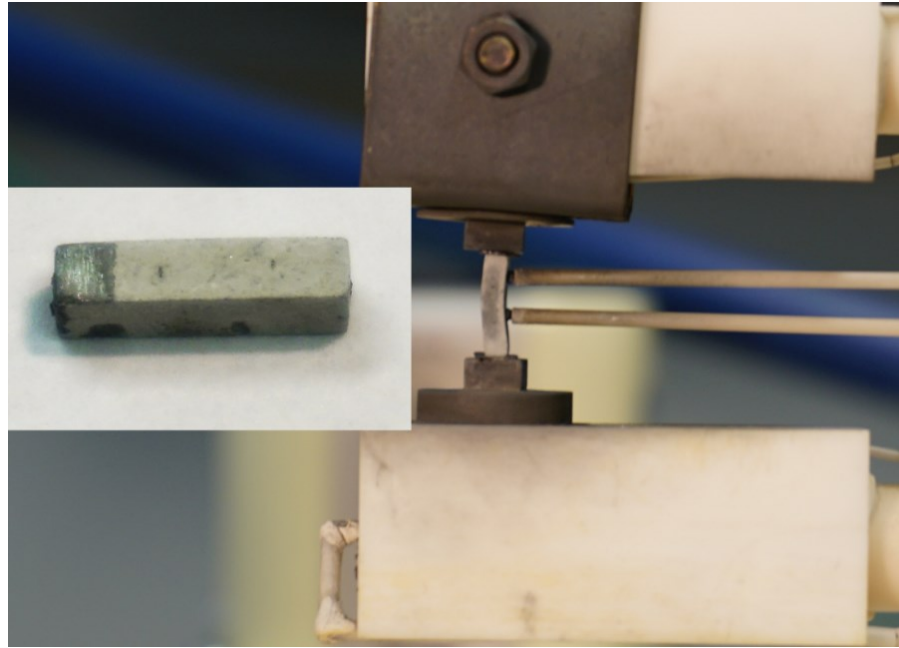
Figure 6.19. Specimens after ZEM measurement at 873 K: after annealing and ZEM (left), after SPS and ZEM (right).

6.4. Conclusions

$(PbTe)_{0.98-x}(EuTe)_x(NaTe)_{0.02}$ ($x = 0$ — 0.03) samples were systematically investigated after different heat treatments: spark plasma sintering (SPS), laser flash measurement (LFA), and long-term annealing. The solubility of Eu (*ca*. 1.0 at.%) in $(PbTe)_{0.98-x}(EuTe)_x(NaTe)_{0.02}$ was established at our investigation temperature. A part of Eu becomes Eu^{3+} within the homogeneity range due to the charge compensation caused by Pb^{2+}–by–Na^{1+} substitution or by change of the sample composition towards Te-rich side.

The most inhomogeneous samples (samples after SPS) were characterized with highest values of ZT_{max} up to 2.1 at 760 K. However, metallographic studies show that there are a large number of micrometer-scale sodium- and europium-rich aggregations in those SPS samples. After additional heat treatment (LFA measurement or long-term annealing), the ZT_{max} are reduced to 1.6. Similar behaviors were also found in $(PbTe)_{0.98-y}(EuTe_{1.5})_y(NaTe)_{0.02}$ samples. The distributions of Eu and Na of the samples have become much more homogeneous along with increased lattice parameters and decreased carrier concentrations.

6. Eu- and Na-substituted PbTe

The structural disorder introduced by Na and Eu substitutions and the formation of non-homogeneity in the materials increase the phonon scattering, which decrease the total and lattice thermal conductivity. The cyclic measurements on thermal conductivity show obvious difference between first heating data and subsequent measured data, which is a common behavior in $Pb_{1-x}Na_xTe$ system.

The cyclic TE properties were measured for all three samples series. The long-term annealed samples show the best reproducible TE properties and good mechanical stability. In summary, the Eu- and Na-substituted PbTe materials can be used in thermoelectric modules, just only after long-term annealing. In order to avoid materials decomposition, surface protection need to be considered for working temperatures above 773 K.

This study clearly demonstrates that out-of-equilibrium materials may have promising high *ZT* values under certain circumstances, but these *ZT* values will generally approach lower values after heat treatment similar to the "working conditions".

7. Summary and Outlook

PbTe-based materials have many fascinating properties needed to be studied. The influence of chemical substitution and temperature on the stability of the PbTe-based solid solutions and their TE properties was the main goal of the present work. The dissertation presents phase analysis and TE properties of binary Pb–Te, substitutional Eu solid solution in PbTe, Na solid solution in PbTe, and reproducibility of TE properties and microstructure evolutions of Eu- and Na-substituted PbTe.

Through investigation of several binary polycrystalline Pb–Te samples, it was found that the mechanical stress during the powder process causes the strong anisotropy of the PXRD-reflection broadening in PbTe, which can be healed by annealing. Compare to stoichiometric $Pb_{0.50}Te_{0.50}$, additional Te in the SPS-prepared $Pb_{0.49}Te_{0.51}$ sample has no obvious influence on the TE properties during the cyclic measurements; additional Pb in the SPS-prepared $Pb_{0.51}Te_{0.49}$ sample results in unstable electronic properties, gradually changing from p-type into n-type conduction under the cyclic measurements. For the 673 K annealing, where the lattice anisotropy disappears, the SPS-prepared sample $Pb_{0.50}Te_{0.50}$ undergoes a chemical change and shows almost "intrinsic" TE properties. However, the single crystal PbTe has no obvious change during the 673 K annealing. The complex diffusion processes in PbTe including processes at grain boundaries and/or under contribution of dislocations provide dynamic chemical reactions during the measurements and the annealing, which are responsible for variable electric properties in polycrystalline PbTe.

Pseudo-binary $(PbTe)_{1-x}(EuTe)_x$ and $(PbTe)_{1-y}(EuTe_{1.5})_y$, binary $Eu_{1-x}Te_x$ series of samples were synthesized to investigate the influence of the Pb substitution by (mostly) divalent element. Eu has small solubility range ($x = 0.02$, $y = 0.01$) in PbTe under 873 K annealing temperature. For temperatures up to 1123 K, $(PbTe)_{1-x}(EuTe)_x$ forms a solid solution over the entire concentration range. For $(PbTe)_{1-y}(EuTe_{1.5})_y$ samples, the single-phase materials can be achieved when $y \leq 0.03$. No significant influence of these two different Eu substitutions on the thermoelectric figure-of-merit was observed in bulk PbTe. Eu can increase the band gap of PbTe when it forms solid solution. However, the high Eu-contained solid solution ($x \geq 0.15$) is not stable at temperature above 673 K, it will decompose into two cubic phases.

7. Summary and Outlook

Two different substitution schemes $Pb_{1-x}Na_xTe$ and $Pb_{1-y}Na_yTe_{1-y/2}$ were investigated to study Na substitution in PbTe. The shape of the solid solution of Na in PbTe in the ternary system Pb–Na–Te was established. Na has limited and different solubility range for each series: 1.0 at.% for $Pb_{1-x}Na_xTe$ and 2.5 at.% for $Pb_{1-y}Na_yTe_{1-y/2}$. Different local atomic arrangements of Na in two substitution schemes in the bulk PbTe were revealed by NMR: Na replacing Pb and Na atoms replacing Pb in vicinity of the Te vacancy. The later Na-aggregation structures may also be responsible for the less than 100% doping efficiency of Pb-by-Na substitution. A long-term heat treatment leads to an equilibration and homogenisation of the samples by reorganization and distribution of the Na clusters and Te vacancies. In addition, the maximum solubility of Na is reduced upon annealing for both series: ~1.0 at.% for $Pb_{1-y}Na_yTe_{1-y/2}$ and 0.5 at.% for $Pb_{1-x}Na_xTe$. The thermoelectric properties of the single-phase materials were proven to be different by different substitution schemes. The maximum ZT values of 1.4 — 1.6 at 760 K are established for both $Pb_{1-x}Na_xTe$ ($x \geq 0.02$) and $Pb_{1-y}Na_yTe_{1-y/2}$ ($0.1 \geq y \geq 0.03$) series. $Pb_{1-x}Na_xTe$ substitution series exhibit better thermoelectric properties after long-term annealing.

$(PbTe)_{0.98-x}(EuTe)_x(NaTe)_{0.02}$ ($x = 0 — 0.03$) samples and $(PbTe)_{0.98-y}(EuTe_{1.5})_y(NaTe)_{0.02}$ ($y = 0 — 0.04$) samples were investigated after different heat treatments. The solubility of Eu (*ca.* 1.0 at.%) in $Pb_{0.98-x}Eu_xNa_{0.02}Te$ was established at the investigated temperature. A part of Eu become Eu^{3+} within the homogeneity range due to the charge compensation caused by Pb^{2+}–by–Na^{1+} substitution or by change of the sample composition towards Te-rich side. The most inhomogeneous samples (samples after SPS) show highest values of figure-of-merit, ZT_{max} of 2.1 at 760 K, due to a large number of micrometer-scale sodium- and europium-rich aggregations in them. After additional heat treatment (LFA measurement or long-term annealing), the ZT_{max} is reduced to 1.6. The distributions of Eu and Na in the samples have become much more homogeneous, along with increased lattice parameters and decreased carrier concentrations. The structural disorder introduced by Na and Eu substitutions and the formation of non-homogeneity in the materials increase the phonon scattering, which decrease the total and lattice thermal conductivity. The cyclic measurements on thermal conductivity show obvious difference between first heating data and subsequent measured data, which is the common feature in the $Pb_{1-x}Na_xTe$ system. The long-term

annealed samples show the best reproducible TE properties and good mechanical stability during the cyclic measurements.

In summary, the chemical structural features, as well as the TE behavior in binary Pb–Te, ternary Pb–Eu–Te, ternary Pb–Na–Te, and quaternary Pb–Eu–Na–Te systems, have been studied for different substitution schemes and different heat treatments. Structural features of PbTe, the Eu-solubility range in PbTe, the shape of the solid solution of Na and local atomic arrangement in PbTe are the main results of this dissertation. We also demonstrate that out-of-equilibrium materials may have promising high ZT values under certain circumstances, but these ZT values will generally approach lower values after heat treatment similar to the thermoelectric "working conditions".

Collecting room temperature physical properties from these five systems (Figure 7.1), we can see that the electric conductivity increases with increasing carrier concentration; compared to binary PbTe and ternary Pb–Na–Te, Eu addition decreases the electric conductivity. The Seebeck coefficient decreases with increasing carrier concentration and keeps constant around a carrier concentration of 10^{20} cm^{-3}. Eu addition increases the Seebeck coefficient. The maximum value of the power factor is located around a carrier concentration of 10^{19} cm^{-3}, Eu addition does not have an obvious effect on power factor. The single crystal PbTe shows the highest values of the Hall carrier mobility, Eu addition decreases the Hall carrier mobility. The ZT values at room temperature are between 0.05 and 0.25 (Figure 7.2). The single crystal shows the highest ZT value. When substituting with Na, Eu addition can increase ZT values.

7. Summary and Outlook
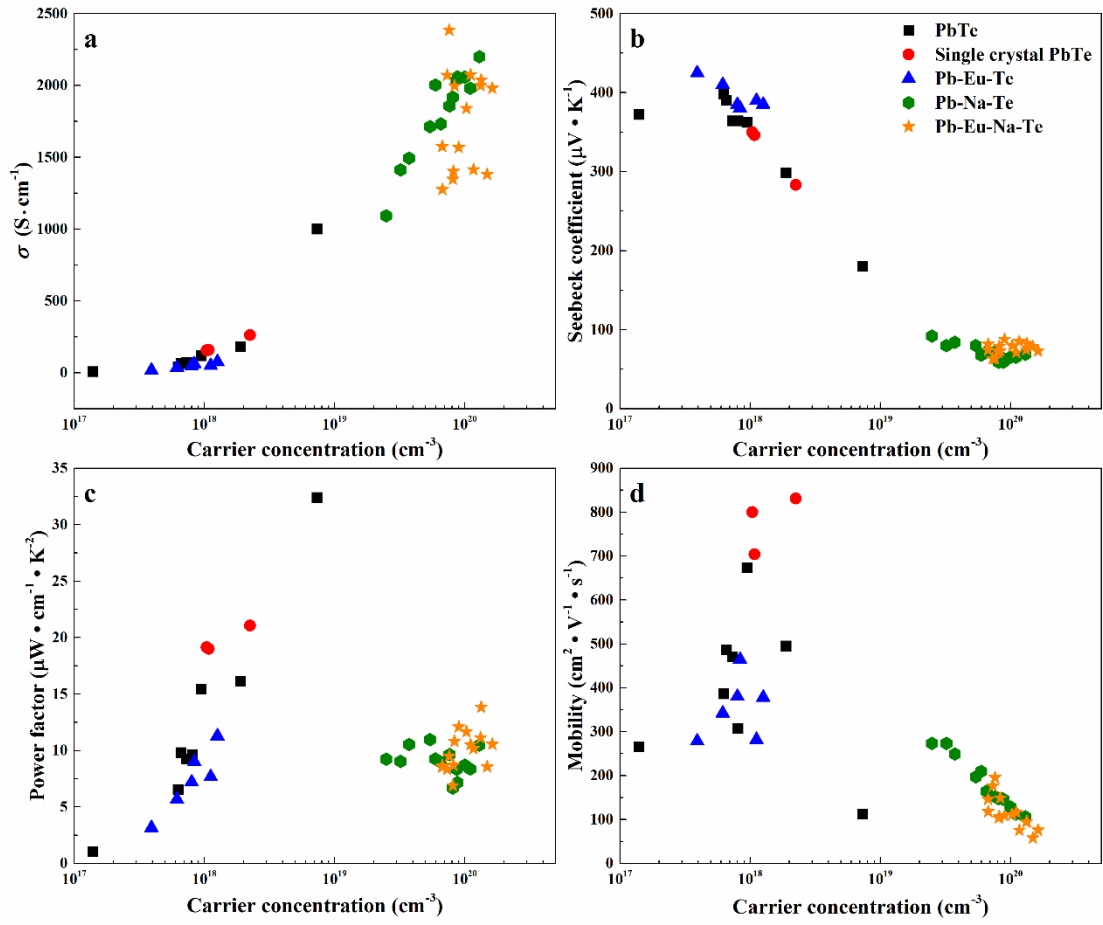
Figure 7.1. Room temperature (a) electric conductivity (b) Seebeck coefficient (c) power factor (d) Hall carrier mobility of *p*-type PbTe, single crystal PbTe, Pb–Eu–Te, Pb–Na–Te, and Pb–Eu–Na–Te *vs.* carrier concentration.
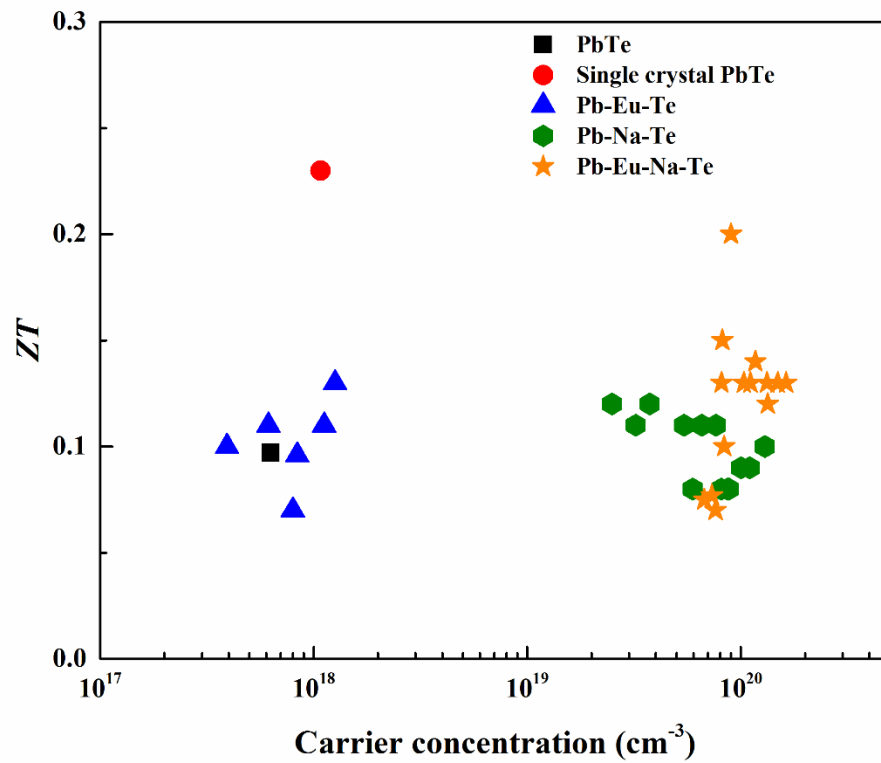
Figure 7.2. Room temperature figure-of-merit (*ZT*) of *p*-type PbTe, single crystal PbTe, Pb–Eu–Te, Pb–Na–Te, and Pb–Eu–Na–Te *vs.* carrier concentration.

Outlook: The following issues are needed to be further investigated: the diffusion process and defects chemical reaction in binary Pb–Te; the connection between the structure and the origin of low lattice thermal conductivity of lead telluride; the reason of the abrupt change of thermal conductivity during the LFA measurements for $Pb_{1-x}Na_xTe$; the influence of the mechanical stress on the thermoelectric properties of $(PbTe)_{0.98-x}(EuTe)_x(NaTe)_{0.02}$; the additional ways to stabilize the solid solutions in PbTe for future applications.

7. Summary and Outlook

References

1. Seebeck, T. J., Magnetische Polarisation der Metalle und Erze durch Temperatur-Differenz, Abhandlungen der physikalischen Klasse der Königlichen Akademie der Wissenschafften zu Berlin, Aus den Jahren **1822** und **1823**, pp. 265–373 (1825). Extracts from four lectures delivered at the Academy of Sciences in Berlin on August 16, 1821, October 18, 25 1821, and February 11, 1822.

2. Rowe, D. M., *Thermoelectrics Handbook: Macro to Nano*. CRC Press 2006.

3. He, J.; Tritt, T. M., Advances in thermoelectric materials research: Looking back and moving forward. *Science* **2017,** *357* (6358), 1369.

4. Zhang, Q. H.; Huang, X. Y.; Bai, S. Q.; Shi, X.; Uher, C.; Chen, L. D., Thermoelectric Devices for Power Generation: Recent Progress and Future Challenges. *Adv. Eng. Mater.* **2016,** *18* (2), 194-213.

5. Goldsmid, H. J., Electronic refrigeration. *London: Pion Limited* **1986**.

6. Altenkirch, E., Über den Nutzeffekt der Thermosäule. *Physikalische Zeitschrift* **1909,** *10*, 560–580.

7. Ioffe, A. F., Semiconductor Thermoelements and Thermoelectric Cooling. *Infosearsh, London* **1957**, translated from Russian, Ioffe A. F., Poluprovodnikovye Termoelementy and Termoelektricheskoe Okhlazhdenie, Publishing House of the U.S.S.R. Academy of Science, Moscow-Leningrad, 1956.

8. DiSalvo, F. J., Thermoelectric cooling and power generation. *Science* **1999,** *285* (5428), 703-706.

9. Sootsman, J. R.; Chung, D. Y.; Kanatzidis, M. G., New and Old Concepts in Thermoelectric Materials. *Angew. Chem.-Int. Edit.* **2009,** *48* (46), 8616-8639.

10. Wood, C., Materials for thermoelectric energy conversion. *Rep Prog. Phys.* **1988,** *51* (4), 459.

11. Tritt, T. M.; Subramanian, M. A., Thermoelectric materials, phenomena, and applications: A bird's eye view. *MRS Bull.* **2006,** *31* (3), 188-194.

12. Mahan, G. D.; Sofo, J. O., The best thermoelectric. *P Natl Acad Sci USA* **1996,** *93* (15), 7436-7439.

13. Toberer, E. S.; May, A. F.; Snyder, G. J., Zintl Chemistry for Designing High Efficiency Thermoelectric Materials. *Chem. Mater.* **2010,** *22* (3), 624-634.

References

14. Xiao, C.; Li, Z.; Li, K.; Huang, P.; Xie, Y., Decoupling Interrelated Parameters for Designing High Performance Thermoelectric Materials. *Acc. Chem. Res.* **2014,** *47* (4), 1287-1295.

15. Snyder, G. J.; Toberer, E. S., Complex thermoelectric materials. *Nat. Mater.* **2008,** *7* (2), 105-114.

16. Nag, B. R., Theory of Electrical Transport in Semiconductors. *Pergamon Press* **1972**.

17. He, J.; Kanatzidis, M. G.; Dravid, V. P., High performance bulk thermoelectrics via a panoscopic approach. *Mater. Today* **2013,** *16* (5), 166-176.

18. Goldsmid, H. J.; Douglas, R. W., The use of semiconductors in thermoelectric refrigeration. *British J. Appl. Phys.* **1954**, *5*, 386-390.

19. Tan, G.; Zhao, L.-D.; Kanatzidis, M. G., Rationally Designing High-Performance Bulk Thermoelectric Materials. *Chem. Rev.* **2016**, *116* (19), 12123-12149.

20. Goldsmid, H. J., Introduction to Thermoelectricity. *Springer* **2010**.

21. Chasmar, R. P.; Stratton, R., The Thermoelectric Figure-of-merit and its Relation to Thermoelectric Generators. *J. Electron. Control* **1959,** *7* (1), 52-72.

22. Pei, Y.; Wang, H.; Snyder, G. J., Band Engineering of Thermoelectric Materials. *Adv. Mater.* **2012,** *24* (46), 6125-6135.

23. Tan, G.; Shi, F.; Hao, S.; Chi, H.; Bailey, T. P.; Zhao, L.-D.; Uher, C.; Wolverton, C.; Dravid, V. P.; Kanatzidis, M. G., Valence Band Modification and High Thermoelectric Performance in SnTe Heavily Alloyed with MnTe. *J. Am. Chem. Soc.* **2015,** *137* (35), 11507-11516.

24. Takagiwa, Y.; Pei, Y.; Pomrehn, G.; Snyder, G. J., Dopants effect on the band structure of PbTe thermoelectric material. *Appl. Phys. Lett.* **2012,** *101*, 092102.

25. Pei, Y.; Gibbs, Z. M.; Gloskovskii, A.; Balke, B.; Zeier, W. G.; Snyder, G. J., Optimum Carrier Concentration in *n*-Type PbTe Thermoelectrics. *Adv. Energy Mater.* **2014,** *4* (13), 1400486.

26. Heremans, J. P.; Wiendlocha, B.; Chamoire, A. M., Resonant levels in bulk thermoelectric semiconductors. *Energy Environ. Sci.* **2012,** *5* (2), 5510-5530.

27. Heremans, J. P.; Jovovic, V.; Toberer, E. S.; Saramat, A.; Kurosaki, K.; Charoenphakdee, A.; Yamanaka, S.; Snyder, G. J., Enhancement of thermoelectric efficiency in PbTe by distortion of the electronic density of states. *Science* **2008,** *321* (5888), 554-557.

28. Liu, W.; Tan, X.; Yin, K.; Liu, H.; Tang, X.; Shi, J.; Zhang, Q.; Uher, C., Convergence of Conduction Bands as a Means of Enhancing Thermoelectric Performance of n-Type $Mg_2Si_{1-x}Sn_x$ Solid Solutions. *Phys. Rev. Lett.* **2012,** *108* (16), 166601.

29. Pei, Y. Z.; Shi, X. Y.; LaLonde, A.; Wang, H.; Chen, L. D.; Snyder, G. J., Convergence of electronic bands for high performance bulk thermoelectrics. *Nature* **2011,** *473* (7345), 66-69.

30. Zebarjadi, M.; Joshi, G.; Zhu, G.; Yu, B.; Minnich, A.; Lan, Y.; Wang, X.; Dresselhaus, M.; Ren, Z.; Chen, G., Power Factor Enhancement by Modulation Doping in Bulk Nanocomposites. *Nano Lett.* **2011,** *11* (6), 2225-2230.

31. Pei, Y.-L.; Wu, H.; Wu, D.; Zheng, F.; He, J., High Thermoelectric Performance Realized in a BiCuSeO System by Improving Carrier Mobility through 3D Modulation Doping. *J. Am. Chem. Soc.* **2014,** *136* (39), 13902-13908.

32. Heremans, J. P.; Thrush, C. M.; Morelli, D. T., Thermopower enhancement in lead telluride nanostructures. *Phys. Rev. B* **2004,** *70*, 115334.

33. Martin, J.; Wang, L.; Chen, L.; Nolas, G. S., Enhanced Seebeck coefficient through energy-barrier scattering in PbTe nanocomposites. *Phys. Rev. B* **2009,** *79*, 115311.

34. Bahk, J.-H.; Bian, Z.; Shakouri, A., Electron energy filtering by a nonplanar potential to enhance the thermoelectric power factor in bulk materials. *Phys. Rev. B* **2013,** *87*, 075204.

35. Medlin, D. L.; Snyder, G. J., Interfaces in bulk thermoelectric materials: A review for Current Opinion in Colloid and Interface Science. *Curr. Opin. Colloid Interface Sci* **2009,** *14* (4), 226-235.

36. Dresselhaus, M. S.; Chen, G.; Tang, M. Y.; Yang, R. G.; Lee, H.; Wang, D. Z.; Ren, Z. F.; Fleurial, J. P.; Gogna, P., New directions for low-dimensional thermoelectric materials. *Adv. Mater.* **2007,** *19* (8), 1043-1053.

37. Harman, T. C.; Spears, D. L.; Manfra, M. J., High thermoelectric figures of merit in PbTe quantum wells. *J. Electron. Mater.* **1996,** *25* (7), 1121-1127.

38. Harman, T. C.; Taylor, P. J.; Walsh, M. P.; LaForge, B. E., Quantum dot superlattice thermoelectric materials and devices. *Science* **2002,** *297* (5590), 2229-2232.

39. Nolas, G. S.; Sharp, J.; Goldsmid, H. J., Thermoelectrics: Basic Principles and New Materials Development. *New York: Springer* **2001**.

40. Berman, R., Thermal Conduction in Solids. *Oxford: Oxford University Press* **1976**.

References

41. Qiu, B.; Bao, H.; Zhang, G.; Wu, Y.; Ruan, X., Molecular dynamics simulations of lattice thermal conductivity and spectral phonon mean free path of PbTe: Bulk and nanostructures. *Comput. Mater. Sci* **2012,** *53* (1), 278-285.

42. Klemens, P. G., Thermal Resistance due to Point Defects at High Temperatures. *Phys. Rev* **1960,** *119* (2), 507-509.

43. Callaway, J., Model for Lattice Thermal Conductivity at Low Temperatures. *Phys. Rev* **1959,** *113* (4), 1046-1051.

44. Callaway, J.; von Baeyer, H. C., Effect of Point Imperfections on Lattice Thermal Conductivity. *Phys. Rev* **1960,** *120* (4), 1149-1154.

45. Biswas, K.; He, J. Q.; Blum, I. D.; Wu, C. I.; Hogan, T. P.; Seidman, D. N.; Dravid, V. P.; Kanatzidis, M. G., High-performance bulk thermoelectrics with all-scale hierarchical architectures. *Nature* **2012,** *489* (7416), 414-418.

46. Li, J.; Tan, Q.; Li, J. F.; Liu, D. W.; Li, F.; Li, Z. Y.; Zou, M.; Wang, K., BiSbTe-Based Nanocomposites with High *ZT*: The Effect of SiC Nanodispersion on Thermoelectric Properties. *Adv. Funct. Mater.* **2013,** *23* (35), 4317-4323.

47. Min, Y.; Roh, J. W.; Yang, H.; Park, M.; Kim, S. I.; Hwang, S.; Lee, S. M.; Lee, K. H.; Jeong, U., Surfactant-Free Scalable Synthesis of Bi_2Te_3 and Bi_2Se_3 Nanoflakes and Enhanced Thermoelectric Properties of Their Nanocomposites. *Adv. Mater.* **2013,** *25* (10), 1425-1429.

48. Biswas, K.; He, J. Q.; Zhang, Q. C.; Wang, G. Y.; Uher, C.; Dravid, V. P.; Kanatzidis, M. G., Strained endotaxial nanostructures with high thermoelectric figure-of-merit. *Nat. Chem.* **2011,** *3* (2), 160-166.

49. Shen, J.-J.; Zhu, T.-J.; Zhao, X.-B.; Zhang, S.-N.; Yang, S.-H.; Yin, Z.-Z., Recrystallization induced in situ nanostructures in bulk bismuth antimony tellurides: a simple top down route and improved thermoelectric properties. *Energy Environ. Sci.* **2010,** *3* (10), 1519-1523.

50. Kanatzidis, M. G., Nanostructured Thermoelectrics: The New Paradigm? *Chem. Mat.* **2010,** *22* (3), 648-659.

51. Lee, Y.; Lo, S.-H.; Androulakis, J.; Wu, C.-I.; Zhao, L.-D.; Chung, D.-Y.; Hogan, T. P.; Dravid, V. P.; Kanatzidis, M. G., High-Performance Tellurium-Free Thermoelectrics: All-Scale Hierarchical Structuring of *p*-Type PbSe-MSe Systems (M = Ca, Sr, Ba). *J. Am. Chem. Soc.* **2013,** *135* (13), 5152-5160.

52. Zhao, L. D.; Wu, H. J.; Hao, S. Q.; Wu, C. I.; Zhou, X. Y.; Biswas, K.; He, J. Q.; Hogan, T. P.; Uher, C.; Wolverton, C.; Dravid, V. P.; Kanatzidis, M. G., All-scale hierarchical thermoelectrics: MgTe in PbTe facilitates valence band convergence and suppresses bipolar thermal transport for high performance. *Energy Environ. Sci.* **2013,** *6* (11), 3346-3355.

53. Slack, G. A., New materials and performance limits for thermoelectric cooling. In *CRC Handbook of Thermoelectrics*, D.M. Rowe, ed. CRC Press, Boca Raton, FL, chap. 34. **1995**.

54. Paschen, S.; Godart, C.; Grin, Y., Recent Progress in the Development of Thermoelectric Materials with Complex Crystal Structures. In *Complex Metallic Alloys*, Wiley-VCH: **2010**; pp 365-384.

55. Morelli, D. T.; Jovovic, V.; Heremans, J. P., Intrinsically minimal thermal conductivity in cubic I-V-VI(2) semiconductors. *Phys. Rev. Lett.* **2008,** *101* (3), 4.

56. Li, C. W.; Ma, J.; Cao, H. B.; May, A. F.; Abernathy, D. L.; Ehlers, G.; Hoffmann, C.; Wang, X.; Hong, T.; Huq, A.; Gourdon, O.; Delaire, O., Anharmonicity and atomic distribution of SnTe and PbTe thermoelectrics. *Phys. Rev. B* **2014,** *90* (21).

57. Liu, H. L.; Shi, X.; Xu, F. F.; Zhang, L. L.; Zhang, W. Q.; Chen, L. D.; Li, Q.; Uher, C.; Day, T.; Snyder, G. J., Copper ion liquid-like thermoelectrics. *Nat. Mater.* **2012,** *11* (5), 422-425.

58. Qiu, W.; Xi, L.; Wei, P.; Ke, X.; Yang, J.; Zhang, W., Part-crystalline part-liquid state and rattling-like thermal damping in materials with chemical-bond hierarchy. *Proc. Natl. Acad. Sci. U. S. A.* **2014,** *111* (42), 15031-15035.

59. Grin, Y., Inhomogeneity and anisotropy of chemical bonding and thermoelectric properties of materials. *J. Solid State Chem.* **2018**, DOI: https://doi.org/10.1016/j.jssc.2018.12.055.

60. Huang, L. H.; Zhang, Q. Y.; Yuan, B.; Lai, X.; Yan, X.; Ren, Z. F., Recent progress in half-Heusler thermoelectric materials. *Mater. Res. Bull.* **2016,** *76*, 107-112.

61. Gayner, C.; Kar, K. K., Recent advances in thermoelectric materials. *Prog. Mater. Sci.* **2016,** *83*, 330-382.

62. Delaire, O.; Ma, J.; Marty, K.; May, A. F.; McGuire, M. A.; Du, M. H.; Singh, D. J.; Podlesnyak, A.; Ehlers, G.; Lumsden, M. D.; Sales, B. C., Giant anharmonic phonon scattering in PbTe. *Nat. Mater.* **2011,** *10* (8), 614-619.

References

63. LaLonde, A. D.; Pei, Y.; Wang, H.; Snyder, G. J., Lead telluride alloy thermoelectrics. *Mater. Today* **2011,** *14* (11), 526-532.

64. Zhu, H.; Sun, W.; Armiento, R.; Lazic, P.; Ceder, G., Band structure engineering through orbital interaction for enhanced thermoelectric power factor. *Appl. Phys. Lett.* **2014,** *104*, 082107.

65. Pei, Y. Z.; LaLonde, A.; Iwanaga, S.; Snyder, G. J., High thermoelectric figure-of-merit in heavy hole dominated PbTe. *Energy Environ. Sci.* **2011,** *4* (6), 2085-2089.

66. Ravich, Y. I.; Efimova, B. A.; Smirnov, I. A., *Semiconducting Lead Chalcogenides*. Plenum Press: **1970**.

67. Smith, R. A., The electronic and optical properties of the lead sulphide group of semi-conductors. *Physica* **1954,** *20* (7–12), 910-929.

68. Allgaier, R. S.; Scanlon, W. W., Mobility of Electrons and Holes in PbS, PbSe, and PbTe between Room Temperature and 4.2 K. *Phys. Rev.* **1958,** *111* (4), 1029-1037.

69. Miller, E.; Komarek, K.; Cadoff, I., Interrelation of Electronic Properties and Defect Equilibria in PbTe. *J. Appl. Phys.* **1961,** *32* (11), 2457-2465.

70. Allgaier, R. S.; Houston, B. B., Hall Coefficient Behavior and the Second Valence Band in Lead Telluride. *J. Appl. Phys.* **1966,** *37* (1), 302-309.

71. Tauber, R. N.; Machonis, A. A.; Cadoff, I. B., Thermal and Optical Energy Gaps in PbTe. *J. Appl. Phys.* **1966,** *37* (13), 4855-4860.

72. Dalven, R., A review of the semiconductor properties of PbTe, PbSe, PbS and PbO. *Infrared Phys.* **1969,** *9* (4), 141-184.

73. Brebrick, R. F.; Allgaier, R. S., Composition Limits of Stability of PbTe. *J. Chem. Phys.* **1960,** *32* (6), 1826-1831.

74. Hansen, M.; Anderko, K., Constitution of Binary AllOYS, 2nd ed. *McGraw-Hill, New York* **1958**.

75. Lin, J. C.; Hsleh, K. C.; Sharma, R. C.; Chang, Y. A., The Pb-Te (lead-tellurium) system. *Bulletin of Alloy Phase Diagrams* **1989,** *10* (4), 340-347.

76. Chou, N.; Komarek, K.; Miller, E., Retrograde Solubility of PbS, PbSe, and PbTe. *Trans. Metall. Aime* **1969,** *245* (7), 1553-1560.

77. Brebrick, R. F., Analysis of the solidus lines for PbTe and SnTe. *J. Electron. Mater.* **1977,** *6* (6), 659-692.

78. Ngai, T. L.; Marshall, D.; Sharma, R. C.; Chang, Y. A., Thermodynamic properties and phase equilibria of the lead-tellurium binary system. *Monatshefte für Chemie / Chemical Monthly* **1987,** *118* (3), 277-300.

79. Sealy, B. J.; Crocker, A. J., The P–T–*x* phase diagram of PbTe and PbSe. *J. Mater. Sci.* **1973,** *8* (12), 1737-1743.

80. Avetisov, I. K.; Kharif, Y. L.; Kovtunenko, P. V., Determination of the range of homogeneity of lead telluride. *Inorg. Mater.* **1987,** *23* (3), 455-457.

81. Bajaj, S.; Pomrehn, G. S.; Doak, J. W.; Gierlotka, W.; Wu, H.-j.; Chen, S.-W.; Wolverton, C.; Goddard, W. A., III; Snyder, G. J., Ab initio study of intrinsic point defects in PbTe: an insight into phase stability. *Acta Mater.* **2015,** *92*, 72-80.

82. Brebrick, R. F.; Gubner, E., Composition Stability Limits of PbTe. II. *J. Chem. Phys.* **1962,** *36* (5), 1283-1289.

83. Masatomo, F.; Yasuo, S., P–T–*x* Phase Diagram of the Lead Telluride System. *Jpn. J. Appl. Phys.* **1966,** *5* (2), 128.

84. Scanlon, W. W., Precipitation of Te and Pb in PbTe crystals. *Phys. Rev.* **1962,** *126* (2), 509-512.

85. Strauss, A. J., Effect of Pb- and Te-saturation on carrier concentrations in impurity-doped PbTe. *J. Electron. Mater.* **1973,** *2* (4), 553-569.

86. Shogenji, K.; Uchiyama, S., On Electrical Resistivity and Hall Coefficient of PbTe Crystals. *J. Phys. Soc. Jpn* **1957,** *12* (3), 252-258.

87. Putley, E. H., The Hall Coefficient, Electrical Conductivity and Magneto-Resistance Effect of Lead Sulphide, Selenide and Telluride. *Proc. Phys. Soc. Sect. B* **1955,** *68* (1), 22.

88. Crocker, A. J.; Rogers, L. M., Interpretation of the Hall coefficient, electrical resistivity and Seebeck coefficient of p-type lead telluride. *Brit. J. Appl. Phys.* **1967,** *18*, 563.

89. Breschi, R.; Olivi, A.; Camanzi, A.; Fano, V., Induced defects in sintered lead telluride. *J. Mater. Sci.* **1980,** *15* (4), 918-924.

90. Schmitz, A.; de Boor, J.; Mull, K.; Muller, E., Tailoring the mechanical properties of thermoelectric lead telluride by alloying with non-doping calcium. *J. Mater. Sci.* **2016,** *51* (14), 6933-6943.

References

91. Wang, X.-K.; Veremchuk, I.; Bobnar, M.; Zhao, J.-T.; Grin, Y., Solid solution $Pb_{1-x}Eu_xTe$: constitution and thermoelectric behavior. *Inorg. Chem. Front.* **2016,** *3* (9), 1152-1159.

92. Schmitz, A.; Stiewe, C.; Zabrocki, K.; de Boor, J.; Mull, K.; Muller, E., Current assisted sintering of PbTe-Effects on thermoelectric and mechanical properties. *Mater. Res. Bull.* **2017,** *86*, 159-166.

93. Hedegaard, E. M. J.; Mamakhel, A. A. H.; Reardon, H.; Iversen, B. B., Functionally Graded $(PbTe)_{1-x}(SnTe)_x$ Thermoelectrics. *Chem. Mater.* **2018,** *30* (1), 280-287.

94. Kovalchik, T. L.; Maslakovets, I. P., Effect of impurities on the electrical properties of lead telluride. *Sov. Phys.-Tech. Phys.* **1956,** *1* (11), 2337-2349.

95. Boltaks, B. I.; Mokhov, I. N., The diffusion of lead in lead telluride. *Sov. Phys.-Tech. Phys.* **1956,** *1* (11), 2366-2368.

96. Boltaks, B. I.; Mokhov, I. N., Self-diffusion and diffusion of impurities in lead telluride and selenide. *Sov. Phys.-Tech. Phys.* **1958,** *3* (5), 974-977.

97. George, T. D.; Jr., J. B. W., Tracer Diffusion of Lead in Lead Telluride. *J. Appl. Phys.* **1971,** *42* (1), 220-221.

98. Gomez, M. P.; Stevenson, D. A.; Huggins, R. A., Self-diffusion of Pb and Te in lead telluride. *J. Phys.Chem. Solids* **1971,** *32* (2), 335-344.

99. Simirskii, Y. N.; Firsova, L. P., Tellurium self-diffusion and point defects in lead telluride. *Inorg. Mater.* **1982,** *18* (9), 1291-1294.

100. Wienecke, M.; Schenk, M., In-situ high-temperature hall and conductivity measurements for investigations of the stability region of PbTe. *Physica Status Solidi a-Appl. Res.* **1987,** *101*, 115-122.

101. Schenk, M.; Berger, H.; Klimakow, A.; Mühlberg, M.; Wienecke, M., Nonstoichiometry and point defects in PbTe. *Crys. Res. Tech.* **1988,** *23* (1), 77-84.

102. Breschi, R.; Camanzi, A.; Fano, V., Defects in PbTe single crystals. *J. Cryst. Growth* **1982,** *58* (2), 399-408.

103. Mühlberg, M.; Hesse, D., TEM precipitation studies in Te-rich as-grown PbTe single crystals. *Phys. status solidi (a)* **1983,** *76* (2), 513-524.

104. Wang, G.; Shi, T.; Zhang, S., Microdefects in Te-Rich PbTe Bulk Crystal. *Chin. Phys. Lett.* **1995,** *12* (8), 469.

105.   Wang, H.; Zhang, Q.; Yu, B.; Wang, H.; Liu, W.; Chen, G.; Ren, Z., Transmission electron microscopy study of Pb-depleted disks in PbTe-based alloys. *J. Mater. Res.* **2011,** *26* (07), 912-916.

106.   Bozin, E. S.; Malliakas, C. D.; Souvatzis, P.; Proffen, T.; Spaldin, N. A.; Kanatzidis, M. G.; Billinge, S. J. L., Entropically Stabilized Local Dipole Formation in Lead Chalcogenides. *Science* **2010,** *330* (6011), 1660-1663.

107.   Kastbjerg, S.; Bindzus, N.; Sondergaard, M.; Johnsen, S.; Lock, N.; Christensen, M.; Takata, M.; Spackman, M. A.; Iversen, B. B., Direct Evidence of Cation Disorder in Thermoelectric Lead Chalcogenides PbTe and PbS. *Adv. Funct. Mater.* **2013,** *23* (44), 5477-5483.

108.   Jensen, K. M. Ø.; Božin, E. S.; Malliakas, C. D.; Stone, M. B.; Lumsden, M. D.; Kanatzidis, M. G.; Shapiro, S. M.; Billinge, S. J. L., Lattice dynamics reveals a local symmetry breaking in the emergent dipole phase of PbTe. *Phys. Rev. B* **2012,** *86*, 085313.

109.   Keiber, T.; Bridges, F.; Sales, B. C., Lead Is Not Off Center in PbTe: The Importance of r-Space Phase Information in Extended X-Ray Absorption Fine Structure Spectroscopy. *Phys. Rev. Lett.* **2013,** *111*, 095504.

110.   Chen, Y.; Ai, X. Y.; Marianetti, C. A., First-Principles Approach to Nonlinear Lattice Dynamics: Anomalous Spectra in PbTe. *Phys. Rev. Lett.* **2014,** *113*, 105501.

111.   Knight, K. S., A high-resolution neutron powder diffraction investigation of galena (PbS) between 10 K and 350 K: no evidence for anomalies in the lattice parameters or atomic displacement parameters in galena or altaite (PbTe) at temperatures corresponding to the saturation of cation disorder. *J. Phys.-Cond. Matter* **2014,** *26*, 385403.

112.   Shiga, T.; Murakami, T.; Hori, T.; Delaire, O.; Shiomi, J., Origin of anomalous anharmonic lattice dynamics of lead telluride. *Appl. Phys. Express* **2014,** *7*,041801.

113.   Christensen, S.; Bindzus, N.; Sist, M.; Takata, M.; Iversen, B. B., Structural disorder, anisotropic micro-strain and cation vacancies in thermo-electric lead chalcogenides. *Phys. Chem. Chem. Phys.* **2016,** *18* (23), 15874-15883.

114.   Crocker, A. J., The role of sodium in lead telluride. *J. Phys. Chem. Solids* **1967,** *28* (10), 1903-1912.

115.   Crocker, A. J.; Dorning, B. F., Diffusion of sodium in lead telluride. *J. Phy. Chem. Solids* **1968,** *29*, 155-161.

References

116.	Ahmad, S.; Mahanti, S. D.; Hoang, K.; Kanatzidis, M. G., Ab initio studies of the electronic structure of defects in PbTe. *Phys. Rev. B* **2006,** *74*, 155205.

117.	Hoang, K.; Mahanti, S. D.; Kanatzidis, M. G., Impurity clustering and impurity-induced bands in PbTe-, SnTe-, and GeTe-based bulk thermoelectrics. *Phys. Rev. B* **2010,** *81*, 115106.

118.	Androulakis, J.; Todorov, I.; Chung, D. Y.; Ballikaya, S.; Wang, G. Y.; Uher, C.; Kanatzidis, M., Thermoelectric enhancement in PbTe with K or Na codoping from tuning the interaction of the light- and heavy-hole valence bands. *Phys. Rev. B* **2010,** *82*, 115209.

119.	Giraldo-Gallo, P.; Sangiorgio, B.; Walmsley, P.; Silverstein, H. J.; Fechner, M.; Riggs, S. C.; Geballe, T. H.; Spaldin, N. A.; Fisher, I. R., Fermi surface evolution of Na-doped PbTe studied through density functional theory calculations and Shubnikov-de Haas measurements. *Phys. Rev. B* **2016,** *94*, 195141.

120.	Müller, U., The Effective Size of Atoms. In *Inorganic Structural Chemistry*, John Wiley & Sons, Ltd: 2007; pp 45-51.

121.	Cohen, I.; Kaller, M.; Komisarchik, G.; Fuks, D.; Gelbstein, Y., Enhancement of the thermoelectric properties of n-type PbTe by Na and Cl co-doping. *J. Mater. Chem. C* **2015,** *3* (37), 9559-9663.

122.	Pei, Y. Z.; LaLonde, A. D.; Heinz, N. A.; Snyder, G. J., High Thermoelectric Figure-of-merit in PbTe Alloys Demonstrated in PbTe-CdTe. *Adv. Energy Mater.* **2012,** *2* (6), 670-675.

123.	Pei, Y. Z.; Wang, H.; Gibbs, Z. M.; LaLonde, A. D.; Snyder, G. J., Thermopower enhancement in $Pb_{1-x}Mn_x$Te alloys and its effect on thermoelectric efficiency. *NPG Asia Mater.* **2012,** *4*, 1-6.

124.	Biswas, K.; He, J.; Wang, G.; Lo, S.-H.; Uher, C.; Dravid, V. P.; Kanatzidis, M. G., High thermoelectric figure-of-merit in nanostructured *p*-type PbTe-MTe (M = Ca, Ba). *Energy Environ. Sci.* **2011,** *4* (11), 4675-4684.

125.	Ohta, M.; Biswas, K.; Lo, S.-H.; He, J.; Chung, D. Y.; Dravid, V. P.; Kanatzidis, M. G., Enhancement of Thermoelectric Figure-of-merit by the Insertion of MgTe Nanostructures in *p*-type PbTe Doped with Na_2Te. *Adv. Energy Mater.* **2012,** *2* (9), 1117-1123.

126.	Ahn, K.; Biswas, K.; He, J.; Chung, I.; Dravid, V.; Kanatzidis, M. G., Enhanced thermoelectric properties of p-type nanostructured PbTe-MTe (M = Cd, Hg) materials. *Energy Environ. Sci.* **2013,** *6* (5), 1529-1537.

127.	Jian, Z.; Chen, Z.; Li, W.; Yang, J.; Zhang, W.; Pei, Y., Significant band engineering effect of YbTe for high performance thermoelectric PbTe. *J. Mater. Chem. C* **2015,** *3* (48), 12410-12417.

128.	Luo, J.; You, L.; Zhang, J.; Guo, K.; Zhu, H.; Gu, L.; Yang, Z.; Li, X.; Yang, J.; Zhang, W., Enhanced Average Thermoelectric Figure-of-merit of the PbTe–SrTe–MnTe Alloy. *ACS Appl. Mater. Interfaces* **2017,** *9* (10), 8729-8736.

129.	Chen, Z.; Jian, Z.; Li, W.; Chang, Y.; Ge, B.; Hanus, R.; Yang, J.; Chen, Y.; Huang, M.; Snyder, G. J.; Pei, Y., Lattice Dislocations Enhancing Thermoelectric PbTe in Addition to Band Convergence. *Adv. Mater.* **2017**, 1606768.

130.	Zhu, T. J.; Liu, Y. T.; Fu, C. G.; Heremans, J. P.; Snyder, J. G.; Zhao, X. B., Compromise and Synergy in High-Efficiency Thermoelectric Materials. *Adv. Mater.* **2017,** *29* (14), 1605884.

131.	Allgaier, R. S., Valence Bands in Lead Telluride. *J. Appl. Phys.* **1961,** *32* (10), 2185-2189.

132.	Pei, Y.; LaLonde, A. D.; Wang, H.; Snyder, G. J., Low effective mass leading to high thermoelectric performance. *Energy Environ. Sci.* **2012,** *5* (7), 7963-7969.

133.	Tan, G.; Shi, F.; Hao, S.; Zhao, L.-D.; Chi, H.; Zhang, X.; Uher, C.; Wolverton, C.; Dravid, V. P.; Kanatzidis, M. G., Non-equilibrium processing leads to record high thermoelectric figure-of-merit in PbTe-SrTe. *Nat. Commun.* **2016,** *7*, 1-9.

134.	Zhang, J.; Wu, D.; He, D.; Feng, D.; Yin, M.; Qin, X.; He, J., Extraordinary Thermoelectric Performance Realized in *n*-Type PbTe through Multiphase Nanostructure Engineering. *Adv. Mater.* **2017,** *29* (39), 1703148.

135.	LaLonde, A. D.; Pei, Y. Z.; Snyder, G. J., Reevaluation of PbTe$_{1-x}$I$_x$ as high performance *n*-type thermoelectric material. *Energy Environ. Sci.* **2011,** *4* (6), 2090-2096.

136.	He, J. Q.; Sootsman, J. R.; Girard, S. N.; Zheng, J. C.; Wen, J. G.; Zhu, Y. M.; Kanatzidis, M. G.; Dravid, V. P., On the Origin of Increased Phonon Scattering in Nanostructured PbTe Based Thermoelectric Materials. *J. Am. Chem. Soc.* **2010,** *132* (25), 8669-8675.

References

137. Li, J. Q.; Li, S. P.; Wang, Q. B.; Wang, L.; Liu, F. S.; Ao, W. Q., Effect of Ce-Doping on Thermoelectric Properties in PbTe Alloys Prepared by Spark Plasma Sintering. *J. Electron. Mater.* **2011,** *40* (10), 2063-2068.

138. Pei, Y. Z.; May, A. F.; Snyder, G. J., Self-Tuning the Carrier Concentration of PbTe/Ag$_2$Te Composites with Excess Ag for High Thermoelectric Performance. *Adv. Energy Mater.* **2011,** *1* (2), 291-296.

139. Ruan, L.; Luo, J.; Zhu, H.; Zhao, H.; Liang, J., Thermoelectric Properties of Heavily Doped *n*-type Pb$_{1−x}$Y$_x$Te Compounds. *J. Electron. Mater.* **2015,** *44* (10), 3556-3562.

140. Xiao, Y.; Wu, H.; Li, W.; Yin, M.; Pei, Y.; Zhang, Y.; Fu, L.; Chen, Y.; Pennycook, S. J.; Huang, L.; He, J.; Zhao, L.-D., Remarkable roles of Cu to synergistically optimize phonon and carrier transport in *n*-type PbTe-Cu$_2$Te. *J. Am. Chem. Soc.* **2017,** *139* (51), 18732–18738.

141. Dow, H. S.; Oh, M. W.; Kim, B. S.; Park, S. D.; Min, B. K.; Lee, H. W.; Wee, D. M., Effect of Ag or Sb addition on the thermoelectric properties of PbTe. *J. Appl. Phys.* **2010,** *108* (11), 7.

142. Ahn, K.; Li, C.; Uher, C.; Kanatzidis, M. G., Improvement in the Thermoelectric Figure-of-merit by La/Ag Cosubstitution in PbTe. *Chem. Mater.* **2009,** *21* (7), 1361-1367.

143. Pei, Y. Z.; Lensch-Falk, J.; Toberer, E. S.; Medlin, D. L.; Snyder, G. J., High Thermoelectric Performance in PbTe Due to Large Nanoscale Ag$_2$Te Precipitates and La Doping. *Adv. Funct. Mater.* **2011,** *21* (2), 241-249.

144. Falkenbach, O.; Hartung, D.; Klar, P. J.; Koch, G.; Schlecht, S., Thermoelectric Properties of Nanostructured Bismuth-Doped Lead Telluride Bi$_x$(PbTe)$_{1−x}$ Prepared by Co-Ball-Milling. *J. Electron. Mater.* **2014,** *43* (6), 1674-1680.

145. Rawat, P. K.; Paul, B.; Banerji, P., Exploration of Zn Resonance Levels and Thermoelectric Properties in I-Doped PbTe with ZnTe Nanostructures. *Acs Appl. Mater. Interfaces* **2014,** *6* (6), 3995-4004.

146. Jood, P.; Ohta, M.; Kunii, M.; Hu, X.; Nishiate, H.; Yamamoto, A.; Kanatzidis, M. G., Enhanced average thermoelectric figure-of-merit of *n*-type PbTe$_{1-x}$I$_x$-MgTe. *J. Mater. Chem. C* **2015,** *3* (40), 10401-10408.

147.   Bali, A.; Chetty, R.; Sharma, A.; Rogl, G.; Heinrich, P.; Suwas, S.; Misra, D. K.; Rogl, P.; Bauer, E.; Mallik, R. C., Thermoelectric properties of In and I doped PbTe. *J. Appl. Phys.* **2016,** *120,* 175101.

148.   Fu, L.; Yin, M.; Wu, D.; Li, W.; Feng, D.; Huang, L.; He, J., Large enhancement of thermoelectric properties in *n*-type PbTe via dual-site point defects. *Energy Environ. Sci.* **2017,** *10* (9), 2030-2040.

149.   Tan, G.; Stoumpos, C. C.; Wang, S.; Bailey, T. P.; Zhao, L.-D.; Uher, C.; Kanatzidis, M. G., Subtle Roles of Sb and S in Regulating the Thermoelectric Properties of *N*-Type PbTe to High Performance. *Adv. Energy Mater.* **2017**, *7* (18), 1700099.

150.   Xiao, Y.; Li, W.; Chang, C.; Chen, Y.; Huang, L.; He, J.; Zhao, L.-D., Synergistically optimizing thermoelectric transport properties of *n*-type PbTe via Se and Sn co-alloying. *J. Alloy. Compd.* **2017,** *724,* 208-221.

151.   Yang, L.; Chen, Z. G.; Hong, M.; Wang, L. H.; Kong, D. L.; Huang, L. Q.; Han, G.; Zou, Y. C.; Dargusch, M.; Zou, J., *n*-type Bi-doped PbTe Nanocubes with Enhanced Thermoelectric Performance. *Nano Energy* **2017,** *31,* 105-112.

152.   Zhang, Q.; Song, Q.; Wang, X.; Sun, J.; Zhu, Q.; Dahal, K.; Lin, X.; Cao, F.; Zhou, J.; Chen, S.; Chen, G.; Mao, J.; Ren, Z., Deep defect level engineering: a strategy of optimizing the carrier concentration for high thermoelectric performance. *Energy Environ. Sci.* **2018**. *11,* 933-940.

153.   Wang, X.; Veremchuk, I.; Bobnar, M.; Burkhardt, U.; Zhao, J.-T.; Grin, Y., Sodium Substitution in Lead Telluride. *Chem. Mater.* **2018,** *30* (4), 1362-1372.

154. Reinfried, N.; Höhn, P.; Grin, Y. Spark-Plasma Synthesis in an Inert Gas Atmosphere. In *Max-Planck-Institut für Chemische Physik fester Stoffe Scientific Report 2003-2005,* **2006**; pp 28-29.

155.   Finogenova, V. K.; Popovkin, B. A.; Novoselova, A. V., Preparation of sodium telluride. *Russ. J. Inorg. Chem.* **1970,** *15,* 749-751.

156.   Akselrud, L.; Grin, Y., WinCSD: software package for crystallographic calculations (Version 4). *J. Appl. Crystallogr.* **2014,** *47,* 803-805.

157.   Thole, B. T.; van der Laan, G.; Fuggle, J. C.; Sawatzky, G. A.; Karnatak, R. C.; Esteva, J. M., 3*d* x-ray-absorption lines and the $3d^{9} 4f^{n+1}$ multiplets of the lanthanides. *Phys. Rev. B* **1985,** *32* (8), 5107-5118.

158.   Wolfram Research, I., *Mathematica, Version 8.0* **2010**.

References

159.   Wang, H.; Porter, W. D.; Böttner, H.; König, J.; Chen, L.; Bai, S.; Tritt, T. M.; Mayolet, A.; Senawiratne, J.; Smith, C.; Harris, F.; Gilbert, P.; Sharp, J.; Lo, J.; Kleinke, H.; Kiss, L., Transport Properties of Bulk Thermoelectrics: An International Round-Robin Study, Part II: Thermal Diffusivity, Specific Heat, and Thermal Conductivity. *J. Electron. Mater.* **2013**, *42* (6), 1073-1084.

160.   Borup, K. A.; de Boor, J.; Wang, H.; Drymiotis, F.; Gascoin, F.; Shi, X.; Chen, L.; Fedorov, M. I.; Muller, E.; Iversen, B. B.; Snyder, G. J., Measuring thermoelectric transport properties of materials. *Energy Environ. Sci.* **2015**, *8*, 423-435.

161.   Pei, Y. Z.; LaLonde, A. D.; Heinz, N. A.; Shi, X. Y.; Iwanaga, S.; Wang, H.; Chen, L. D.; Snyder, G. J., Stabilizing the Optimal Carrier Concentration for High Thermoelectric Efficiency. *Adv. Mater.* **2011,** *23* (47), 5674-5678.

162.   Kim, H.-S.; Gibbs, Z. M.; Tang, Y.; Wang, H.; Snyder, G. J., Characterization of Lorenz number with Seebeck coefficient measurement. *Apl. Mater.* **2015,** *3*, 041506.

163.   Mühlberg, M., Investigations on the structural perfection of bridgman-grown PbTe single crystals. *Kristall und Technik* **1980**, *15* (5), 565-573.

164.   Miller, E.; Komarek, K.; Cadoff, I., Lead-Tellurium Binary Alloy Phase Diagram. *Trans. AIMM* **1959,** *215*, 882-887.

165.   Lugscheider, W.; Ebel, H.; Langer, G., The phase diagram of Pb–Te system. *Z. Metallkd.* **1965,** *56*, 851-852.

166.   Avetisov, I. K.; Kharif, Y. L.; Kovtunenko, P. V., Determination of the range of homogeneity of lead telluride. *Inorg. Mater.* **1987,** *23* (3), 455-457.

167.   Houston, B.; Strakna, R. E.; Belson, H. S., Elastic Constants, Thermal Expansion, and Debye Temperature of Lead Telluride. *J. Appl. Phys.* **1968,** *39*, 3913-3916.

168.   Yoneda, S.; Kato, M.; Ohsugi, I. J., Anomalous thermal expansion of Pb–Te system semiconductors. *J. Appl. Phys.* **2010,** *107*, 074901.

169.   Liu, W.; Jie, Q.; Kim, H. S.; Ren, Z., Current progress and future challenges in thermoelectric power generation: From materials to devices. *Acta Mater.* **2015,** *87*, 357-376.

170.   Alcock, C. B.; Itkin, V. P.; Horrigan, M. K., Vapour Pressure Equations for the Metallic Elements: 298–2500 K. *Canadian Metallurgical Quarterly* **1984,** *23* (3), 309-313.

171. Huang, Y.; Brebrick, R. F., Partial Pressures and Thermodynamic Properties of PbTe - SnTe Solid and Liquid Solutions with 13, 20, and 100 Mole Percent SnTe. *J. Electr. Soc.* **1988,** *135* (6), 1547-1559.

172. Leute, V.; Schmidtke, H., Untersuchungen zum Diffusionsmechanismus in den quasibiniiren Halbleiterlegierungen (Pb, Sn)Te und (Pb, Sn)Se. *Berichte der Bunsengesellschaft für physikalische Chemie* **1975,** *79* (11), 1134-1140.

173. Fritts, R.W., Lead Telluride Alloys and Junctions, in *Thermoelectric Materials and Devices*, Cadoff I.B. and Miller E., Ed., Reinhold Publishing Corporation, New York, *1960*, 143–162.

174. Partin, D. L., Lead telluride doped with rare-earth elements. *J. Appl. Phys.* **1985,** *57* (6), 1997-2000.

175. Alekseeva, G. T.; Vedernikov, M. V.; Gurieva, E. A.; Konstantinov, P. P.; Prokof'eva, L. V.; Ravich, Y. I., Donorlike behavior of rare-earth impurities in PbTe. *Semiconductors* **1998,** *32* (7), 716-719.

176. Gromovoi, Y. S.; Darchuk, S. D.; Konovalov, V. N.; Lakeenkov, V. M.; Plyatsko, S. V.; Sizov, F. F., State of Eu and Mn in lead telluride. *Soviet Physics Semiconductors-Ussr* **1989,** *23*, 639-643.

177. Volkov, B. A.; Ryabova, L. I.; Khokhlov, D. R., Mixed-valence impurities in lead telluride-based solid solutions. *Physics-Uspekhi* **2002,** *45*, 819-846.

178. Iida, M.; Shimizu, T.; Enomoto, H.; Ozaki, H., Experimental Studies on the Electronic Structure of $Pb_{1-x}Eu_xTe$. *Jpn. J. Appl. Phys. Part 1* **1993,** *32* (10), 4449-4453.

179. Syoji, T.; Miyahara, Y.; Ozaki, H., Tunneling study of the valence band structure of $Pb_{1-x}Eu_xTe$. *Jpn. J. Appl. Phys. Part 2 - Lett.* **1996,** *35* (4B), L471-L472.

180. Casian, A.; Sur, I.; Scherrer, H.; Dashevsky, Z., Thermoelectric properties of *n*-type $PbTe/Pb_{1-x}Eu_xTe$ quantum wells. *Phys. Rev. B* **2000,** *61* (23), 15965-15974.

181. Sur, I.; Casian, A.; Balandin, A., Electronic thermal conductivity and thermoelectric figure-of-merit of *n*-type $PbTe/Pb_{1-x}Eu_xTe$ quantum wells. *Phys. Rev. B* **2004,** *69*, 035306.

182. Ishida, A.; Yamada, T.; Cao, D.; Inoue, Y.; Veis, M.; Kita, T., Seebeck effect in PbTe films and EuTe/PbTe superlattices. *J. Appl. Phys.* **2009,** *106*, 023718.

References

183.   Nasibov, I. O.; Sultanov, T. I.; Valiev, V. K.; Alidzhanova, S. M., Properties of $(PbTe)_{1-x}(Eu_2Te_3)_x$ solid-solutions for x less than or equal to 0.14. *Inorg. Mater.* **1987,** *23* (3), 457-458.

184.   Ishida, A.; Matsuura, S.; Mizuno, M.; Sase, Y.; Fujiyasu, H., Properties of $Pb_{1-x}Eu_xTe$ films prepared by hot-wall epitaxy. *J. Appl. Phys.* **1988,** *63* (9), 4572-4574.

185.   Ravot, D., Synthesis and magnetic properties of the $Pb_{1-x}Eu_xTe$ solid solution. *J. Less-Comm. Met.* **1990,** *161* (2), 313-319.

186.   Krenn, H.; Herbst, W.; Pascher, H.; Ueta, Y.; Springholz, G.; Bauer, G., Interband Faraday and Kerr rotation and magnetization of $Pb_{1-x}Eu_xTe$ in the concentration range $0 < x \le 1$. *Phys. Rev. B* **1999,** *60* (11), 8117-8128.

187.   Sadovskaya, O. A.; Yarembash, E. I., Phase diagram of the system Eu-Te. *Izvestiya Akademii Nauk SSSR, Neorganicheskie Materialy* **1970,** *6* (7), 1252-1256.

188.   Pearson's Crystal Data: Crystal Structure Database for Inorganic Compounds. ASM International.

189.   Salamancayoung, L.; Partin, D. L.; Heremans, J., Ordering and stability of $Pb_{1-x}Eu_xTe$ alloys. *J. Appl. Phys.* **1988,** *63* (5), 1504-1508.

190.   He, J.; Zhao, L.-D.; Zheng, J.-C.; Doak, J. W.; Wu, H.; Wang, H.-Q.; Lee, Y.; Wolverton, C.; Kanatzidis, M. G.; Dravid, V. P., Role of Sodium Doping in Lead Chalcogenide Thermoelectrics. *J. Am. Chem. Soc.* **2013,** *135* (12), 4624-4627.

191.   Yamini, S. A.; Ikeda, T.; Lalonde, A.; Pei, Y.; Dou, S. X.; Snyder, G. J., Rational design of p-type thermoelectric PbTe: temperature dependent sodium solubility. *J. Mater. Chem. A* **2013,** *1* (31), 8725-8730.

192.   Kang, C.; Wang, H.; Kim, H.; Kim, S.-J.; Kim, W., Effect of Excess Na on the Morphology and Thermoelectric Properties of $Na_xPb_{1-x}Te_{0.85}Se_{0.15}$. *J. Electron. Mater.* **2014,** *43* (2), 353-358.

193.   Doak, J. W.; Michel, K. J.; Wolverton, C., Determining dilute-limit solvus boundaries in multi-component systems using defect energetics: Na in PbTe and PbS. *J. Mater. Chem. C* **2015,** *3* (40), 10630-10649.

194.   Böttcher, P.; Keller, R., The crystal structure of NaTe and its relationship to tellurium-rich tellurides. *J. Less-Common Met.* **1985,** *109* (2), 311-321.

195.   Finogenova, V. K.; Klimakov, A. M.; Popovkin, B. A.; Novoselova, A. V., The cross sections PbTe–Na_2Te and PbTe–NaTe of the system Na–Te–Pb. *Inorg. Mater.* **1971,** *7*, 1662.

196.   Blum, I. D.; Isheim, D.; Seidman, D. N.; He, J.; Androulakis, J.; Biswas, K.; Dravid, V. P.; Kanatzidis, M. G., Dopant Distributions in PbTe-Based Thermoelectric Materials. *J. Electron. Mater.* **2012,** *41* (6), 1583-1588.

197.   Kim, Y.-J.; Blum, I. D.; He, J.; Kanatzidis, M. G.; Dravid, V. P.; Seidman, D. N., Three-Dimensional Atom-Probe Tomographic Analyses of Lead-Telluride Based Thermoelectric Materials. *Jom* **2014,** *66* (11), 2288-2297.

198.   Kim, Y.-J.; Zhao, L.-D.; Kanatzidis, M. G.; Seidman, D. N., Analysis of Nanoprecipitates in a Na-Doped PbTe–SrTe Thermoelectric Material with a High Figure-of-merit. *ACS Appl. Mater. Interfaces* **2017,** *9* (26), 21791-21797.

199.   He, J.; Androulakis, J.; Kanatzidis, M. G.; Dravid, V. P., Seeing Is Believing: Weak Phonon Scattering from Nanostructures in Alkali Metal-Doped Lead Telluride. *Nano Lett.* **2012,** *12* (1), 343-347.

200.   Dec, S. F.; Maciel, G. E.; Fitzgerald, J. J., Solid-state sodium-23 and aluminum-27 MAS NMR study of the dehydration of $Na_2O.Al_2O_3.3H_2O$. *J. Am. Chem. Soc.* **1990,** *112* (25), 9069-9077.

201.   Nemov, S. A.; Ravich, Y. I., Thallium-doped lead chalcogenides: investigation methods and properties. *Uspekhi Fiz. Nauk* **1998,** *168* (8), 817-842.

202.   Wang, X.; Veremchuk, I.; Burkhardt, U.; Bobnar, M.; Böttner, H.; Kuo, C.-Y.; Chen, C.-T.; Chang, C.-F.; Zhao, J.-T.; Grin, Y., Thermoelectric stability of Eu- and Na-substituted PbTe. *J. Mater. Chem. C* **2018,** *6*, 9482-9493.

203.   Jovovic, V.; Thiagarajan, S. J.; West, J.; Heremans, J. P.; Story, T.; Golacki, Z.; Paszkowicz, W.; Osinniy, V., Transport and magnetic properties of dilute rare-earth-PbSe alloys. *J. Appl. Phys.* **2007,** *102*, 043707.

204.   Wiendlocha, B.; Kim, S.; Lee, Y.; He, B.; Lehr, G.; Kanatzidis, M. G.; Morelli, D. T.; Heremans, J. P., Eu^{2+}-Eu^{3+} valence transition in double, Eu-, and Na-doped PbSe from transport, magnetic, and electronic structure studies. *Phys. Chem. Chem. Phys.* **2017,** *19*, 9606-9616.

References

205.	Yamini, S. A.; Brewis, M.; Byrnes, J.; Santos, R.; Manettas, A.; Pei, Y. Z., Fabrication of thermoelectric materials – thermal stability and repeatability of achieved efficiencies. *J. Mater. Chem. C* **2015,** *3* (40), 10610-10615.

206.	Ren, F.; Schmidt, R.; Keum, J. K.; Qian, B. S.; Case, E. D.; Littrell, K. C.; An, K., In situ neutron scattering study of nanoscale phase evolution in PbTe-PbS thermoelectric material. *Appl. Phys. Lett.* **2016,** *109*, 081903.

207.	Su, C. H., Thermal stability of melt grown Tl-doped PbTeSe material for thermoelectric applications. *Mater. Sci. Semicond. Process.* **2016,** *56*, 94-99.

208.	Wang, X.; Guo, K.; Veremchuk, I.; Burkhardt, U.; Prots, Y.; Zhao, J.-T., Preparation and bulk thermoelectric properties of PbTe-based multinary systems. *ICT & ECT 2015, Dresden* **2015**.

209.	Grin, Y.; Fedorchuk, A. A., *Russ. Metall* **1992,** *5*, 197-200.

210.	Coaquira, J. A. H.; Chitta, V. A.; Oliveira, N. F.; Rappl, P. H. O.; Ueta, A. Y.; Abramof, E.; Bauer, G., Electrical characterization of p-type $Pb_{1-x}Eu_xTe$. *J. Supercond.* **2003,** *16* (1), 115-118.

Acknowledgements

When looking at the scenario of my PhD journey, I truly want to acknowledge those people who have contributed to this thesis and supported me in one way or another during this amazing journey.

I would like to express my sincere gratitude to my advisor Prof. Juri Grin. Thank you for accepting me as a PhD student in your esteemed group. As the busiest one in the group, you are truly willing to spend a lot of time on your PhD students. You cared about every detail on improving my working ability as well as my research progress. I have learnt a lot from you in our each discussion about my research projects and scientific manuscripts.

Dear Dr. Igor Veremchuk, my supervisor, thank you so much for your daily instructions and discussions. You are the most responsible supervisor. You taught me how to use those instruments and how to communicate with other departments in our institute. You came to my office almost every day and discussed each new result and idea. At the same time, you cared about my personal life and gave me encouragement. It is so great to have one friend like you.

Dear Dr. Harald Böttner, I am very grateful and fortunate to have one supervisor like you with extreme patience and kindness, immense knowledge and a precise scientist. Thank Prof. Grin again for introducing you to me and giving me opportunities to learn from you. You have taught me how a paper should be written and how a conference poster should be presented. Thank you very much!

Sincere gratitude to my previous advisor Prof. Dr. Jing-Tai Zhao, who has introduced me to the world of scientific research since the beginning of my Master study and continued guiding me during my doctoral study.

I am very grateful to Prof. Dr. Michael Ruck as my second referee, your interest in this work and helpful discussions and comments.

I am very grateful to my committee members for serving on my doctoral committee and for their insightful comments.

Many special thanks to my colleagues and collaborators: Dr. Ulrich Burkhardt, Sylvia Kostmann and Petra Scheppan for microscopy analysis; Dr. Matej Bobnar for low

Acknowledgements

Xinke Wang

MPI CPfS, Dresden

January 2019

Versicherung

Hiermit versichere ich, dass ich die vorliegende Arbeit ohne unzulässige Hilfe Dritter und ohne Benutzung anderer als der angegebenen Hilfsmittel angefertigt habe; die aus fremden Quellen direkt oder indirekt übernommenen Gedanken sind als solche kenntlich gemacht. Die Arbeit wurde bisher weder im Inland noch im Ausland in gleicher oder ähnlicher Form einer anderen Prüfungsbehörde vorgelegt.

Die vorliegende Dissertation wurde unter der Leitung von Dr. Igor Veremchuk und Prof. Juri Grin am Max-Planck-Institut für Chemische Physik fester Stoffe im Zeitraum Juli 2015 bis Januar 2019 angefertigt.

_____

(Ort/Datum/Unterschrift)